



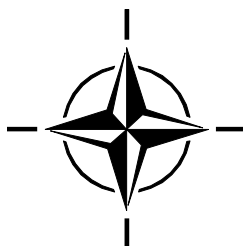
RTO TECHNICAL REPORT

TR-AVT-149

Unsteady Aerodynamics for Micro Air Vehicles

(Aérodynamique instable pour
micro-véhicules aériens)

Final Report of Task Group AVT-149.



Published September 2010





RTO TECHNICAL REPORT

TR-AVT-149

Unsteady Aerodynamics for Micro Air Vehicles

(Aérodynamique instable pour
micro-véhicules aériens)

Final Report of Task Group AVT-149.

The Research and Technology Organisation (RTO) of NATO

RTO is the single focus in NATO for Defence Research and Technology activities. Its mission is to conduct and promote co-operative research and information exchange. The objective is to support the development and effective use of national defence research and technology and to meet the military needs of the Alliance, to maintain a technological lead, and to provide advice to NATO and national decision makers. The RTO performs its mission with the support of an extensive network of national experts. It also ensures effective co-ordination with other NATO bodies involved in R&T activities.

RTO reports both to the Military Committee of NATO and to the Conference of National Armament Directors. It comprises a Research and Technology Board (RTB) as the highest level of national representation and the Research and Technology Agency (RTA), a dedicated staff with its headquarters in Neuilly, near Paris, France. In order to facilitate contacts with the military users and other NATO activities, a small part of the RTA staff is located in NATO Headquarters in Brussels. The Brussels staff also co-ordinates RTO's co-operation with nations in Middle and Eastern Europe, to which RTO attaches particular importance especially as working together in the field of research is one of the more promising areas of co-operation.

The total spectrum of R&T activities is covered by the following 7 bodies:

- AVT Applied Vehicle Technology Panel
- HFM Human Factors and Medicine Panel
- IST Information Systems Technology Panel
- NMSG NATO Modelling and Simulation Group
- SAS System Analysis and Studies Panel
- SCI Systems Concepts and Integration Panel
- SET Sensors and Electronics Technology Panel

These bodies are made up of national representatives as well as generally recognised 'world class' scientists. They also provide a communication link to military users and other NATO bodies. RTO's scientific and technological work is carried out by Technical Teams, created for specific activities and with a specific duration. Such Technical Teams can organise workshops, symposia, field trials, lecture series and training courses. An important function of these Technical Teams is to ensure the continuity of the expert networks.

RTO builds upon earlier co-operation in defence research and technology as set-up under the Advisory Group for Aerospace Research and Development (AGARD) and the Defence Research Group (DRG). AGARD and the DRG share common roots in that they were both established at the initiative of Dr Theodore von Kármán, a leading aerospace scientist, who early on recognised the importance of scientific support for the Allied Armed Forces. RTO is capitalising on these common roots in order to provide the Alliance and the NATO nations with a strong scientific and technological basis that will guarantee a solid base for the future.

The content of this publication has been reproduced
directly from material supplied by RTO or the authors.

Published September 2010

Copyright © RTO/NATO 2010
All Rights Reserved

ISBN 978-92-837-0118-7

Single copies of this publication or of a part of it may be made for individual use only. The approval of the RTA Information Management Systems Branch is required for more than one copy to be made or an extract included in another publication. Requests to do so should be sent to the address on the back cover.

Table of Contents

	Page
List of Figures	vi
List of Tables	x
Programme Committee	xi
 Executive Summary and Synthèse	 ES-1
 Chapter 1 – Introduction	 1-1
1.1 Philosophical Preliminaries	1-1
1.2 Résumé of Prior Research in 2D Pitching and Plunging	1-2
1.3 Hierarchy of Analysis for Unsteady Airfoil and Wing Aerodynamics	1-3
1.3.1 Classical Methods and Closed-Form Solutions	1-3
1.3.1.1 Further Remarks on Theodorsen’s Method	1-4
1.3.1.2 Modern Extensions of Classical Methods	1-4
1.3.2 Viscous Solutions and Modelling	1-5
1.3.2.1 3D Effects	1-5
1.3.2.2 Importance in Capturing Transition for Low Reynolds Number Unsteady Aerodynamics Computations	1-6
1.4 The Different Kinds of Flapping in Nature	1-6
1.4.1 Large Birds in Forward Flight	1-10
1.4.2 Medium Birds in Forward Flight, Hovering Flight (Large and Medium)	1-11
1.4.3 Small Birds and Insects in Forward Flight or Hover	1-11
1.5 The Need for Canonical Problems	1-12
1.5.1 From Fundamental Research to Applications	1-13
1.5.2 Role of Longitudinal Problems	1-13
1.6 General Outline of the Report	1-13
1.6.1 Listing of the Cases and Philosophy for Why They Were Chosen	1-13
1.6.1.1 Airfoils	1-13
1.6.1.2 Flat Plates – Wall-to-Wall	1-15
1.6.1.3 Flat Plates of Finite Aspect Ratio	1-15
 Chapter 2 – Facilities and Methods	 2-1
2.1 General Comments	2-1
2.2 Water Tunnels and Water Tow Tanks	2-1
2.2.1 University of Michigan Water Tunnel	2-1
2.2.2 U.S. Air Force Research Laboratory Water Tunnel	2-3
2.2.3 Cambridge University Towing Tank	2-5
2.2.4 ONERA Tow Tank	2-6

2.3	Wind Tunnels	2-7
2.3.1	Technical University of Braunschweig Wind Tunnel	2-7
2.3.2	DLR Wind Tunnel PIV Measurements	2-10
2.3.3	TU Darmstadt Wind Tunnel	2-11
2.3.4	University of Florida Wind Tunnel	2-14
2.4	Force Balances	2-15
2.4.1	AFRL Fibre-Bragg Grating Balance	2-15
2.4.2	Cambridge University External Balance	2-16
2.4.3	TU Braunschweig Internal Balance	2-17
2.4.4	ONERA Force Balance	2-17
2.4.5	TU Darmstadt Force Balance	2-18
2.5	Computational Methods	2-20
2.5.1	AFRL Implicit Large Eddy Simulation	2-20
2.5.2	AFRL Vortex-Particle Method	2-21
2.5.3	METU RANS Approach	2-22
2.5.4	University of Michigan RANS Approach	2-23
2.5.5	TU Darmstadt RANS Approach	2-24
2.5.6	NRC Large Eddy Simulation	2-26
2.5.7	U of Toronto Lumped-Vortex Model	2-26

Chapter 3 – Pure-Plunge of the SD7003 Airfoil **3-1**

3.1	Résumé of Experimental and Computational Results for the Flowfield: Velocity and Vorticity	3-1
3.1.1	Computations	3-1
3.1.2	Experiments	3-6
3.2	Reynolds Number Effects	3-9
3.3	Aerodynamic Force Coefficients	3-13

Chapter 4 – Combined Pitch-Plunge of the SD7003 Airfoil **4-1**

4.1	Résumé of Experimental and Computational Results for the Flowfield: Velocity and Vorticity	4-1
4.1.1	Computations	4-1
4.1.2	Experiments	4-4
4.2	Reynolds Number Effects	4-10
4.3	Aerodynamic Force Coefficients	4-13

Chapter 5 – Plunge and Pitch-Plunge of a Flat Plate **5-1**

5.1	Résumé of Experimental and Computational Results for the Flowfield: Velocity and Vorticity	5-1
5.1.1	Computations, Pitching-Plunging Plate	5-1
5.1.2	Experiments, Pitching-Plunging Plate	5-3
5.2	Reynolds Number Effects	5-5
5.2.1	Computations, Plate in Pure-Plunge	5-6
5.2.2	Experiments, Plate in Pure-Plunge	5-8
5.3	Aerodynamic Force Coefficients for the Flat Plate	5-9

5.3.1	Pure-Plunge	5-9
5.3.2	Pitch-Plunge	5-10

Chapter 6 – Finite Aspect Ratio Effects: Plunge and Pitch-Plunge of an Aspect Ratio 2 Flat Plate **6-1**

6.1	Motivations and Problem Definition	6-1
6.2	The Pure-Plunge Case	6-1
6.2.1	Computations, AR = 2 Plate in Pure-Plunge	6-1
6.2.2	Experiments, AR = 2 Plate in Pure-Plunge	6-2
6.3	The Pitch-Plunge Case	6-6
6.3.1	Computations, Pitching-Plunging Plate, AR = 2	6-6
6.3.2	Experiments, Pitching-Plunging Plate, AR = 2	6-7
6.4	Aerodynamic Force Time Histories for the AR = 2 Flat Plate	6-9
6.4.1	Forces for the AR = 2 Plate in Pitch-Plunge	6-10
6.4.2	Forces for the AR = 2 Plate in Pure-Plunge	6-11
6.5	Experiments on AR = 2 Plate Pure-Plunge at Smaller Strouhal Number	6-13

Chapter 7 – High-Frequency Low-Amplitude Airfoil Pure-Plunge Oscillations **7-1**

7.1	Motivations	7-1
7.2	Flowfield Results	7-1
7.3	Force Computations	7-6

Chapter 8 – Non-Rectilinear Motions: Whirling Flat Plate **8-1**

8.1	Purpose and Type of “Whirling” Motions	8-1
8.1.1	Rotational Motions and Leading Edge Vortex Retention	8-1
8.1.2	Details of Motion Kinematics	8-1
8.2	Force Data	8-2
8.3	Flowfield Measurements with Particle Image Velocimetry	8-6
8.3.1	Vortex Tracking	8-6
8.3.2	Leading Edge Vortex Circulation	8-7
8.3.3	Three-Dimensional Effects	8-9
8.3.4	Flow Model Development	8-10
8.4	Summary of the Whirling Wing Experiments	8-11

Chapter 9 – Conclusions and Outlook **9-1**

9.1	Recapitulation of the Test Cases in the Present Study	9-1
9.2	General Conclusions	9-1
9.3	Recommendations for Further Work	9-2
9.3.1	Extensions of Cases Studied in This Work	9-3
9.3.2	Conceptual Departures Towards Other Kinds of Motions	9-3
9.3.3	Passage to More Flight-Like Problems	9-4

Chapter 10 – References **10-1**

List of Figures

Figure		Page
Figure 1-1	Scaling of Bird Wing Area vs. Body Mass	1-7
Figure 1-2	Weight and Flight Speed for Animals and Aircraft	1-8
Figure 1-3	Maximum Lift Coefficients Reported in Literature for Various Reynolds Numbers	1-9
Figure 1-4	Condor in Fast Forward Flight	1-10
Figure 1-5	Comparison of Inner and Outer Wing Motion for Condor in Fast Flapping Flight	1-10
Figure 1-6	Hovering Flight in Pigeons and Bats	1-11
Figure 1-7	Hummingbird in Hover	1-12
Figure 1-8	Schematic of SD7003 Airfoil and Parameters of Motion	1-14
Figure 1-9	Motion Kinematics and Effective Angle of Attack Time History for Pure-Plunge and Combined Pitch-Plunge	1-14
Figure 2-1	University of Michigan Water Tunnel: Motion Rig Schematic and Installation Above Tunnel Test Section	2-2
Figure 2-2	AFRL Horizontal Free-Surface Water Tunnel; Schematic of Pitch-Plunge Rig and Airfoil Model; SD7003 Airfoil Installed Inside Test Section, Showing Smooth Suction-Side of Airfoil and Plunge Rod Coupling on Pressure-Side of Airfoil	2-4
Figure 2-3	Schematic of Section of CUED Water Tow Tank and “Waving Arm” Setup	2-5
Figure 2-4	ONERA Tow Tank SD7003 Wing Installation; View of Model and Oscillation Rig Atop the Towing Tank	2-7
Figure 2-5	Low-Noise Wind Tunnel of Technische Universität Braunschweig	2-8
Figure 2-6	Arrangement of PIV Interrogation Windows and Stereo PIV Setup Used for the Flowfield Measurements of TUBS	2-9
Figure 2-7	DLR Optical Setup Inside TUBS Wind Tunnel Test Section	2-11
Figure 2-8	Schematic of Wind Tunnel; Note Intake (A-A) and Test Section (C-C) Cross-Sections	2-12
Figure 2-9	Test Section of TU Darmstadt Wind Tunnel, Showing Two Linear Motor Pairs for Tandem-Wing Pitch-Plunge; Only One Set of Motors and One Wing was Used in the Present Study	2-13
Figure 2-10	University of Florida REEF Open-Jet Wind Tunnel; Exterior View and Diffuser Bellmouth as Viewed Inside Chamber Enclosing Test Section	2-14
Figure 2-11	3-Component Force Balance Based on Fibre Bragg Grating (FBG) Sensors, Integrated with Airfoil Mount; Schematic and Photograph from Underside, with Detail of a Flexure Joint	2-15
Figure 2-12	Sampled CUED Tow Tank Force Balance Data, with Various Types of Signal Filtering	2-16
Figure 2-13	Motion Scheme of 3D Model Support and Photo of AR = 2 Flat-Plate Model Mounted in the TUBS Wind Tunnel Test Section	2-17
Figure 2-14	Inertial Tares in Air, ONERA Tow Tank	2-18

Figure 2-15	Location of Piezo-Electric Force Sensors Directly Below SD7003 Profile	2-19
Figure 2-16	Positioning of Dummy Cylinder at Center-of-Mass Position Inside Wind-Tunnel Test Section and Comparison of Dummy Cylinder with Original SD7003 Profile	2-19
Figure 2-17	Computational Mesh for SD7003 Airfoil; Full Grid and Zoomed-In to Airfoil Region	2-23
Figure 2-18	Top: Numerical Domain Representative of Wind-Tunnel Test Section; Bottom: Middle of Domain	2-25
Figure 2-19	UTIAS Lumped Vortex Method: Vortex Panelling for a 3D Rectangular Wing and Schematic of Lag Parameters for Dynamic Stall Model	2-27
Figure 3-1	2D Computations, FDL3DI	3-2
Figure 3-2	3D Computations, FDL3DI	3-3
Figure 3-3	METU Computations, Fluent, 2D	3-4
Figure 3-4	IAR NRC Computations, LES	3-5
Figure 3-5	University of Michigan Computations	3-6
Figure 3-6	AFRL Water Tunnel, Entry #1	3-7
Figure 3-7	AFRL Water Tunnel, Entry #2	3-8
Figure 3-8	University of Michigan PIV	3-9
Figure 3-9	AFRL Water Tunnel Dye Injection for Pure-Plunge	3-10
Figure 3-10	TU Darmstadt PIV and CFD Vorticity Contours	3-12
Figure 3-11	University of Michigan Computations	3-12
Figure 3-12	METU Computations	3-12
Figure 3-13	Lift Coefficient Time History, SD7003 Pure-Plunge	3-13
Figure 3-14	Drag Coefficient Time History, SD7003 Pure-Plunge	3-14
Figure 3-15	Trends in Lift Coefficient and Drag Coefficient for SD7003 Pure-Plunge vs. Reynolds Number (60 K, 30 K and 10 K)	3-15
Figure 3-16	Lift Coefficient and Drag Coefficient Comparison Between METU and Standard vs. Modified UM RANS	3-16
Figure 3-17	Pitching Moment Coefficient for SD7003 Airfoil in Pure-Plunge	3-17
Figure 4-1	METU Computations	4-2
Figure 4-2	IAR NRC Computations, LES	4-3
Figure 4-3	University of Michigan Computations	4-4
Figure 4-4	University of Michigan PIV	4-5
Figure 4-5	AFRL PIV, First Data Series	4-5
Figure 4-6	AFRL PIV, Second Data Series	4-7
Figure 4-7	AFRL PIV, Third Data Series	4-8
Figure 4-8	TUBS PIV	4-8
Figure 4-9	PIV-Derived Planar Turbulent Kinetic Energy Contours, AFRL Data Sets	4-9
Figure 4-10	TU Braunschweig PIV; Contours of Streamwise Velocity and Normalized Reynolds Stress, $-u'v'$, at Motion Phase of 180 Degrees (Bottom of Plunge Downstroke)	4-10
Figure 4-11	TU Darmstadt PIV and CFD Vorticity Contours	4-11

Figure 4-12	University of Michigan Computations	4-12
Figure 4-13	Middle East Technical University Computations	4-12
Figure 4-14	AFRL Water Tunnel Dye Injection	4-13
Figure 4-15	Lift Coefficient Time History, SD7003 Pitch-Plunge	4-13
Figure 4-16	Drag Coefficient Time History, SD7003 Pitch-Plunge	4-14
Figure 4-17	Trends in Lift Coefficient and Drag Coefficient for SD7003 Pitch-Plunge vs. Reynolds Number (60 K, 30 K and 10 K)	4-15
Figure 4-18	Lift Coefficient and Drag Coefficient Comparison Between METU and Standard vs. Modified UM RANS	4-16
Figure 5-1	University of Michigan Computations	5-2
Figure 5-2	Flat-Plate Pitch-Plunge, METU Computations, Fluent, 2D	5-3
Figure 5-3	AFRL Water Tunnel	5-4
Figure 5-4	University of Michigan Water Tunnel	5-4
Figure 5-5	AFRL Water Tunnel Dye Injection for Pitching-Plunging Flat Plate	5-5
Figure 5-6	Flat-Plate Plunge, METU Computations, Fluent, 2D	5-7
Figure 5-7	University of Michigan Computations, Wall-to-Wall Plunging Flat Plate	5-8
Figure 5-8	University of Michigan PIV, Wall-to-Wall Plunging Flat Plate	5-8
Figure 5-9	Lift Coefficient History for the Flat Plate in Pure-Plunge, Plotted vs. Time and Angle of Attack	5-9
Figure 5-10	Drag Coefficient History for the Flat Plate in Pure-Plunge, Plotted vs. Time and Angle of Attack	5-10
Figure 5-11	Lift Coefficient History for the Flat Plate in Pitch-Plunge, Plotted vs. Time and Angle of Attack	5-10
Figure 5-12	Drag Coefficient History for the Flat Plate in Pitch-Plunge, Plotted vs. Time and Angle of Attack	5-11
Figure 6-1	U of Michigan Computations, AR = 2 Plate in Pure-Plunge	6-2
Figure 6-2	PIV, U of Michigan, AR = 2 Plate in Pure-Plunge	6-3
Figure 6-3	PIV, AFRL, AR = 2 Plate in Pure-Plunge	6-5
Figure 6-4	PIV, U of Florida REEF, AR = 2 Plate in Pure-Plunge	6-5
Figure 6-5	U of Michigan Computations, Pitching-Plunging AR = 2 Plate	6-6
Figure 6-6	U of F REEF PIV Results for AR = 2 Plate Pitch-Plunge	6-7
Figure 6-7	AFRL PIV Results for AR = 2 Plate Pitch-Plunge	6-8
Figure 6-8	U of Michigan PIV Results for AR = 2 Plate Pitch-Plunge	6-9
Figure 6-9	Lift Coefficient for AR = 2 Pitching-Plunging Plate; Time History and vs. Angle of Attack	6-10
Figure 6-10	Drag Coefficient for AR = 2 Pitching-Plunging Plate; Time History and vs. Angle of Attack	6-11
Figure 6-11	Lift Coefficient for AR = 2 Plate in Pure-Plunge; Time History and vs. Angle of Attack	6-12
Figure 6-12	Drag Coefficient for AR = 2 Plate in Pure-Plunge; Time History and vs. Angle of Attack	6-12

Figure 6-13	DLR PIV; $k = 0.25$ $h = 0.206$ Pure-Plunge of AR = 2 Plate, with $\alpha(t) \sim$ Pitch-Plunge of $\lambda = 0.6$	6-13
Figure 6-14	DLR PIV; $k = 0.125$ $h = 0.412$ Pure-Plunge of AR = 2 Plate, with $\alpha(t) \sim$ Pitch-Plunge of $\lambda = 0.6$	6-14
Figure 7-1	AFRL PIV; Re = 40 K; Vorticity Contours, $k = 3.93$ Plunge; Phases Phi = 0, 90, 180 and 270; Phase-Averaged Measurements and Representative Instantaneous Measurements	7-2
Figure 7-2	AFRL PIV; Re = 40 K; Velocity Contours, $k = 3.93$ Plunge; Phases Phi = 0, 90, 180 and 270	7-2
Figure 7-3	AFRL LES Computations; Re = 40 K; Vorticity Contours, $k = 3.93$ Plunge; Phases Phi = 0, 90, 180 and 270; Phase-Averaged Measurements and Representative Instantaneous Measurements	7-3
Figure 7-4	AFRL LES Computations; Re = 40 K, Velocity Contours, $k = 3.93$ Plunge; Phases Phi = 0, 90, 180 and 270	7-4
Figure 7-5	AFRL LES Computations; Re = 10 K; Vorticity Contours, $k = 3.93$ Plunge; Phase Phi = 0; Phase-Averaged and Instantaneous; and Phase-Averaged AFRL PIV	7-4
Figure 7-6	UM RANS Computations; Re = 40 K; Velocity Contours, $k = 3.93$ Plunge	7-5
Figure 7-7	UM RANS Computations; Re = 40 K; Vorticity Contours, $k = 3.93$ Plunge	7-5
Figure 7-8	Vortex Particle Calculation for $k = 3.93$ Plunge	7-6
Figure 7-9	Lift Coefficient Time History and vs. Angle of Attack (right); $k = 3.93$ $h = 0.05$ Pure-Plunge of SD7003 Airfoil at Re = 40 K and 10 K	7-7
Figure 7-10	Drag Coefficient Time History; $k = 3.93$ $h = 0.05$ Pure-Plunge of SD7003 Airfoil at Re = 40 K and 10 K	7-7
Figure 8-1	Commanded Wing Kinematics Plotted vs. Time, for First Quarter-Stroke Accelerating Over 0.25 c; Angular Velocity and Acceleration as a Function of Time	8-2
Figure 8-2	Commanded Wing Kinematics Plotted vs. Angular Displacement, for the First Quarter-Stroke; Angular Velocity for a Wing Accelerating Over the First 0.25 c of Travel	8-2
Figure 8-3	Lift Coefficients for a Waving Wing Accelerating Over 0.10 c, 0.25 c, 0.60 c and All Exponential Velocity Profiles	8-3
Figure 8-4	Angular Acceleration for the Three Velocity Profiles: Linear, Sinusoidal and Exponential Over 0.10 c, 0.25 c and 0.60 c	8-4
Figure 8-5	Comparison of Unsteady Lift Coefficients Observed for a Waving Wing and Translating Wing Accelerating Over 0.60 c	8-5
Figure 8-6	Lift Coefficient as a Function of Angle of Attack	8-6
Figure 8-7	Flowfield Observed at Three Points During the Wing Stroke	8-7
Figure 8-8	Normalized Circulation Computed from PIV Data at Half-Span; AR = 4, $\alpha = 25$ deg	8-8
Figure 8-9	Chordwise View of Vorticity ($\omega/U'c$) and Λ -Contours; AR = 4, $\alpha = 25$ deg	8-9
Figure 8-10	Spanwise View of Vorticity ($\omega/U'c$) and Λ -Contours; AR = 4, $\alpha = 25$ deg	8-10
Figure 8-11	Proposed Model of Three Phases of Flowfield Development for the Whirling Plate	8-11

List of Tables

Table		Page
Table 2-1	Summary of 95% Confidence Intervals for UM PIV Data	2-3
Table 2-2	Original and Modified SST Turbulence Model, U of Michigan Computation	2-24
Table 4-1	Mean Lift and Drag Coefficients for SD7003 Pitch-Plunge	4-16
Table 7-1	Computed Integrated Force Coefficients; $k = 3.93$ $h = 0.05$ Pure-Plunge	7-8

Programme Committee

CHAIR

Dr. M.V. OL
Air Force Research Lab, AFRL/RBAA
2130 8th St., Bldg. 45, Wright-Patterson AFB, OH 45433-7542
Email: Michael.Ol@wpafb.af.mil

Members and Associates

AUSTRALIA

Prof. S. WATKINS
RMIT, Bundoora East Campus
264 Plenty Road, Mill Park
Victoria 3082
Email: simon@rmit.edu.au

BELGIUM

Prof. D.R. DECUYPERE
R-D Scientific Consulting
Lombeekstraat 88
B-1790 Affligem
Email: roland.decuypere@skynet.be

CANADA

Dr. E. HANFF
National Research Council Canada
Institute for Aerospace Research
Building M10, 1200 Montreal Road
Ottawa, Ontario K1A 0R6
Email: ernest.hanff@nrc-cnrc.gc.ca

Dr. M. KHALID
National Research Council Canada
Institute for Aerospace Research
1200 Montreal Road
Ottawa, Ontario K1A 0R6
Email: mahmood.khalid@nrc-cnrc.gc.ca

FRANCE

Mr. J-Y. ANDRO
ONERA, Département DAFE
Centre de Meudon
8 rue des Vertugadins
92190 Meudon
Email: jean-yves.andro@onera.fr

Mr. D. BARBERIS
ONERA
8 rue des Vertugadins
92190 Meudon
Email: barberis@onera.fr

Dr. J-B. PAQUET
ONERA
5 Blvd. Painlevé
59045 Lille Cedex
Email: jean-bernard.paquet@onera.fr

GERMANY

Dipl. Ing. S. BANSMER
Institute of Fluid Mechanics
Technical University of Braunschweig
Bienrolder Weg 3
38106 Braunschweig
Email: s.bansmer@tu-bs.de

Prof. Dr. A. DILLMANN
German Aerospace Center
Institute of Aerodynamics and Flow Technology
37073 Göttingen
Email: Andreas.Dillmann@dlr.de

Dr. Ing. R. KONRATH
Institute für Aerodynamik und Strömungstechnik
Experimentelle Verfahren
Bunsenstrasse 10
37073 Göttingen
Email: robert.konrath@dlr.de

Prof. Dr. Ing. R. RADESPIEL
Technical University Braunschweig
3 Bienroder Weg
38106 Braunschweig
Email: r.radespiel@tu-bs.de

GERMANY (cont'd)

Dr. D. RIVAL
Darmstadt University of Technology
Fachgebiet Strömungslehre und Aerodynamik
Flughafenstrasse 19
64347 Griesheim
Email: rival@aero.tu-darmstadt.de

Prof. Dr. C. TROPEA
Technische Universität Darmstadt
Fachgebiet Strömungslehre und Aerodynamik
Petersenstr. 30
64287 Darmstadt
Email: ctropea@sla.tu-darmstadt.de

POLAND

Dr. K. SIBILSKI
Air Force Institute of Technology
Ks Boleslaw 6
P.O. Box 96, 01-494 Warsaw
Email: sibilski@hotmail.pl

SPAIN

Dr. R. BARDERA MORA
INTA
Ctra. Ajalvir, p.k. 4
28850 Torrejón de Ardoz, Madrid
Email: barderar@inta.es

Mr. F. MONGE
INTA
Ctra. Ajalvir, p.k. 4
28850 Torrejón de Ardoz, Madrid
Email: mongef@inta.es

Mrs. S. SALECEDO
Ctra. Ajalvir, p.k. 4
28850 Torrejón de Ardoz
Madrid
Email: sonia.salcedo@inta.es

TURKEY

Assoc. Prof. F.O. EDIS
Istanbul Technical University
Faculty of Aeronautics and Astronautics
Istanbul teknik Universitesi ucak ve Usay
Bilimleri
Fakultesi Maslak Kampüsü
34469 Istanbul
Email: edis@itu.edu.tr

Dr. I. GURSUL
University of Bath
Department of Mechanical Engineering
Bath BA2 7AY
Email: i.a.gursul@bath.ac.uk

Asst. Prof. Dr. D.F. KURTULUS
Middle East Technical University
Aerospace Engineering Department
06531 Ankara
Email: dfunda@ae.metu.edu.tr

Dr. M. TUTAR
Mersin University
Engineering Faculty
Mechanical Engineering
33343 Ciftlikkoy-Mersin
Email: m_tutar@mersin.edu.tr

Prof. F. UNAL
Istanbul Technical University
Uçak Müh Böl
Maslak, Istanbul
Email: munal@itu.edu.tr

UNITED KINGDOM

Dr. H. BABINSKY
University of Cambridge, Engineering Dept.
Cambridge CB2 1PZ
Email: hb@eng.cam.ac.uk

Prof. J.P. GOSTELOW
University of Leicester, Dept. of Engineering
University Road
Leicester LE1 7RH
Email: jpg7@le.ac.uk

UNITED STATES

Dr. G. ABATE
Air Force Research Laboratory
AFRL/RWGN
101 W. Elgin Parkway
Eglin AFB, FL 32542
Email: gregg.abate@eglin.af.mil

Dr. P. BERAN
Air Force Research Laboratory
AFRL/RBSD
2130 Eighth Street
Wright-Patterson AFB, OH 45433-7542
Email: philip.beran@wpafb.af.mil

UNITED STATES (cont'd)

Prof. L. BERNAL
University of Michigan
1320 Beal Avenue
Ann Arbor, MI 48109-2140
Email: lpb@umich.edu

Prof. C. CESNIK
University of Michigan
1320 Beal Avenue
Ann Arbor, MI 48109-2140
Email: Cesnik@umich.edu

Dr. C. COX
Air Force Research Laboratory
AFRL/RBAA
2130 Eighth Street, Bldg. 45
Wright-Patterson AFB, OH 45433
Email: Craig.Cox@wpafb.af.mil

Mr. J. EVERS
Air Force Research Laboratory
AFRL/RWAV
101 W. Eglin Boulevard, Suite 212
Eglin AFB, FL 32542-6810
Email: johnny.evers@eglin.af.mil

Dr. R. GORDNIER
Air Force Research Laboratory
AFRL/RBAC, Bldg. 146
Wright-Patterson AFB, OH, 45433-7512
Email: Raymond.gordnier@wpafb.af.mil

LtCol. R. JEFFERIES
Air Force Research Laboratory, AFOSR/NA
875 N. Randolph Street
Suite 325
Arlington, VA 22203-1768
Email: Rhett.jefferies@afosr.af.mil

Prof. D. ROCKWELL
Department of Mechanical Engineering
Lehigh University
354 Packard
Bethlehem, PA 18015
Email: dor0@lehigh.edu

Prof. W. SHYY
University of Michigan
Department of Aerospace Engineering
3064 FXB, 1320 Beal Avenue
Ann Arbor, MI 48109
Email: weishyy@umich.edu

Dr. D. SMITH
Air Force Office of Scientific Research
875 N. Randolph Street
Suite 325, Room 3112
Arlington, VA 22203
Email: douglas.smith@afosr.af.mil

Dr. S. SURAMPUDI
Air Force Research Laboratory
European Office of Aerospace Research
223/231 Old Marylebone Road
London NW1 5TH
Email: surya.surampudi@london.af.mil

Prof. L. UKEILEY
University of Florida REEF
Dept. of Mechanical and Aerospace Eng.
1350 N. Poquito Road
Shalimar, FL 32579
Email: ukeiley@reef.ufl.edu

Dr. M.R. VISBAL
Air Force Research Lab
AFRL/RBAC, Bldg. 146
Wright-Patterson AFB, OH 45433-7512
Email: Miguel.visbal@wpafb.af.mil

Panel Mentor

Dr. D. BLAKE
U.S. Air Force Research Laboratory, AFRL/RB
2210 8th St., Bldg. 45, Wright Patterson AFB, OH 45433-7512
Email: douglas.blake@wpafb.af.mil

**Additional Contributors
(not noted in above listing)**

CANADA

Mr. T. REICHERT
University of Toronto
4925 Dufferin Street
Toronto, Ontario M3H 5T6
Email: todd.reichert@gmail.com

Dr. W. YUAN
Institute for Aerospace Research
National Research Council Canada
Montreal Road
Ottawa, Ontario K1A 0R6
Email: Weixing.Yuan@nrc-cnrc.gc.ca

TURKEY

Mr. E. GUNAYDINOGLU
Middle East Technical University
Aerospace Engineering Department
06531 Ankara
Email: gunaydin@ae.metu.edu.tr

UNITED KINGDOM

Ms. A. JONES
University of Cambridge
Engineering Department
Cambridge CB2 1PZ
Email: arj28@cam.ac.uk

UNITED STATES

Mr. Y. BAIK
University of Michigan
1320 Beal Avenue
Ann Arbor, MI 48109-2140
Email: yeon.baik@gmail.com

Mr. C.-K. KANG
University of Michigan
1320 Beal Avenue
Ann Arbor, MI 48109-2140
Email: kangck@umich.edu

Unsteady Aerodynamics for Micro Air Vehicles (RTO-TR-AVT-149)

Executive Summary

The flowfield environments encountered by Micro Air Vehicles (MAVs) are fundamentally unsteady – whether for fixed-wing, rotary-wing or flapping-wing configurations. The AVT-149 Task Group addressed fundamental questions in unsteady low Reynolds number aerodynamics, studying computationally, experimentally and analytically a progression of abstracted configurations, from 2D airfoils in pure-plunge through 3D wing planforms in plunge and pitch-plunge. The result was a better understanding of the interplay between the motion, the flowfield, and the aerodynamic loads history.

Research objectives included:

- 1) Extension of prior work on airfoil laminar boundary layers, separation bubbles and transition to unsteady cases, where large excursions in effective angle of attack and production of concentrated vorticity interacts with the transition process to affect integrated forces and moments. The result is an assessment of low Reynolds number effects for MAVs, and survey of how off-the-shelf and research-type computational tools can cope with the subject flowfields.
- 2) Assessment of the relation between vortex shedding (for example, from airfoil leading edges) and the time-dependent integrated aerodynamic forces and moments. How quasi-steady is the force response, and how does it relate to classical dynamic stall? How important is resolution of the flowfield in capturing accurately the time history of lift, drag/thrust, and pitching moment?
- 3) Assessment of configuration effects; we compare a 2D airfoil (the SD7003), a 2D thin flat plate with round edges, and an aspect ratio = 2 thin flat plate with round edges.
- 4) Benchmarking of recently-built facilities and rigs; validation of recently-developed computational fluid dynamics codes; and progress in flowfield diagnostics methods.

By comparing results from 14 research groups, the following conclusions were reached, in brief:

- Airfoils at moderate Reynolds number (10,000 – 60,000) and near-stall peak effective angle of attack are strongly sensitive to boundary layer transition effects.
- On the other hand, high effective angle of attack, well beyond stall, means that effects of transition are of secondary importance, at least for lift production.
- Flat plates with round edges have much lower sensitivity to either Reynolds number or boundary layer transition effects.
- Moderate aspect ratio plates ($AR = 2$) evince flowfield features irreducible to infinite aspect ratio, but the lift and drag history is more quasi-steady and more similar to simple theoretical prediction than what one finds for a wall-to-wall or 2D plate.
- Lift coefficient history is more quasi-steady than the large flow separation would imply, whence low-level methods still have good potential for MAV aerodynamics prediction.
- High-frequency low-amplitude oscillations are dominated by non circulatory effects, whence classical planar-wake models have good predictive utility.
- Comparison of translational vs. rotational impulsive-start problems shows no appreciable difference in lift history, and neither case evinces a stable, attached leading edge vortex.

Aérodynamique instable pour micro-véhicules aériens (RTO-TR-AVT-149)

Synthèse

Les écoulements rencontrés par les micro-véhicules aériens (MAV) sont fondamentalement instables – que ce soit pour les voilures fixes, les voilures tournantes ou les ailes battantes. Le Groupe de Travail AVT-149 a traité des questions fondamentales sur l'aérodynamique instable à faible nombre de Reynolds, en étudiant par le calcul, l'expérimentation et l'analyse un ensemble de configurations abstraites, allant du profil 2D en immersion simple à la forme en plan d'aile 3D en immersion et en immersion latérale. Il en est résulté une meilleure compréhension de l'interaction entre le déplacement, l'écoulement et les charges aérodynamiques.

Les objectifs de la recherche ont inclus :

- 1) Une extension des travaux prioritaires sur les couches limites laminares du profil, les bulles de séparation et la transition vers des cas d'instabilité avec d'importantes digressions sur l'angle d'attaque réel et la production de tourbillons concentrés qui agissent sur le processus de transition affectant les forces intégrées et les moments. Il en a résulté une évaluation des effets du faible nombre de Reynolds pour les MAV, et une étude expliquant pourquoi des outils informatiques de recherche classiques sur étagère peuvent faire face au problème de l'écoulement.
- 2) Une évaluation de la relation entre la chute du vortex (par exemple, à partir du bord d'attaque du profil) et les forces et les moments aérodynamiques temporaires intégrés. Comment la réponse de la force est quasi stable et comment elle correspond à un décrochage dynamique classique ? L'importance de la résolution de l'écoulement dans la capture précise de l'historique de portance, de traînée/poussée et le moment de tangage ?
- 3) Une évaluation des effets liés à la configuration ; comparaison du profil 2D (le SD7003), du plan horizontal fin 2D avec des bords arrondis et un plan horizontal fin avec des bords arrondis d'un allongement géométrique = 2.
- 4) L'étalonnage concurrentiel des installations et des équipements ; la validation de codes dynamiques des fluides informatisés récemment développés ; et les progrès dans les méthodes de diagnostics des écoulements.

En comparant les résultats de 14 groupes de recherche, les conclusions suivantes ont été obtenues, en résumé :

- Les profils avec un nombre de Reynolds modéré (10,000 – 60,000) et un angle d'attaque réel près du pic de décrochage sont fortement sensibles aux effets de la couche limite de transition.
- D'autre part, un angle d'attaque, au-delà du décrochage, signifie que les effets de transition sont secondaires au moins en ce qui concerne la portance.
- Les plans horizontaux avec des bords arrondis sont moins sensibles au nombre de Reynolds ou aux effets de la couche limite de transition.
- Des plans avec un allongement géométrique modéré ($AG = 2$) présentent des caractéristiques d'écoulement irréductibles à l'allongement géométrique infini, mais l'historique de la portance et de la traînée est quasi stable et semblable à celui de la prédiction théorique simple que l'on trouve pour un « mur contre mur » ou un plan 2D.

- L'historique du coefficient de portance est plus stable que ce que la séparation d'écoulement large devrait impliquer, cependant les méthodes à niveau faible donnent toujours un bon potentiel de prédiction aérodynamique des MAV.
- Les oscillations hautes fréquences à faible amplitude sont dominées par des effets non circulaires, cependant les modèles classiques de sillage planaire sont utiles pour une bonne prédiction.
- La comparaison des problèmes de translation avec les problèmes de rotation à démarrage impulsif montre peu de différence avec l'historique de la portance et aucun cas ne montre un vortex de bord d'attaque attaché et stable.



Chapter 1 – INTRODUCTION

1.1 PHILOSOPHICAL PRELIMINARIES

Now well into the second century of powered flight, we have much cause to wonder what great advances shall be bequeathed by our generation, and whether what passes for research in aeronautics is not an excess of the first syllable and dearth of the second. Fortunately, complicated problems are never truly solved. Perhaps the great remaining challenges in aeronautics, which are least solved, lie at the extremes: the very fast, and the very small and slow. The former, in large measure, are problems of propulsion, heat transfer and the like. But the latter are fundamental questions of vorticity transport, and of the behaviour of separated flows; in short, they are questions of classical aerodynamics, still fresh even in our time, and still complex.

The so-called “Micro Air Vehicles”, or MAVs, have been a great boon to aerospace engineers eager for the elusive combination of relevance to modern applications and substantive fundamental problems. MAVs are therefore not only a topical application, but an intriguing problem of fundamental interest to the fluid mechanistic, the aeronautical designer and the biologist, as the relation between flight of natural creatures and MAVs is not merely a metaphorical motivation, but is quite literally true. The definition of MAVs is somewhat amorphous, depending on the biases of the definer. Loosely following Pines and Bohorquez [1], Shyy et al. [2], and Mueller [3], we can “define” MAVs for present purposes as flyers in the Reynolds number range of 10^4 to 10^5 based on the relevant length scale (typically wing chord) and velocity scale (typically flight speed), which translates into vehicle maximal dimensions on the order of 10 – 30 cm.

MAVs and small birds share a direct connection in size, speed, flight regime and even mission. They share the same problems of manoeuvring to avoid obstacles or to reach points of interest precisely, to negotiate gusts and other ambient flow disturbances, and to combine lift-propulsion-control in a robust, efficient manner. While doing so depends on favourable confluence of so many subjects, from flight mechanics to materials and actuation and efficient energy storage, the core problem for aeronautical conceptual design and flight requirements definition is the relationship between the aerodynamic loads and the kinematics of motion or the vehicle “state”. Motion kinematics may come from flapping wings or any other relative motion between the fluid and the body. The over-arching condition is that motion kinematics are aggressive – fast, and of high amplitude – relative to the usual aeronautical engineering time/length scales developed for fixed-wing aircraft in cruise or gentle manoeuvre. Exploring the consequences of such motion kinematics, in an abstracted sense, is the subject of the present report.

Unsteady aerodynamics in two and three dimensions is a critical area for scientific understanding of Micro Air Vehicle flight, for without it, we return to haphazard beating of the air much akin to the first attempts in powered flight. Applications of unsteady aerodynamics include perching, gust response, manoeuvring flight, flapping wings, aeroelastic interactions and in general all sorts of departures from the steady regime – which, for small vehicles, includes the majority of the flight envelope. For engineering applications, the central question is whether the aerodynamic loads are essentially quasi-steady with the motion kinematics. For example if the lift and pitch coefficients are quasi-steady with effective angle of attack, then the distinction from steady aerodynamics is trivial. The secondary question is the extent to which the relative motion between body and fluid forces the aerodynamic response such that the usual variables in aerodynamics – Reynolds number, boundary layer transition, roughness and leading edge curvature, and geometry in general – become relatively unimportant; or, if these various factors require consideration just as they do in steady aerodynamic problems.

We begin by reviewing the classical problem of pitching and plunging airfoils, and then consider its relation to the aerodynamics of flight in nature. Next, we propose a set of canonical problems for experiments and

computations in low Reynolds number unsteady aerodynamics. After describing the various facilities and computational methods used to obtain the results for the canonical problems, the bulk of this report recites the various results case-by-case, drawing hopefully insightful inferences for each. We then consider related problems not covered in the main under the canonical case, and conclude with recommendations for generalizing the canonical problems and for other points of departure.

1.2 RESUME OF PRIOR RESEARCH IN 2D PITCHING AND PLUNGING

In two dimensions the possible motions are rotation, or pitch; up and down translation, or plunge – sometimes called heave; and fore and aft translation, or surge. The latter we largely ignore in the present work, because of the complexity of realizing this degree of freedom in experiments, and because it is usually absent in classical pitch-plunge problems. Some of the experimental setups used in the present study can, however, accommodate all 3 longitudinal degrees of freedom.

For all of the geometric and kinematic complexity of the MAV problem, especially for flapping wings, 2D problems remain important. Simply put, one has to begin somewhere, especially if the context is passage from the steady case. Classical airfoil problems, steady and unsteady, are framed in 2D, and the present approach is to begin with 2D aerodynamics in the longitudinal plane (lift, pitch, drag/thrust), then to extend to longitudinal-type motions of a 3D planform, and finally to consider non-longitudinal motions such as rotations.

Perhaps the first appearance of pitching/plunging airfoil physics was in applications of fixed-wing aircraft aeroelasticity. Prior to current interest in flapping wing aerodynamics, dynamic stall of helicopter blades was the main application for unsteady airfoils that included significant motion amplitude as well as frequency, resulting in the so-called dynamic stall [5]. Small reduced frequencies, meanwhile, traditionally fell under the more usual problem of airplane flight dynamics, in the sense of phugoid and short-period-mode oscillations [4]. But even the short-period mode is low frequency in the sense of unsteady aerodynamics, and almost without question is amenable to quasi-steady treatment. Helicopter blade stall problems are another matter, introducing at least two fundamental problems. One is how to account for shedding of vorticity into the wake whenever there is a change in effective angle of attack, either due to geometric pitch change or to plunge. This is an essentially inviscid problem. The second problem is how to account for flow separation, of which the most celebrated example is the leading edge vortex (LEV), whose formation, residency time, shedding and downstream convection form the core problem of dynamic stall. McCroskey et al. [5] pointed out that as this vortex passes over the airfoil surface, it significantly changes the chordwise pressure distribution and produces transient forces and moments fundamentally different from those in static stall. Comprehensive reviews of dynamic stall are given by McCroskey [6], Carr [7], Liiva [8] and Carr and McCroskey [9]. These works inform the origin of MAV-related pitch-plunge problems, but now the Reynolds number is a factor of $O(100)$ smaller than in helicopter applications, and in the past 20 – 30 years this has led to a spate of investigations on what happens with flow separation due to airfoil motions at low Reynolds number. The motivation for these works is not necessarily MAVs, as the MAV-relevant Reynolds number just happens to be the operational Reynolds number in many small-scale facilities, especially in water tunnels and water tow tanks, and therefore many fundamental studies not motivated by MAVs nevertheless speak to MAV-relevant results. A comprehensive review is beyond the scope of the present work, but our purpose is to systematize the available results in a new, clean-sheet effort that attempts to benchmark the various experimental and computational approaches, opening vistas for parameter studies for targeted applications.

By far the most common configuration in 2D problems is the venerable NACA 0012 airfoil – which is perhaps regrettable, because the NACA 0012 performs poorly at MAV Reynolds numbers. Ohmi et al. [10,11] considered a sinusoidally-pitching NACA0012 airfoil with impulsive-start to steady translation in a water tow tank. Both the reduced frequency and amplitude were found to affect the structure of the

vortex wake. Visbal and Shang [12] studied the high-rate high-angle of attack linear pitch-ramp of a NACA0015 airfoil at $Re = 10^4$ by solving the full 2D Navier-Stokes equations, finding that lags between evolution of leading-edge flow separation and the airfoil motion kinematics should increase with increasing reduced frequency. Ghosh Choudhuri and Knight [13] examined the effects of compressibility, pitch rate, and Reynolds number on the initial stages of 2D unsteady separation of laminar subsonic flow over a pitching airfoil in the Reynolds number ranging from 10^4 to 10^5 , finding that increasing the Reynolds number hastens the appearance of the primary re-circulating region.

The aforementioned studies focus mostly on transients following the initiation of the airfoil motion from rest. Others considered the periodic or phase-averaged behaviour of pitch-plunge motions after initial transients have relaxed, typically with a focus on motion kinematics for optimal thrust efficiency. Platzer and Jones [14] discussed theoretical prediction of thrust efficiency vs. flow visualization and thrust measurements for an airfoil in pure-plunge, over a range of reduced frequencies and reduced amplitudes. Koochesfahani studied high-frequency low-amplitude airfoil pitch oscillations with quantitative and qualitative visualization, identifying vortex shedding patterns vs. motion kinematic parameters [15]. McAlister and Carr [16], and Walker et al. [17] examined the interplay between leading-edge and trailing-edge vortices. Anderson et al. [18] and Triantafyllou et al. [19] used particle image velocimetry and direct force measurement to study the combined pitch-plunge parameter space for propulsive efficiency optimization, conducting a large parameter study, albeit force measurements and flowfield data were obtained at quite disparate Reynolds numbers. Young and Lai [20] used a 2D Reynolds-Averaged Navier-Stokes (RANS) approach to study the frequency-amplitude parameter space for optimal thrust efficiency for a plunging NACA 0012 airfoil at $Re = O(10^4)$, and Jones et al. [21] demonstrated good agreement in wake vortex structure between dye injection at the airfoil trailing edge in a water tunnel, 2D laminar Navier-Stokes computation, and a 2D vortex-particle method. Lian and Shyy [22] showed similar agreement using a RANS solver run fully-turbulent. Here we seek to extend these results to more complex kinematics of motion, to a range of Reynolds numbers bracketing transition-dominated effects evinced in the static measurements and in lower-amplitude pitch-plunge oscillations [23], and to include effects of leading-edge separation.

One important issue in periodic oscillatory airfoil flows is the lag between the aerodynamic response and the airfoil motion kinematics in 2-degree-of-freedom pitch-plunge. As a natural extension of the strictly quasi-steady model, one seeks to construct an explicit relation of the lag of putatively sinusoidal force response to sinusoidal motion kinematics, as a function of reduced frequency, of amplitudes of pitch and plunge, of phase difference between pitch and plunge, of Reynolds number and so forth. This could then form a model for the lift response to more general motions and in more general configurations, serving as an engineering tool for parameter studies.

1.3 HIERARCHY OF ANALYSIS FOR UNSTEADY AIRFOIL AND WING AERODYNAMICS

1.3.1 Classical Methods and Closed-Form Solutions

Analytical methods in aerodynamics are most successful for small disturbances, and in unsteady aerodynamics this means small amplitudes of motion, though not necessarily low frequencies. Analytical methods for the aerodynamics of moving airfoils and wings date back to the period of 1920 – 1940 when increasing aircraft flight speeds pushed the need to estimate and to analyse flutter instabilities of flight surfaces. This therefore predates the helicopter-motivated problems cited earlier. The early work of Birnbaum [24] solved the unsteady, inviscid flow problem of flat plates for harmonic low-frequency pitch and plunge motions. Improved ansatz functions along the frequency were found independently by Küssner [25] and Theodorsen [26], and these yielded closed-form solutions for the aerodynamic forces of harmonically oscillating lifting airfoils at small amplitude but with no restriction on frequency. While

INTRODUCTION

starting and stopping vortices in the airfoil wake are modelled, the wake shape is assumed to be a straight line. Theodorsen's solution was used by Garrick [27] to compute drag or thrust as well. Along similar lines Wagner [28] derived the lift function for the problem of impulsive start, which is more suited for hover problems.

These theories may be used for rapid calculations for parameter studies, yielding reasonable estimates of thrust and propulsive efficiency for 2D problems, and they can be used as the 2D element of strip theories for wing flows. But there are two key obstacles. First, what is conventionally lumped as "viscous effects" must be small, for example limited to skin friction or laminar separations closed in the time-averaged sense. Second, 3D effects must be small, in that spanwise variations can be accounted by a local effective angle of attack. Both assumptions in general fail for flapping wing aerodynamics at large effective angles of attack or for small aspect ratios. Thus there is a need to extend the classical methods to applications such as insect flight and the flapping-wing MAVs, ideally retaining the simplicity of closed-form solutions.

1.3.1.1 Further Remarks on Theodorsen's Method

In Theodorsen's model [26], for harmonic motions in pitch and plunge, the lift coefficient is given by:

$$C_L(t) = 2\pi\alpha_0 + \frac{\pi c}{2} \left(\frac{\dot{\alpha}}{U_\infty} + \frac{\ddot{h}}{U_\infty^2} - \frac{c(2x_p - 1)\ddot{\alpha}}{2U_\infty^2} \right) + 2\pi \left(\frac{\dot{h}}{U_\infty} + \alpha - \alpha_0 + c(1.5 - 2x_p) \frac{\dot{\alpha}}{2U_\infty} \right) C(k). \quad (1)$$

The pitch and plunge are input as complex exponentials, $\alpha(t) = \alpha_0 + Ae^{i(\omega t + 2\pi\phi)}$ and $h(t) = h_0 e^{i\omega t}$. The phase lead of pitch vs. plunge, in fractions of motion period, is ϕ . The reduced frequency, k , is defined as $k \equiv \omega c / 2U_\infty = \pi f c / U_\infty$. The first term in Eqn. 1 is the steady-state lift. The second term is the "apparent mass" or non-circulatory lift, due to acceleration effects. It is progressively larger for larger k . The third term models circulatory effects. $C(k)$ is the complex-valued "Theodorsen function", with magnitude ≤ 1 . It is essentially a transfer function, accounting for attenuation of lift amplitude and phase lag in lift response, from its real and imaginary parts, respectively. Setting $C(k) = 1$ ($k = 0$) and ignoring non-circulatory effects recovers quasi-steady thin airfoil theory. The non-circulatory term follows instantaneously the kinematics of motion, but evolution of vorticity in the wake yields phase lag relative to the kinematics of airfoil motion in the circulatory term, which is predicted to peak for $k \sim 0.3$.

Equation (1) assumes a planar wake and a trailing-edge Kutta condition, thus excluding wake rollup and vortex streets, vortex shedding, convection of large separations over the airfoil, open separations, large laminar separation bubbles, leading edge and trailing edge vortices and so forth. But the simplicity of such a model obviously makes it attractive as an engineering tool. Thus, we consider to what extent this model is useful for kinematics where the flow separation in portions of the airfoil oscillation ranges from moderate to severe, and compare the Theodorsen prediction with that of a range of computations and experiments.

1.3.1.2 Modern Extensions of Classical Methods

Aerodynamic analysis of insect flight indicates that the classical airfoil theories together with present knowledge in airfoil stall result in much too low lift coefficients as compared to those observed with natural flyers. It was concluded that wing-wake interactions and leading edge separation contribute significantly to the overall forces and semi-empirical models for these effects were recently developed, i.e. by Penderson and Zbikowski [29].

Extension of airfoil theories to thick airfoils and modelling the effect of deforming wakes is possible with panel methods, which approximate the required vortex distributions along the airfoil and in the wake using discrete surface panels [30,21]. However, the numerical discretization and iterative determination of the

wake require higher computation efforts, and the robustness of correctly capturing separation, shedding, reattachment and other vortical effects remains a subject of controversy. More details on airfoil theory assessment for predicting flapping wing propulsion are available from a recent review paper of Platzer [31]. In sum, aerodynamic designers of today lack a robust method that would allow one to analyse the dynamics of inviscid and viscous flowfields of moving airfoils similarly to the state of the art with the XFOIL code for steady flows.

1.3.2 Viscous Solutions and Modelling

Perhaps the effects of boundary layers and the development of complex flow separations from edges and smooth parts of aerodynamic surfaces can only be computed by solving the non-linear equations of motion for viscous flows. This is a rather straight forward task for wing chord Reynolds numbers below values around 10^4 where the flow around the wing is expected to be laminar, under normal circumstances; but even then, computations are too large to support extensive parameter studies, and a modelling approach remains imperative. At larger Reynolds numbers flow instabilities present in adverse pressure boundary layers and in separated flowfields will eventually transition into turbulence, thereby introducing strong momentum transport normal to the mean streamwise flow directions. The direct numerical simulation of the flow instabilities and their break down to turbulence as part of solving the equation of motion of the unsteady flowfield is very time consuming since this task requires the numerical resolution of broad ranges of scales in space in time. It is no surprise that this has only been accomplished for some limited research flows [32] and there is no hope of using this approach routinely for exploring the design space of practical flapping wings within the mid-term future.

Hence the development of suited engineering models for transition and turbulence is of current interest to achieve reasonable prediction capabilities at affordable computation costs. Turbulence models compute turbulent transport in terms of Reynolds stresses that appear as new unknown after ensemble averaging the unsteady equations of motion. The models consist of one or more transport equations that determine the physical behaviour of turbulence quantities and the needed Reynolds stresses are derived from these. The overall approach is labelled URANS. The conceptually quite simple application is then to use the chosen model of turbulence along the complete wing surface. However, this can result in a simulation of fully turbulent flow in regions where laminar boundary layers are observed in experiments and hence, physical flow separations may be suppressed which would otherwise generate significant contributions to the aerodynamic forces and moments.

The instabilities of the laminar boundary layers that lead to transition on airfoils and wings exhibit a convective character. It is then straight forward to model transition to turbulence by assuming an additional transport equation for an intermittency parameter that discriminates between laminar and turbulent boundary layer flow regions. This approach is followed by Menter et al. [33], but it has not yet been validated for Reynolds numbers below 10^5 . Transition on airfoils and wings at low Reynolds numbers depends on the growth of harmonic modes in the laminar boundary layer in many cases. This observation motivates the so-called e^N -approach where the point of transition onset is correlated with computed amplitude ratios of the primary boundary layer instabilities. This transition method has been successfully coupled to URANS solvers in steady and unsteady formulations [34,35] and validation results for unsteady low-Reynolds-number airfoil flows with moderate flow separations seem promising.

1.3.2.1 3D Effects

Classical theories for computing the effect of finite span of flapping wings may be divided into unsteady wing theory for forward flight and blade element theory that is more suited for hover and low-speed flight. While some of the potential flow methods for wings developed for flutter in forward flight are only valid for small geometric amplitudes others were specifically developed for flapping wings. Philips et al. [36] developed a lifting line theory with a suited model of axial and transverse vortices in the wake. Hall et al.

INTRODUCTION

[37] presented an unsteady vortex lattice method for more general wing planforms. These approaches are used to assess propulsive efficiencies of wings in forward flight.

Blade element theory, on the other hand, can model both steady and unsteady flow effects along the 3D wing in hover and many variants of this approach appeared over the last 25 years [38,39,40,29], using 2D quasi-steady force coefficients or unsteady 2D theories as elementary data source. The use of certain flow models in these wing theories has generally been validated along a small amount of force data available from dedicated experiments for specific motion kinematics. This appears as a major weakness today, as a truly predictive capability for complex flows can likely not be obtained by this approach.

1.3.2.2 Importance in Capturing Transition for Low Reynolds Number Unsteady Aerodynamics Computations

While it is well known that laminar-turbulent transition in boundary layers has a large impact on airfoil drag at moderate to high Reynolds numbers, but the impact in low-Reynolds-number airfoils is different. The importance of the transition at low Reynolds numbers stems from the observation that laminar boundary layers separate more early under adverse pressure gradients than their turbulent counterparts. Low-Reynolds-number airfoils exhibit therefore three important flow phenomena that depend on the angle of attack and possibly on its unsteady variation. These are laminar separation bubbles (LSB), laminar airfoil stall and dynamic airfoil stall.

The LSB denotes a flow where a laminar separation takes place caused by an adverse pressure gradient along the aerodynamic surface. Small harmonic disturbances present in the laminar boundary layer are strongly amplified in the shear layer of the separated flow [41] and rapid transition to turbulence takes place. The turbulence, in turn, creates a large momentum transport normal to the shear layer so that the flow reattaches to the surface and a closed bubble is formed in the time-averaged mean. LSBs can create additional pressure drag as they displace the outer, inviscid flow.

A more important aerodynamic effect occurs for steady-state onset flow if the transition process in the separated shear layer is relatively slow and the adverse pressure gradient is strong. Then turbulent momentum transport is not sufficient to close the bubble and a large separation occurs that extends right to the trailing edge. This causes a sudden loss of lift and a strong increase of drag along with significant hysteresis effects of force coefficients with varying angle of attack. Note that the separated flow region is characterized by continuous vortex shedding because of the unstable behaviour of the shear layers present.

For large unsteady increases of the airfoil angle of attack beyond the steady stall limits the laminar flow separation at the leading edge may develop into a strong and well organized vortex. This vortex induces significant suction on the airfoil surface with an overshoot of lift and usually significant variations of the pitching moment. Airfoil drag is also increased by this dynamic stall effect. As a consequence it may be assumed that truly predictive computations should take into account transition in laminar boundary layers and particular within laminar separations since steady and dynamic airfoils stall depends on the boundary layer state.

1.4 THE DIFFERENT KINDS OF FLAPPING IN NATURE

A large but not exclusive motivation for our work is the engineering abstractions of flapping-flight in nature, both as routes for rational application of bio-inspiration in MAV design, and for first-principles understanding of the aerodynamics of natural flyers. Obviously analysis of the full spectrum of natural flight is hubristically ambitious and is not attempted here. It is however worthwhile to attempt to place the present work in context. Thus we provide a very brief and somewhat superficial summary of the different flapping regimes found in nature, at least in terms of their aerodynamic context.

The method of flight best understood to date is fixed wing flight, where lift is obtained by mainly attached flow over a nominally rigid wing. Many birds are seen to spend a lot of their air-time in a similar flight regime, soaring in thermals or gliding some distance between bursts of flapping. However, we can also observe that steady gliding flight becomes increasingly uncommon with reducing size (compare insects with large birds), and the first question to ask is whether there are fundamental constraints that prevent gliding flight at small scales.

Assuming steady flight, lift equals weight, and we can use observations from zoologists to estimate the scaling of wing performance of birds and insects. As with airplanes, $\frac{1}{2} \rho U^2 S C_L = mg$, where ρ is the air density, U is the forward (gliding) velocity, S is the wing area, C_L is the wing lift coefficient, mg is the total weight. Figure 1-1 shows data collected for a very large range of birds, comparing typical wing areas with total mass. Here we see that for most birds (except the smallest hummingbirds) there is a clear relationship between wing area and body mass which can be expressed by a best fit as $S \propto m^{0.72}$.

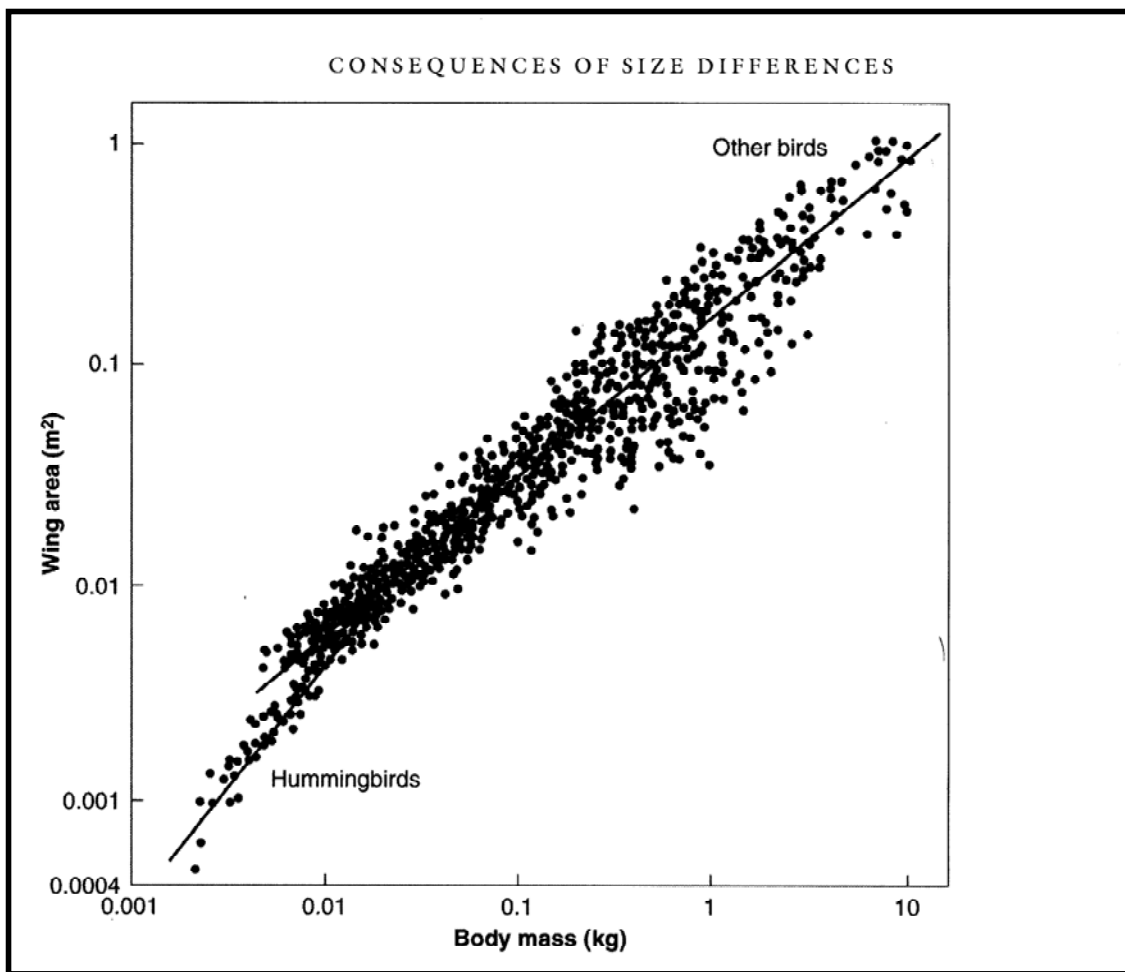


Figure 1-1: Scaling of Bird Wing Area vs. Body Mass – from McMahon and Bonner [42].

From the above we can then write for the gliding speed:

$$U = \sqrt{\frac{2mg}{\rho C_L S}}. \quad (2)$$

INTRODUCTION

If, for the moment, we assume that gliding flight for all birds is achieved with the same wing lift coefficient, then the above would imply (making use of the approximate proportionality between wing area and $m^{0.72}$) that the relationship between ‘cruise’ speed and body mass is $U \propto m^{0.14}$. Fortunately, zoologists have observed bird and insect flight in nature. Figure 1-2 shows typical measured forward velocities for a large number of animals and aircraft. Again it can be seen that the data follows a clear trend (albeit with fairly large departures for individual examples). The best fit line is $U \propto m^{0.17}$, which is surprisingly close to the expected result from the above.

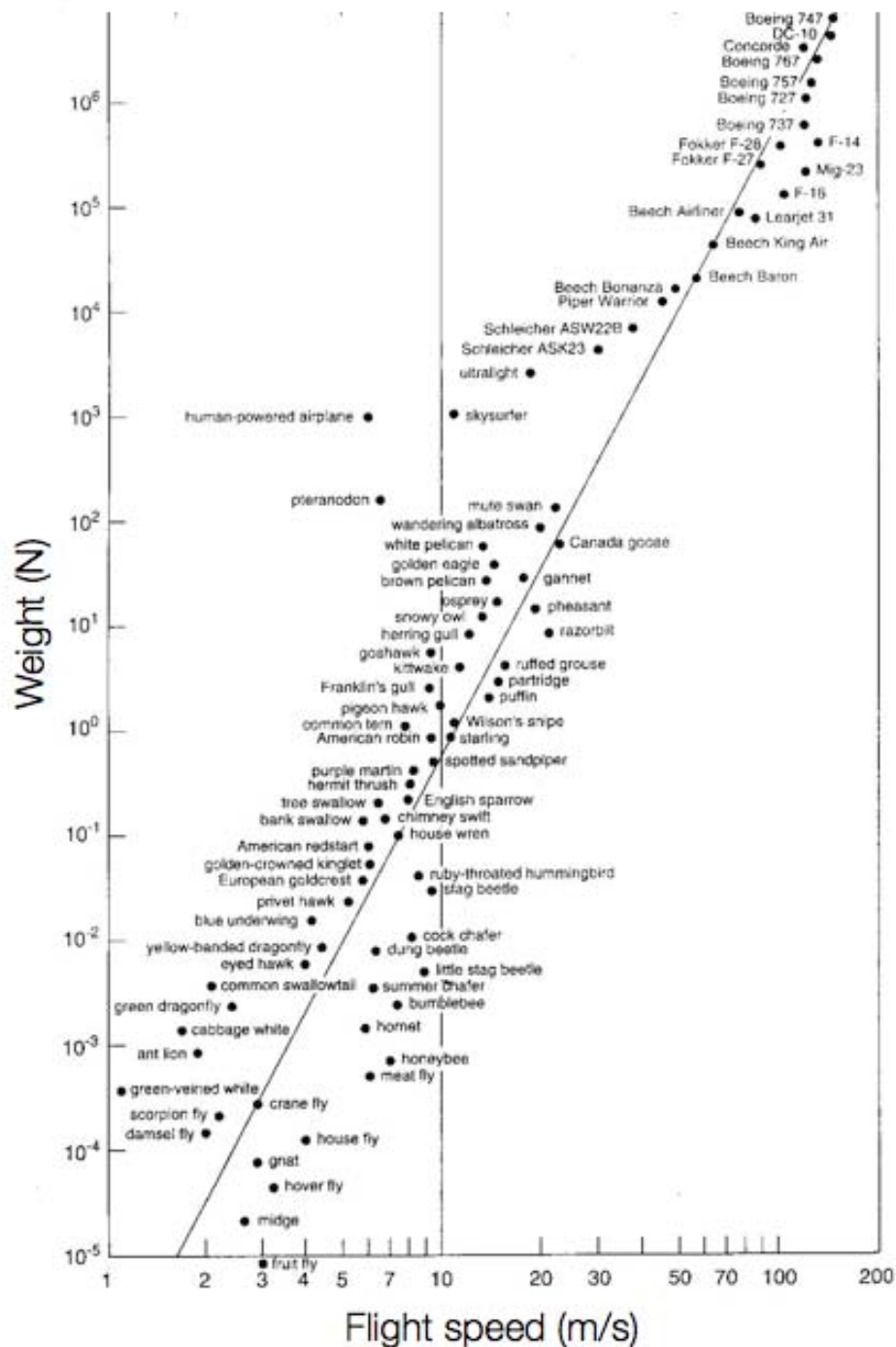


Figure 1-2: Weight and Flight Speed for Animals and Aircraft – from Tennekes [45].

From this simple discussion we can conclude that for gliding flight in nature (and aeronautics) the wing lift coefficient is almost completely independent of vehicle/animal size. The wing on a small bird must generate the same overall lift coefficient as that on a large aircraft. In fact, closer examination would suggest that lift coefficients might even slightly increase as size reduces (although at small sizes gliding flight is increasingly rare making this crude analysis invalid). Others, such as Ellington [38], have analysed hovering flight and concluded the required lift coefficients are at least as great as these observed in gliding flight at larger scales.

Therefore, the wing sections employed in any aircraft need to be capable of achieving similar lift coefficients regardless of scale, and thus Reynolds number. This, however, is not at all straightforward.

Figure 1-3 shows the result of a literature survey of airfoil performance across a wide range of Reynolds numbers. Here, it can be seen that there is a critical range between roughly $Re = 10000$ and $Re = 100000$, where maximum airfoil lift coefficients experience a clear drop as a result of laminar separation. This critical range is roughly in the regime where small to medium sized birds operate. The performance of wings in this critical range can be improved by employing additional transition mechanisms, such as roughness or leading edge devices, and such techniques can indeed be found in nature [43,44]. However, while the useful range can be extended down towards smaller Reynolds numbers with such flow control, this does not remove the fundamental problem that below the critical Re regime steady airfoil performance is insufficient for gliding flight.

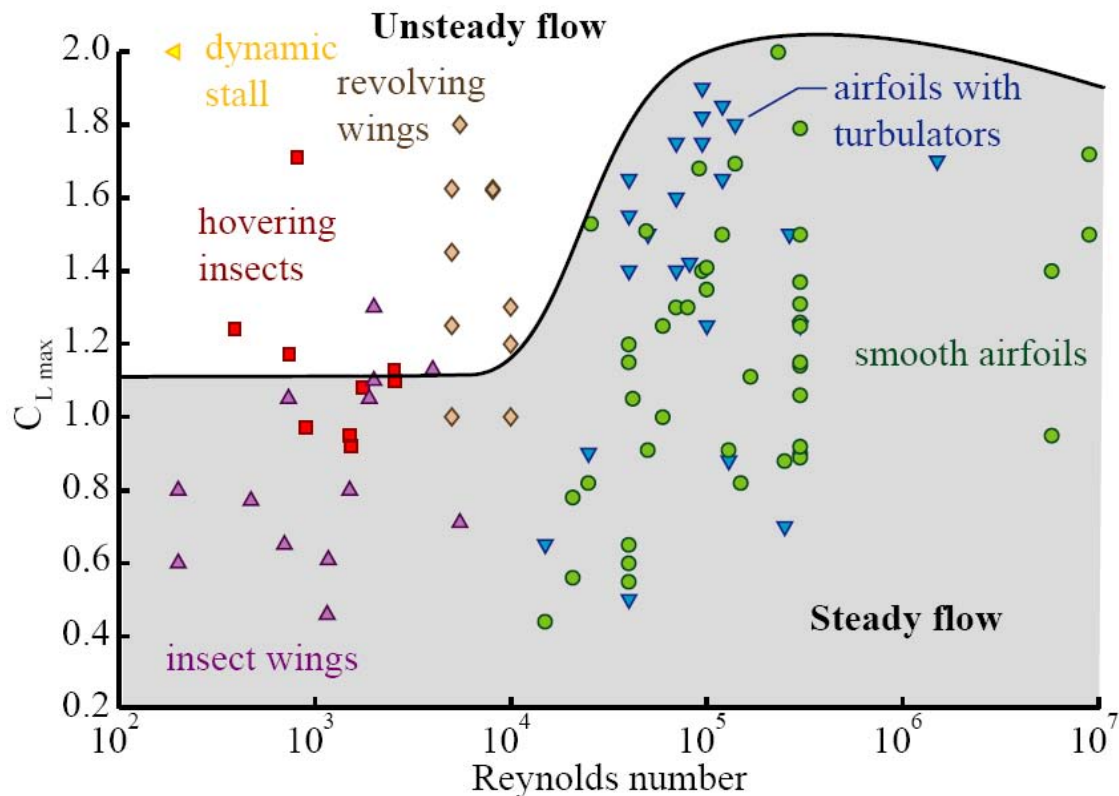


Figure 1-3: Maximum Lift Coefficients Reported in Literature for Various Reynolds Numbers.

There are, however, some data included in Figure 1-3 which show significantly higher lift coefficients in the sub-critical Re regime. These are found in experiments that either feature unsteadiness (stopping/starting wings) or three-dimensionality (rotating wings). This suggests that for smaller sized vehicles, unsteady lift mechanism (or at least three-dimensional ones) are necessary.

INTRODUCTION

Depending on the size of the animal and the type of flight we can now observe several types of flapping wing flight in nature which will be discussed in turn below.

1.4.1 Large Birds in Forward Flight

For flight in this regime the wing size and flight velocity are large enough for airfoil Reynolds numbers to be in excess of the critical range. Here, flapping is only necessary to generate thrust, and since many birds are highly efficient (in terms of lift/drag) this is not a large force.

To generate thrust birds make use of the fact that a vertical (plunging) motion of the wing – a vertical stroke plane – rotates the effective angle of attack vector as seen in Figure 1-4. During a downstroke this generates thrust. In contrast, the upstroke is relatively passive – the wing is rotated to a near zero effective angle of attack.

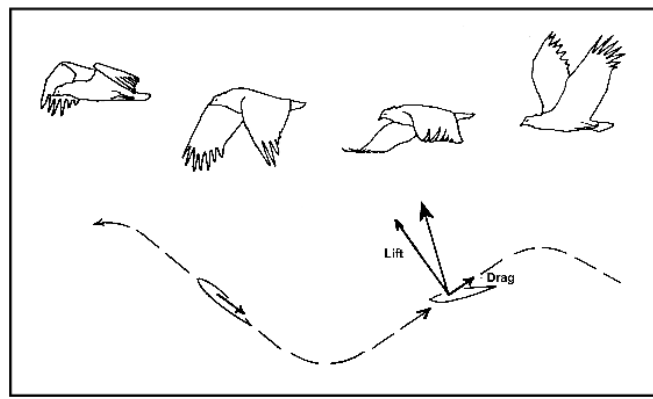


Figure 1-4: Condor in Fast Forward Flight – after McGahan [46].

Typically (because of the low thrust requirement) only the outer wing is used for thrust generation and the inner wing flaps much less. This is shown in Figure 1-5. The relatively small plunge experienced by the inner wing ensures that it continues to generate lift through the cycle and there is only a minor variation of the lift vector. By contrast the outer wing, which undergoes a greater amplitude plunging motion (together with pitch variation) produces the thrust and lift during the downstroke only. Flapping frequencies are typically quite low and the flowfield is effectively quasi-steady (and attached) throughout. However, the forces experienced by the wing are not quasi-steady as unsteady effects already have an impact, for example through the time-varying vorticity in the wake.

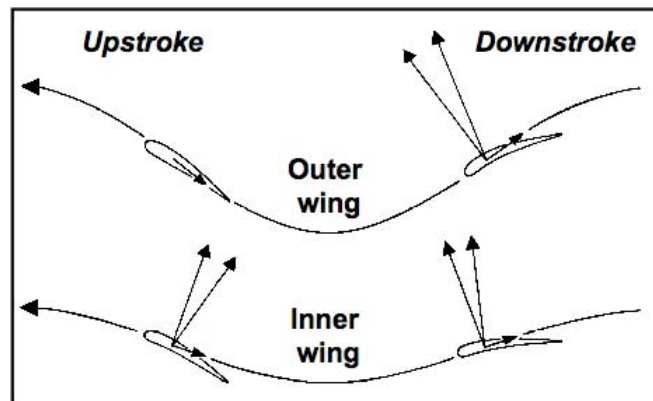


Figure 1-5: Comparison of Inner and Outer Wing Motion for Condor in Fast Flapping Flight [46].

1.4.2 Medium Birds in Forward Flight, Hovering Flight (Large and Medium)

At lower flight speeds, for example before landing or after take-off, there is insufficient forward velocity to produce the required lift. Medium sized birds are also approaching the critical Reynolds regime making lift generation more difficult. In such a situations wing motion is employed to achieve greater effective velocity. The extreme case is during hover when all the effective free-stream velocity is generated by the wing motion. For flight in this category the downstroke is generally sufficient to produce the necessary forces – consistent with the observation that downstroke-enabling vs. upstroke-enabling flight muscles are highly unequal in strength.

Figure 1-6 shows a pigeon and a bat in hover. Here the stroke plane is rotated to produce a net force acting in vertical direction. During the upstroke the wings are folded for minimum affective area – the upstroke is effectively passive. Note that both lift and drag (relative to the effective local flow angle) contribute to the force production.

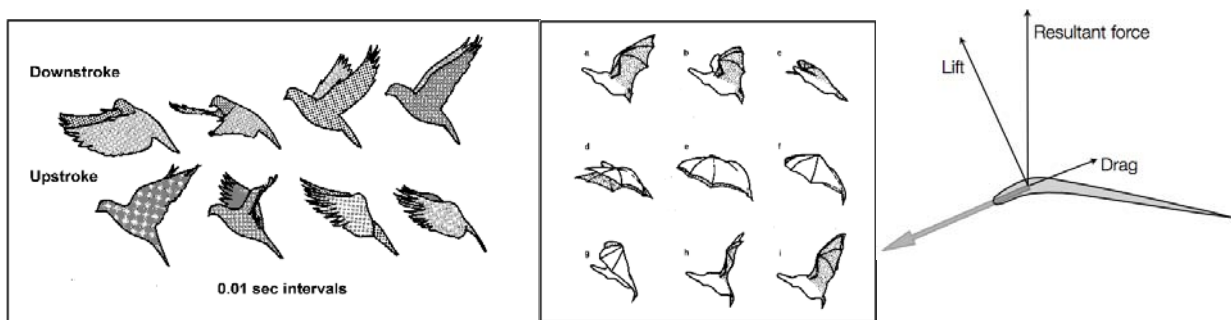


Figure 1-6: Hovering Flight in Pigeons and Bats – after Brown [47].
Lift is generated during the downstroke only, the upstroke is passive.
The stroke plane is rotated to give an effective vertical force vector.

In this regime, the combination of wing size and speed of motion is sufficient to ensure that the flow remains above the critical Reynolds number range. This means that lift is primarily generated in the traditional manner (that is, attached and quasi-steady airfoil lift) during the down-stroke. However, extreme manoeuvres are likely to require genuine unsteady and separated flow aerodynamics.

1.4.3 Small Birds and Insects in Forward Flight or Hover

When the wing size reduces even further the flight speed also reduces. To some extent this is offset by an increase in flapping frequency, however, this is no longer sufficient to avoid the drop in lift experienced due to two factors: the Reynolds number is now in or below the critical range; and the maximum effective velocity relative to the wing is reduced. In this regime the downstroke alone is insufficient to generate the necessary lift (and wing muscles are more equal in strength). As seen in Figure 1-7, showing a hovering hummingbird, the stroke plane is now almost horizontal and the wing is pitched at either end of the stroke to give an effective positive angle of attack during both the up- and downstroke. Effectively the wing now works in a propeller-type motion, similar to a helicopter. As a result of the horizontal stroke-plane, the total force vector is no longer vertical during each up/downstroke. This is because the drag component introduces a horizontal force. Because of the symmetry of the up/downstroke motion, the cycle-averaged horizontal force cancels out.

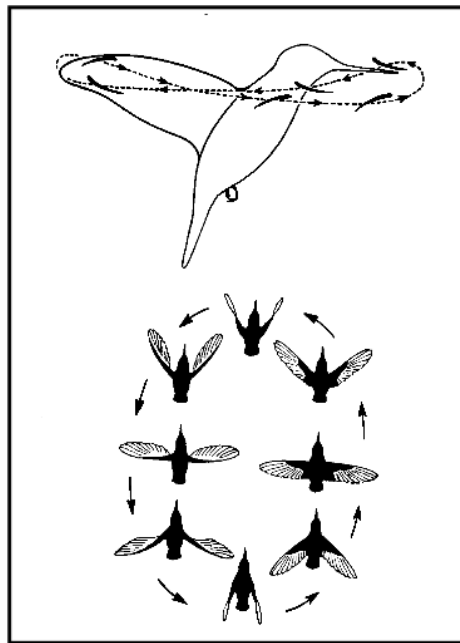


Figure 1-7: Hummingbird in Hover – after Stolpe and Zimmer [48].

Similar wing kinematics are also applied by insects. For forward flight the stroke plane is rotated from the horizontal to achieve a thrust component. Gliding flight is virtually non-existent in this regime as a result of the poor lift coefficients available at low Reynolds numbers.

Even at high flapping frequencies, the effective Reynolds number is too low to ensure good lift coefficients and in this regime unsteady and three-dimensional effects, such as the leading edge vortex, play a major role in lift generation.

In surveying the various regimes of flapping-wing flight from an engineering viewpoint, perhaps the overarching question is how to assess the dependency of aerodynamic force production on the wealth of parameters – Reynolds number, reduced frequency, wing geometric details such as aspect ratio and airfoil section, the role of structural flexibility, surface roughness and so forth. One is overwhelmed by the sheer range of independent variables. Then there is the question of how much fidelity or accuracy is required in a given experiment or computation, to answer the basic question at hand. This latter question, at least, can be addressed with some rigor by considering what we call “canonical problems”.

1.5 THE NEED FOR CANONICAL PROBLEMS

By “canonical problems” one means abstracted test cases of general appeal, with clear parameter definitions, which are to be studied by several computational and experimental efforts, by different research groups working towards a common reporting goal. Objectives include:

- 1) Cross-validation of the various methods;
- 2) Baselining the state of the art;
- 3) Engendering interest in the subject amongst researchers with affinity towards this area but otherwise lack of connection to the specific subject;
- 4) Establishment of a known test case for archival reference; and
- 5) Providing a point of departure for individual researchers to run parameter studies.

The idea is that once a common baseline is achieved, the subsequent parameter studies have better contextual motivation and are on firmer ground because the “correct” answer was found for the canonical case. If, on the other hand, significant difference is found in results for the canonical case, and obvious errors have been excluded, then the canonical problem itself requires a revisit to assess flaws in state-of-the-art computations or experiments, before further work can be justified.

1.5.1 From Fundamental Research to Applications

The present work tends toward the “fundamental”, in the sense that no flight vehicle or prototype in nature is analyzed, and the methods of investigation are the traditional approach in laboratory fluid mechanics. However, the range of Reynolds numbers, motion parameters and model geometries must necessarily be informed by the applications – that is, MAV configurations. Pitching/plunging airfoils most naturally tend themselves to flapping-wing MAV applications, for example in problems of finding good thrust efficiency due to leading edge suction.

1.5.2 Role of Longitudinal Problems

Noting the complexity of flight in nature, we must nevertheless begin with suitably simple abstractions, ideally those stemming from classical work in unsteady aerodynamics and dynamic stall, but suited to the Reynolds numbers and reduced frequencies encountered in animal flight and in MAV applications. A logical point of departure is longitudinal problems, where the airfoil or wing is oscillated in the longitudinal plane; that is, with three degrees of freedom: an in-plane rotation, or pitch; and in-plane translation normal to the nominal free-stream direction, or plunge; and the second in-plane translation, parallel to the nominal free-stream, or surge. In the present study, interest is limited to pitch and plunge, but as discussed below, some experimental installations have a slight unintentional but unavoidable surge.

1.6 GENERAL OUTLINE OF THE REPORT

We consider three geometries: a low Reynolds number airfoil nominally in two dimensions, a thin flat plate likewise in nominally two dimensions, and a thin flat plate of aspect ratio 2. “Nominally two dimensions” means for experiments that the model spans the facility test section from wall-to-wall, with ideally a very small gap at the tips. For computations the meaning is more ambiguous, as it can be solving the Navier-Stokes equations (or some simplification) in a plane, or in some volume of spanwise extent but spanwise periodic boundary conditions.

The purpose of the three geometries is a multi-way comparison of sectional geometry effects and a preliminary foray into 3D effects, but which we mean whether there is strong departure from sectional aerodynamics for a case where the aspect ratio is clearly small.

1.6.1 Listing of the Cases and Philosophy for Why They Were Chosen

We consider the following kinematics for combined pitch and plunge:

$$\text{Plunge: } h(t) = h_0 c \cos(2\pi ft) = 0.5c \cos(0.5U_\infty t / c); \text{ and}$$

$$\text{Pitch: } \alpha(t) = \alpha_0 + A \cos(2\pi(ft + \phi)) = 8^\circ + 8.42^\circ \cos(0.5U_\infty t / c + \pi/2). \quad (3)$$

1.6.1.1 Airfoils

Our first set of cases features the Selig SD7003 airfoil, with a design Reynolds number in the 60000 – 100000 range [49]. This was also motivated by the steady-problem studied in NATO RTO AVT-101, “MAV Low Reynolds Number Aerodynamics” [50]. The parameters of Eqn. 3 for the SD7003 airfoil are

INTRODUCTION

noted schematically in Figure 1-8, while the time traces of effective angle of attack for combined pitch-plunge and for pure-plunge are given in Figure 1-9. Our choice of reduced frequency, $k = 0.25 = \omega c / 2U_\infty = \pi f c / U_\infty$, was motivated in part by cruise-type conditions for flapping flight of birds. Although the Strouhal number, $St = 0.08$, is below the range for maximum propulsive efficiency for most flyers in nature [51], the present flow conditions are on the upper-end of the dynamic-stall literature for helicopter blade applications [5,8], for which the traditional analytical or phenomenological models in aeronautics tend to focus. As is often taken in applications motivated by propulsive efficiency of pitch/plunge [18], pitch leads plunge by one quarter of phase ($\phi = 0.25$) and thus the airfoil “feathers”, with the geometric pitch angle partially cancelling the plunge-induced angle of attack, $\arctan(\dot{h} / U_\infty)$.

The amplitude of pitch, $A = 8.42^\circ$, was chosen from the expression $\lambda \equiv \frac{A}{\arctan(\dot{h}_{\max} / U_\infty)}$. λ is the ratio of

pitch angle amplitude to the peak angle of attack induced by the plunge motion; we chose $\lambda = 0.6$, which as will be shown below, leads to shallow dynamic stall. $\lambda = 0$, on the other hand, is a pure-plunge, which produces a strong leading edge vortex, and is more akin to deep dynamic stall.. Variation of λ is an option for parameter studies (not pursued here) for search for lift and thrust efficiency, while keeping Strouhal number constant. Alternatively, Strouhal number can be varied (by changing reduced frequency or reduced amplitude) and λ varied such that the effective angle of attack history, when disregarding pitch rate effects, is kept constant.

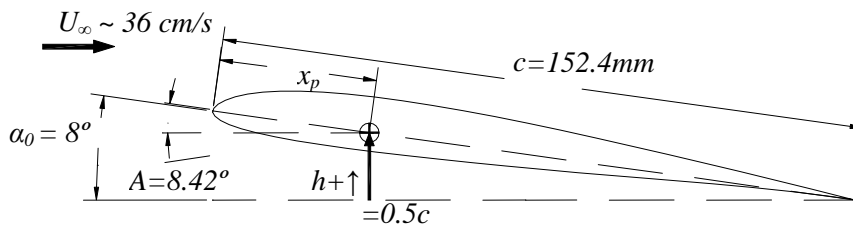


Figure 1-8: Schematic of SD7003 Airfoil and Parameters of Motion.

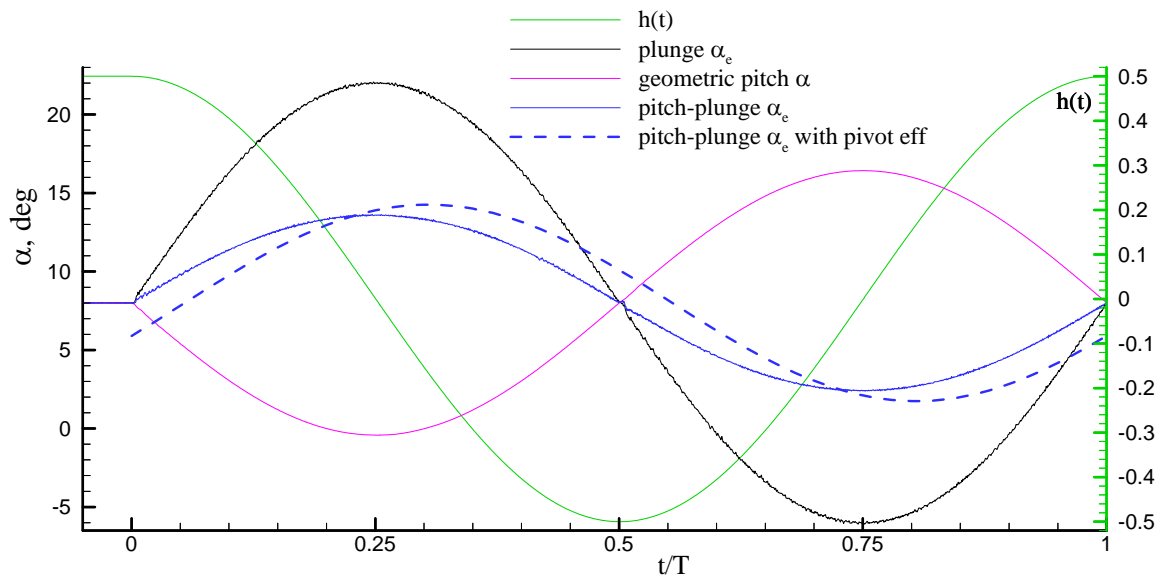


Figure 1-9: Motion Kinematics and Effective Angle of Attack Time History for Pure-Plunge and Combined Pitch-Plunge.

Figure 1-9 shows the plunge trajectory (green curve), total effective angle of attack in pure-plunge (black curve), pitch geometric angle of attack (purple curve) and total effective total angle of attack for combined pitch-plunge (blue curves). For pitch-plunge, the total effective angle of attack time-trace, α_e , straddles the static stall value of $\sim 11^\circ$ [52]; this is just the sum of the pitch and plunge cosines with appropriate phase shift. But α_e can be taken to include the effect of pitch rate, which depends on the pitch pivot point location, by summing all of the components inside the brackets in the third term of Equation 1; this is the dashed blue curve in Figure 1-9. The difference, vs. disregarding the effect of pitch pivot point location (solid blue curve) is a phase shift of $\sim 0.05 t/T$. With inclusion of the pivot effect, the limits on α_e become $2.03^\circ < \alpha_e < 14.03^\circ$, whereas for pure-plunge they are $-6.0^\circ < \alpha_e < 22.0^\circ$.

1.6.1.2 Flat Plates – Wall-to-Wall

The second set of cases is flat plates, nominally of 3% thickness and round (circular) edges. In some sense the flat plate is a more fundamental problem than the airfoil, because apart from the immediate vicinity of the leading edge, there is no pressure gradient due to the model geometry itself. Plates are also easy to manufacture for experiments, while the round trailing edge somewhat simplifies the computational grid. And if the plate thickness is large enough, bending and other structural deflections should be avoided.

The airfoil cases are deeply concerned with understanding the role of boundary layer transition in unsteady aerodynamics, but in many MAV applications transition is perhaps of secondary importance. Wings tend to be thin, with sharp edges; and transition only occurs in the wake, or in the late evolution of large separated structures. For a flat plate with round leading edge (as opposed to say a “super-ellipse”), presumably transition would occur near the leading edge, and would be fixed across a broad range of cases. We therefore repeated the pitch-plunge and pure-plunge cases for the airfoil, but now with the plate. But as with the airfoil, the geometry is nominally 2D, with the model wall-to-wall for the experimental facilities, and 2D or spanwise periodic in computations.

1.6.1.3 Flat Plates of Finite Aspect Ratio

A key question in MAV aerodynamics is the role of aspect ratio effects [3]. The question is both elementary and subtle. Of course one is interested in verifying to what extent lifting-line or lifting-surface theory can be used at low Reynolds number [53], just as it has been so successful for manned aircraft. Beyond this, there is the question of how the tip vortices of low aspect ratio wings might interact with the LEV to maintain flow regularity at high angle of attack and therefore to delay stall or to otherwise provide lift enhancement, beyond what is possible in 2D or for high aspect ratio wings. There is also the question of how lags between aerodynamic forces and motion kinematics would differ in 3D vs. 2D.

Experimentally, high but finite aspect ratio wings are awkward to test. Blockage considerations limit span, while high aspect ratio means very small chord, which in turn means a high physical oscillation frequency for a given reduced frequency. This can exceed the operating parameters of motion rigs, especially in wind tunnels. The small chord is also problematic for optical flowfield velocimetry methods. In computations, the grid would have to be large in the spanwise direction to capture the entire wing (or half-wing) and the tip region. Thus high-aspect ratio wings are more difficult to study. But more importantly, we deem high but finite aspect ratio wings to be not very interesting, apart from very applied problems such as the cruising performance of large birds. Low aspect ratio problems, on the other hand, are both very interesting and geometrically more amenable to investigation in unsteady conditions.

We therefore somewhat arbitrarily chose the case of a rectangular wing of aspect ratio = 2, with the same flat-plate section as in the wall-to-wall case, and round edges on the entire perimeter. Conveniently, for AR = 2 lifting-line theory and slender body theory give the same inviscid lift curve slope, π .

INTRODUCTION



Chapter 2 – FACILITIES AND METHODS

2.1 GENERAL COMMENTS

Here we describe the various experimental facilities and computational methods used by the Task Group. As the entire approach is predicated on cross-validation between the various facilities, between the various codes, and between the two, it is important to recite the capabilities and limitations of each. For example, a given facility might have higher or lower turbulence intensity than another, or a given model motion rig might have higher or lower fidelity of motion (vibration, elastic deflection, motion overshoot, etc.) than another. These may result in transition effectively further upstream. Further, blockage may differ, as would the role of “3D effects”, support interference, flow non-uniformity, and on and on. Similarly, the computational approaches differ in resolution and mesh type, 2D vs. 3D, treatment of boundary conditions, modelling of the far-field, type of filtering and averaging, turbulence and transition modelling, and so forth. While it is impossible to rigorously note all of these features, our aim is to be sufficiently descriptive to enable placement in context of the various results, such that, for example, a large laminar separation in a “quiet” tunnel and a much smaller separation in a “noisier” tunnel for nominally identical conditions could be ascribed to the right interpretation of the respective tunnel properties. Towards that end, the more experiments and computations on identically-posed runs, the better.

We note separately the various facilities using water as the working fluid, the facilities using air, the force measurement schemes, and the computational methods.

2.2 WATER TUNNELS AND WATER TOW TANKS

For unsteady aerodynamics, the advantage of liquid-based facilities, as opposed to wind tunnels, is that for the same reduced frequency the physical frequency of motion is much lower. This reduces loads on motion mechanisms and reduces the data acquisition rate requirements for diagnostics. Disadvantages include corrosion and conductivity of water, which complicate choices for materials and for force balances. Water tunnels also tend to have higher turbulence intensity than do the comparable wind tunnels. In theory tow tanks are the best choice, with zero turbulence intensity, but have the disadvantage of requiring drive mechanisms and long settling times between successive tests.

2.2.1 University of Michigan Water Tunnel

The University of Michigan (UM) water tunnel has a test cross-section 61 cm wide by 61 cm high and free stream speed range of 5 cm/s – 40 cm/s, with a turbulence intensity of approximately 1%, as measured by taking free-stream PIV images over a time-window of hours. However, the short time turbulence intensity computed by averaging over a time period on the order of the test section residence time is less than 0.5%. The larger value of the long time average is associated with very low frequency sloshing.

SD7003 and flat plate airfoil models with 152 mm chord were tested. The SD7003 airfoil model was fabricated with stereo lithography and a transparent resin (DSM Somos 11122) to minimize laser reflection at the model surface, while the flat plate model was built of stainless steel, with a polished surface to reduce laser glare. Both models were hung vertically, spanning the depth of the test section and terminating at 1 mm from the bottom, with an end plate at the free-surface. This cantilevered mounting scheme results in a maximum tip deflection of ~0.5 cm for the airfoil, and 0.1 cm for the plate. Pitch is produced by a rotary stage (Velmex B4872TS Rotary Table). One linear traverse (Velmex 20-inch BiSlide) produces plunge, and a second (Velmex 40-inch BiSlide) produces streamwise motion or surge (not used here). All are mounted above the test section and controlled by a Velmex VXM-1-1 motor controller. The experimental setup is illustrated in Figure 2-1.

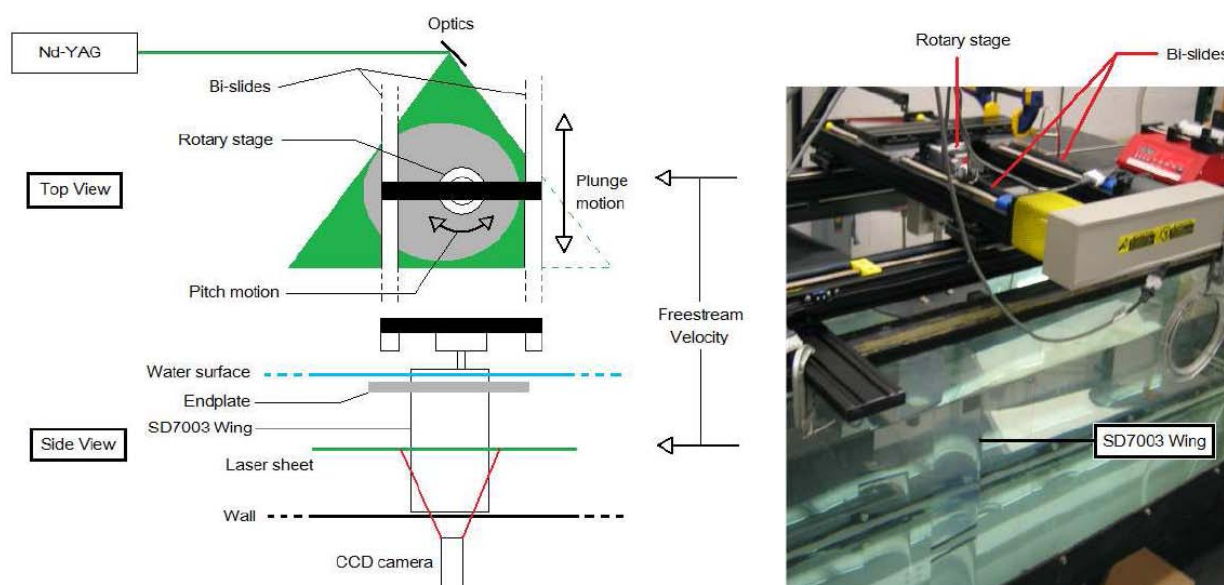


Figure 2-1: University of Michigan Water Tunnel: Motion Rig Schematic (left) and Installation Above Tunnel Test Section (right).

Measurements consisted of dye flow visualization and particle image velocimetry (PIV). The dye injection system is a probe rake with seven evenly spaced dye streams introduced half chord in front of the leading edge of the model. Two syringe pumps are used to match the dye speed at the injection point and the water channel flow speed to minimize disturbances. The dye streams are held fixed and the airfoil through the dye streams. The resulting streaklines capture flow direction and recirculation zones.

The PIV system includes a double-pulsed Nd:YAG laser (Spectra Physics PIV 300) and two dual frame digital cameras (Cooke Corp. PCO.4000). PIV seeding was with 3 μm diameter Titanium Dioxide particles. A small amount (8 drops) of a dispersant (DARVAN C-N, Vanderbilt) was added to the 5,000 gallon water tunnel to improve particle distribution and suspension, and to avoid clumping. The cameras were installed underneath the test section and were equipped with Nikon 105-mm Micro-Nikkor lenses to produce a magnification of approximately 25 pixels/mm and a field of view of 160 by 107 mm. Time between exposures was adjusted to produce a nominal particle displacement of 8 pixels at the free stream velocity for all cases. To capture the $h = 0.5 c$ plunge motion and to avoid shadowing of the field of view, the leading edge and trailing edge of the model were imaged separately, with an overlap region, and stitched together before processing. The accuracy of the axial Velmex BiSlide traverse is 0.00635 mm, giving approximately 1/6 of a pixel of image overlap uncertainty.

200 PIV pairs were taken at each phase, with the Nd:YAG laser, CCD cameras, rotary stage, and BiSlide were phase-locked. Every run recorded 12 periods and only the last 10 used to compute the phase averages. Recording was initiated by the PIV system data acquisition, which triggered the motion controller. The PIV laser timing and the motion period were matched with an accuracy of 0.1 ms for a typical period of approximately 10 s. This produced a slight discrepancy in the model position between the first image and the last image at phases with large plunge speed (7 pixels max, or 0.28 mm). This discrepancy resulted in an elimination of a datum point near the model surface.

PIV images were analyzed with in-house MATLAB-based PIV software. Particle displacement is determined in two passes using cross-correlation of displaced interrogation windows and Gaussian fit for sub-pixel fit. The first pass uses 64 x 64 pixel windows with uniform 8 pixel window displacement. The second pass uses 32 x 32 pixel windows with window displacement from the PIV calculation in the first pass, giving an approximate spatial resolution of 0.64 mm.

Several validation criteria were applied to the measured particle displacements. The displacement must be within a predetermined range of values in the x- and y-directions. The range of values in the first pass is fairly large, to capture the large range of particle displacements found near the model surface; and small (10 pixels displacement) in the second pass. A median filter is used to find the particle displacement at the points where the PIV validation failed, and to remove outliers. A square grid with 16 pixel spacing was used for all the images. Near the surface of the airfoil, data points within 32 pixels from the boundary were discarded because the interrogation window would include pixels inside the model. This corresponds to two data points in the measurement grid. To further remove outliers based on large sample-to-sample fluctuations, a 3-sigma filter was used. First, the sample mean and standard deviation from the 200 PIV images at each phase were calculated at each point in the flowfield. Then with the sample mean and standard deviation value, each datum point was revisited and the value was compared to ± 3 standard deviation of the mean value. The datum point was discarded if it lied outside the 3-sigma region and the remaining data were used to calculate a more accurate mean flow and turbulence statistics. Out of 200 images recorded, approximately 195 images were used for phase averages for relatively attached flowfields. For flows with large separation regions, approximately 180 images were retained after the 3-sigma filter. The calculated 95% confidence interval for the mean and turbulence statistics is tabulated in Table 2-1.

Table 2-1: Summary of 95% Confidence Intervals for UM PIV Data

95% Confidence Interval	Pitch-plunge case						Pure-plunge case	
	SD7003 ($Re = 10k$)		SD7003 ($Re = 30k, 60k$)		Flat Plate ($Re = 10k, 30k, 60k$)		SD7003 + Flat Plate ($Re = 60k$)	
	mean	max	Mean	max	mean	max	mean	max
u, v (% error U_∞)	$\sim \pm 1.5\%$	$\sim \pm 5\%$	$\sim \pm 0.5\%$	$\sim \pm 7\%$	$\sim \pm 1.5\%$	$\sim \pm 7\%$	$\sim \pm 2\%$	$\sim \pm 9\%$
$\overline{u'^2}, \overline{v'^2}, \overline{u'v'}$ (% error U_∞^2)	$\sim \pm 0.07\%$	$\sim \pm 0.42\%$	$\sim \pm 0.01\%$	$\sim \pm 0.53\%$	$\sim \pm 0.07\%$	$\sim \pm 0.7\%$	$\sim \pm 0.13\%$	$\sim \pm 1.25\%$

In Table 2-1 the values of the 95% confidence intervals are normalized. Velocities such as u are normalized by the free stream value, and statistics such as $u'v'$ are normalized by the free stream velocity squared. For each model and Reynolds number combination two values of the 95% confidence interval are reported; the mean and the maximum. The mean is the mean of the 95% confidence intervals computed for all the phases in a particular case. The maximum simply reports the maximum 95% confidence interval in the entire flowfield for all phases. This value indicates the worst possible uncertainty on the calculated mean value for a given airfoil kinematics. In general, the mean and the maximum confidence intervals at motion phases where the flow is largely attached were an order of magnitude less than at phases with large separation.

2.2.2 U.S. Air Force Research Laboratory Water Tunnel

The U.S. Air Force Research Laboratory's horizontal free-surface water tunnel has 4:1 contraction and 46 cm wide by 61 cm high test section. Free-stream speed range is 3 – 45 cm/s. A photograph of the tunnel, schematic of the pitch-plunge rig and installation of the SD7003 airfoil model in the tunnel are shown in Figure 2-2. In the photograph, the model is inside the test section, but the test section glass sidewalls are not visible.

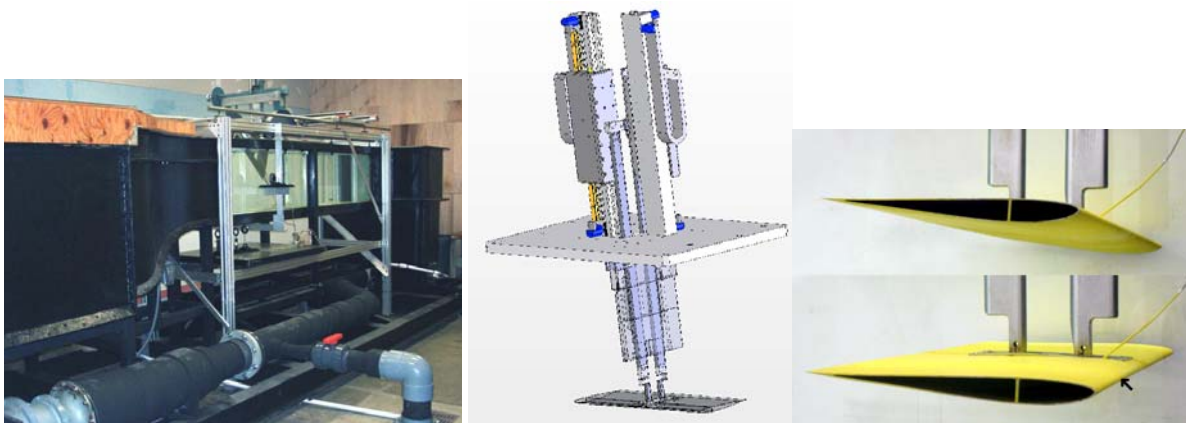


Figure 2-2: AFRL Horizontal Free-Surface Water Tunnel (left); Schematic of Pitch-Plunge Rig and Airfoil Model (middle); SD7003 Airfoil Installed Inside Test Section, Showing Smooth Suction-Side of Airfoil (top right) and Plunge Rod Coupling on Pressure-Side of Airfoil (bottom right). Black arrow in bottom-right points to dye injection exit port location.

Water tunnel turbulence intensity (u and v components) as determined from PIV free-stream data and confirmed by laser-Doppler velocimetry, is estimated at 0.4% at $U_\infty = 30 - 40$ cm/s. A surface skimmer plate at the entrance to the test section and a sealed lid of the intake plenum (visible as plywood cover in Figure 2-2) damp sloshing in the tunnel, that could otherwise have been excited as a first-mode shallow water wave, and would have resulted in low-frequency (~ 0.16 Hz) sinusoidal variation in U_∞ . More detail on the facility is given in Ol et al. [52].

The tunnel is fitted with a 3-component oscillator rig, with three electric linear motors, controlled through a Galil DMC 4040 Ethernet controller. Pitch and plunge are made possible by a pair of motors mounted vertically on a plate above the tunnel test section. Each motor actuates a vertical “plunge rod”, which connects via a bushing to the model at a fixed pivot point on the model chord, in the test section vertical plane of symmetry. The upstream plunge rod is constrained to move purely vertically, whereas the downstream plunge rod is allowed to pivot in the test section vertical plane of symmetry. The desired angle of attack and vertical position time history of the model are converted to position commands for each linear motor. This allows for single degree-of-freedom motions such as pure-pitch about a prescribed fixed pivot point, or pure-plunge. Pitch and plunge can be combined, and the pitch pivot point can be varied by suitable choice of phase and amplitude difference in trajectory of front or rear plunge rod. For all cases where the pitch pivot point is not coincident with the bushed end of the front plunge rod, there will be a small parasitic streamwise displacement of the model, which would be unavoidable unless the front plunge rod were to be allowed to pivot similarly to the downstream one. A third degree of freedom, surge, is made possible by a larger linear motor mounted horizontally aft of the pitch-plunge carriage. It is used to remove the aforementioned parasitic streamwise displacement, as was necessary for aft-mount sting experiments with an $AR = 2$ plate described in Chapter 6.

Particle image velocimetry measurements were taken with a PCO 4000 11Mpix camera run in single A-D mode, triggered from an external pulse train derived from the position encoder of the motion rig, thus allowing for selection of motion phase at which to acquire data, and for phase averaging. Velocity data were acquired once per period of oscillation, for a sequence of 120 periods. The first 5 periods were removed from each data set, and the remaining 115 velocity data sets were ensemble averaged for each phase of motion. Vorticity was calculated by explicit differentiation of cubic spline fits to the velocity field (as discussed by Willert and Gharib [54]). PIV resolution was typically 156 pixels/cm, which for 32×32 -pixel windows with 16×16 overlap gives 148 vectors per chord length. Because of laser reflections from the model surface (polished stainless steel, spray-painted flat-black) and lack of corrections for PIV windows which at least partially intersect with the model surface, data in the first row

of PIV windows adjacent to the airfoil surface are not reliable. Light sheet thickness was approximately 1.5 mm max, though the large field of coverage (up to 45 cm across in some cases) makes precise collimation of the light sheet difficult. To obtain the “most 2-dimensional” flowfield, the PIV light sheet was placed at the 3/4 span location; that is, approximately halfway between the plunge rods and the tunnel wall, and 0.05 c inboard of the dye injection slot. More detail on the rig operation and discussion of experimental error is given in Ol et al. [55].

For dye injection, a wand with 0.5 mm internal diameter, injecting concentrated blue food colouring, was fitted inside the model and exits flush with the outer mould lines near the airfoil leading edge, firing approximately wall-normal. The dye exit location is not visible in Figure 2-2, but is marked by the black arrowhead in the bottom-right-hand portion of Figure 2-2.

2.2.3 Cambridge University Towing Tank

The Cambridge University Engineering Department (CUED) towing tank is 7 m long and has a 1 m x 1 m cross-section with a central 2 m long Perspex test section. A three-dimensional model and photo of the waving arm mechanism is shown in Figure 2-3, where the entire mechanism is shown suspended from the tow tank carriage on four vertical struts. The Perspex sides and the water volume of the tank are shown to provide a sense of scale. The water depth is 0.8 m.

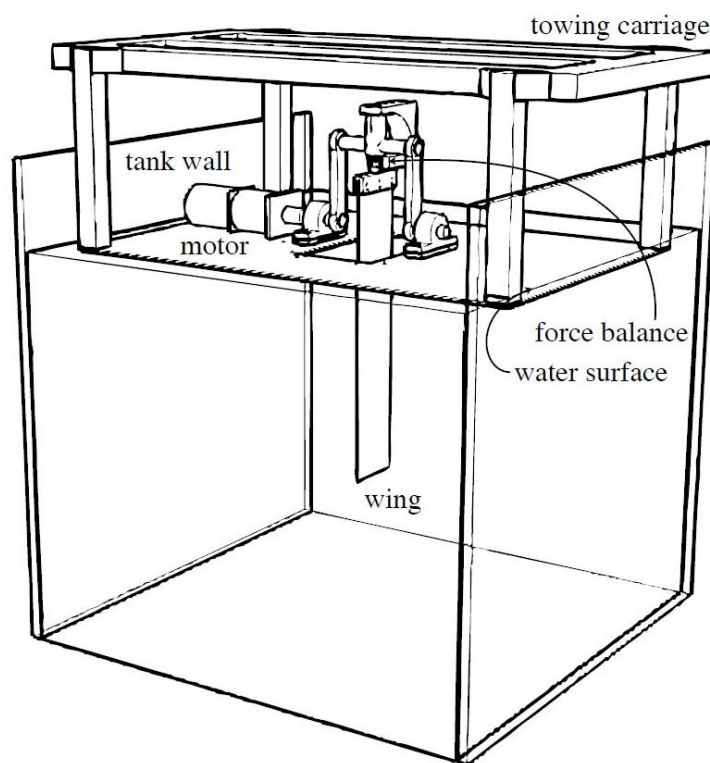


Figure 2-3: Schematic of Section of CUED Water Tow Tank and “Waving Arm” Setup.

The waving wing mechanism was designed to mimic the translational phases of an insect wing stroke, extending the propeller experiments to include wing starting and stopping. The wing is started from rest and swept through a wing stroke angle θ up to 90 degrees, with or without a “freestream” generated by translating the mechanism via a towing tank carriage. The wing’s angular velocity can be programmed to any profile.

The mechanism is mounted on a stainless steel plate suspended just below the water surface. The waving motion is controlled by a servomotor and gearbox programmable through LabView, and a slotted optical switch is mounted near one end of the axle to confirm wing position. A force balance can be mounted on the wing to provide unsteady lift and drag force measurements. The distance from the wing root (defined as the bottom of the skim plate when the wing is vertical) to the axis of rotation is 10% of the span. The angle of attack is selectable from 0 to 45 degrees in 5 deg increments. The wing is a 2.5% thick carbon fibre flat plate with rounded edges, a chord of 0.125 m, and an aspect ratio of 4 as measured from the free surface to wingtip. A 90 deg wing stroke is equivalent to 5.37 chords of travel at 3/4 span. At a 15 deg angle of attack blockage of the towing tank is 2%.

The wing stroke was programmed using three different velocity profiles: linear, sinusoidal, and exponential. The wing was accelerated such that it reached its maximum velocity after 0.10 (exponential only), 0.25, or 0.60 chord-lengths of travel for each profile. Velocity profiles were symmetric such that the wing decelerated in the same way before reaching a maximum stroke angle of 90 degrees. The maximum velocity was chosen as that which gives a local wing Reynolds number of 60000 at 3/4 span.

2.2.4 ONERA Tow Tank

The ONERA (Lille) water towing tank has a carriage system with towing speed of between 0.1 m/s and 1.4 m/s. Speeds below 0.1 m/s are unstable, while at speed above 1.4 m/s the available test duration is too short. The towing tank can alternatively be run as a water tunnel, but the flow is not uniform and is unsteady with a large turbulence level (>3%). So the results presented here are only obtained in towing-tank mode. Tests with hot wires in the water show that the residual velocities before test start are too low to be measured (<1 mm/s). As the facility was built quite some time ago, the servo command of the carriage velocity is not as efficient as desired. The length needed to reach operating velocity is a couple of periods. As the unsteady hydrodynamic effects are important during these first periods, the measured forces on the model are retained only after a couple of periods. To ensure that the frequency of movement is constant and to phase the measurement at the same position from each period, an optical trigger system is used on one of the rotating wheels.

The model oscillation mechanism consists of two crank wheel systems with a phase lag between the two wheels. The amplitude in pitch depends on the difference of phase between the wheels. The mechanisms were conceived for flap and pitch motions as well as plunge and pitch motions, and therefore require adjustment to produce true pitch-plunge. Approximation to true trigonometric motion depends on the crank stroke to connecting rod length ratio, which is large – and hence the approximation is close. To reduce vibrations, a belt drive system is used. Servo control motors generate excitation of the mechanism at frequencies higher than the periodic oscillations; specific transfer functions of the servo mechanism are necessary to eliminate excitations at a frequency near the structural resonance. As the system, with a constant rotation rate motor, is not controlled in a closed loop, the movement is forced by the mechanism. The mechanism and model installation are shown in Figure 2-4.

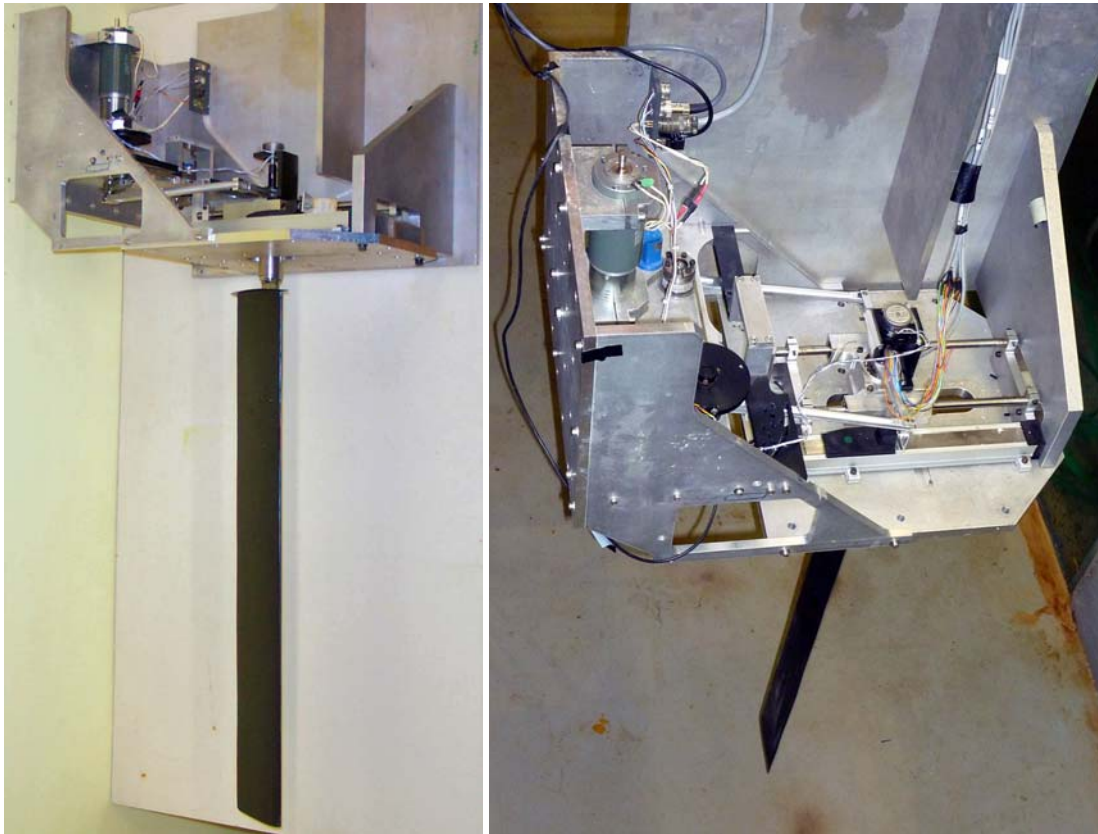


Figure 2-4: ONERA Tow Tank SD7003 Wing Installation; View of Model (left) and Oscillation Rig Atop the Towing Tank (right).

To avoid free surface effects, that are important at relatively high velocity (>0.5 m/s), a flat plate moving with the wing can be fixed on the strut supporting the balance. For quasi-2D runs the tip of the wing can be close to the tank ceiling, but because the tank floor is somewhat uneven, the tip gap can not be too small. The physical aspect ratio of the SD7003 airfoils tested in the tank was 7 or 14.

2.3 WIND TUNNELS

2.3.1 Technical University of Braunschweig Wind Tunnel

The TUBS facility is an atmospheric Eiffel-type wind tunnel with a closed test section (Figure 2-5). The settling chamber with nozzle, the diffuser and the motor mounting are made from glass fibre reinforced epoxy and the test section is transparent. A 3 kW motor drives the tunnel in suction mode. The wind tunnel is installed in a room which allows circulation of the flow. Motor and fan are decoupled from the rest of the tunnel.

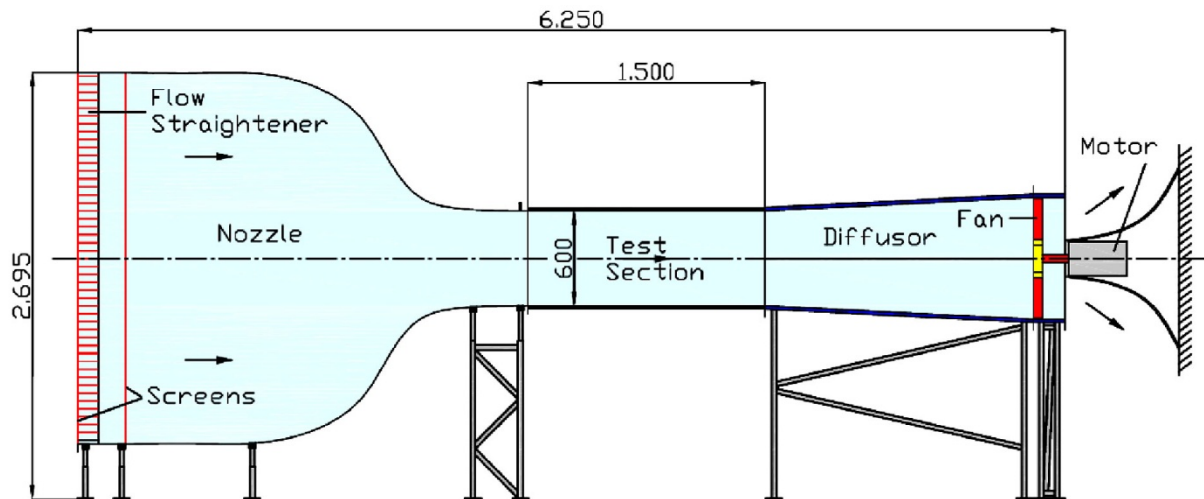


Figure 2-5: Low-Noise Wind Tunnel of Technische Universität Braunschweig.

The wind tunnel nozzle has a rectangular cross-section with a Boerger-type axial area distribution. The contraction ratio is about 16 to achieve low-turbulence flow in the test section. The exterior wall is covered with acoustic foam plates to suppress noises reflections. At the inlet to the settling chamber several devices are installed to reduce turbulence and to achieve a uniform flow. At first the air flows through a 30 mm thick fleece mat. It then passes through a honeycomb flow straightener and finally through a fine woven screen to decrease the size of the turbulent structures. The test section has a height of 600 mm, a width of 400 mm and a length of 1500 mm. A vane anemometer is used to control the speed of the flow in the test section. The measured velocity variations in the core flow are below 1%. The turbulence level was measured by means of the hot wire anemometry. The turbulence level measured along the vertical symmetry axis of the test section is around 0.16% at 10 m/s.

The 2D airfoil motion apparatus of TU BS is mounted around the test section. The task of the apparatus is to simultaneously perform plunging and pitching motion: A 3 kW motor drives a 4:1 ratio transmission which transfers the rotation motion to two interdependent systems: The plunging motion system and the pitching motion system. Plunging motion is created by a sliding carriage connected to a balanced flywheel. The sliding carriage has a lightweight design. A timing belt drives a second sliding carriage for supplying the pitching motion. The apparatus allows adjusting plunge amplitudes of 100 mm, pitch angles up to 25 deg, and the motion frequency may be as large as 5 Hz.

Boundary layer resolution for phase-locked PIV measurements is obtained from 11 measurement windows along the upper surface of SD 7003 airfoil, according to Figure 2-6. For each of the selected phase angles at least 800 image pairs are obtained. Lack of a direct camera view of the PIV light sheet in the streamwise plane resulted in the need for askance viewing, which fits naturally with rotational-type stereoscopic PIV with Scheimpflug camera-lens adapters to remove astigmatism.

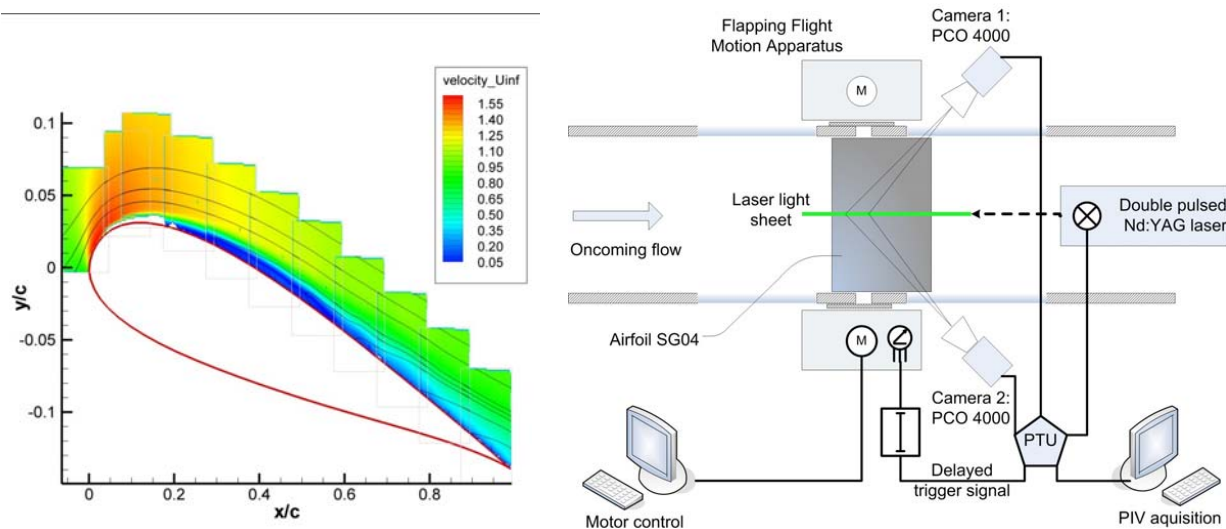


Figure 2-6: Arrangement of PIV Interrogation Windows (left) and Stereo PIV Setup Used for the Flowfield Measurements of TUBS (right).

Accurate calibration is critical to successful stereo PIV. A calibration plate is therefore positioned coplanar to the laser light sheet, and set a several displacements normal to the light sheet. The images will not be sharp for every position y since the cameras are only focused on one certain plane and so the aperture of the camera objective has to be optimized. The calibration concerns capturing images of the grid on the calibration plate. Note that one optical path from one camera has to pass the plate. When performing PIV measurements, i.e. capturing particle images of the laser light sheet, there is no plate in the optical path, and the optical path is slightly different. This difference is called disparity. It is estimated by correlating a single particle image seen by the different views of the two cameras. The disparity map is used afterwards to correct the calibration matrix by analytical formulations.

PIV data processing for a moving model requires several steps in addition to the usual PIV cross-correlations. One issue is “wobbling” of the airfoil surface, because the oscillatory motion is not exact from period to period. A wobble correction is therefore performed. When the laser light sheet reaches the airfoil surface, the reflection line is visible on the camera images. Due to the phase locked imaging, this reflection line which indicates the position of the airfoil should be always at the same location. However, the reflection line is wobbling about 0.5 millimetres in the camera images. This wobbling has to be removed since the airfoil has to be at the same position for the later ensemble averaging procedure of the vector fields. The required shifting is performed with a correlation algorithm.

In the next step of improving the particle image quality, all particle image pairs are averaged. Hence, the particle information vanishes, but the laser reflection line and the average noise in the image background remain. This average image is now subtracted from each particle image. Consequently, the intensity of the reflection line and the background noise decreases, there is a better signal to noise ratio. Furthermore, the areas in the particle images inside the airfoil without information are masked out.

Having completed several image pre-processing techniques to improve the particle image quality, the particle displacement evaluation is executed in the next step using a cross-correlation scheme. A multi-pass interrogation scheme is applied with decreasing interrogation window size (from 128 x 128 pixels down to 32 x 32 pixels), 50% overlap and elliptical weighting function. The resulting set of vector fields for each measurement window is later post processed. This is necessary to filter out non-physical vectors in the vector fields which would corrupt the results of the ensemble averaging procedure. For this purpose a correlation peak ratio filter is employed with a peak ratio of 3. Furthermore, iterative remove and replace filtering is

used. The vector of a certain interrogation window was only considered for ensemble averaging if at least 800 image pairs produced valid vector data. More details are found in Bansmer et al. [56,57].

2.3.2 DLR Wind Tunnel PIV Measurements

The German Aerospace Centre (DLR), Institute for Aerodynamics and Flow Technology, pursued a combination of particle image velocimetry and surface photogrammetry for a range of flexible wing pitch-plunge experiments in the TUBS wind tunnel, already described above. The surface photogrammetry enabled determination of deflection time history of flexible structures and thus fluid-structure interaction, but for the nominally rigid wings of the present study, this capability was not of direct priority. Accomplishing both measurements simultaneously requires care in surface coatings and optical filters of the imaging cameras; unfortunately this sometimes leads to camera pixel saturation from laser reflections, exacerbating the usual problem of an “optical boundary layer” plaguing PIV at the model surface.

The same optical setup is used for measuring the model position and orientation and to measure the wing shape and deformation (Figure 2-7). Two JAI A1 cameras (1392 x 1024 pix) are arranged above the top window of the test section symmetrically along the centre line of the model. The lenses ($f = 16$ mm) are chosen such that the model is always completely captured from both cameras at viewing angles 20° . The upper model surface is homogeneously illuminated from above by an extended beam from a 25 mJ Nd:YAG pulse laser. The PIV setup has two laser light sheets to capture the flowfield in a streamwise plane below and above the moving wing at a fixed span position of $b/4$. Two double pulsed Nd:YAG laser heads (Big Sky CF-400) each providing about 150 mJ light energy per pulse are located behind the top and bottom window of the test section. Two separate PCO-1600 double shutter cameras (1600 x 1200 pix) are used to observe the flowfield below and above the wing at a right angle to the light sheets. The optical measurements were performed simultaneously at 10 different phase positions of the sinusoidal movement of the model. For each run 1050 images were taken by each camera allowing a phase averaging of the results using 105 samples. For data processing, the “Point Tracker” and “Strain Master” of the DaVis PIV software are used; more details are given in Kirmse and Wagner [58], and Konrath et al. [59].

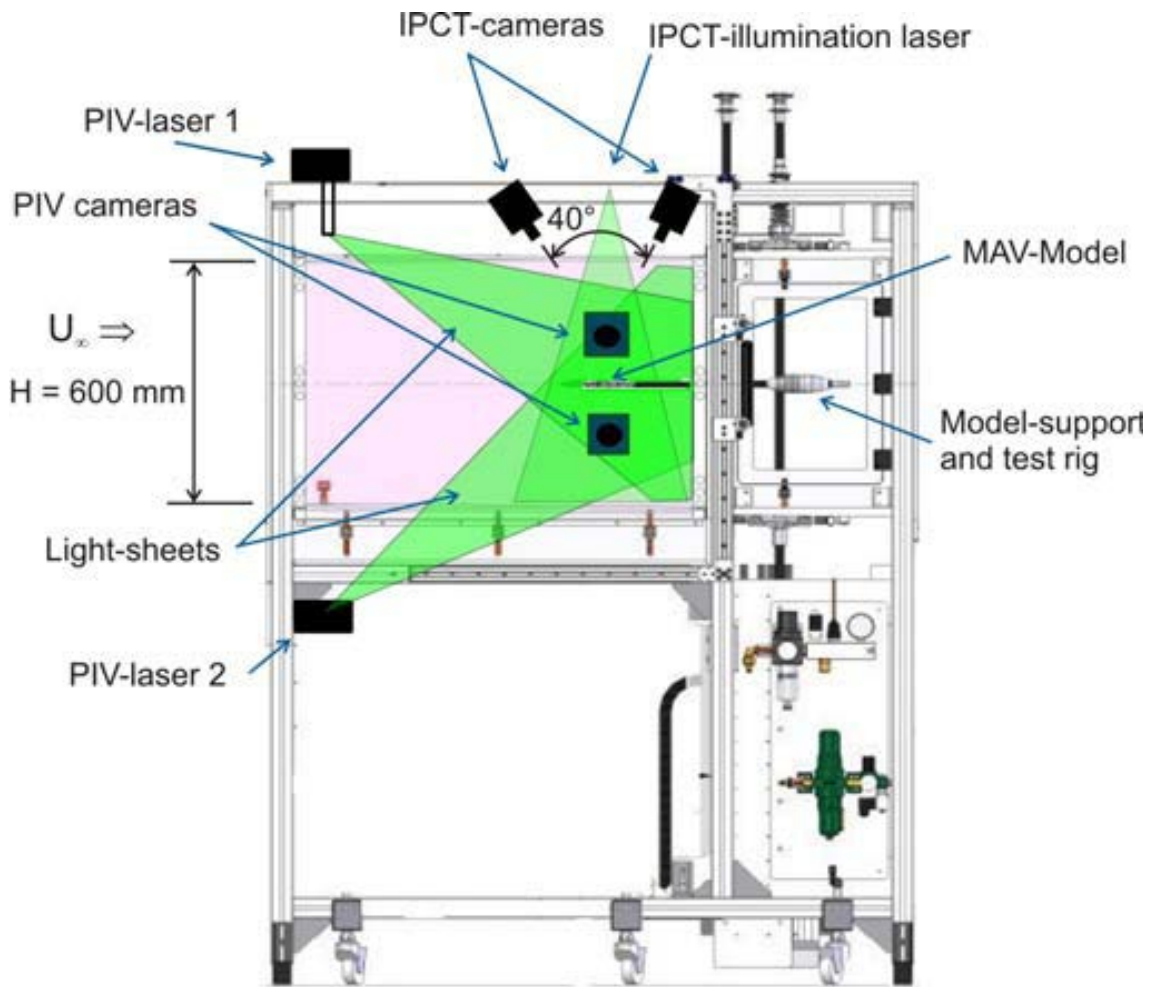


Figure 2-7: DLR Optical Setup Inside TUBS Wind Tunnel Test Section.

2.3.3 TU Darmstadt Wind Tunnel

The TU Darmstadt experimental setup consists of a pair of pitch-plunge motion rigs and an Eiffel-type wind tunnel with test section of cross-section of 45 cm by 45 cm and a length of 2 m. The tunnel has a contraction ratio of 24:1 with five turbulence filters in the settling chamber and produces turbulence levels on the order of 1.0% at the test speeds of interest here. A schematic of the wind tunnel is shown in Figure 2-8. The free-stream velocity was controlled via closed-loop control, with the tunnel speed input obtained from a hot-wire anemometer (Dantec Dynamics A/S type 55P11) positioned at the entrance of the test section. The hot-wire anemometer was calibrated for each new set of measurements using a miniature vane anemometer.

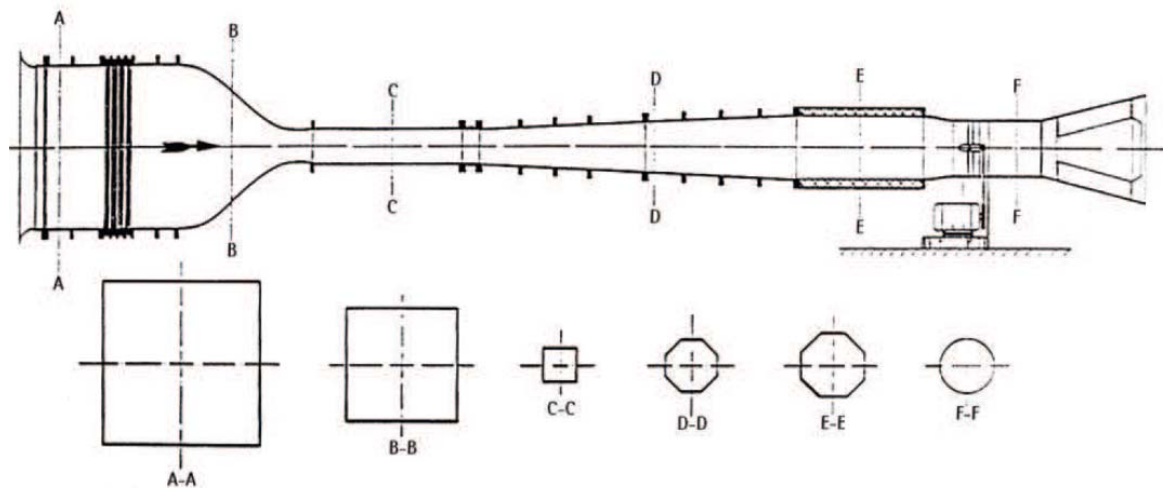


Figure 2-8: Schematic of Wind Tunnel; Note Intake (A-A) and Test Section (C-C) Cross-Sections.

A commercial PIV system (Dantec Dynamics A/S) consisted of a Nd:YAG ($\lambda = 532$ nm) Litron dual-cavity laser with a maximum power output of 135 mJ per cavity and two 10-bit FlowSense 2M CCD cameras each with a 1600 x 1200 pix resolution. Due to the large imaging field required, 60 mm f/2.8 Nikkor lenses were used. To reduce reflections, the model was painted mat-black and monochromatic filters, with a corresponding wavelength of $\lambda = 532$ nm, were installed on the lenses. The light sheet was approximately 2 mm in thickness, set parallel to the flow direction and aligned onto the airfoil quarter-span position. Due to the large imaging area of 0.0864 m² the laser power was set to 90% for both cavities. With the use of compressed air driven through four Laskin nozzles, DEHS seeding particles less than 1 μ m in diameter were introduced into the settling chamber using a vertical rake aligned with the measurement plane.

The oscillation rig consists of a base structure, a set of linear-motors connected with each other via a linkage system and a carbon-fibre SD7003 wall-spanning profile weighing 306 g. The profile has a chord length of 120 mm and a span of 450 mm. The profile-tip spacing at the walls is less than 2 mm on either side. Maximum static blockage in the test section based on the frontal area was under 3%. A schematic of the tandem configuration integrated into the Eiffel-type wind tunnel test section at the Institute of Fluid Mechanics and Aerodynamics (TU Darmstadt) is shown in Figure 2-9. The various components of the standard Particle Image Velocimetry (PIV) system used for these measurements are also included in the schematic.

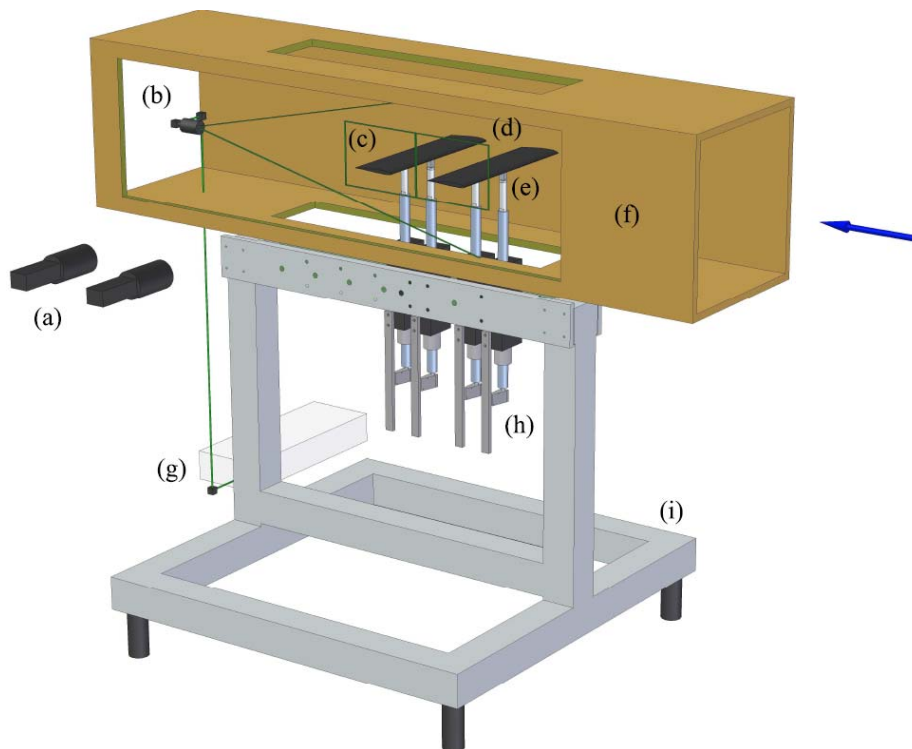


Figure 2-9: Test Section of TU Darmstadt Wind Tunnel, Showing Two Linear Motor Pairs for Tandem-Wing Pitch-Plunge; Only One Set of Motors and One Wing was Used in the Present Study: (a) PIV Cameras; (b) Beam Expander; (c) PIV Image Frames; (d) Wall-Spanning Carbon-Fibre Profile; (e) Embedded Piezo-Electric Force Sensors; (f) Test Section; (g) Laser Head; (h) Linear Motors with Linkage System; and (i) Base Structure.

LinMot PS01-48 x 240F-C linear motors used to drive the pitch-plunge motion. A displacement accuracy of <0.5 mm was achieved in the setup, depending on the duration of the experiment and the temperature of the bushings. The control of the linear motors was achieved with a combination of digital inputs for high-speed triggering and a serial port communication. A LabView 8.2 control program was developed to operate the communication system with the linear motors. Setup and configuration of the motors was done via LinMot's own configuration and test program (LinTalk). Additional external position sensors were mounted on the motor units for higher positional accuracy, allowing for a dynamic angle-of-attack accuracy of less than 0.5 deg.

PIV image pairs were sampled at 15 Hz allowing for 6 phases to be recorded per cycle at $k = 0.25$. In order to construct the ensemble velocity fields of 12 phases per cycle, two staggered sets with 100 images per phase were ensemble-averaged. In all cases the first two starting cycles were removed from all ensembles. Each camera imaged a field corresponding to $x/c = 2$ and $y/c = 1.5$, with a resolution of 800 pix/c (6.7 pix/mm). Reflections on the model surface were strongest at the bottom of the stroke where a region 0.04 c normal to the airfoil surface was deemed to be unreliable. Shadows and strong reflections on the pressure (lower) side required masking. Parallax effects were strongest at the top of the stroke and at this position were responsible for hiding a region 0.03 c normal to the airfoil surface. The vector fields were calculated using an adaptive correlation with 32×32 pix interrogation windows and a 50% overlap. A 3×3 filter was used to lightly smooth the vector fields in order to more clearly define the vortical structures in the wake. A local neighbourhood validation using a 9×9 moving-average filter and an acceptance factor of 0.2 was employed to eliminate outliers. This, however, also had the effect of smoothing the velocity gradients, thereby thickening the shear layers.

2.3.4 University of Florida Wind Tunnel

The UF-REEF/AFRL low Reynolds number Aerodynamic Characterization Facility (ACF) is an open jet wind tunnel. The test section is a 42" square column of air with a length of 15 ft. What is unique about the ACF is that it offers uniform air flow at mean free stream velocities ranging from 1 to 22 m/s. Turbulence intensities measured are less than 0.11% between free stream velocities of 1 and 7.5 m/s. Photographs of the tunnel are given in Figure 2-10.

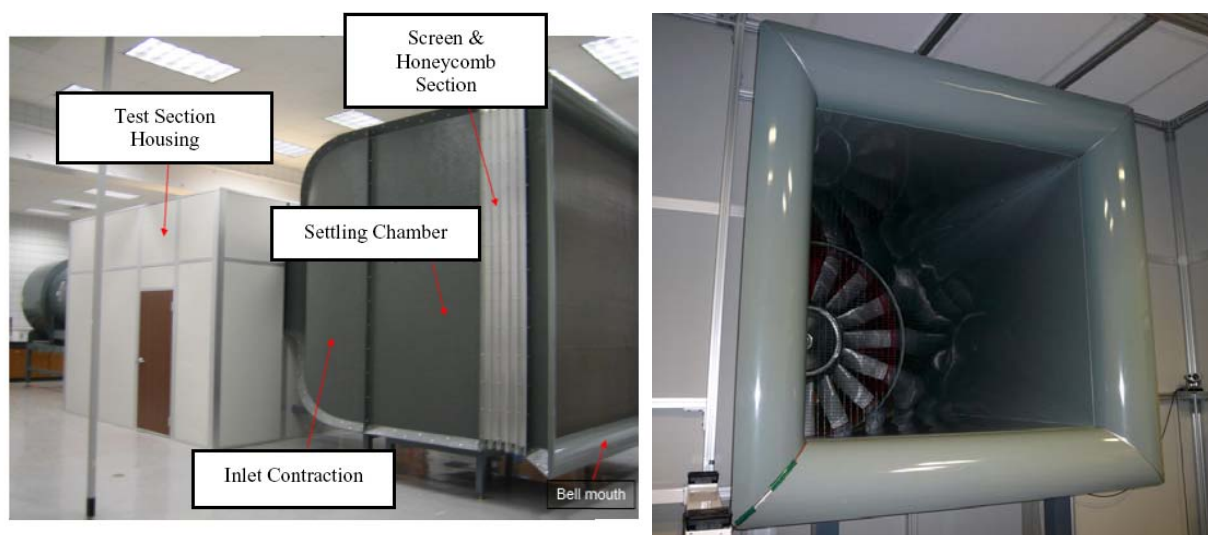


Figure 2-10: University of Florida REEF Open-Jet Wind Tunnel; Exterior View (left) and Diffuser Bellmouth as Viewed Inside Chamber Enclosing Test Section (right).

The ACF's Dynamic Pitching-Plunging Motion Rig (DPPMR) consists of two Parker ironless linear motors each connected to an Aries model AR-20AE driver. Each linear motor has a 767 mm travel length with an encoder of 5 micron resolution. The Aries drivers are controlled by a Galil DMC-2020 motion controller. Based on a user input through a LabView interface, the rig can be commanded to output a standard TTL trigger at a desired encoder position, allowing for reliable PIV phase averaging.

A LaVision particle image velocimetry (PIV) system was used to make velocity field measurements, typically at four instantaneous phases (0° , 90° , 180° , and 270°) throughout the cyclical motion. The laser is a Litron Nano L 135-15, double-pulsing at 135 mJ/pulse perpendicular to the model planform. The camera is an Imager ProX-4M (2048 x 2048 pixel CCD) capable of acquiring images at 14 frames/sec for an external trigger. A Nikon 60 mm lens with an f-number of 2.3 was used. These components were controlled through a system computer running LaVision DaVis software. The system computer was externally triggered from the TTL signal from the DPPMR. This signal initialized the laser/camera trigger sequence. A time delay of 300 μ s was assigned between the image pairs of the camera which resulted in 19 pixel displacement in the free stream. The Imager ProX-4M was camera oriented to view a two dimensional cross-section of the flat plate at 75% of the span. For all of the measurements presented, the streamwise domain of interest was split into two domains, each approximately 119 mm long. This allowed for increased resolution with resulting grids 1.87 mm square. The flow was seeded with a Laskin nozzle seeder using Olive Oil as the medium. This seeder generated particles approximately 1 μ m in diameter at a rate of 7×10^{10} particles per second.

DaVis 7.2 PIV software package from LaVision was used to analyze the PIV images using a multi-pass cross-correlation method. The first pass consisted of an interrogation region of 64 x 64 pixels with 50% overlap. Two more passes were conducted using a 32 x 32 pixel interrogation window with 50% overlap. As a rough filtering mechanism, DaVis was used to post process each single vector field to remove vectors

which are greater than 2.5 times the root mean squared (rms) value of its neighbours. This procedure is completed for 420 images at a single phase of motion. As a final processing step, the mean velocity field is calculated by averaging each interrogation region through all the valid velocity vectors throughout all the ensembles. Any velocity vector that resulted in a deviation outside of two standard deviations throughout the ensemble was also removed. This effectively removes any erroneous velocity vectors calculated from lack of seeding between images.

2.4 FORCE BALANCES

Force measurement in unsteady aerodynamics is notoriously difficult. Especially in wind tunnels, where physical motion rates are high, subtraction of inertial loads is a challenge, because inertial loads can easily overwhelm the aerodynamic loads that one ultimately wishes to extract. Sting and model vibration produce additional force errors and cycle-to-cycle variations. Aggressive low-pass filtering is generally required, but of course one must take care that the filter does not remove too much of the “true” aerodynamic component. These difficulties are quite attenuated in water-based facilities, where physical motion rates are much smaller, but there one must contend with the problem of fluid conductivity and rusting or oxidation of metals. Thus, a large part of the present work was the development, calibration and proof-of-concept testing of force balances.

2.4.1 AFRL Fibre-Bragg Grating Balance

To circumvent difficulties associated with electrical strain gauges in water – waterproofing, routing of wires, drift, gauge delamination and so forth – an optical approach, using fibre-Bragg gratings (FBGs) [60], was used. Coherent light is sent through the fibre and through gratings written onto the fibre. Each grating reflects light of very narrow bandwidth. If the segment of the fibre containing a grating is strained, the reflected light wavelength shifts proportionately. Strain of the fibre could be due to mechanical strain of the underlying substrate (the flexure joint in the force balance) and to thermal effects, which must be removed through appropriate compensation. In the present application, a single fibre with 4 grating elements was integrated into a two-flexure-joint airfoil mount, thus serving as an integrated force balance (Figure 2-11). The balance can resolve axial force, normal force and pitching moment, though only the lift is reported here.

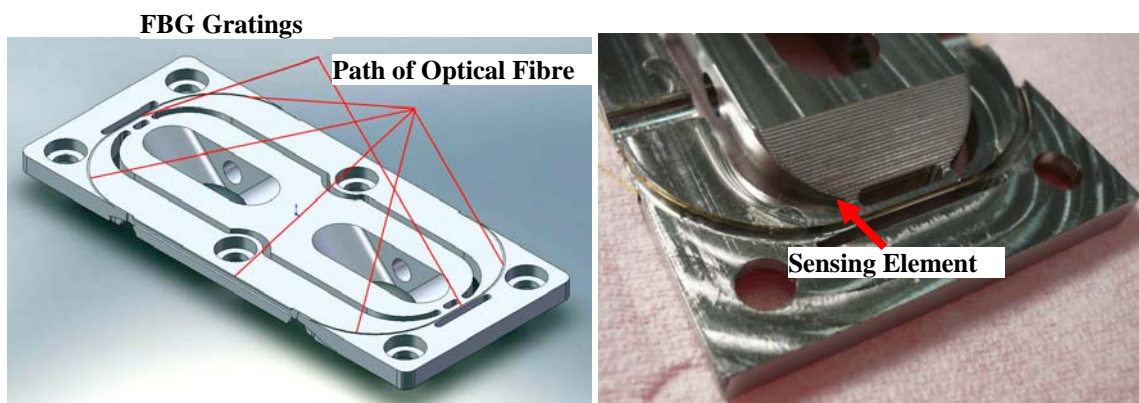


Figure 2-11: 3-Component Force Balance Based on Fibre Bragg Grating (FBG) Sensors, Integrated with Airfoil Mount; Schematic (left) and Photograph from Underside, with Detail of a Flexure Joint (right).

The FBG signal was interrogated via a Micron Optics sm130 instrument [61], with sampling at 250 Hz phase-averaged over 200 periods of oscillation and low-pass filtered at 6.5 Hz, with the first 5 periods

removed from the sample. Inertial tares were conducted by draining the water tunnel and repeating the airfoil motion.

The balance was calibrated in benchtop tests with loads applied at 0° and $\pm 45^\circ$. These data were used to compute the load cell calibration matrix. The standard error of the calibration matrix for the lift force is 0.16 N, which corresponds to a lift coefficient standard error of 0.03.

2.4.2 Cambridge University External Balance

Two-component force balance measurements were taken in both air and water for the wing waving through 90 degrees or 5.37 chord-lengths of travel at 3/4 span. Data was sampled at 7 kHz with and without a 30 Hz low pass filter. Wing lift and drag coefficients were obtained by subtracting the inertial forces measured in air from the forces measured in water and normalizing by the local wing velocity such that $C_L = 6L/[\rho\omega^2c(r_t^3 - r_r^3)]$ where r_t and r_r are the distances from the axis of rotation to the wing tip and wing root. Force data was averaged over five runs.

The force balance is capable of measuring two force components to 10 N with a resolution of at least 0.01 N. When paired with a Fylde FE-379-TA transducer amplifier and National Instruments USB-6221 Multi-Function DAQ, unsteady lift and drag forces can be measured at frequencies up to 250 kHz.

Figure 2-12 shows the lift coefficient values calculated from the unfiltered data, data acquired using a hardware 30 Hz low pass filter, and the same data with a moving-average smoothing applied. The unfiltered lift signal contains high-frequency electrical noise near 100 Hz and a mechanical vibration between 15 and 20 Hz. This vibration is evident in both air and water when the motor is run with and without the wing attached. There is frequency shift between air and water thus the inertial data acquired in air is smoothed before it is subtracted from the force data acquired in water. The force data shown in the following plots was acquired with the low pass filter in place to remove the electrical noise, the inertial data subtracted, then smoothed to eliminate the signal from the vibrations.

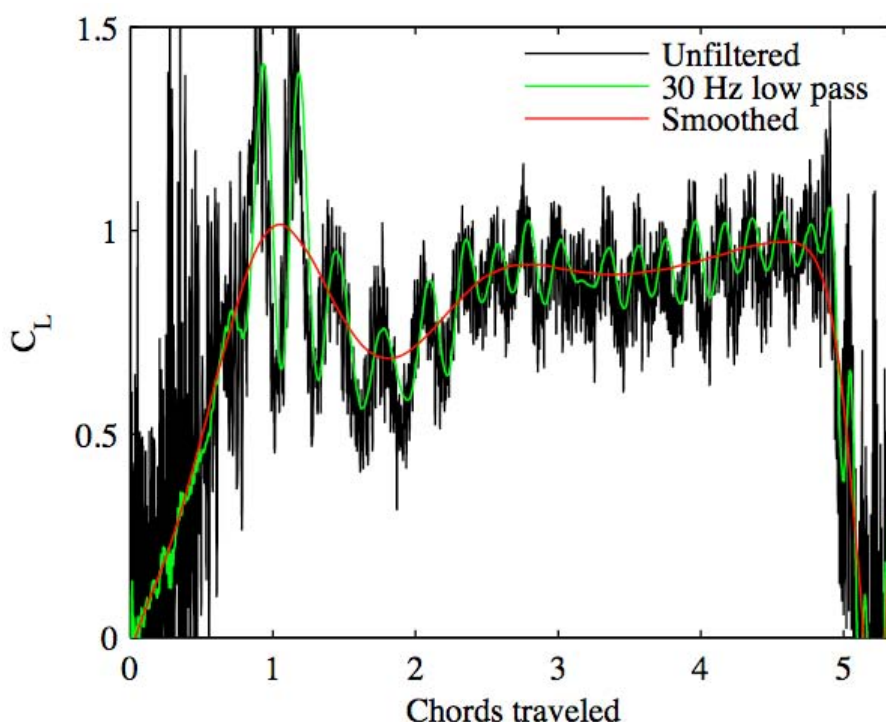


Figure 2-12: Sampled CUED Tow Tank Force Balance Data, with Various Types of Signal Filtering.

2.4.3 TU Braunschweig Internal Balance

The 3D model support of TU BS is designed for high precision movements with 3 degrees of freedom in the upright plane. The model support is driven by linear synchronous direct drives with moving coil, with a maximum of 700 N or a speed of 5.3 m/s, during high dynamic and high precision movements. The standard movements are a plunging motion up to ± 150 mm @ 3 Hz and a pitching motion with max. $\pm 20^\circ$ @ 3 Hz. The position accuracy is ± 0.1 mm or $\pm 0.1^\circ$. The repetitive accuracy of both types of motion is ± 0.05 mm or $\pm 0.1^\circ$.

A sketch of the actuation principle is shown in Figure 2-13. The two vertical actuators are used to create pitch and plunge motion of the model. This set up generally causes a small longitudinal motion in the streamwise direction. To remove this problem, additional horizontal actuators will be added in the future.

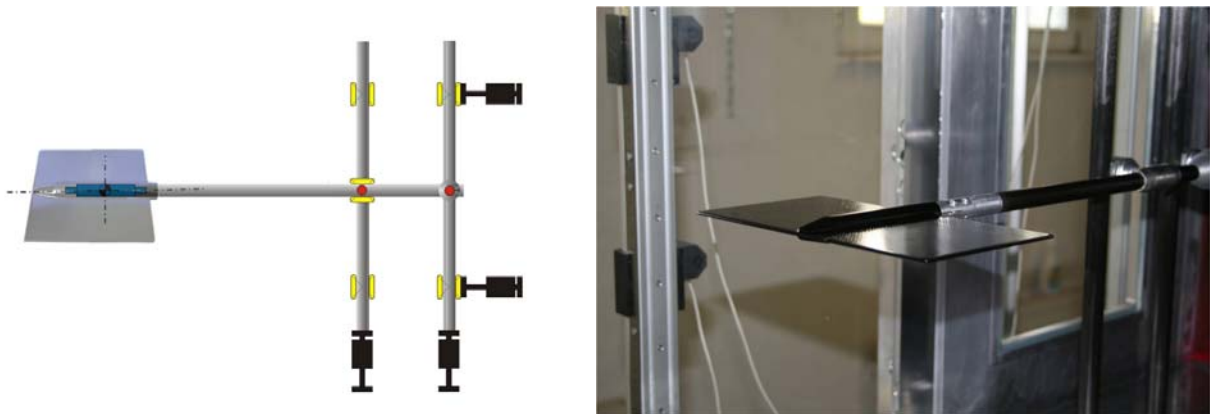


Figure 2-13: Motion Scheme of 3D Model Support (left) and Photo of AR = 2 Flat-Plate Model Mounted in the TUBS Wind Tunnel Test Section (right).

A small six-component internal strain gauge balance is used to determine the aerodynamic forces. Dynamic measurements with wind-off conditions are performed to eliminate inertial forces. Wind-off measurements with both the original flat-plate model and a cylindrical dummy model with the same mass and inertia moments revealed a significant effect of wind-off aerodynamic forces on the results. Hence the final force data is based on the dummy model wind-off data. The wind-on and wind-off data are then subtracted, after averaging the raw data over 80 periods. After this averaging there still appear high-frequency perturbations caused by the harmonics of the natural vibration of the actuator mechanism. These are removed by low-pass filtering using a limit frequency of 15 Hz. More details are found in Wokoeck et al. [62] and Moeller et al. [63].

2.4.4 ONERA Force Balance

An internal balance is fitted inside the hollow wing model. For a 10% thick airfoil, the minimum chord necessary to fit the balance is 12.5 cm. The centre of the balance is placed 15 cm under the free surface to improve its accuracy; but the wing has to pierce the free surface and therefore the balance housing must be watertight. A linear potentiometer placed directly on the wing axis indicated that for a desired pure-plunge motion, there was a pitch oscillation of $\sim 0.5^\circ$.

As the towing tank can be easily filled or emptied, tests without water were run to analyze the electrical signals of the balance. The only significant forces generated during sinusoidal translations in horizontal movements in air are due to the wing inertia. The weight of the wing is well known but the inertial forces are a little higher than the product of its mass by its acceleration, because a part of the balance weight is measured. The important variations of the electric signals are due to the vibrations induced by the oscillation

mechanism and by the towing tank carriage system. Tests are run with and without motion of the carriage system. Rubber isolators are placed between the oscillation system and the frame to avoid transmission of the carriage vibrations. The level of vibration with and without the longitudinal velocity is the same; the structural frequency of the frame is >10 Hz.

It appears that the structural frequency of the wing is of about 8 Hz in the air (Figure 2-14). Data is acquired at 2 kHz without any filter. Numerical filtering is adjusted to maintain, for every periodic plunging motion, some small fluctuations of the signal. The value of the mass to be considered, such that the RMS value of the measured minus the inertial forces is minima, is computed from several tests in air. The residual forces are less than 0.1 N; that is small compared to the forces of about 10 N measured in the water. In the water the vibration of the wing is rapidly damped and the structural frequency is decreased (3.5 Hz) due to the virtual mass effect. A compromise has to be found between the balance sensitivity and the rigidity necessary to get a high structural frequency.

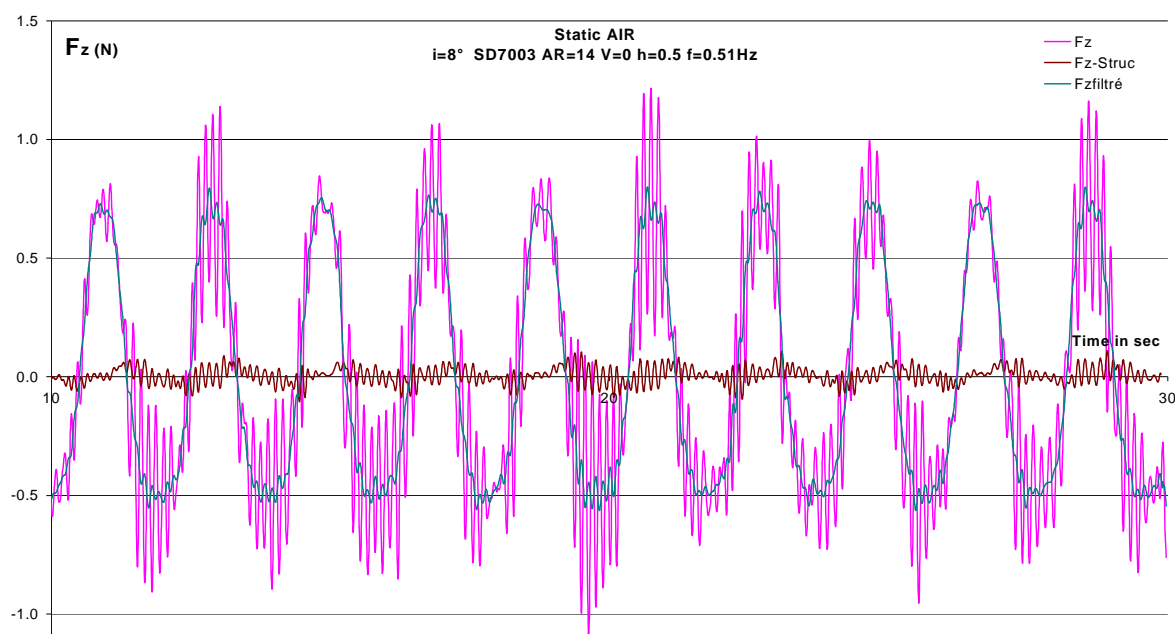
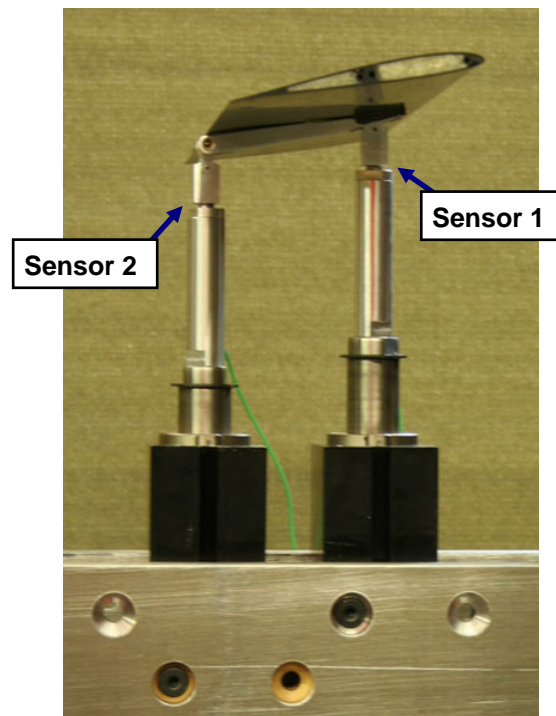


Figure 2-14: Inertial Tares in Air, ONERA Tow Tank.

2.4.5 TU Darmstadt Force Balance

For direct lift and pitching moment measurements in the TU Darmstadt wind tunnel, a pair of one-component Kistler 9217A piezo-electric force sensors were integrated directly below the SD7003 profile, one at the quarter-chord position (point of rotation) and one at the trailing edge, as shown in Figure 2-15. Together the two sensors measure the inertial and aerodynamic forces during the prescribed movement. Similar piezo-electric sensors have been used successfully for the measurement of pitching and plunging foils in a tow-tank, both for a single foil and in the wake of a cylinder; see Anderson et al. [18] and Beal et al. [64], respectively. The total static tare weight of the system (airfoil and linkage combined) was 394 g. The analogue-output charge signals from the two piezo-electric force sensors were sent through the wind-tunnel floor to a Kistler 5073A411 charge amplifier, which in turn converted the signals into an analogue voltage which was fed into a 16-bit National Instruments 6259 A/D board. Since the physical and sting natural frequencies were on the order of 1 Hz and 20 Hz, respectively, the signals were run through a 5 Hz low-pass filter in LabView 8.2 and then further post-processed using MATLAB 7.3.



**Figure 2-15: Location of Piezo-Electric Force Sensors Directly Below SD7003 Profile;
Note Sensor 1 Located at Quarter Chord Position (Point of Rotation)
and Sensor 2 Located at Trailing Edge.**

All lift and moment measurements were based on an ensemble of 30 clean cycles, sampled at 1 kHz, where the first four cycles as well as the last cycle were discarded to avoid aerodynamic and inertial starting and stopping effects. To subtract the inertial tare, a corresponding ensemble of 30 clean cycles was measured with the wind tunnel turned off. This technique proved to be very repeatable ($< 1\%$) for the lower reduced frequencies ($k < 0.15$) where the aerodynamic contribution was always equal or larger than the inertial contribution. Results at these lower reduced frequencies are presented in Rival and Tropea [65], where the accuracy was estimated to lie within $\Delta C_l = \pm 0.05$ and $\Delta C_m = \pm 0.02$, respectively. However, at higher reduced frequencies ($k > 0.2$), the inertial loads grew with the frequency squared and therefore very quickly dominated the total measured forces, thus degrading the accuracy of the measurements. For these cases a dummy cylinder was used to determine the wind-off aerodynamic contribution (Figure 2-16) but had only limited success. For more details, see Rival et al. [66].



**Figure 2-16: Positioning of Dummy Cylinder at Center-of-Mass Position Inside Wind-Tunnel Test
Section (left) and Comparison of Dummy Cylinder with Original SD7003 Profile;
Note Cylinder Identical to Profile in Mass (± 0.5 g) and Spanwise Distribution.**

2.5 COMPUTATIONAL METHODS

Computations range from analytical formulas based on conformal mapping and inviscid 2D vortex particle methods, to commercial and custom in-house RANS methods, to higher-order 3D LES methods. Each has its place and each has tradeoffs of computational cost/complexity of implementation vs. accuracy. One of our objectives is to assess what level of accuracy is necessary for this or that objective, such as lift coefficient prediction (at a minimum) to capturing the main flowfield features such as shed vortices, all the way to accurately resolving boundary layer transition.

2.5.1 AFRL Implicit Large Eddy Simulation

The governing equations are the unfiltered full compressible Navier-Stokes equations cast in strong conservative form after introducing a general time-dependent curvilinear coordinate transformation $(x, y, z, t) \rightarrow (\xi, \eta, \zeta, \tau)$ from physical to computational space. In terms of non-dimensional variables, these equations can be written in vector notation as:

$$\frac{\partial Q}{\partial \tau} + \frac{\partial F_I}{\partial \xi} + \frac{\partial G_I}{\partial \eta} + \frac{\partial H_I}{\partial \zeta} = \frac{1}{\text{Re}} \left[\frac{\partial F_v}{\partial \xi} + \frac{\partial G_v}{\partial \eta} + \frac{\partial H_v}{\partial \zeta} \right], \quad (1)$$

the vector of dependent variables and inviscid fluxes are given by:

$$Q = \frac{1}{J} [\rho \quad \rho u \quad \rho v \quad \rho w \quad \rho E_t]^T \quad (2)$$

$$F_I = \frac{1}{J} \begin{bmatrix} \rho U \\ \rho u U + \xi_x p \\ \rho v U + \xi_y p \\ \rho w U + \xi_z p \\ \rho E_t U + p \tilde{U} \end{bmatrix}, \quad G_I = \frac{1}{J} \begin{bmatrix} \rho V \\ \rho u V + \eta_x p \\ \rho v V + \eta_y p \\ \rho w V + \eta_z p \\ \rho E_t V + p \tilde{V} \end{bmatrix}, \quad H_I = \frac{1}{J} \begin{bmatrix} \rho W \\ \rho u W + \zeta_x p \\ \rho v W + \zeta_y p \\ \rho w W + \zeta_z p \\ \rho E_t W + p \tilde{W} \end{bmatrix}, \quad (3)$$

with:

$$\begin{aligned} U &= \xi_t + \xi_x u + \xi_y v + \xi_z w = \xi_t + \tilde{U} \\ V &= \eta_t + \eta_x u + \eta_y v + \eta_z w = \eta_t + \tilde{V} \\ W &= \zeta_t + \zeta_x u + \zeta_y v + \zeta_z w = \zeta_t + \tilde{W} \\ E_t &= \frac{T}{(\gamma - 1)M_\infty^2} + \frac{1}{2}(u^2 + v^2 + w^2) \end{aligned} \quad (4)$$

Here, $\xi_x = J^{-1} \partial \xi / \partial x$ with similar definitions for the other metric quantities. The viscous fluxes, F_v , G_v and H_v can be found, for instance, in Anderson et al. [67]. In the expressions above, u , v , w are the Cartesian velocity components, ρ the density, p the pressure, and T the temperature. The perfect gas relationship $p = \rho T / (\gamma M_\infty^2)$, as well as Sutherland's law for viscosity are also assumed. All flow variables have been normalized by their respective reference freestream values except for pressure which has been normalized by $\rho_\infty V_\infty^2$.

The above governing equations correspond to the original *unfiltered* Navier-Stokes equations, and are used without change in laminar, transitional or fully turbulent regions of the flow. Unlike the standard LES approach, no additional sub-grid stress (SGS) and heat flux terms are appended. Instead, a high-order low-pass filter operator (to be described later) is applied to the conserved dependent variables during the solution of the standard Navier-Stokes equations. This highly-discriminating filter selectively damps only the evolving poorly-resolved high-frequency content of the solution. This filtering regularization procedure provides an attractive alternative to the use of standard SGS models, and has been found to yield suitable results for several canonical turbulent flows (Visbal et al. [68] and Visbal et al. [69]) on LES-level grids.

All simulations are performed with the extensively validated high-order *FDL3DI* Navier-Stokes solver, described in more detail in Visbal and Gaitonde [70]. In this code, a finite-difference approach is employed to discretize the governing equations, and all spatial derivatives are obtained employing a 6th-order compact-differencing scheme. In order to eliminate high-frequency spurious components, an 8th-order Pade-type low-pass spatial filtering operator [70] is applied to the conserved variables along each transformed coordinate direction after each time step or sub-iteration. For transitional and turbulent flows, this filtering technique provides an effective implicit LES approach.

For the case of a manoeuvring airfoil, the grid is moved in rigidly using the prescribed airfoil motion. To ensure that the Geometric Conservation Law (GCL) is satisfied, the time metric terms are evaluated as in Visbal and Gaitonde [71]. The original airfoil sharp trailing edge was rounded with a circular arc of radius $r/c \sim 0.0004$ to use an O-mesh topology. The computational mesh consisted of $(649 \times 395 \times 101)$ points in the streamwise, normal and spanwise direction, respectively. Grid points were concentrated near the airfoil to capture the transition process. For the three-dimensional simulations, which invoked periodicity in the spanwise direction, the mesh had a span $s/c = 0.2$. Further details on the mesh and boundary conditions can be found in Visbal [98].

Plunging simulations were started from previously computed static solutions at the corresponding mean angle of attack. Simulations were then advanced in time for more than 25 cycles in order to guarantee a time-asymptotic nearly-periodic state. A very small computational nominal time step $\Delta t U/c = 0.00005$ was prescribed in order to provide sufficient temporal resolution of the abrupt spanwise breakdown of the leading-edge vortices. This value of Δt corresponds to 16,000 time steps per cycle for a reduced frequency $k = 3.93$. Finally, all computations were performed employing a low freestream Mach number $M = 0.1$, as required with the present compressible Navier-Stokes solver. The good agreement of the computed lift coefficient with the inviscid incompressible theory for $k = 3.93$ demonstrated that compressibility effects were minor.

2.5.2 AFRL Vortex-Particle Method

The method presented in this work is based on a 2D inviscid point vortex method similar to those presented in Katz [72] and Karamcheti [73]. Several important modifications have been incorporated. First, conservation of circulation is implicitly satisfied, rather than being imposed as an additional constraint. Second, a vortex decay model is made available for flow that is separated into the wake.

In two dimensions, a body can be represented by a collection of bound vortices particles. Each vortex particle can be interpreted as an infinitely-long vortex filament oriented normal to the plane. Each vortex induces a purely rotational velocity field. According to the Biot-Savart law, the magnitude of the induced velocity varies directly with the strength of the vortex, Γ , and inversely with the distance between the vortex and the point of interest. Since this results in an infinite velocity at the location of a vortex particle, in practice the velocity must be kept finite according to some rule. Although several possibilities exist, we use the following formulation based on the error function:

$$\vec{v}(\vec{r}) = -\frac{\Gamma}{2\pi} \frac{1}{|\vec{r}|^2} \text{erf}\left(\frac{|\vec{r}|^2}{r_{cutoff}^2}\right) \vec{r} \times \vec{k}, \quad (5)$$

where \vec{v} is the velocity vector, \vec{r} is displacement vector from the vortex to the point of interest, \vec{k} is the unit normal vector out of the plane, and r_{cutoff} is the cutoff radius below which the inverse relationship with r does not hold.

For a thin body represented by N_{bv} bound vortices ordered along the body's length, we solve for the strengths of the bound vortices at a given moment in time. We introduce a control point in between each pair of bound vortices. Let $N_{cp} = N_{bv} - 1$ be the number of control points. At each control point, assign a strength representing the strength of a ring of vorticity. In 2D, we imagine the ring to extend to $\pm\infty$ in the out-of-plane direction, so the two segments parallel to the 2D plane have no contribution to the flow. The strength of the bound vortices $\vec{\Gamma}$ are related to the control point strengths $\vec{\gamma}$ by:

$$\vec{\Gamma} = T\vec{\gamma} + \vec{S}, \quad (6)$$

where T is a mapping matrix with elements of +1 on the main diagonal and -1 on the lower off-diagonal. \vec{S} is the amount of vorticity that has been shed into the wake from the given bound vortex at the previous moment in time, if any. In this manner, vorticity is implicitly conserved since each vortex ring contributes a net vorticity of zero. At each time step, the velocity at each control point is calculated by enforcing flow tangency. Let I be an $N_{cp} \times N_{bv}$ influence matrix with elements ij equal to the velocity induced by a bound vortex j of unit strength on control point i . Let \vec{N} be a vector of length N_{cp} with elements v_i that are the normal component of velocity at the bound vortex i , equal to the velocity of the body plus the velocity induced by the bound vorticity and the wake. Flow tangency leads to:

$$\begin{aligned} I\vec{\Gamma} &= -\vec{N} \\ IT\vec{\gamma} &= -I\vec{S} - \vec{N} \end{aligned} \quad (7)$$

Once the bound vortex strengths have been computed for a given time step, vorticity is shed into the wake at the trailing edge. A new wake panel is created a distance behind the trailing edge panel equal to the time step times the local velocity. The strength of this panel is set equal to $\lambda\gamma_{N_{cp}-1}^n$, where λ is an attenuation factor typically taken to be one. The bound vortex strength $\Gamma_{N_{bv}-1}^n$ and the wake vortex strength $\Gamma_{w_{TE}}^n$ can then be calculated. Once the vortices have been shed and convected, the state is ready to be advanced by another time step.

The resulting calculation gives values of lift coefficient time history, accounting for airfoil camber (but not explicitly for thickness) and time-history of vorticity shed from the trailing edge. It does not however account for leading-edge vortex formation or shedding.

2.5.3 METU RANS Approach

Computations use Fluent [74] – an unsteady, pressure based Reynolds-Averaged Navier-Stokes solver with second order upwind spatial discretization. The pressure-velocity coupling is handled by the SIMPLE algorithm. Motion kinematics is implemented using ‘dynamic mesh’ feature of Fluent. To model the

motion, the whole grid is divided into two parts: inner grid with 20 c diameter and outer grid with 60 c diameter. In solution process, the inner grid around the airfoil performs the prescribed motion while the outer grid is stationary and deforming with appropriate rules. The dynamic mesh feature of the code limits the unsteady formulation to the first order in time and so for all calculations first-order temporal discretization is used. The far-field boundary conditions are set as velocity inlet and pressure outlet. The free-stream flow is assumed to be turbulent and Menter's Shear Stress Transport model is used for turbulence closure, which is a favourable model in prediction of adverse pressure gradients [75].

An unstructured O-type grid with outer diameter of 60 c is used. The y^+ value for all cases is chosen as less than 1. Figure 2-17 shows the whole domain and the grid around the airfoil. A grid refinement process is conducted to have grid-independent solution. The previous studies showed that a grid with 92358 cells is enough to have the grid-independent solution for SD 7003 airfoil [76]. For flat plate with 2.5% thickness, 132804 cells are used. Moreover, 960 time steps per period are chosen for all calculations. The results are represented for [6T-7T] period.

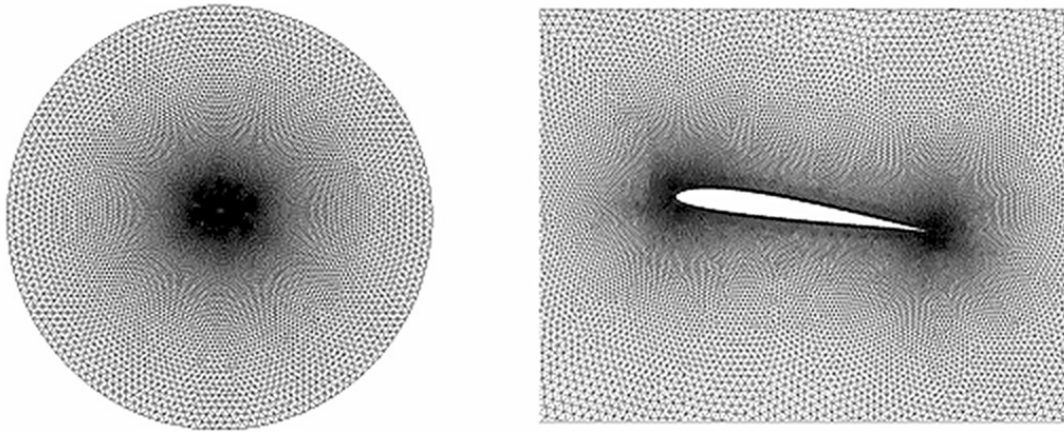


Figure 2-17: Computational Mesh for SD7003 Airfoil; Full Grid (left) and Zoomed-In to Airfoil Region (right).

2.5.4 University of Michigan RANS Approach

Computations by the University of Michigan are unsteady RANS, closed with Menter's SST turbulence model [77,78]. The momentum equation becomes:

$$\frac{\partial}{\partial t} (u_i) + \frac{\partial}{\partial x_j} (u_j u_i) = -\frac{1}{\rho} \frac{\partial p}{\partial x_i} + \frac{\partial}{\partial x_j} \left\{ (\nu + \nu_t) \frac{\partial u_i}{\partial x_j} \right\},$$

the eddy viscosity, ν_t , given by $\nu_t = \frac{a_1 k}{\max(a_1 \omega, S F_2)}$, $S = \sqrt{2S_{ij}S_{ij}}$ is the invariant measure of the strain rate. u_i is the velocity component in the i^{th} direction, x_i is the i^{th} component of the position vector, t is time, ρ is density, p is pressure, ν is the kinematic viscosity. The transport equation for turbulent kinetic energy k is:

$$\frac{\partial k}{\partial t} + \frac{\partial}{\partial x_j} (u_j k) = \hat{P}_k - \beta^* \omega k + \frac{\partial}{\partial x_j} \left\{ (\nu + \sigma_k \nu_t) \frac{\partial k}{\partial x_j} \right\}.$$

The transport equation for ω is:

$$\frac{\partial \omega}{\partial t} + \frac{\partial}{\partial x_j} (u_j \omega) = -\frac{\gamma}{\nu_t \rho} \frac{\partial u_i}{\partial x_j} - \beta \omega^2 + \frac{\partial}{\partial x_j} \left\{ (\nu + \sigma_\omega \nu_t) \frac{\partial \omega}{\partial x_j} \right\} + 2(1 - F_1) \sigma_{\omega 2} \frac{1}{\omega} \frac{\partial k}{\partial x_j} \frac{\partial \omega}{\partial x_j}.$$

Finally, the quantities $\alpha_1, \beta, \beta^*, \gamma, \sigma_k, \sigma_\omega, \sigma_{\omega 2}, F_1, F_2$ are defined as in Menter's SST formulation [77,78].

Compared to Menter's original SST turbulence model, a limiter was built in to the production term, \hat{P}_k , in the turbulence kinetic energy (TKE) equation, as $P_k = \mu_t \frac{\partial u_i}{\partial x_j} \left(\frac{\partial u_i}{\partial x_j} + \frac{\partial u_j}{\partial x_i} \right)$, and $\hat{P}_k = \min(P_k, 10 \cdot \beta^* \rho k \omega)$, where P_k is the production term in the original SST formulation, to prevent the build-up of turbulence in stagnation regions. Another change is the use of invariant measure of the strain-rate tensor in the formulation for the eddy viscosity instead of the vorticity magnitude, $\Omega = \sqrt{2\Omega_{ij}\Omega_{ij}}$. The strain-rate invariant is considered to be a better measure for the fluid deformation, since the Boussinesq approximation is also based on the strain-rate. The two differences between the original and the modified SST formulation are summarized in Table 2-2.

Table 2-2: Original and Modified SST Turbulence Model, U of Michigan Computation

	Original SST	Modified SST
Production Term of TKE Equation	$P_k = \mu_t \frac{\partial u_i}{\partial x_j} \left(\frac{\partial u_i}{\partial x_j} + \frac{\partial u_j}{\partial x_i} \right)$	$\hat{P}_k = \min(P_k, 10 \cdot \beta^* \rho k \omega)$
Eddy Viscosity	$\nu_t = \frac{a_1 k}{\max(a_1 \omega, \Omega F_2)}$	$\nu_t = \frac{a_1 k}{\max(a_1 \omega, S F_2)}$

These equations are solved with the in-house solver Loci-STREAM [79], a parallelized unstructured curvilinear pressure-based finite-volume code with moving grid capabilities. The present calculations use implicit first order time stepping. The convection terms are treated using the second order upwind scheme [80,81] while pressure and viscous terms are treated using second order schemes. The geometric conservation law [82,83], a necessary consideration in domains with moving boundaries, is satisfied. The numerical solutions were computed in an open bounded domain with Loci-STREAM on unstructured grids of different resolutions. More details can be found in Kang et al. [84] and Kang et al. [85].

2.5.5 TU Darmstadt RANS Approach

Simulations used Fluent 6.3.26, and were run with second-order upwind spatial and first-order temporal discretization, where the latter was limited by the dynamic-meshing process in the code. To compensate for this limitation in the temporal discretization, fine time-stepping of 0.5 ms was used, equivalent to 800 time steps per cycle for $Re = 30000$ and $k = 0.25$. Further refinement of the time-stepping was performed to check for a time-step independent solution analogous to the grid-independency tests described below. 20 to 30 iterations were run for a given time step with a convergence criterion based on residuals dropping $O(10^4)$ in magnitude. Pressure-velocity coupling was performed using the SIMPLE scheme. For all simulations the procedure was to run two complete cycles to establish the appropriate initial conditions and then to begin recording data on the following cycle.

The numerical domain was modelled after the TU Darmstadt Eiffel-type open-return, closed test section wind tunnel. The present computations were a sub-set of a study on tandem airfoils, but here we report only on the single airfoil; Figure 2-18 depicts tandem airfoils. The domain extends the entire length of the wind-tunnel test section, and is filled with block-structured cells in sections a) and d) before and after the dynamic meshing region, as shown in Figure 2-18. In these block-structured regions the skewness is zero, and the aspect ratio and cell growth are nearly one.

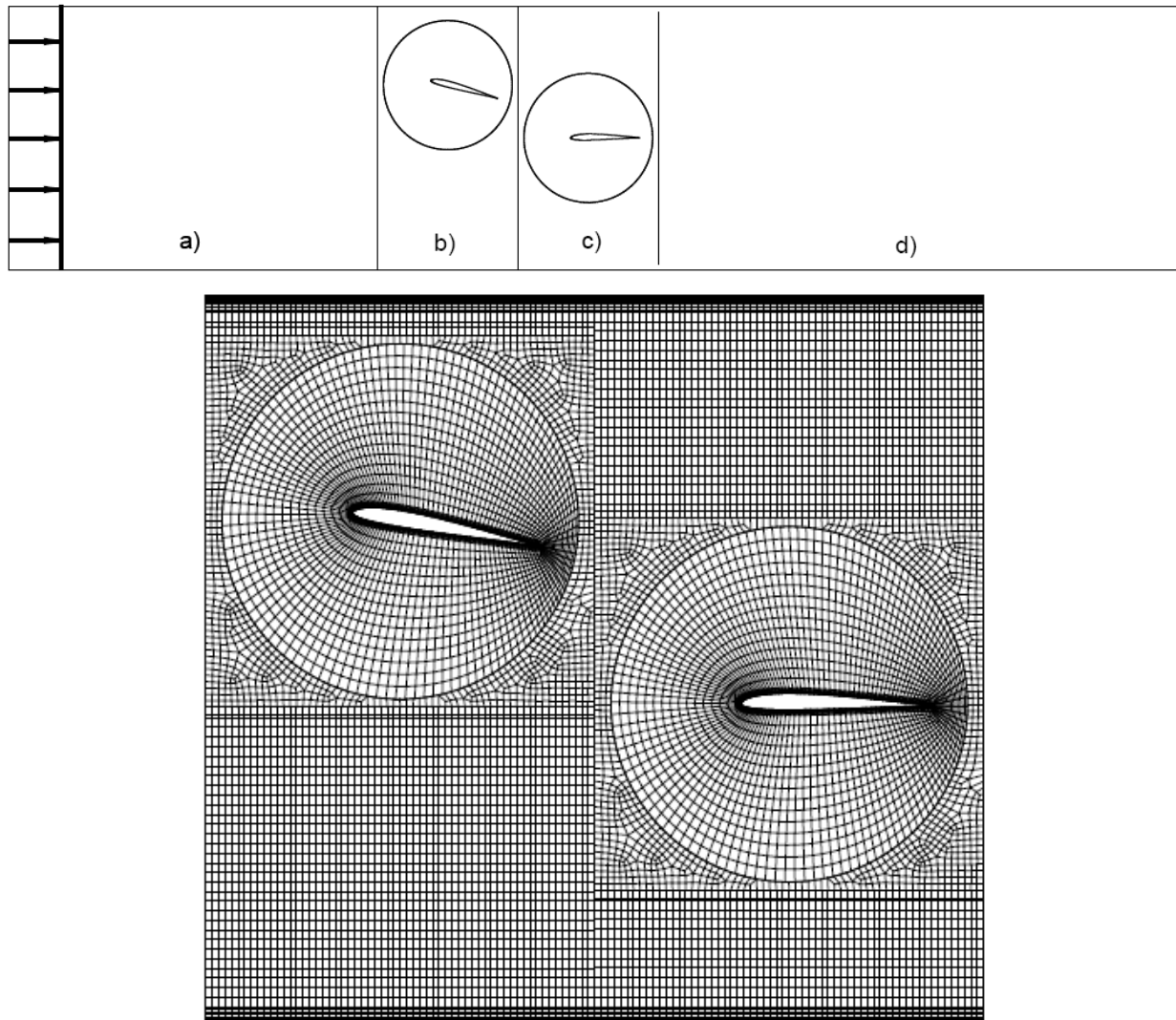


Figure 2-18: Top: Numerical Domain Representative of Wind-Tunnel Test Section; Zones a) and d) Contain Pure Block-Structured Cells Whereas Zones b) and c) Contain Dynamic Layering and Sliding Zones; Bottom: Middle of Domain; Zones b) and c), with Two Circular-Structured Cores Encompassing the Airfoils. Tandem airfoils depicted, but only one airfoil was computed here.

The circular-core zones surrounding the airfoils provide for the pitching movement (through non-conformal boundaries) whereas the plunging movement was realized through the dynamic-layering method where rows of structured cells above and below the circular cores were created and destroyed. The two unstructured regions in the entire mesh were filled with quadrilateral cells, providing the coupling of the non-conformal boundaries between the circular cores and the block-structured outer region. This dynamic-meshing arrangement allows for high pitch- and plunge amplitudes while maintaining good mesh quality.

Both airfoil and wind-tunnel wall boundary layers were fully-resolved satisfying the $y^+ = 1$ condition throughout. Cell growth in all boundary layers was limited to 1.25. The trailing edges of the airfoils were set with radii of 0.1 mm so as to be more representative of actual experimental airfoils and to ease the meshing constraints. An overall maximum skewness of 0.41 and maximum aspect ratio of 4.1 existed within the circular cores. A grid-independency study was performed and a resulting grid of approximately 32000 cells was established. The relatively low number of cells and thus fast simulation times (on the order of six hours on a single Linux machine) can be attributed to the nearly complete block-structured mesh.

2.5.6 NRC Large Eddy Simulation

Computations at the Canadian National Research Council Institute for Aerospace Research used the in-house 3D unsteady incompressible LES/RANS code INSflow [86]. Recent numerical investigations of low-Reynolds-number and flapping-wing aerodynamics can be found in Yuan et al. [87,88,89]. INSflow uses the integral form of the conservation law for mass and momentum. A fully implicit second-order temporal differencing scheme makes the algorithm stable for large time steps. The discretization of the convective and diffusive fluxes was carried out in a co-located variable arrangement using a finite-volume approach that was second-order accurate in space. The coupling of the pressure and the velocity was handled using the SIMPLE algorithm [90]. The continuity equation was transformed into a pressure-correction equation that had the same general form as the discretized momentum equations. The use of the co-located variable arrangement on non-orthogonal grids required that the SIMPLE algorithm be slightly modified to dampen numerical oscillations. A pressure-velocity coupling method for complex geometries used by Ferziger and Perić [91] was implemented, where an additional pressure gradient term was subtracted from the velocity value at the surface of the control volume to prevent non-physical oscillations. A number of two-equation turbulence models and two sub-grid-scale (SGS) models were implemented for RANS and LES.

The calculations were performed on a moving grid whose velocity was included in the governing equations [86,92] in an inertial frame of reference. To avoid artificial mass sources generated by the grid velocity, a space conservation law was introduced to ensure a fully conservative property in the computations, as applied by Demirdžić and Perić [93].

Two-dimensional (2D) simulations were performed for both pure plunging and combined pitching-plunging cases. The 2D calculations were LES-like since the eddy viscosity was added to the diffusion term. Calculations were initiated from stationary flow conditions. A C-mesh with 737×65 grid points was used for the pure plunging SD7003 airfoil case, an O-mesh with 961×65 grid nodes was used for the combined pitching-plunging SD7003 airfoil case, and an O-mesh with 461×65 grid nodes was used for the combined pitching-plunging flat-plate case. The C-mesh was generated using the hyperbolic method proposed by Barth et al. [94], and the O-meshes were generated using an algebraic method similar to the one of Perić [91]. In these calculations, the far field was set at 10 chords away from the airfoil for the O-meshes and 25 chords away from the airfoil the C-mesh. The far field was thus correctly assumed to be sufficiently distanced not to warrant any circulation corrections. These C- and O-grids were generated based on experience gained from previous work [87,88] and ensured that the streamwise spacing in wall units satisfied $\Delta x^+ < 100$. In the calculations of the pitching cases, the inner part of the O-mesh pitched in unison with the airfoil with the outer part fixed. The timestep was set at $\Delta t = T/1920$, where T was the period of one pitching cycle. Computations were run for 30 cycles for the 2D plunging SD7003, 20 cycles for the 2D pitching-plunging SD7003, and 6 cycles for the 2D pitching-plunging flat-plate.

2.5.7 U of Toronto Lumped-Vortex Model

An unsteady, lumped-vortex method is used to compute 2D and 3D lift and drag. The method is an extension of DeLaurier's [95] unsteady strip-theory model that was originally developed for the design of large flapping-wing aircraft in the range of 1.5 m to 12 m span.

The method models all bound circulation, including any bound leading-edge vortices, as being lumped at the quarter chord with the no flow-through boundary condition imposed at the three-quarter chord. The method accounts for the unsteady wake by computing the influence of wake vortices that are shed one quarter chord aft of the trailing edge and convected downstream at each time step. Apparent mass (non-circulatory force) is computed separately and added to the normal force. Viscous forces are modelled by correlating the bound circulation at each spanwise station with a parameterized fit of the static lift-drag polar of the airfoil. Dynamic stall is modelled by a reduction in the bound circulation as the leading-edge vortex is shed off the trailing edge. 2D results are computed simply by using an infinite wing with only one spanwise panel, as a special case of 3D panelling (Figure 2-19).

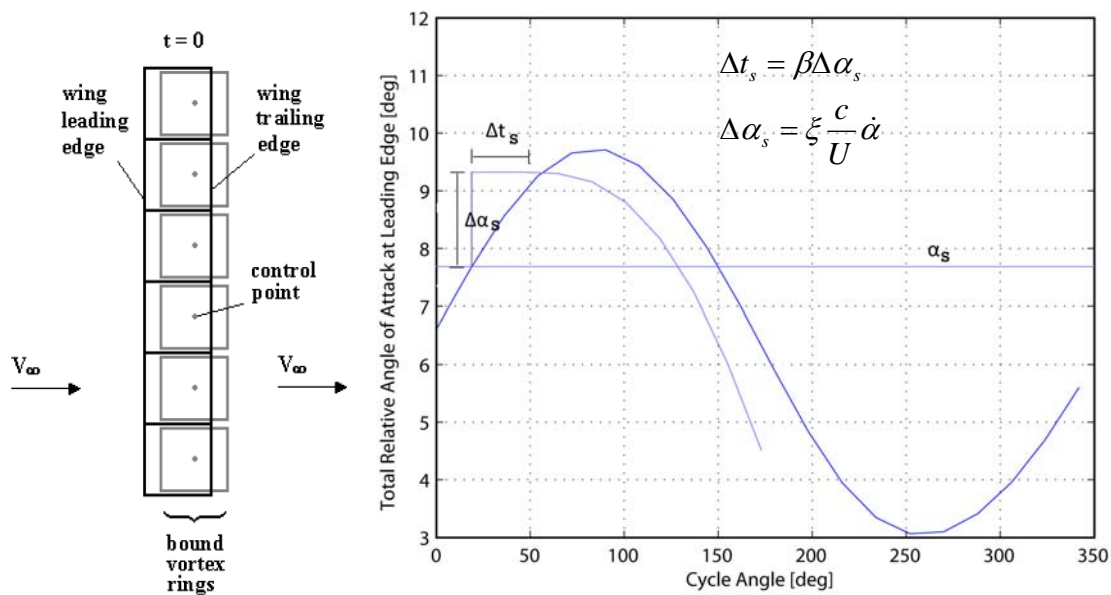


Figure 2-19 UTIAS Lumped Vortex Method: Vortex Panelling for a 3D Rectangular Wing (left) and Schematic of Lag Parameters for Dynamic Stall Model (right).

When performing a parametric fit on the lift-drag polar of the desired airfoil, the attached and stalled portions of the data are fit separately. This allows for predictions of lift and drag on the airfoil at angles above the static stall angle when the airfoil is undergoing dynamic stall delay. The delay is thus modelled as an effective shift in the stall angle, $\Delta\alpha_s$, that depends on the rate of change of angle of attack and the time that has passed since the angle of attack exceeded the static stall angle (schematic in Figure 2-19). This is an extension of Prouty's dynamic stall model for helicopter blades [96] that incorporates the elements of the formation time for a leading-edge vortex. The model is currently employed only for the 2D cases and needs to be extended for the generalized 3D case.



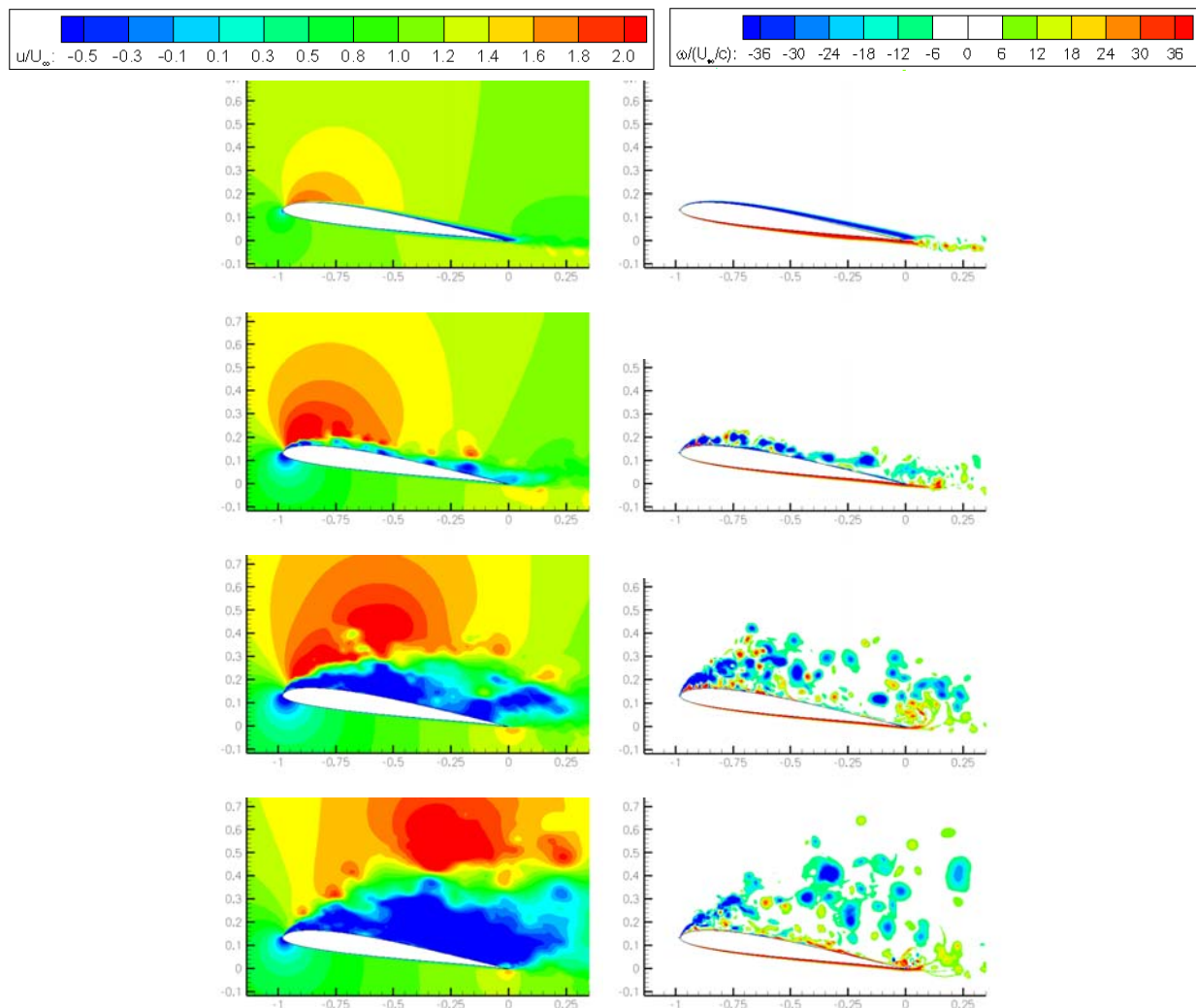
Chapter 3 – PURE-PLUNGE OF THE SD7003 AIRFOIL

3.1 RESUME OF EXPERIMENTAL AND COMPUTATIONAL RESULTS FOR THE FLOWFIELD: VELOCITY AND VORTICITY

We begin by comparing the various experimental and computational results for the flowfield about the airfoil. Experiments are particle image velocimetry, and in general are limited to the suction-side of the airfoil, as the pressure-side is in the PIV light sheet shadow. Computations of course do not have this limitation. For velocity, we use the normalized streamwise component, u/U_∞ , as the metric of choice. Vorticity is limited to the out-of-plane component, and normalization is by free-stream velocity, U_∞ , and airfoil chord, c . For velocity the contour levels are 0 to 1.5, while for vorticity they are -36 to +36, unless otherwise noted in the respective plot.

3.1.1 Computations

2D and 3D LES computations from AFRL are given in Figure 3-1 and Figure 3-2, respectively. METU RANS computations are in Figure 3-3, NRC 2D RANS are in Figure 3-4, and the UM RANS are in Figure 3-5.



PURE-PLUNGE OF THE SD7003 AIRFOIL

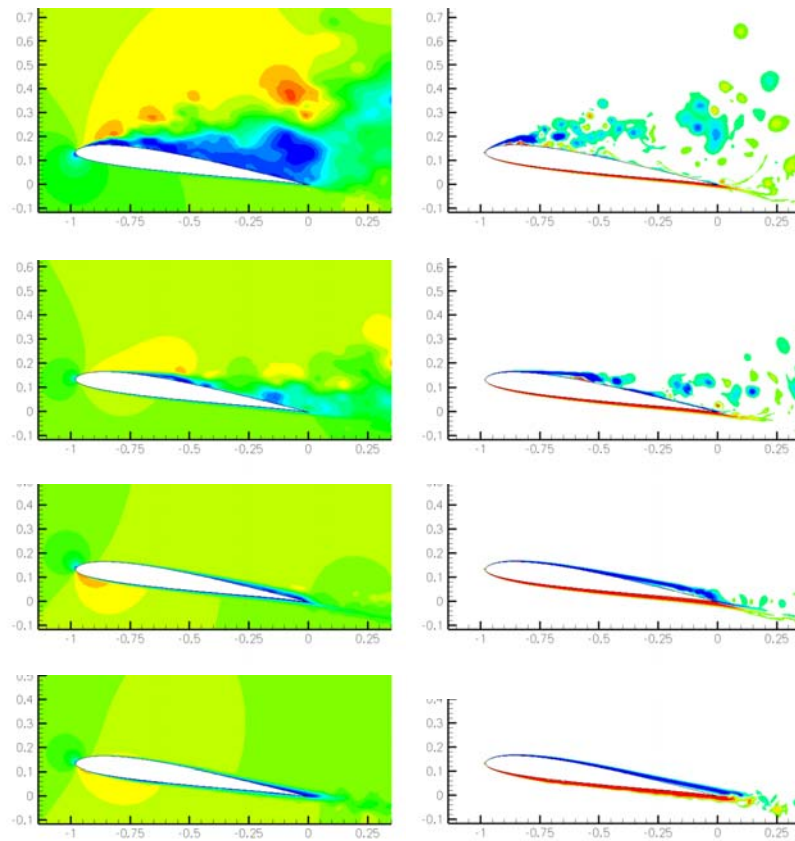
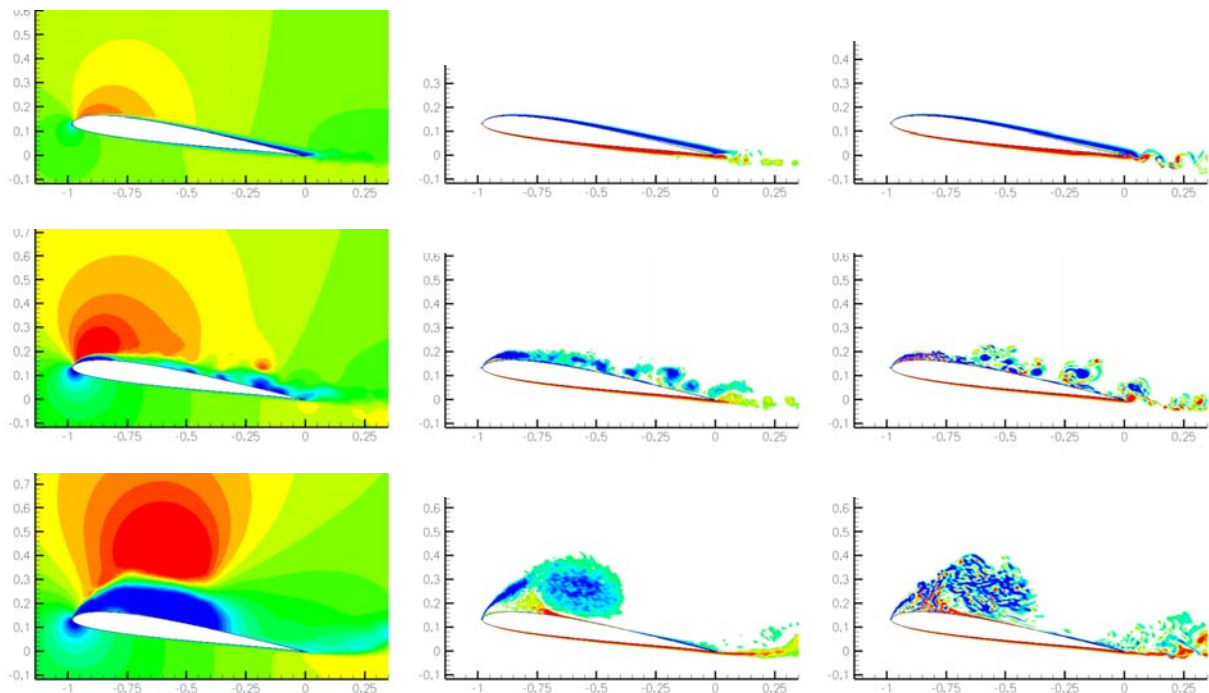


Figure 3-1: 2D Computations, FDL3DI; Phases $\Phi = 0, 45, 90, 135, 180, 225, 270$ and 315 .



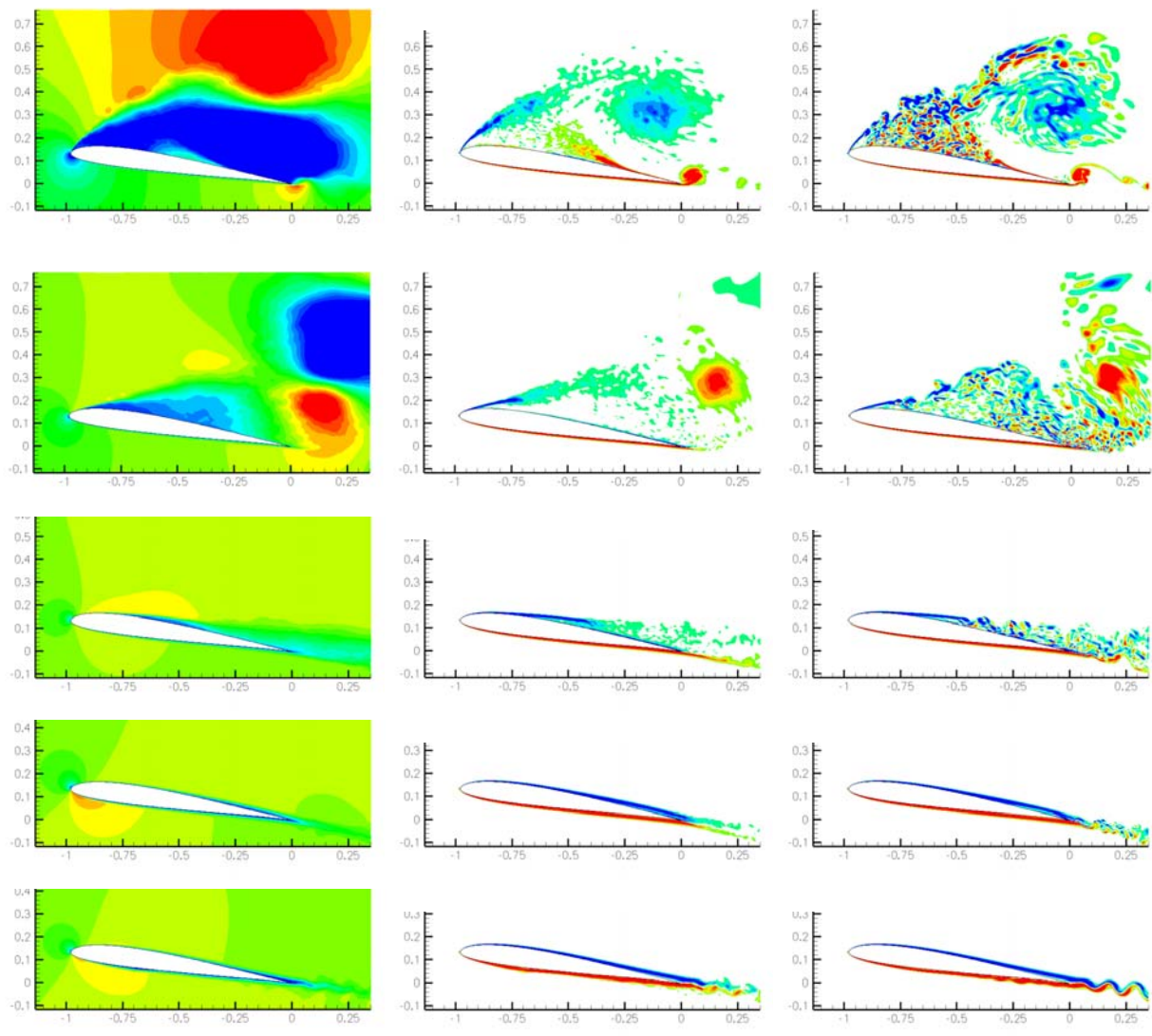
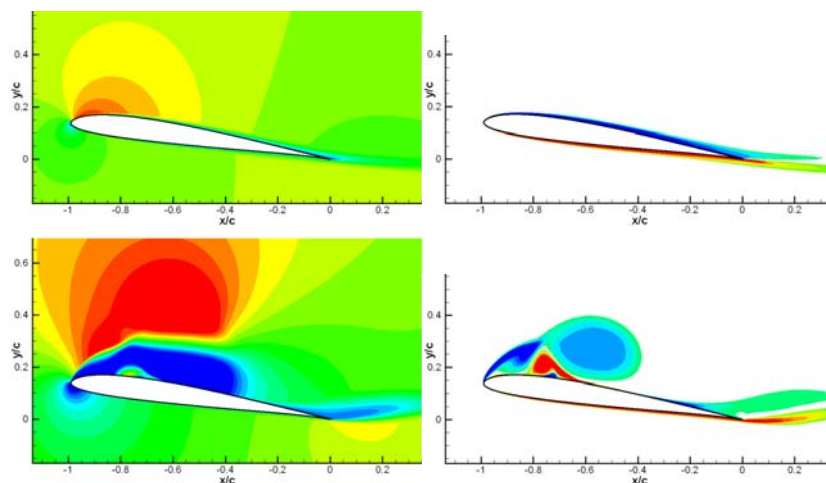


Figure 3-2: 3D Computations, FDL3DI; Phases $\Phi = 0, 45, 90, 135, 180, 225, 270$ and 315 ; Phase-Averaged Velocity (left column), Phase-Averaged Vorticity (middle column) and Instantaneous Vorticity (right column).



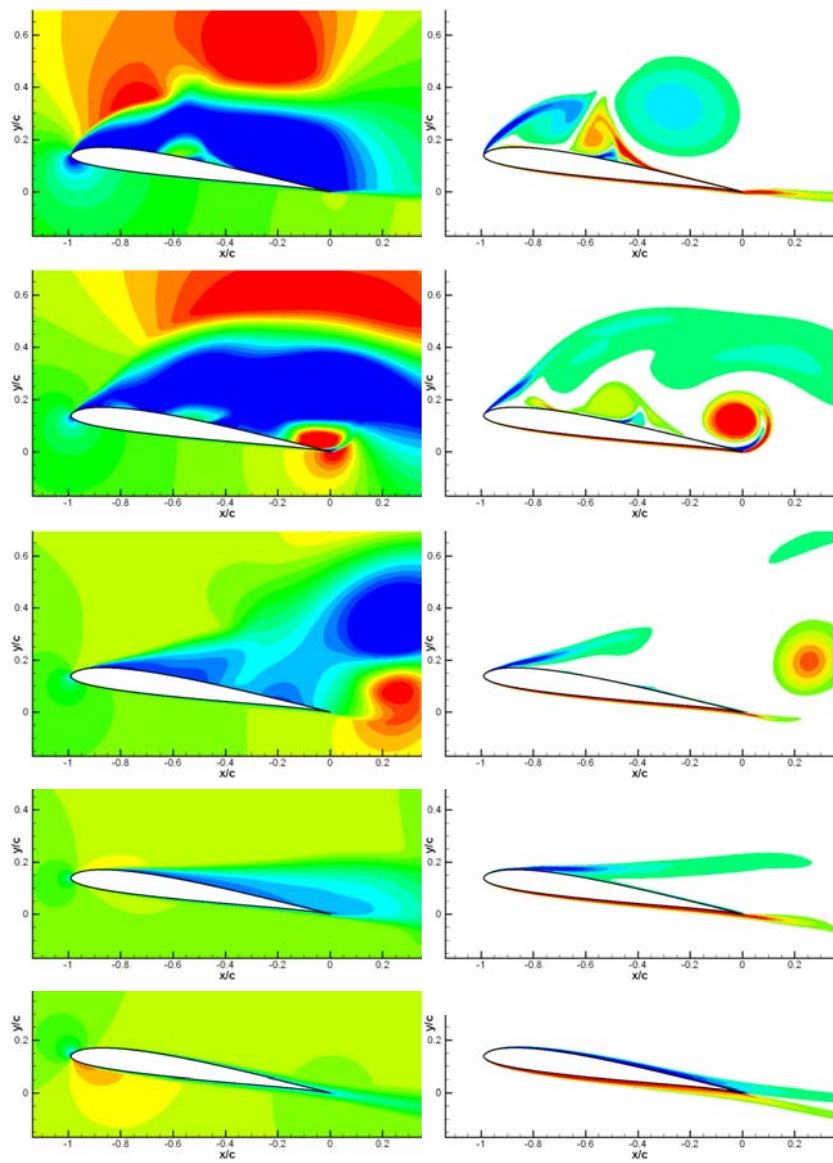
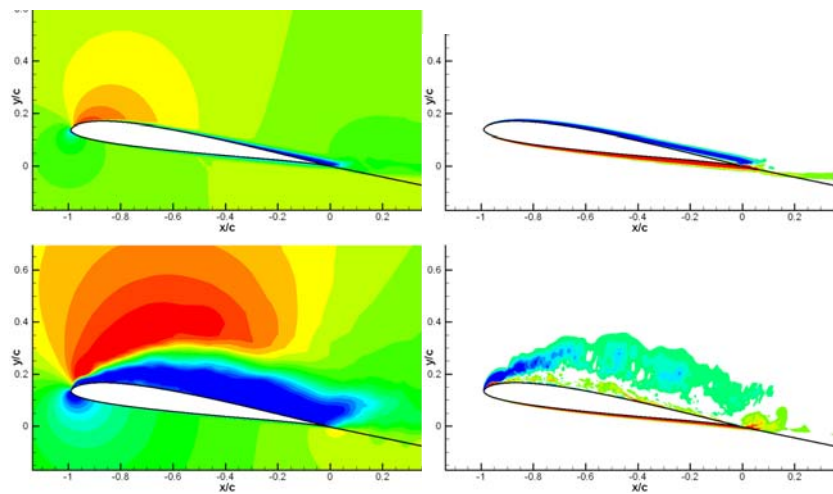


Figure 3-3: METU Computations, Fluent, 2D; Phases $\Phi = 0, 90, 120, 150, 180, 210$ and 270 .



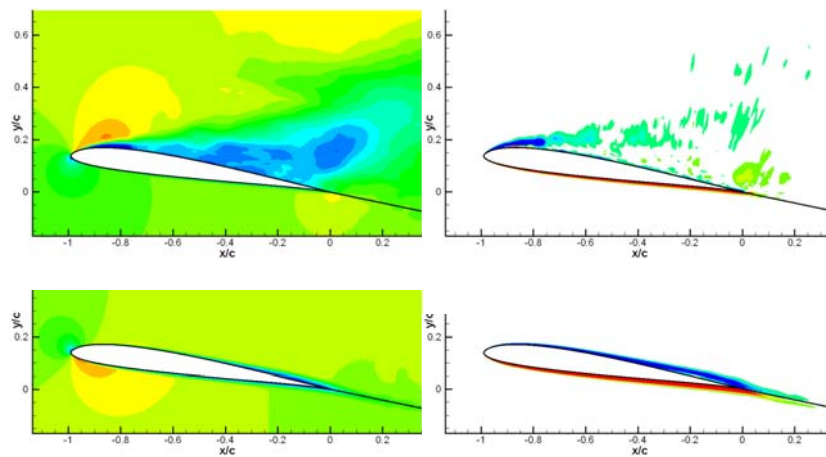
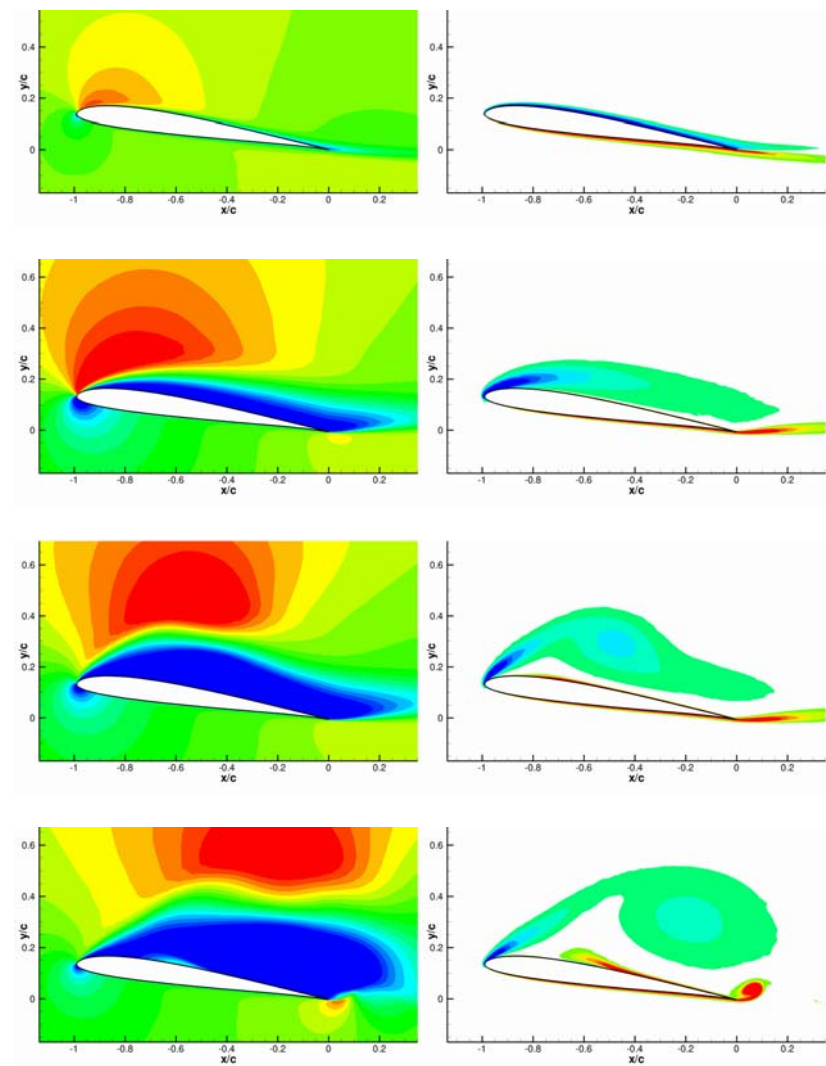


Figure 3-4: IAR NRC Computations, LES; Phases $\Phi = 0, 90, 180$ and 270 .



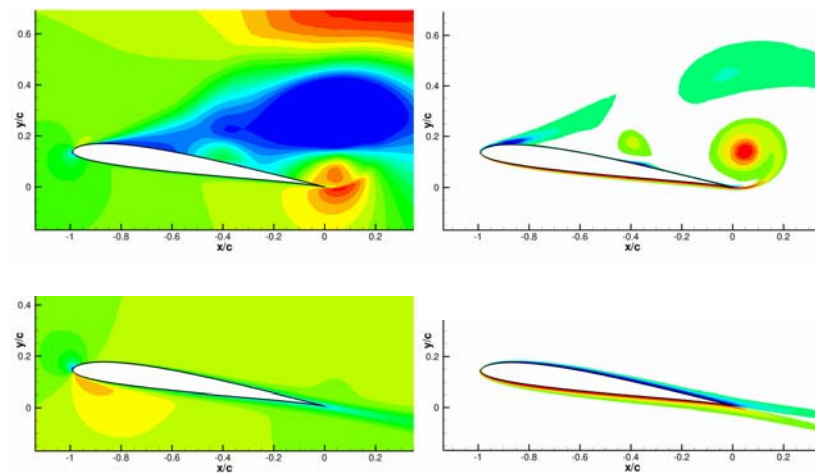
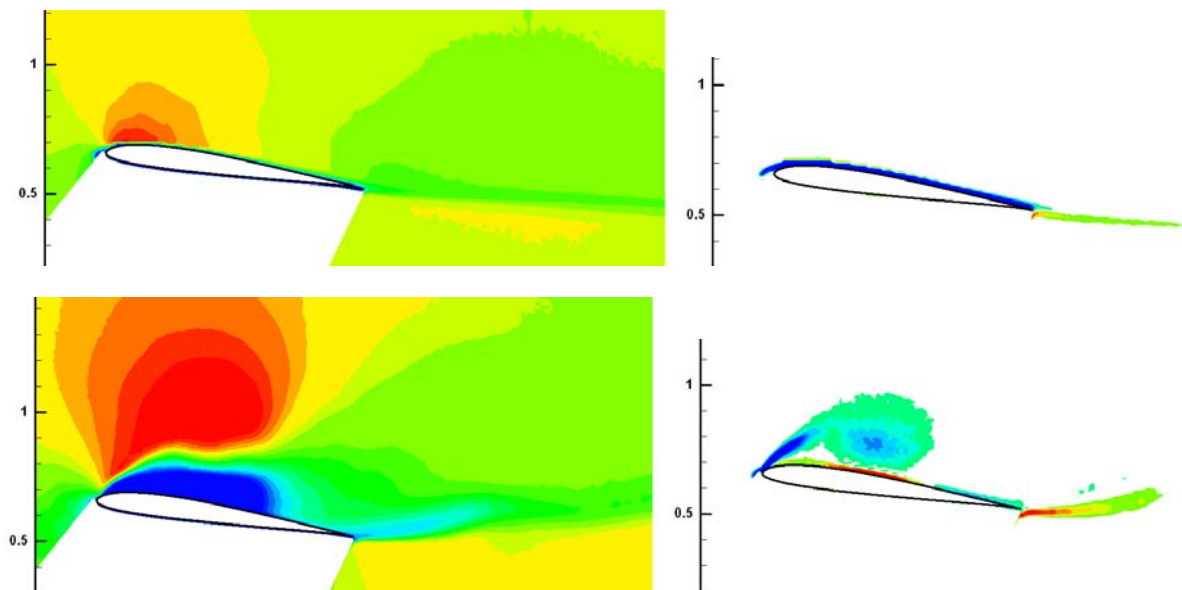


Figure 3-5: University of Michigan Computations; Phases $\Phi = 0, 90, 120, 150, 180$ and 270 .

3.1.2 Experiments

Velocity and vorticity contour plots from PIV are presented as follows: AFRL water tunnel Series #1 is in Figure 3-6 and Series #2 is in Figure 3-7; and the UM water tunnel results are in Figure 3-8. We note that because the AFRL water tunnel model is mounted horizontally across the test section with rig linkages on the pressure-side along the midspan, the natural PIV light sheet location is the $\frac{3}{4}$ span. But the UM water tunnel installation is with the wing hanging vertically with no rig linkages submerged in the water, and the most natural PIV light sheet location is the midspan. For the first AFRL campaign, the PIV light sheet was somewhat inboard of the $\frac{3}{4}$ span, and for the second campaign it was somewhat outboard of this location. We speculate, barring further information such as from a desirable but impractical full 3D computation that includes the tunnel test section sidewalls, bottom and free-surface, that the differences between the two AFRL runs and between the AFRL runs and UM run is 3D variation, or spanwise variation, which is especially strong at the bottom of the downstroke.



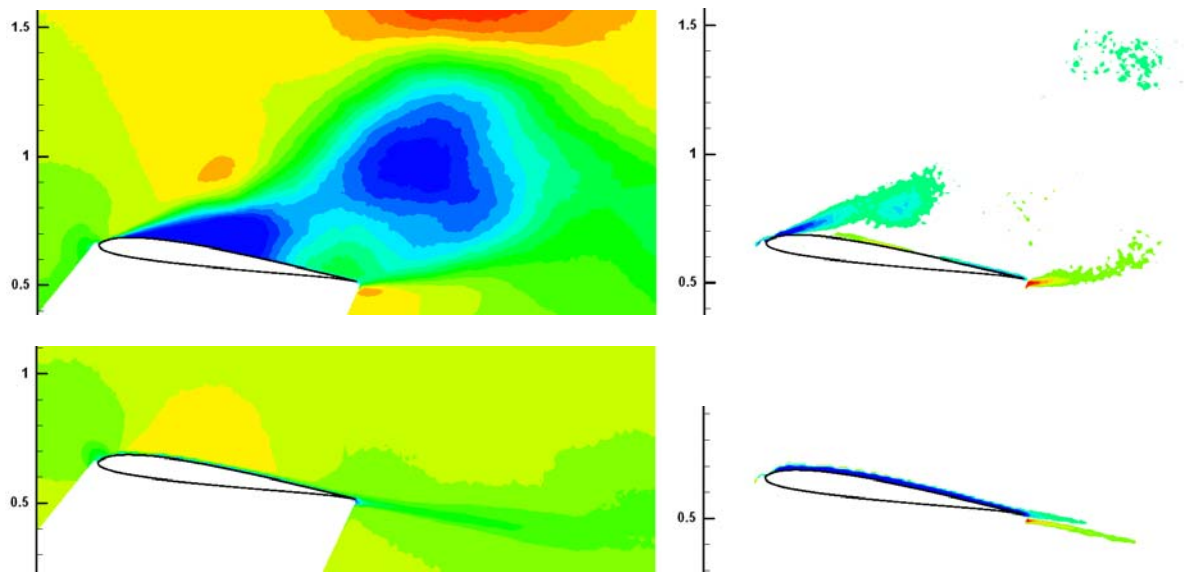
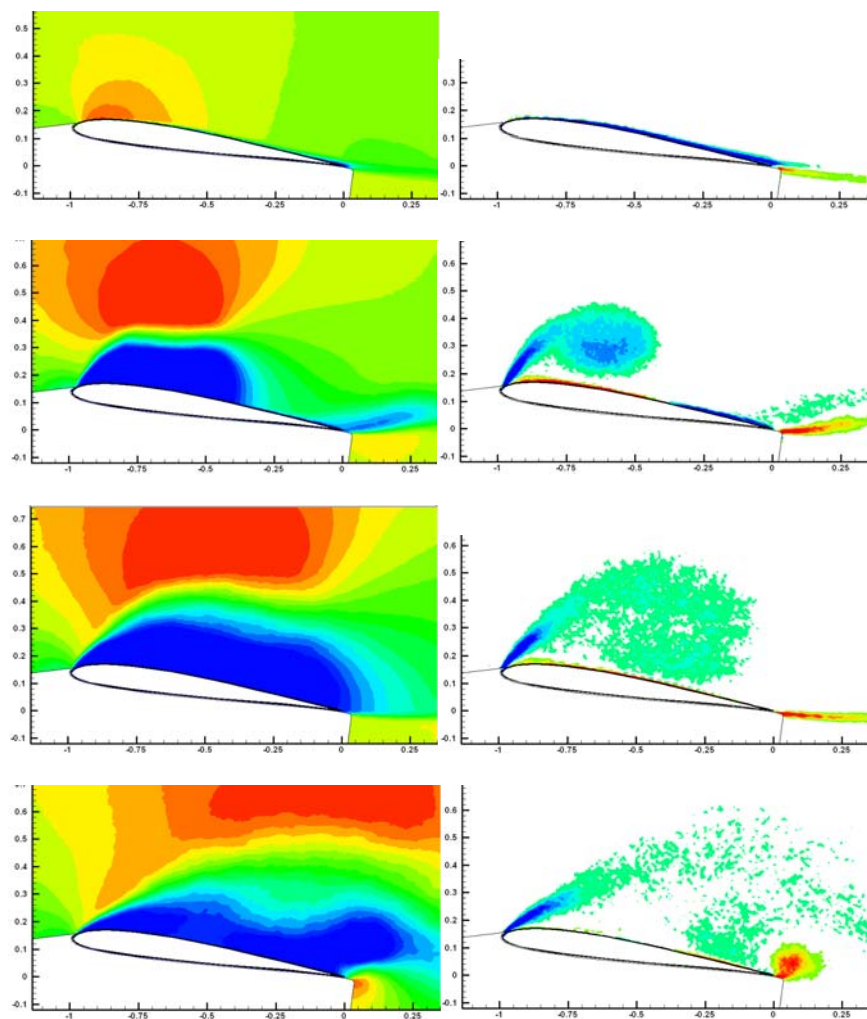


Figure 3-6: AFRL Water Tunnel, Entry #1; Phases $\Phi = 0, 90, 180$ and 270 .



PURE-PLUNGE OF THE SD7003 AIRFOIL

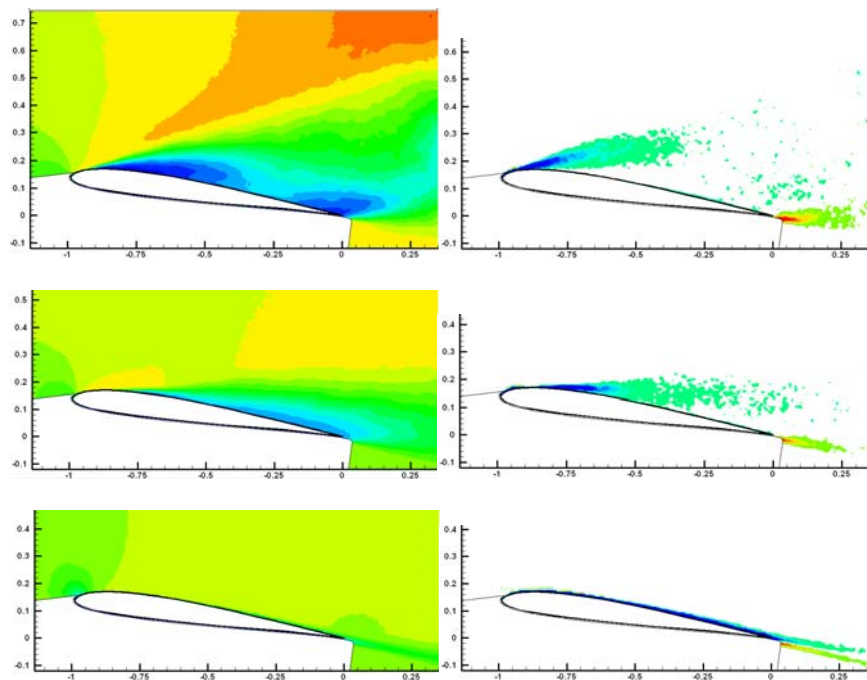
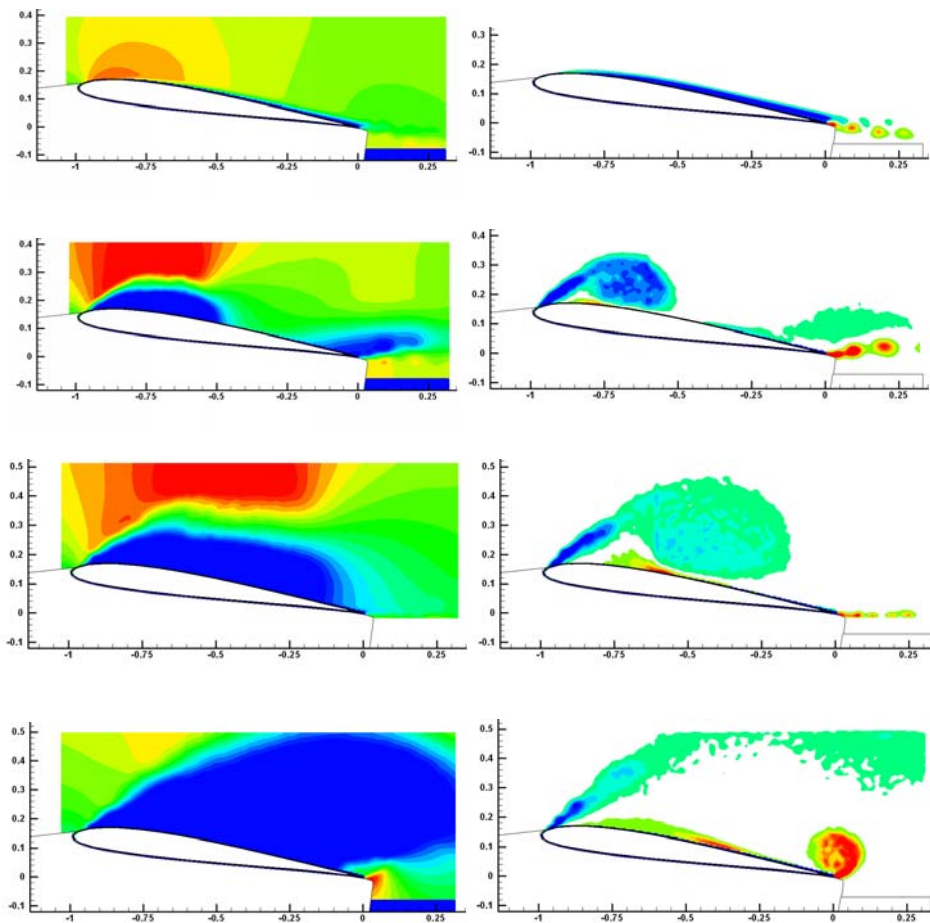


Figure 3-7: AFRL Water Tunnel, Entry #2; Phases $\Phi = 0, 90, 120, 150, 180, 210$ and 270 .



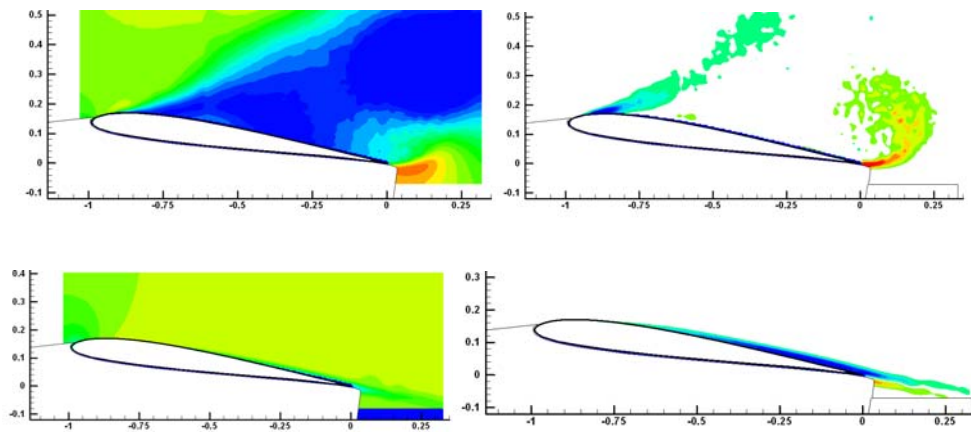
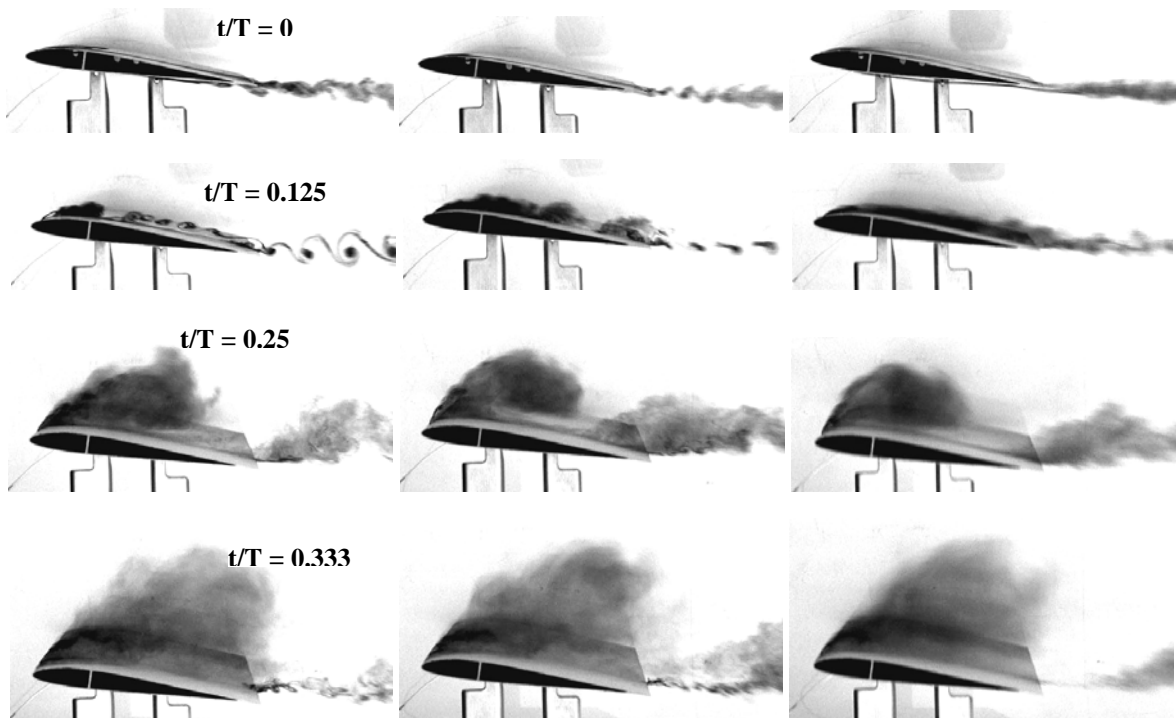


Figure 3-8: University of Michigan PIV; Phases $\Phi = 0, 90, 120, 150, 180$ and 270 .

3.2 REYNOLDS NUMBER EFFECTS

Because of the variation from facility to facility and computation to computation, Reynolds number variations are difficult to verify in detail, as for example a facility with larger turbulence intensity or more vibration of the motion rig may evince similar flowfield features at Reynolds number X , to those of a quieter facility at Reynolds number $2X$. One can, of course, do a Reynolds number sweep in one facility, but even there the conclusion is not definite because of issues with repeatability from run to run, which may be no smaller than the Reynolds number variation that one seeks to identify. Perhaps a statistical approach is required, where runs at different Reynolds numbers are repeated some number of times, in random order. This is perhaps possible for dye injection, but not for PIV. With that in mind, Figure 3-9 compares $Re = 20\text{ K}$, 30 K and 60 K dye injection in the AFRL water tunnel. To lower the operating Re , the tunnel is run more slowly, and the rig and the dye discharge rate are proportionately slower.



PURE-PLUNGE OF THE SD7003 AIRFOIL

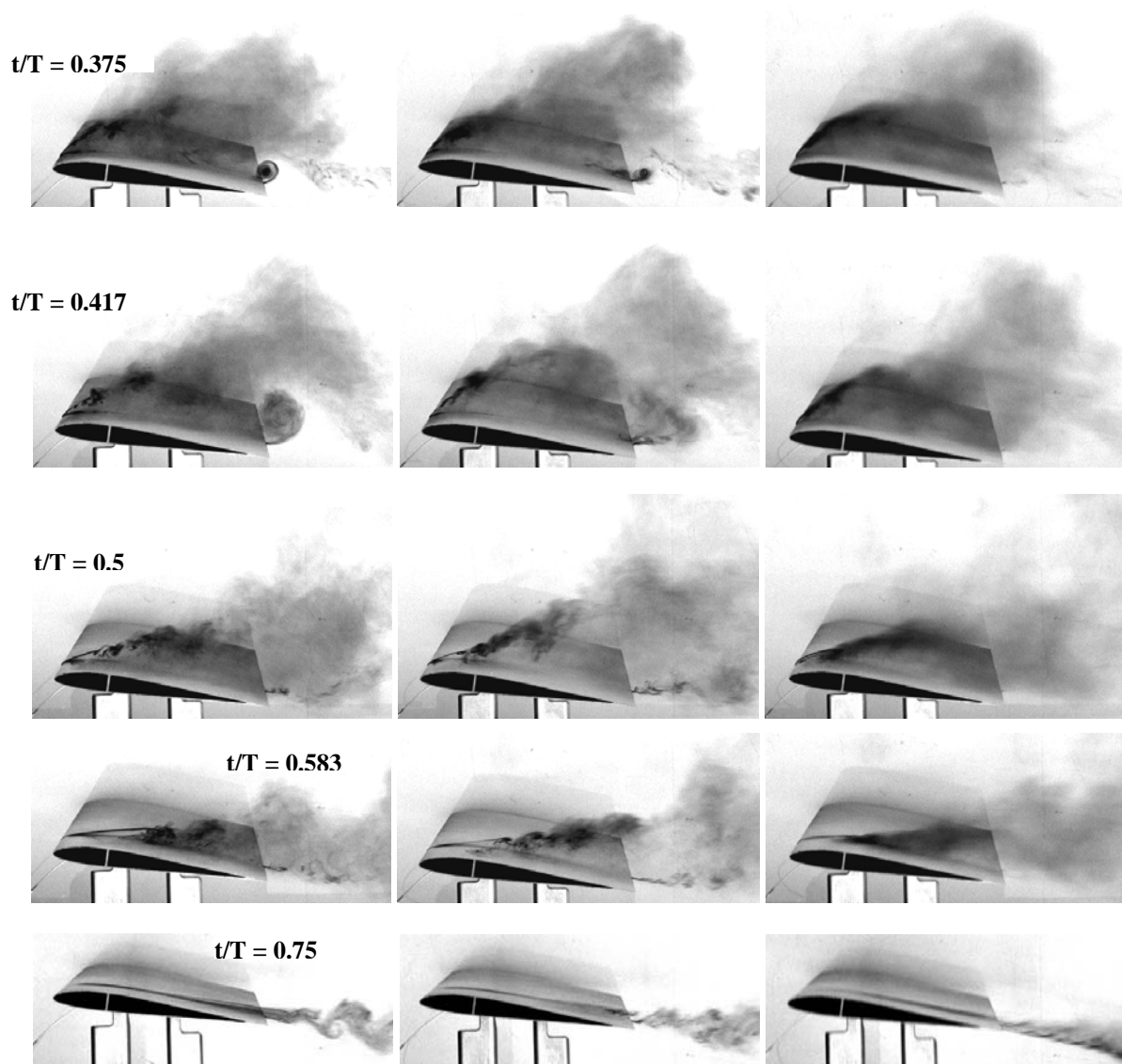
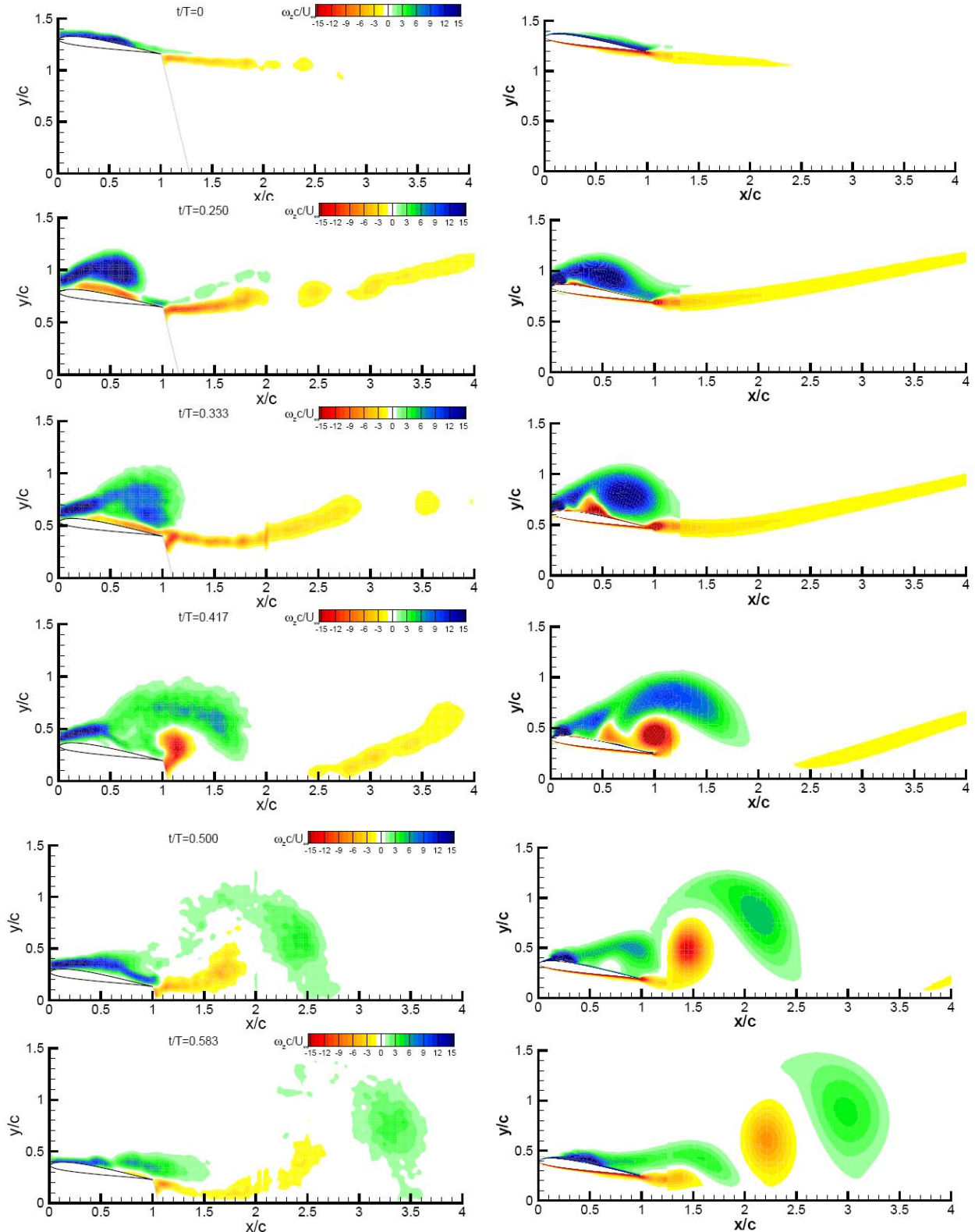


**Figure 3-9: AFRL Water Tunnel Dye Injection for Pure-Plunge;
Re = 20 K (left column), 30 K (middle column) and 60 K (right).**

At the trailing edge, at $Re = 30$ K and especially at $Re = 20$ K there is a discernable trailing edge vortex at $t/T = 0.375 - 0.417$, with a region of reverse flow just ahead of the trailing edge. At $Re = 60$ K, no TEV is clearly visible in the dye injection, but it was strongly apparent at $t/T = 0.417$ in the PIV, and at $t/T = 0.5$ in the CFD, as mentioned in the previous section. The near-wake at the top of the plunge stroke also shows a discernable Re-effect, with coherent vortices seen for $Re = 20$ K. In going from $t/T = 0$ to 0.125 to 0.25 , the suction-side dye concentrations splits, as it were, into a leading-edge and trailing-edge portion, the former coagulating into the LEV at $t/T = 0.25$. Towards the bottom of the plunge stroke, the pocket of dye lacuna just aft of the leading edge is smaller for higher Re , further suggesting that this region can be thought of as a laminar separation bubble.

RANS computations and PIV measurements were performed at TU Darmstadt at $Re = 30$ K. In the TU Darmstadt wind tunnel, rig max-speed considerations precluded testing at $Re = 60$ K, but $Re = 30$ K was readily attainable. Vorticity results are presented in Figure 3-10. Note that in these results the dimensionless vorticity contour levels are -15 to $+15$, not -36 to $+36$. Consistent with the dye injection at $Re = 30$ K in

Figure 3-9, there is indeed a TEV in experiments at $Re = 30 K$, and it is stronger in computation than in experiment. But LEV formation does not show much Re -dependency. Similar to the UM RANS, the LEV is thinner and delayed in the computation relative to the experiment.



PURE-PLUNGE OF THE SD7003 AIRFOIL

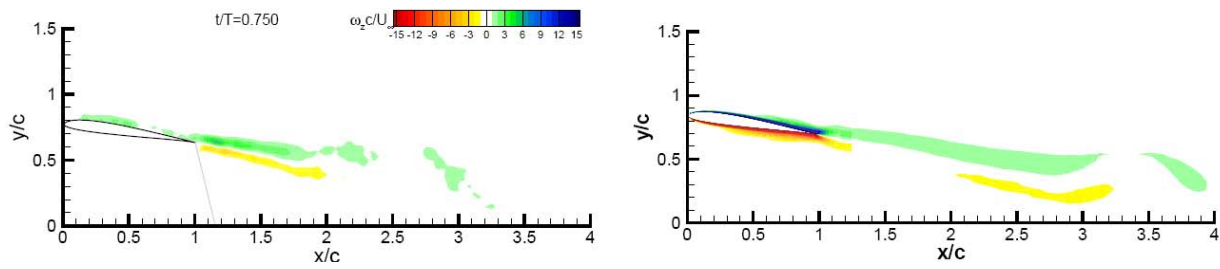


Figure 3-10: TU Darmstadt PIV (left column) and CFD (right column) Vorticity Contours; $Re = 30$ K; Phases of Motion $\Phi = 0, 90, 120, 150, 180, 210$ and 270 ; Contour Levels -15 to +15.

Turning to the computational results, data are available from the University of Michigan (Figure 3-11) and the Middle East Technical University (Figure 3-12). For brevity, we focus on the phases $\phi = 90$ and $\phi = 180$. Both data sets are shown at $Re = 60$ K, 30 K and 10 K. As Re decreases, the LEV formation process in the UM computation begins to approach that of the METU computation. Curiously, and contradicting the available experimental data, the TEV is stronger in UM computation at higher than at lower Re .

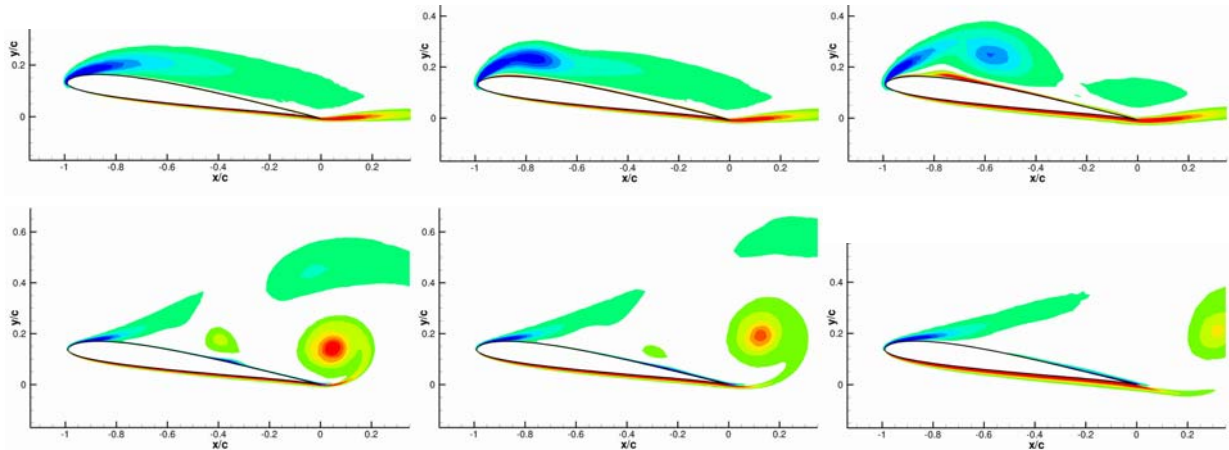


Figure 3-11: University of Michigan Computations; Phases $\Phi = 90$ (top row) and 180 (bottom row); $Re = 60$ K (left column), 30 K (middle column) and 10 K (right column).

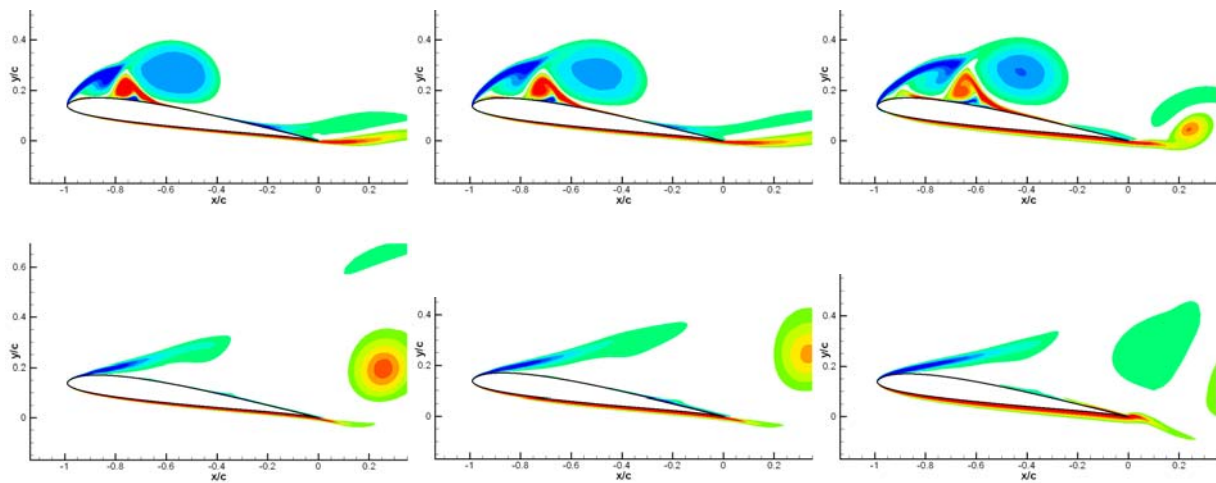


Figure 3-12: METU Computations; Phases $\Phi = 90$ (top row) and 180 (bottom row); $Re = 60$ K (left column), 30 K (middle column) and 10 K (right column).

Thus far we have considered variations in the flowfield – resolution of LEVs, “laminar” vs. “turbulent” separations, and so forth. Next, we turn to arguably the more important question of aerodynamic force coefficients – lift, pitch and drag. How well do RANS methods predict force data, and how much variation is there with Reynolds number? We consider this in the following section.

3.3 AERODYNAMIC FORCE COEFFICIENTS

The most basic quantity of interest is lift coefficient, and indeed one hopes to obtain reasonably correct lift coefficient time history at $Re = 60\text{ K}$ across the full range of analytical and computational methods, including the lower-order methods. Figure 3-13 shows computational and measured lift coefficient time history at $Re = 60\text{ K}$. The encouraging result is that all curves qualitatively follow the same trend. However, we note that because of the large peak-to-peak lift coefficient excursion, relatively large errors – say, $C_L \sim 0.4$ – appear small. This is the amount by which the simple $C_L = 2\pi\alpha$ over-predicts positive and negative lift extrema. Also interesting is that the lift time history is essentially sinusoidal and has small phase difference with respect to angle of attack time history, despite the obvious presence of an LEV and its putative dynamic-stall effects on lift, which ought to manifest itself as a large hysteresis for lift plotted vs. angle of attack.

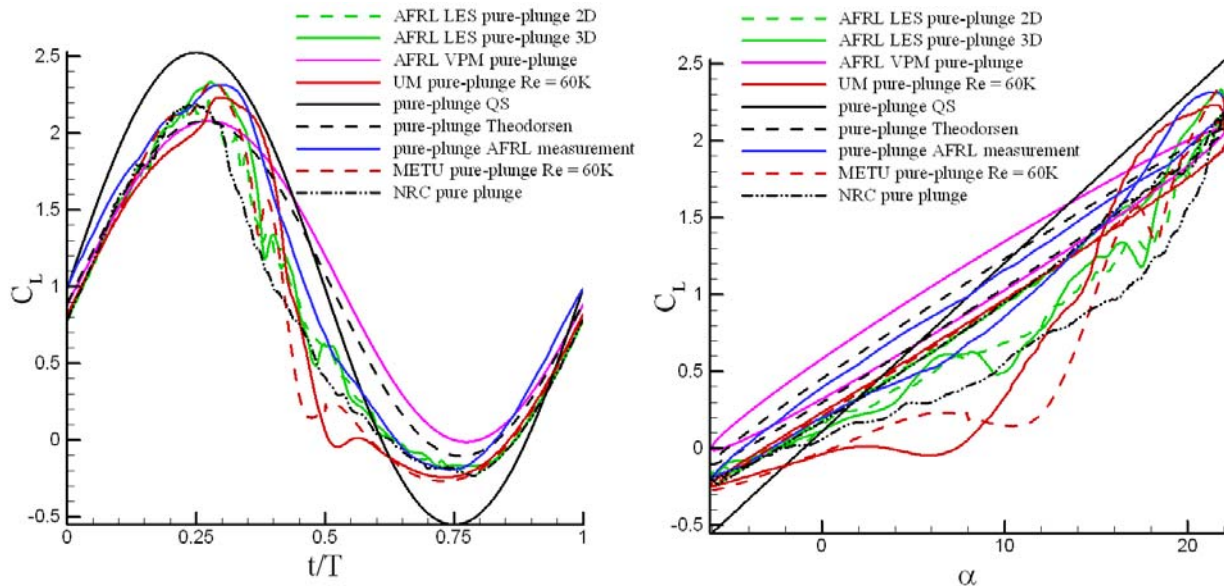


Figure 3-13: Lift Coefficient Time History, SD7003 Pure-Plunge; $Re = 60\text{ K}$; Plotted vs. Motion Phase (left) and Effective Angle of Attack (right).

Experiment and AFRL 3D LES are very close, as would be expected from a high-fidelity computation. NRC 2D LES essentially splits the difference between AFRL LES and RANS, as is to be expected from the resolution of the NRC computation. But the most remarkable fact is that Theodorsen’s formula (dashed black curve in Figure 3-13) also follows fairly closely with the 3D LES computations, slightly under-predicting dynamic lift at the max effective angle of attack ($t/T = 0.25$) and in turn over-predicting lift on the first half of the upstroke ($t/T = 0.5$ to 0.75).

RANS computations predict slight lift coefficient peaks near $t/T \sim 0.25$, evidently due to the LEV. This is missed by the methods that ignore smooth-surface flow separation – Theodorsen and VPM. The closeness of the VPM and Theodorsen results implies that wake curvature is not important for the lift time history in this case. However, RANS methods over-predict loss of lift at the plunge downstroke ($t/T = 0.5$), relative to LES and experiment, and in general show a slightly stronger dynamic stall than does the LES; in other

PURE-PLUNGE OF THE SD7003 AIRFOIL

words, a fuller hysteresis loop. Curiously, the large difference in velocity/vorticity contour plots between the AFRL 2D and 3D LES and between AFRL and NRC LES does not correspond to much difference in the lift time history.

We note that the effect of LEVs on the lift time history is modest – at most 10% – 20% of the maximum lift. This helps to explain why lower-order methods are fairly successful. But the not unreasonable result from $C_L = 2\pi\alpha$ is misleading, because quasi-steady thin airfoil theory ignores unsteady effects rather than taking separation into account. Thus, whatever accuracy to which it may lay claim, this accuracy is fortuitous. We also note that period-to-period variations in the experiment may be smeared in the ensemble average, in the sense that dynamic-stall peaks and troughs in the lift coefficient time history in any one period are attenuated in the average because they vary randomly from period to period. This is disappointing from the viewpoint of fundamental fluid mechanics, but from the viewpoint of applied engineering one concludes that dynamic stall effects are uncorrelated and therefore of limited importance, and the lift time history is quite sinusoidal, with small phase lag.

Variations in drag coefficient (Figure 3-14) are somewhat larger than in lift. This is to be expected, because drag is a smaller quantity than lift and therefore more sensitive to error, and because drag will depend more than lift on local variations in pressure distribution (presence or absence of an LEV, for example) and on prediction of boundary layer properties. The VPM and Theodorsen's method are inviscid, and therefore disregard skin friction and LEVs; but they do capture Knoller-Betz type of thrust [27]. Clearly the effects of boundary layers and flow separation are evident in the failure of Theodorsen's formula (or more properly, Garrick's extension [27]) to capture the correct drag vs. thrust balance. The UTIAS method, which is inviscid but has empirical corrections for viscous effects, performs acceptably in phases of motion where the flow is nominally attached, but misses the effect of LEV formation and growth entirely, predicting a thrust near $t/T \sim 0.25$, instead of a drag. AFRL 2D LES tends to slightly under-predict drag due to the LEV relative to 3D LES, and NRC 2D LES under-predicts further. The METU RANS computations track closely with the 3D LES, evidently because they happen to resolve the LEV qualitatively in a manner much akin to the 3D LES vorticity result. The UM RANS computation tracks closely with the 3D LES starting at $t/T \sim 0.4$, but predicts a slight thrust at the phase of motion where the LEV forms, evidently because it does not sufficiently penalize the airfoil for loss of leading edge suction due to leading edge separation. Indeed all of the drag computations, except for UM RANS, mutually track in a narrow range except for $0.25 < t/T < 0.5$, which is the period from LEV formation to shedding.

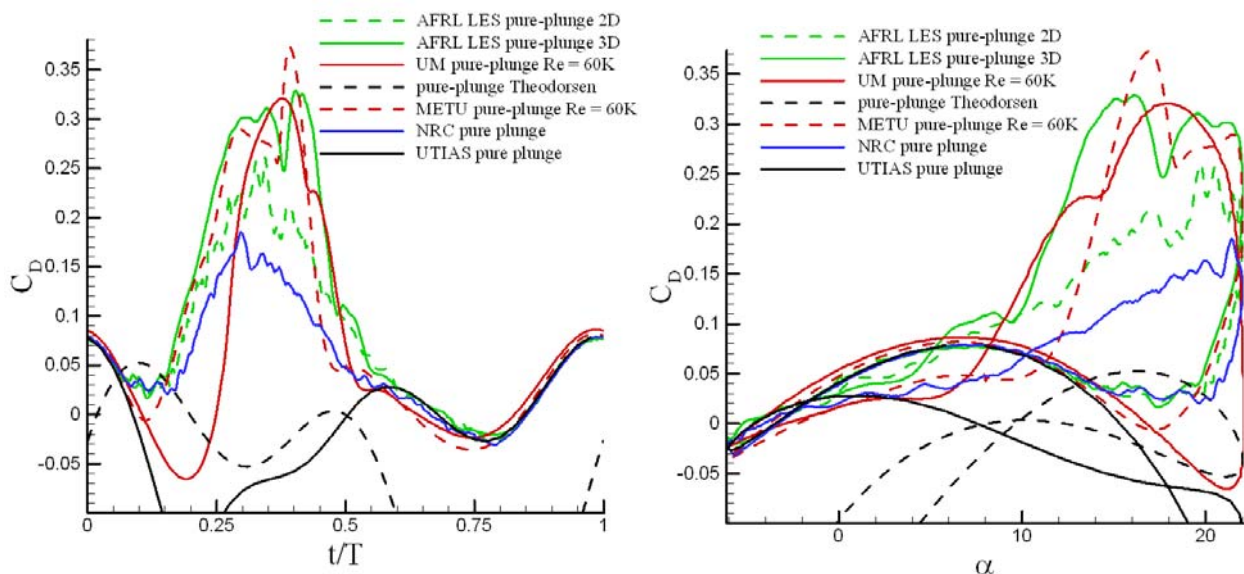


Figure 3-14: Drag Coefficient Time History, SD7003 Pure-Plunge; Re = 60 K; Plotted vs. Motion Phase (left) and Effective Angle of Attack (right).

Overall one can note that whereas lift varies very close to sinusoidally, despite all of the various flow separation effects, drag is not sinusoidal, but rather peaks quite strongly just before the bottom of the plunge downstroke, where evidently flow separation is the largest. Drag, to belabour the obvious, is much more sensitive than lift to the actual flowfield structure, and to calculate drag accurately one must resolve the flowfield more accurately than is necessary for just calculating the lift.

We next turn to aerodynamic force trends with respect to Reynolds number (Figure 3-15), comparing AFRL 3D LES, UM RANS at $Re = 60\text{ K} - 30\text{ K} - 10\text{ K}$, METU RANS at $Re = 60\text{ K} - 30\text{ K} - 10\text{ K}$, and TUD RANS at $Re = 30\text{ K}$. Other than the TUD lift relative overshoot at $t/T \sim 0.25$, there is little variation amongst the various curves, and thus little lift dependency with Reynolds number – even less than flowfield differences seen in for example in Figure 3-9. A similar but more tempered observation holds for drag. As decreases, the UM RANS drag prediction gets ever closer to the other curves on the second half of the downstroke, as evidently the predicted loss of LE suction intensifies with decreasing Reynolds number. Low sensitivity of aerodynamic forces to Reynolds number is consistent with classical dynamic stall observations, for example McCroskey et al. [5].

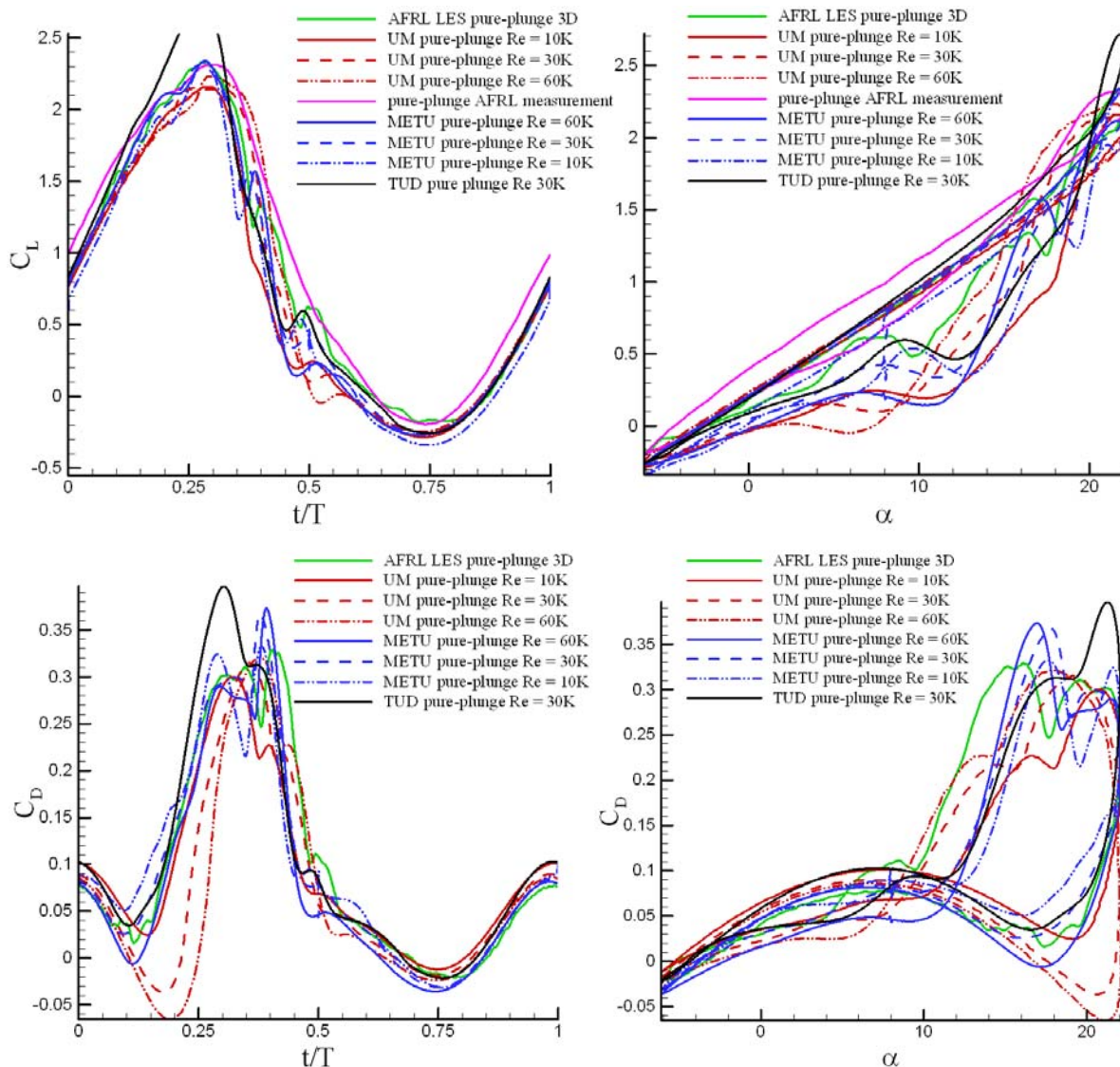


Figure 3-15: Trends in Lift Coefficient (top row) and Drag Coefficient (bottom row) for SD7003 Pure-Plunge vs. Reynolds Number (60 K, 30 K and 10 K).

The discrepancy between the UM and METU RANS codes deserves further mention; both are 2D and use the same nominal turbulence model. However, the UM computation has two variations: “standard” and “modified”, as described in Chapter 2. Figure 3-16 compares the three RANS results for lift and drag. The “modified” version of the UM computation gives results very close to those to the METU computation. While the differences between all of these curves are comparatively minor in the larger picture of peak-to-peak coefficient variations, nevertheless in the details the computational result is clearly sensitive to choice of implementation of turbulence model. It is perhaps disappointing that comparatively significant variations in aerodynamic force prediction can arise from a subtlety of numerical implementation.

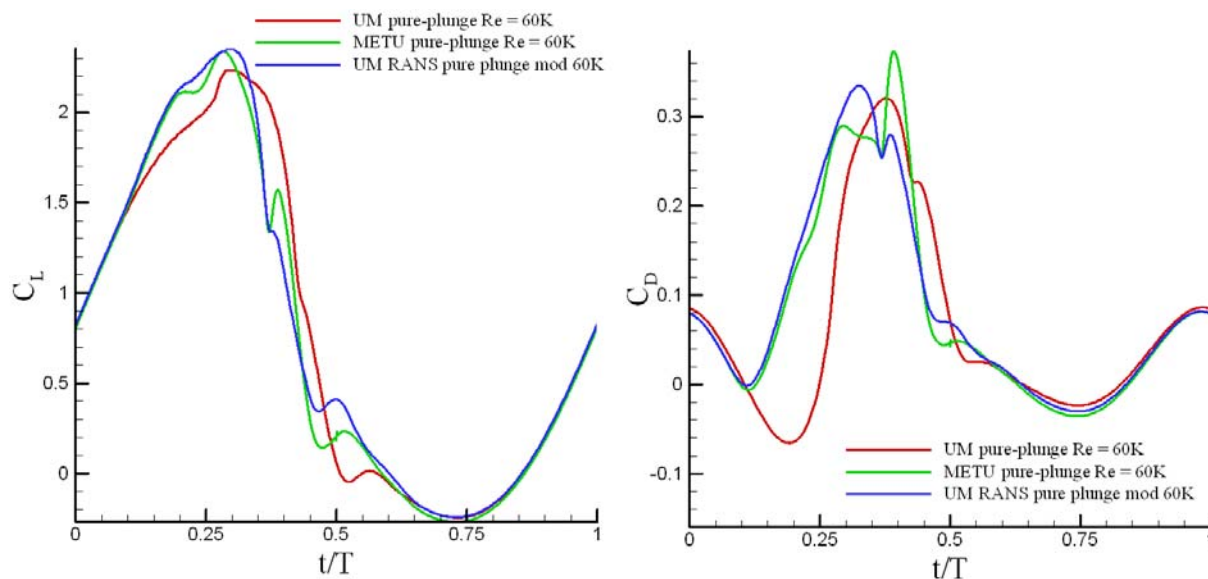


Figure 3-16: Lift Coefficient (left) and Drag Coefficient (right) Comparison Between METU and Standard vs. Modified UM RANS.

Finally we consider pitching moment coefficient. C_M is notoriously difficult to measure or compute, because it depends not only on the area between the airfoil upper-surface and lower-surface pressure distributions, but on the pressure *distributions* directly. “Correct” calculation of lift can sometimes arise from cancellation of errors; quite the opposite happens for pitch, where small errors can amplify. In experiments, inertial tares for C_M in a dynamic experiment require not only model mass tares, but also moment of inertia tares – unless testing in liquids, where inertia plays a much smaller role.

Dynamic stall in classical applications such as helicopter blades and manoeuvring aircraft is even more notorious for its effect on pitching moment, than on lift. Formation of the LEV in dynamic stall causes a small nose-down pitching moment relative to the quarter-chord, because the LEV is close to the quarter-chord and its local suction has a small moment arm. However, as the LEV convects downstream and reaches the trailing edge, the pitching moment coefficient becomes strongly nose-up. Then, when the vortex is aft of the airfoil, C_M snaps back up, producing a violent hysteresis when plotted against α [6]. It is also possible that the strong trailing edge vortex found in the computations, if present in the flow, would add to a moment-stall as it forms and convects downstream from the trailing edge.

The available C_M data are shown in Figure 3-17. Clearly there is a classical dynamic moment stall – in contradistinction to the situation for lift. This is missed by the inviscid methods, because these methods like a LEV model. Because the METU RANS have qualitatively similar LEV resolution to AFRL 3D LES, the two C_M results are similar. 2D AFRL LES does not predict a coherent LEV, whence there is much less moment stall. C_M prediction, completely unlike C_L and to a large extent unlike C_D , requires accurate

rendition of the flowfield. But that accuracy, if achieved by a low-order method, can occasionally be serendipitous. We mention the trite but true platitude that test cases across a broad range of motion parameters are necessary, before one can speak definitively about the accuracy of low-order methods.

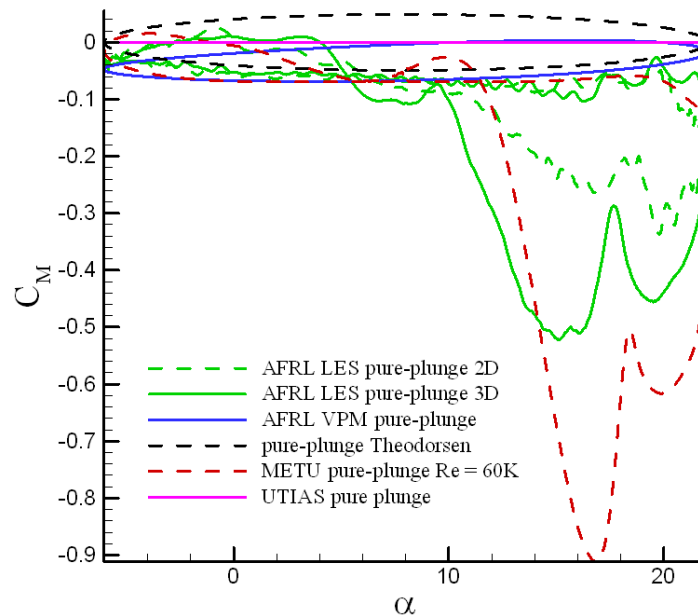


Figure 3-17: Pitching Moment Coefficient for SD7003 Airfoil in Pure-Plunge.

To summarize, an effective peak angle of attack of 22° at $Re = 60 K$ is large enough to cause moment-stall in the sense of classical dynamic stall, but not lift stall. Boundary layer physics does not appear to be a main driver of integrated aerodynamic effects. This is largely positive news for engineering-level predictive methods. Clearly a larger parameter study is warranted, exploring for example the role of airfoil LE radius and its effect on boundary layer physics, and looking at more aggressive motions with larger effective angle of attack. Presently, however, we turn to the arguably more complicated problem of combined pitch-plunge, where the effective angle of attack is smaller due to partial cancellation of plunge-induced angle of attack from pitch. As we will see, the resulting flow physics are rather less spectacular, but perhaps more complex from the viewpoint of engineering prediction.



Chapter 4 – COMBINED PITCH-PLUNGE OF THE SD7003 AIRFOIL

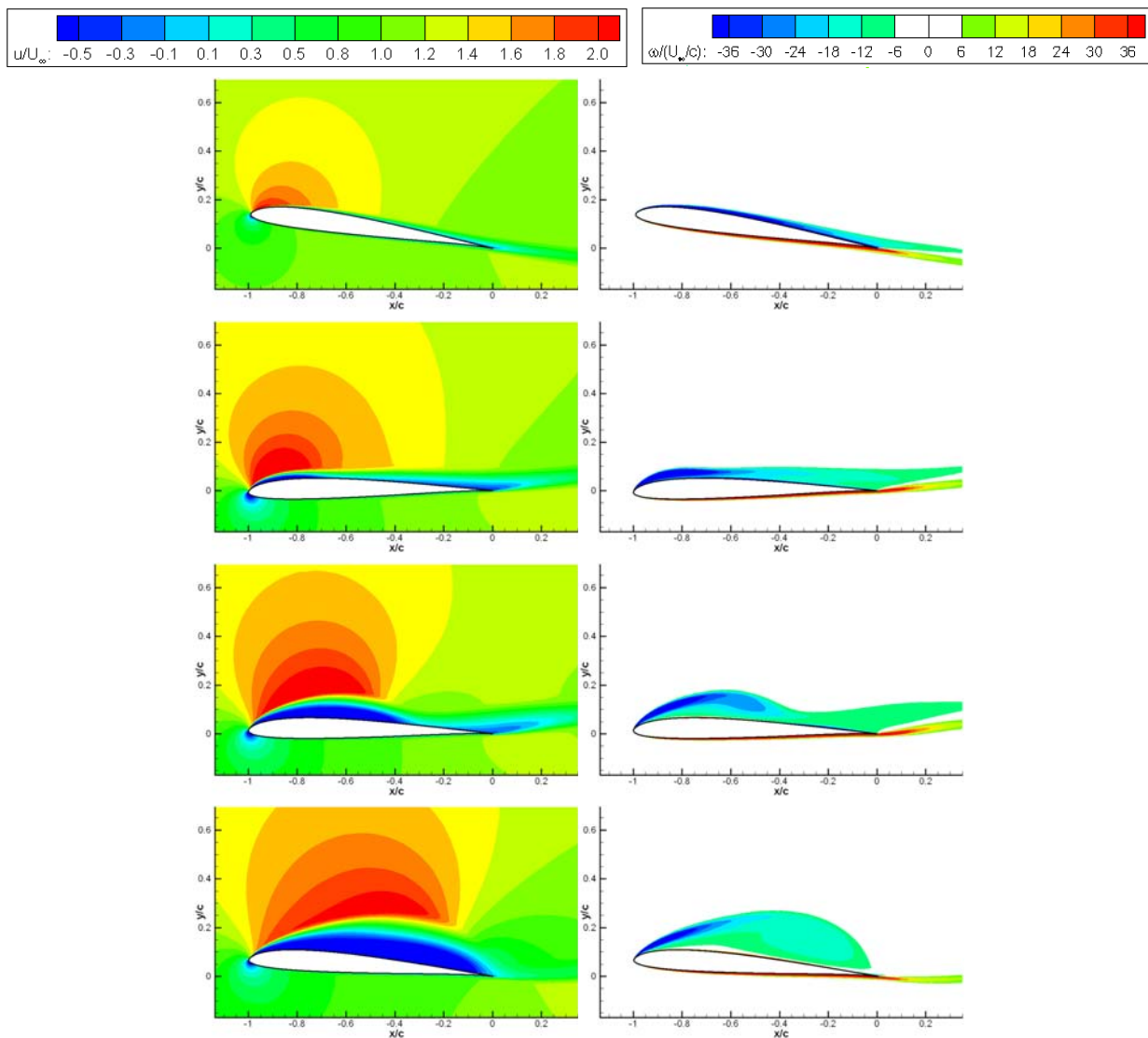
In contrast with the pure-plunge motion, the combined pitch-plunge motion is at effective angle of attack not far above static stall, with the motivation of serving as a case for useful propulsive thrust.

4.1 RESUME OF EXPERIMENTAL AND COMPUTATIONAL RESULTS FOR THE FLOWFIELD: VELOCITY AND VORTICITY

As for the pure-plunge case, we first consider velocity and vorticity contours, and then proceed to comparing results for aerodynamic loads. The canonical Reynolds number remains at 60000.

4.1.1 Computations

RANS computations were conducted by METU (Figure 4-1) and UM (Figure 4-3). NRC performed 2D LES (Figure 4-2).



COMBINED PITCH-PLUNGE OF THE SD7003 AIRFOIL

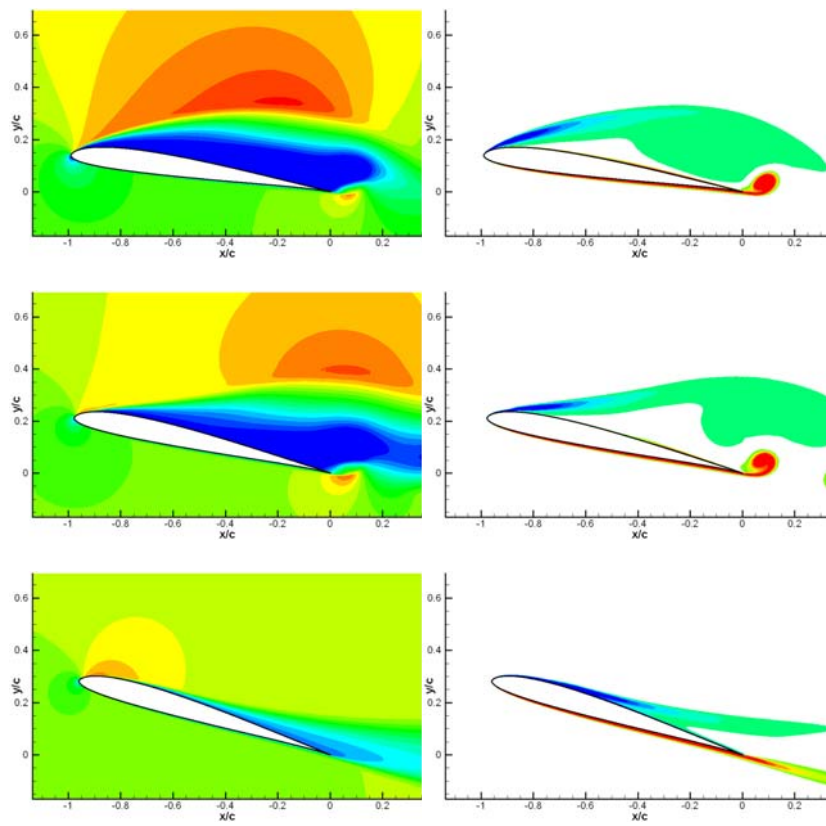
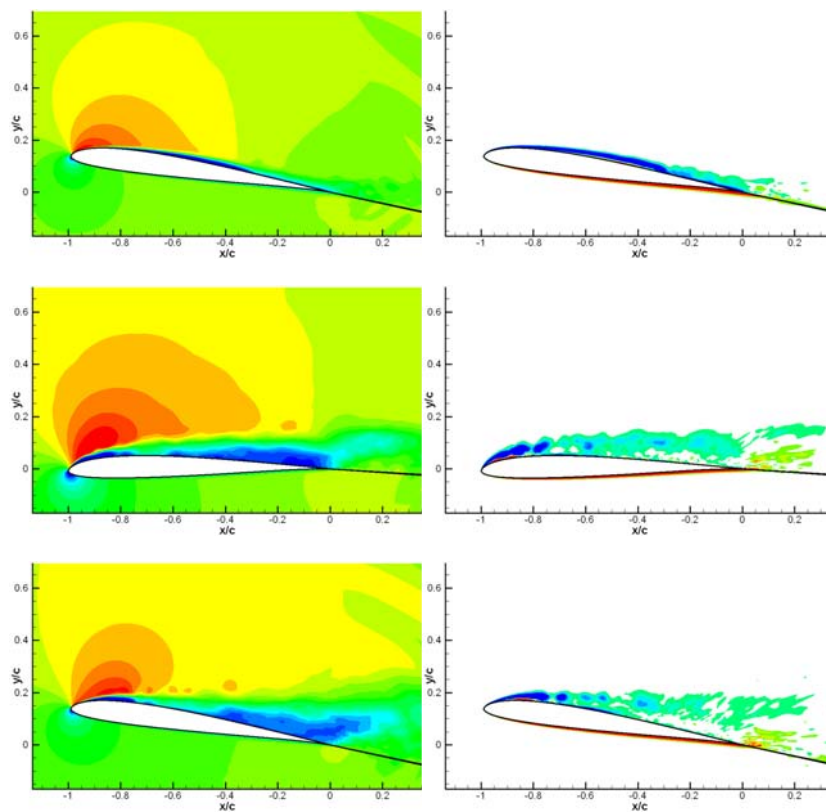


Figure 4-1: METU Computations; Phases $\Phi = 0, 90, 120, 150, 180, 210$ and 270 .



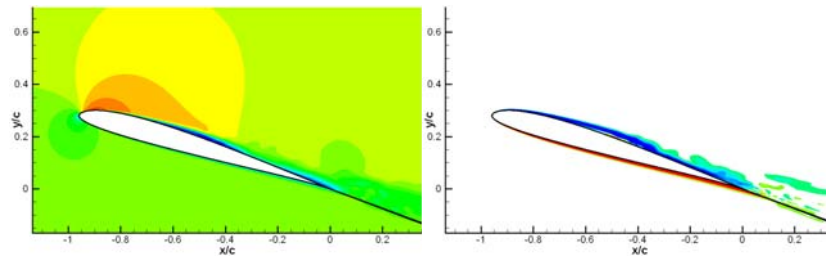
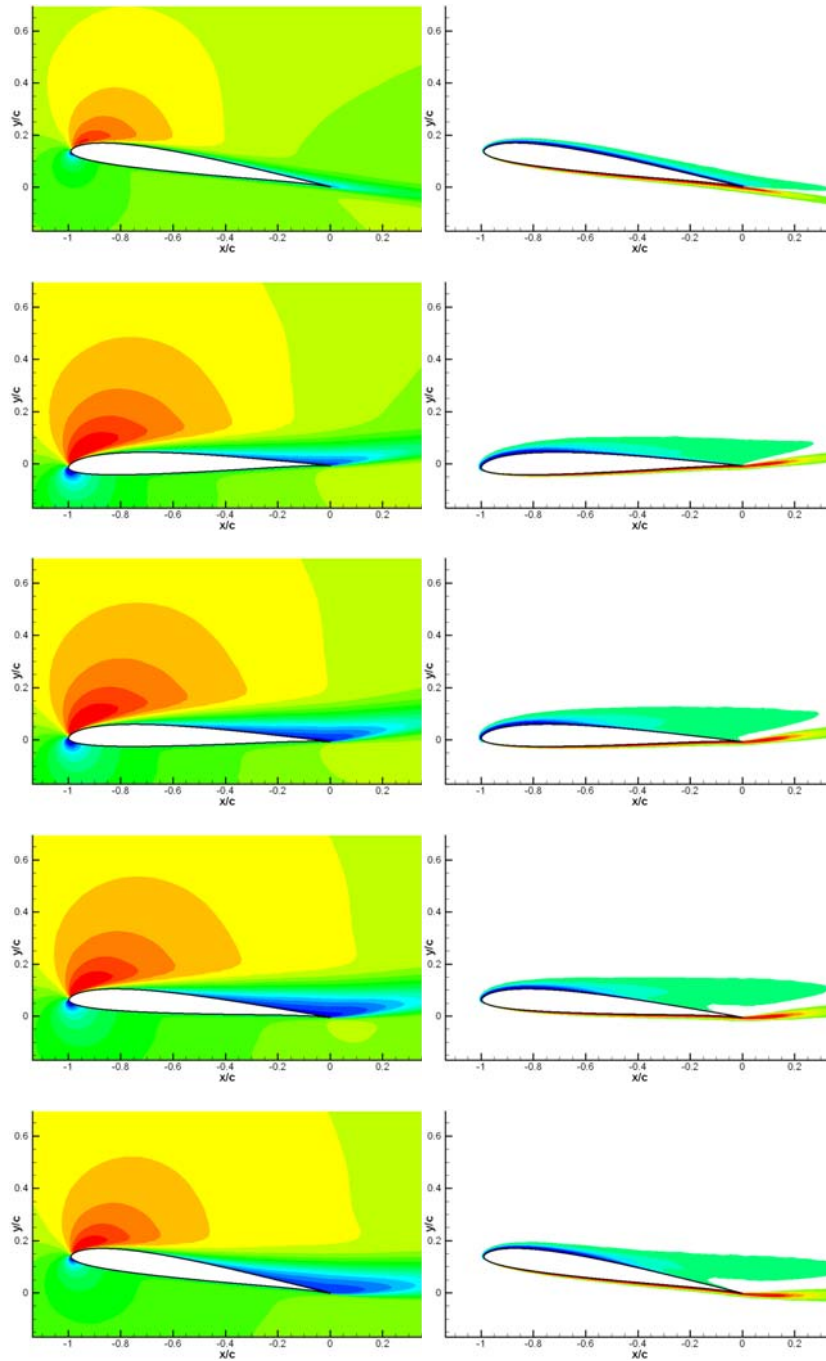


Figure 4-2: IAR NRC Computations, LES; Phases $\Phi = 0, 90, 180$ and 270 .



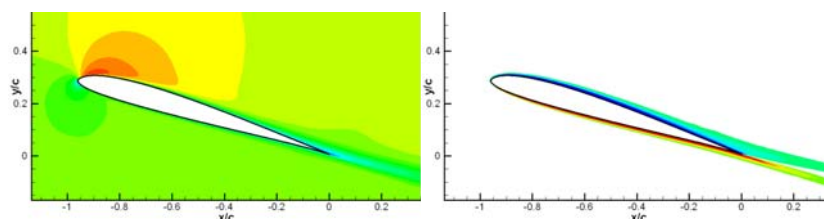
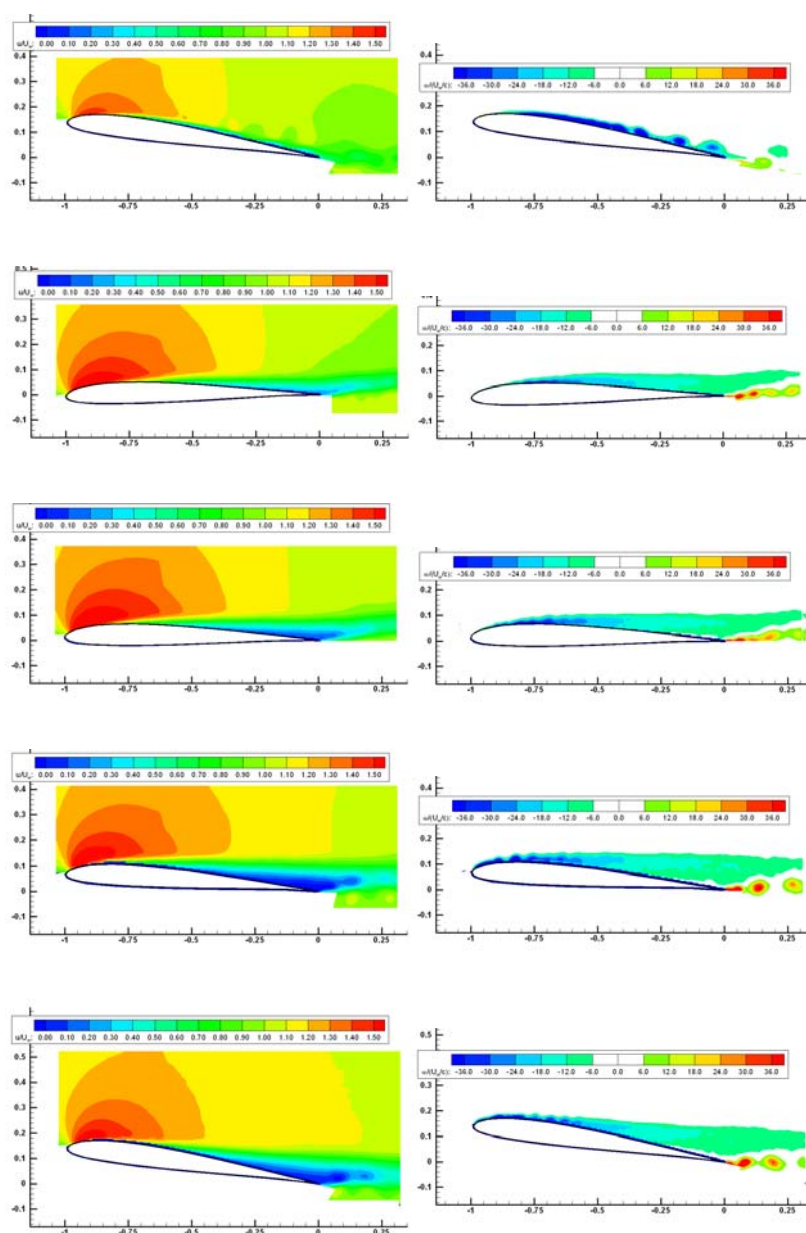


Figure 4-3: University of Michigan Computations; Phases $\Phi = 0, 90, 120, 150, 180$ and 270 .

4.1.2 Experiments

Experiments were performed by UM (Figure 4-4), AFRL (three iterations spaced over two years: Figure 4-5, Figure 4-6 and Figure 4-7, respectively), and TUBS (Figure 4-8).



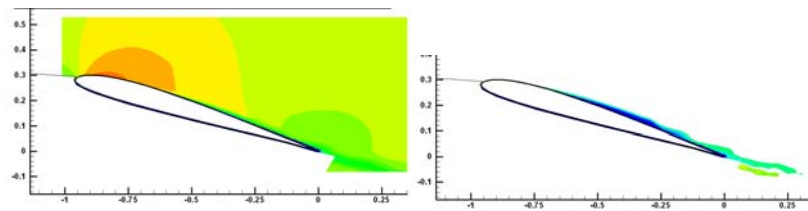


Figure 4-4: University of Michigan PIV; Phases $\Phi = 0, 90, 120, 150, 180$ and 270 .

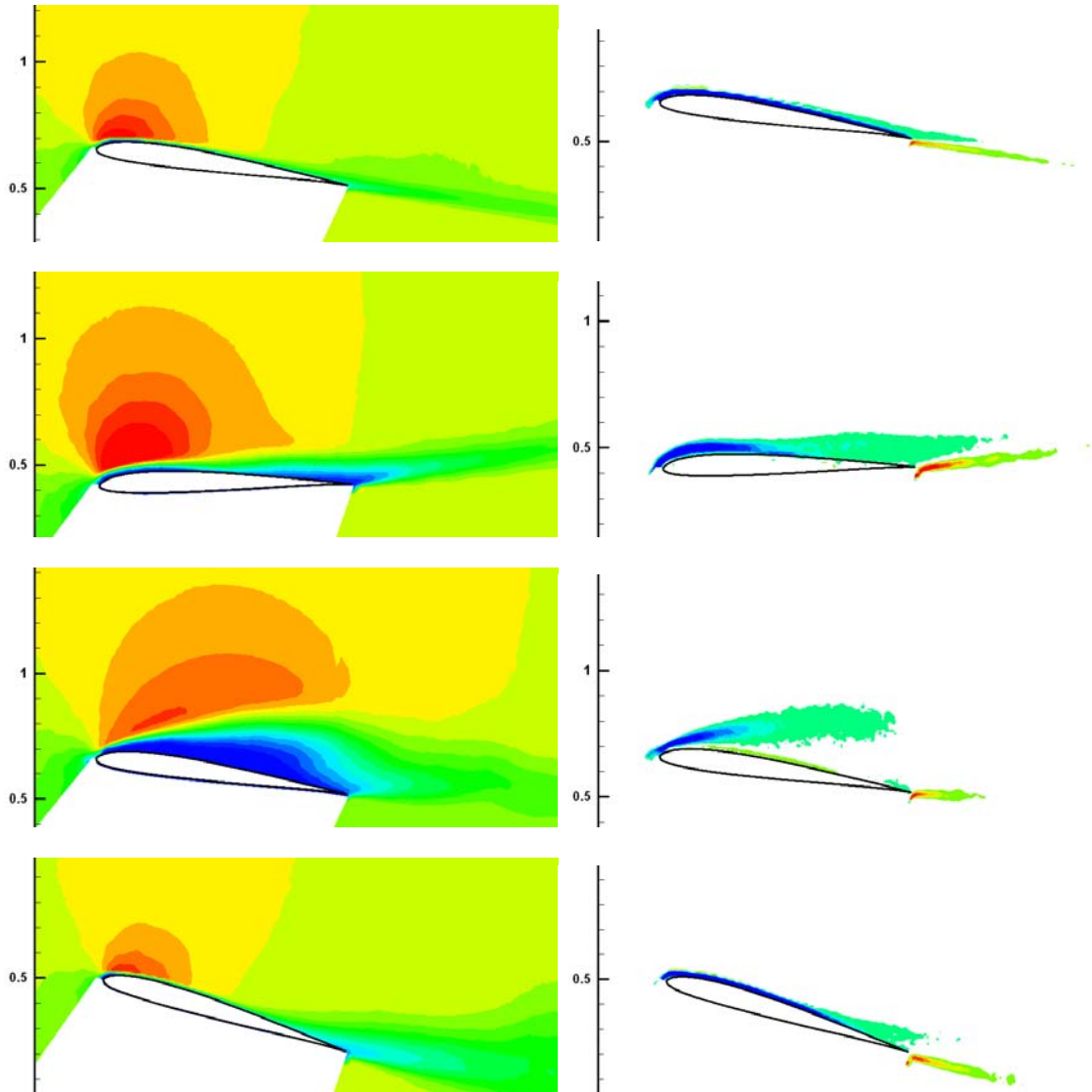
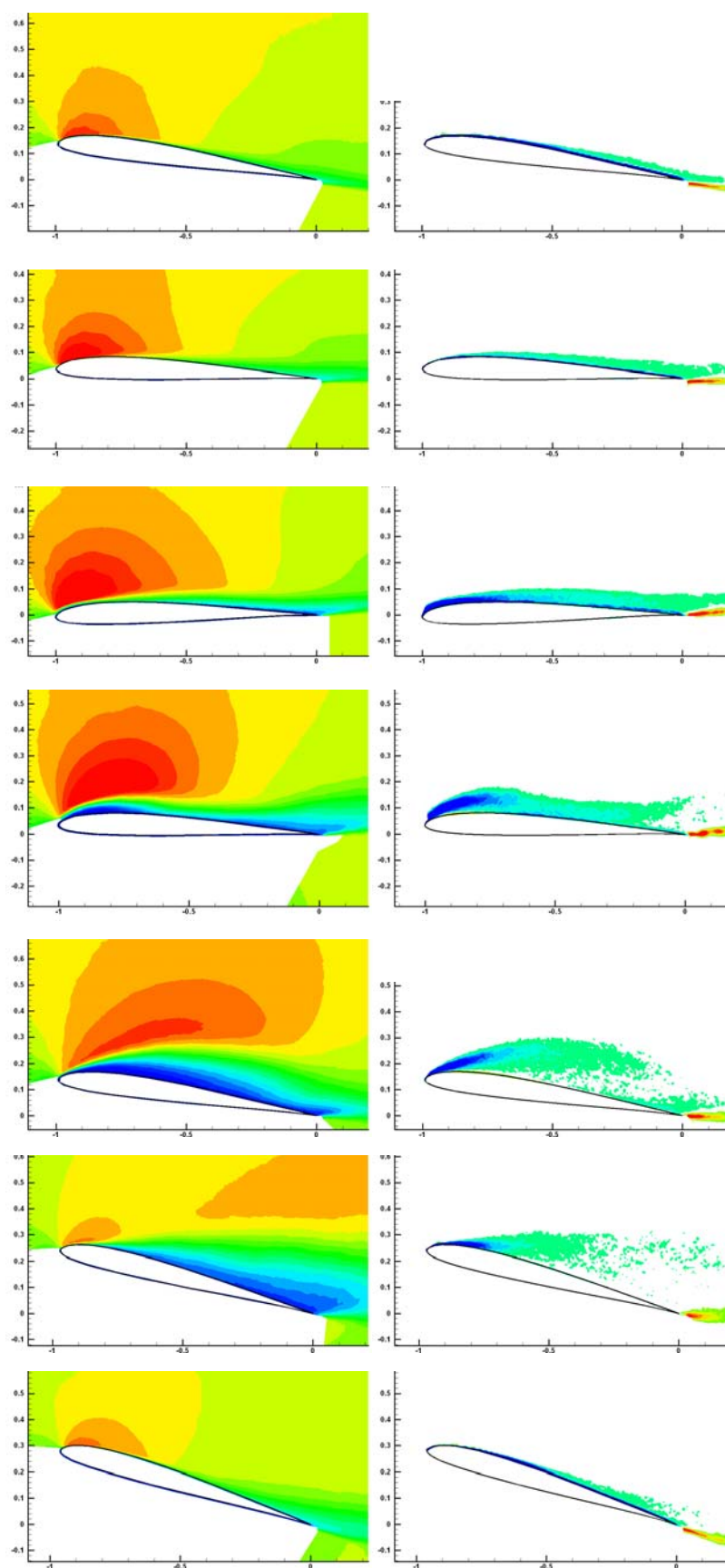


Figure 4-5: AFRL PIV, First Data Series; Phases $\Phi = 0, 90, 180$ and 270 .

COMBINED PITCH-PLUNGE OF THE SD7003 AIRFOIL



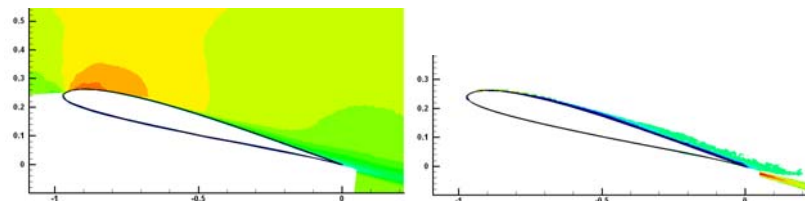
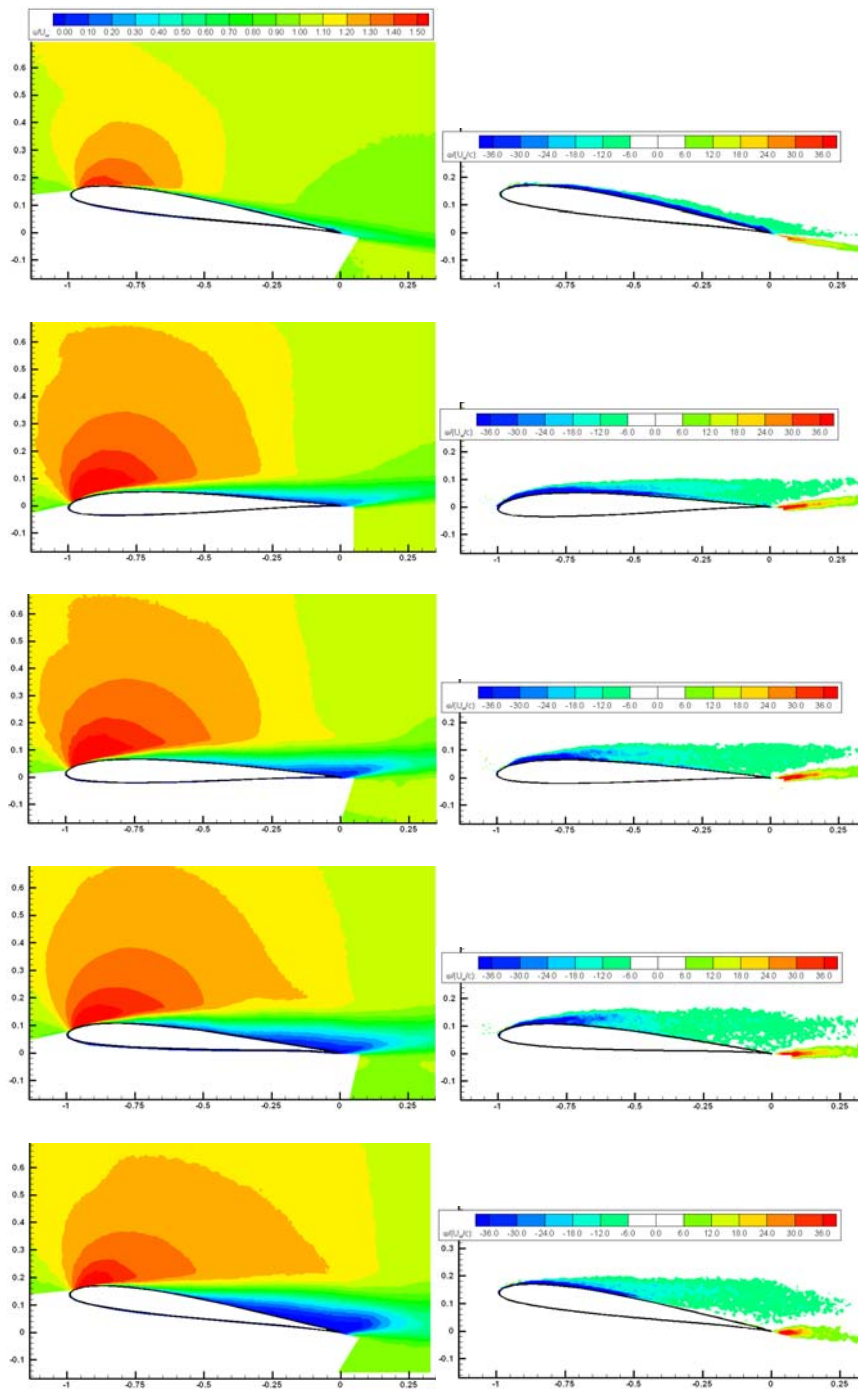


Figure 4-6: AFRL PIV, Second Data Series; Phases $\Phi = 0, 45, 90, 135, 180, 225, 270$ and 315 .



COMBINED PITCH-PLUNGE OF THE SD7003 AIRFOIL

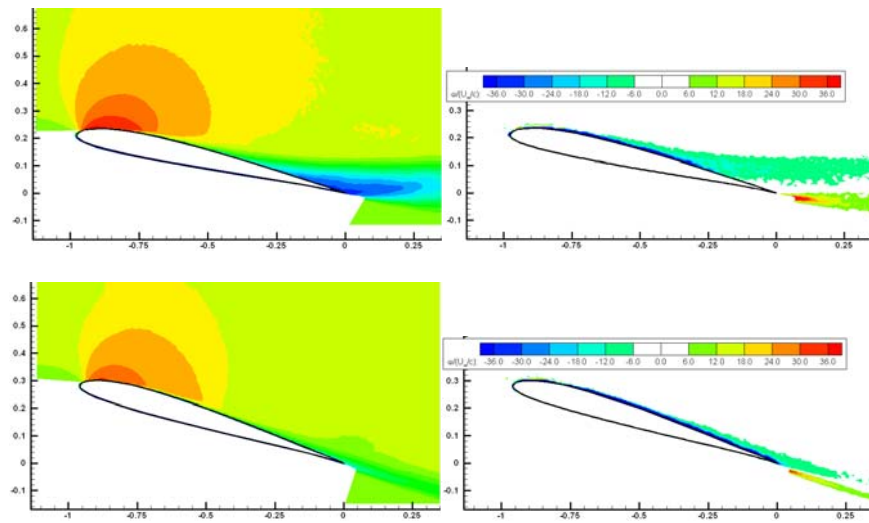


Figure 4-7: AFRL PIV, Third Data Series; Phases $\Phi = 0, 90, 120, 150, 180, 210$ and 270 .

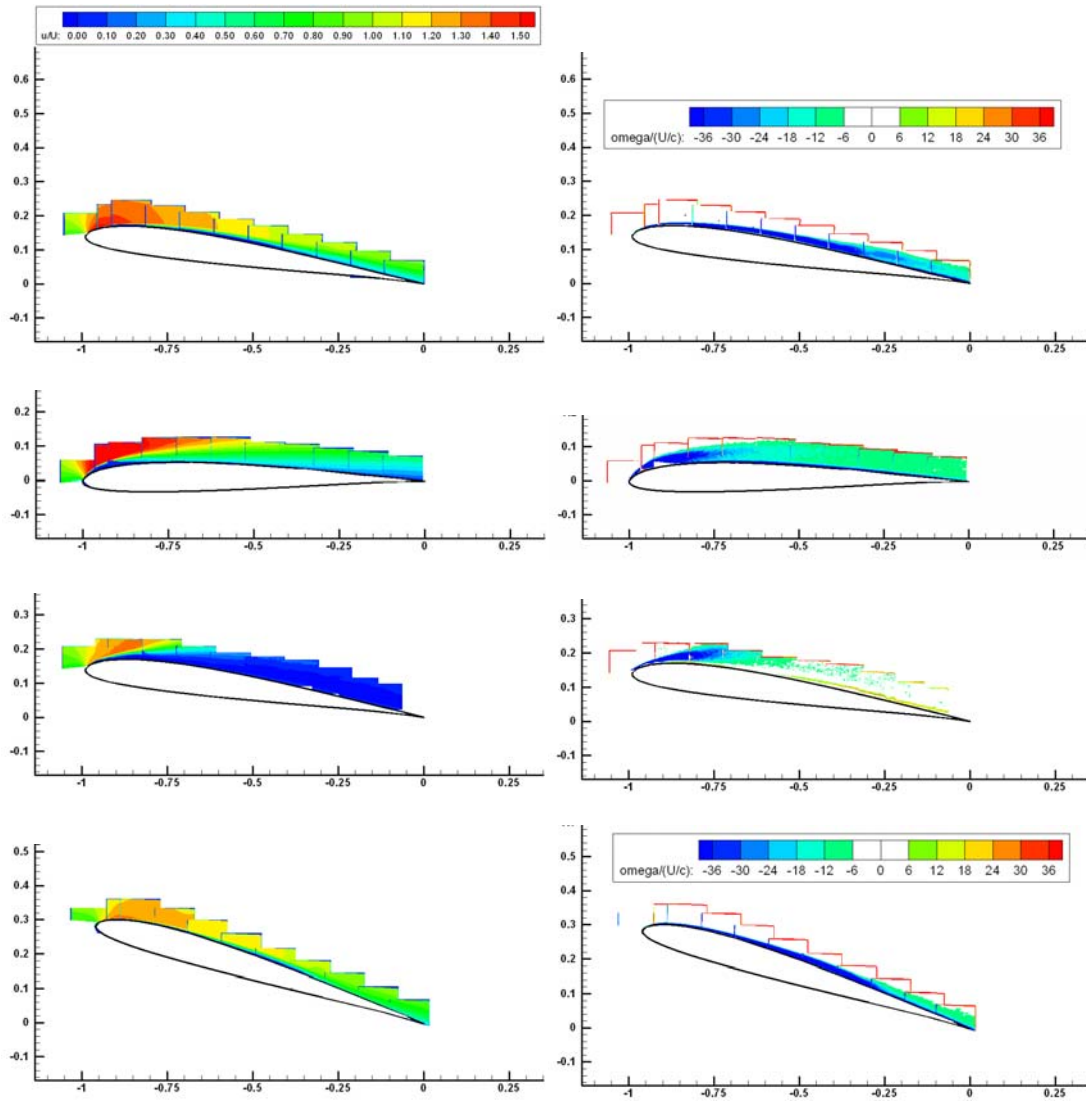


Figure 4-8: TUBS PIV; Phases $\Phi = 0, 90, 180$ and 270 .

Reviewing the streamwise velocity contour plots for the pitch-plunge case, results group into three types: “small” separation, where the region of stagnant or reversed flow at the bottom of the plunge downstroke is thin and does not begin until towards the airfoil mid-chord; “large” separation, which is still closed in the phase-averaged sense but begins smoothly shortly aft of the leading edge, and LEV-dominated large separation. The U of Michigan experiment and computation, and one of the AFRL experiments fall under “small” separation. The NRC computation, TUBS experiment and another AFRL experiment fall under the “large” separation. The METU computation shows an LEV.

The disparity between the three kinds of separation is loosely associable with laminar to turbulent transition. The METU computations appear to me “more laminar”, while the U of Michigan computations are “more turbulent”. The AFRL water tunnel is evidently on the edge between “laminar” and “turbulent” results, sometimes favouring the one and on occasion the other.

It is perhaps worthwhile to briefly note the factors behind turbulent-like or laminar-like results. In the computations, causes include of course the choice of turbulence model, the inputs to that model, the role of the mesh and treatment of far-field boundary conditions, the relative balance between turbulent kinetic energy production and dissipation, and so forth. For experiments, the main cause is disturbances, which can be flowfield related or model-related. Flowfield disturbances include spatial variation of flow speed and possible secondary flows in the test section, temporal variation (“turbulence intensity”), blockage effects and streamline curvature and change in the effective angle of attack, vortical disturbances that survive the screens in the settling chamber and enter the test section, and on and on. Model-related problems are especially acute for dynamic testing. The include elastic deflections and vibrations of the model or the rig linkages, departure of actual model motion from the prescribed motion, vibrations, model surface imperfections and so forth. The list is vast and ambiguous, as indeed the recitation of problems basically speaks to aerodynamic computation and experiment in general, not just at low Reynolds number and not just for dynamic testing. The point here is not to attempt to identify flowfield features with specific factors such as drawbacks of some turbulence model or blockage in a wind tunnel, but rather to note that the present case, where the effective angle of attack just slightly exceeds the static stall angle of the SD7003 airfoil, is very sensitive to “transition” in general. If one wishes to optimize for flapping-wing cruising propulsion, say, and it is important to capture the aerodynamic coefficient time history quantitatively, then RANS-type computations and ground-facility tests would alike require great care. This is in marked contrast with the deep-stall case in the previous chapter.

However, the meaning of turbulence can be subtle; smaller free-stream turbulence leads to larger separation, and inside the larger separated flowfield structure the turbulent kinetic energy can be larger than in the smaller one. As a rough comparison, contours of 2D turbulent kinetic energy from two AFRL PIV data sets, both at the bottom of the plunge stroke, are given in Figure 4-9.

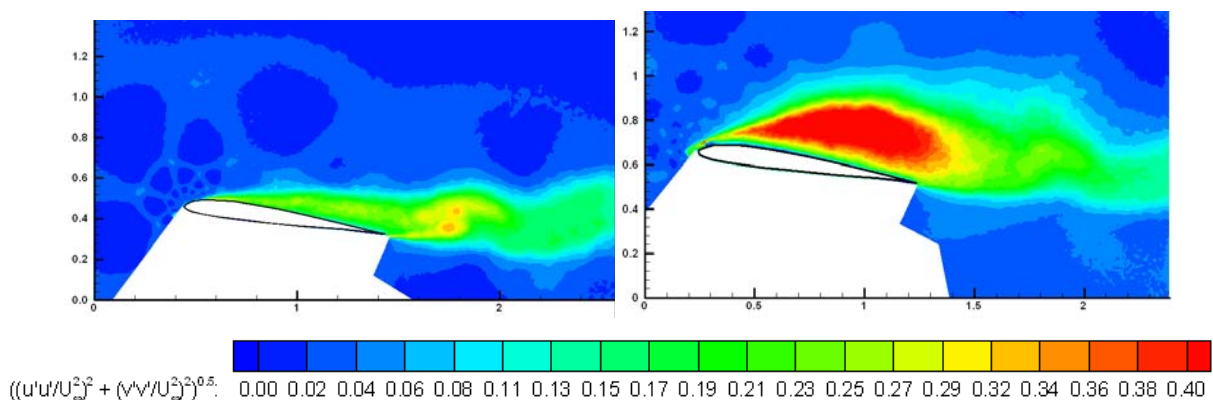


Figure 4-9: PIV-Derived Planar Turbulent Kinetic Energy Contours, AFRL Data Sets; Phase Phi = 180 (Bottom of Plunge Downstroke); “Small” Separation (left) and “Large” Separation (right).

Another potential area of concern is spanwise variations. The spanwise extent of flow separation for both the pure-plunge and pitch-plunge SD7003 cases was reported in Ol et al. [55], and indeed this has implications for the role of blockage (for experiments) and spanwise extent of the domain (for computations). But a related question, not explored in Ol et al. [55], is the extent to which the flow separation varies in going across the model span towards the tunnel wall; that is, how prominent are the sidewall effects? If the PIV light sheet is placed too close to the tunnel sidewalls, then possibly the measured flowfield will depart from that in the “core” of the test section flow. Some evidence is available from the cross-flow-plane PIV data of TU Braunschweig, where contours of streamwise velocity and normalized Reynolds stress are plotted in Figure 4-10, for the chordwise location of $x/c = 0.40$, at the bottom of the plunge downstroke. Data are taken from nearly at the tunnel test section starboard wall, towards ~ 0.45 of the airfoil span. It is evident that the region around 0.2 or 0.25 spans away from the wall is a dividing point; inboard of this region, the flow is spanwise-uniform, while outboard of this region and approach the tunnel wall, there is a spanwise variation. The implication is important for example for the AFRL experiments; since there the PIV light sheet was approximately at the $3/4$ span location, slight variations further inboard or outboard could materially affect the resulting data. This, presumably, is even more true for the more separated flow in the pure-plunge case, but unfortunately data analogous to Figure 4-10 is not available for that case.

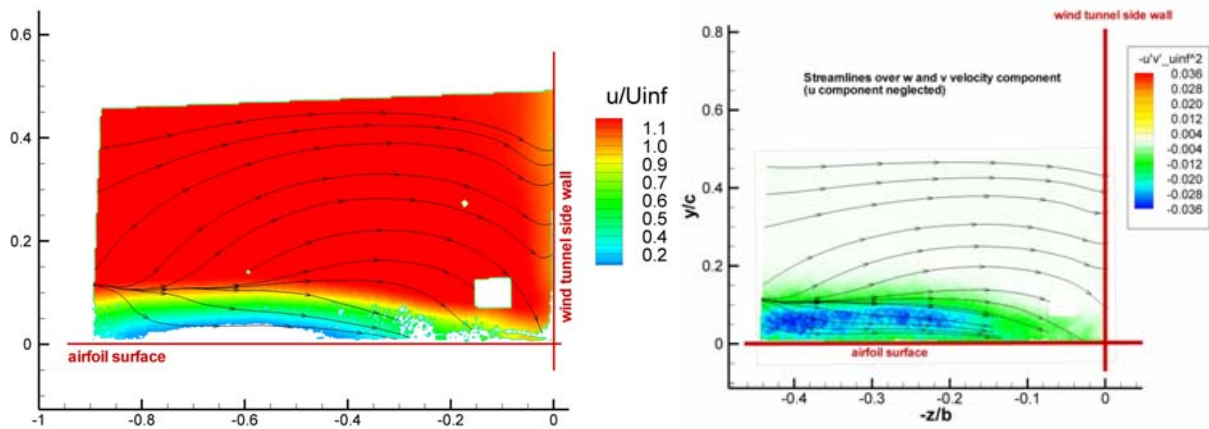
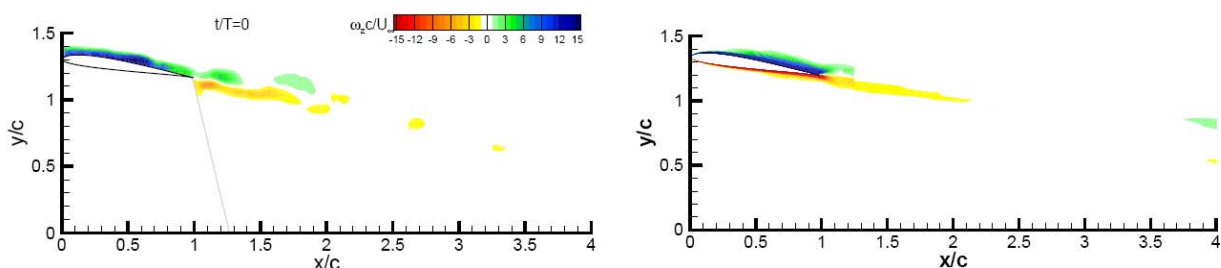


Figure 4-10: TU Braunschweig PIV; Contours of Streamwise Velocity (left) and Normalized Reynolds Stress, $-u'v'$ (right), at Motion Phase of 180 Degrees (Bottom of Plunge Downstroke); Chordwise Location $x/c = 0.40$.

4.2 REYNOLDS NUMBER EFFECTS

As for the pure-plunge case presented in the previous chapter, we consider Reynolds numbers below 60 K. Such an assessment is even more important for the lower total effective angle of attack case considered presently, because presumably natural transition effects should be less overwhelmed by high pressure gradients at the leading edge, caused by the airfoil motion. At $Re = 30$ K we again consider vorticity contour plots for the Darmstadt PIV vs. RANS comparison (Figure 4-11), with contour levels -15 to +15.



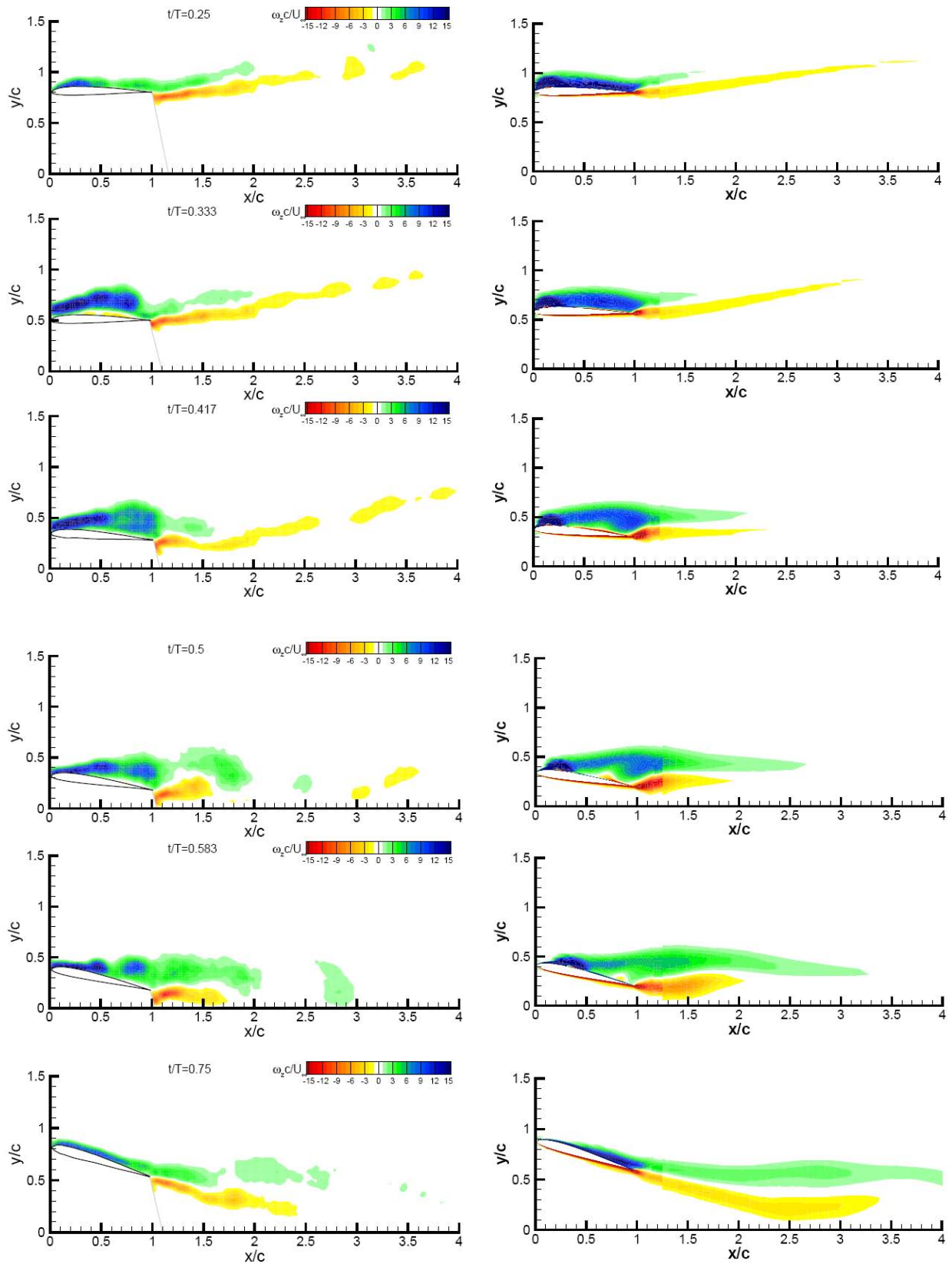


Figure 4-11: TU Darmstadt PIV (left column) and CFD (right column) Vorticity Contours; Phases of Motion $\Phi = 0, 90, 120, 150, 180, 210$ and 270 ; $Re = 30 K$; Contour Levels -15 to +15.

COMBINED PITCH-PLUNGE OF THE SD7003 AIRFOIL

Next we compare the series of RANS computations from the University of Michigan (Figure 4-12) and Middle East Technical University (Figure 4-13), for phases $\phi = 90$ and 180 , at $Re = 60$ K, 30 K and 10 K. In all cases there is a general trend towards larger flow separation at lower Re . This is confirmed by the AFRL water tunnel dye injection results, which were timed to find the “small” separation at $Re = 60$ K (Figure 4-14).

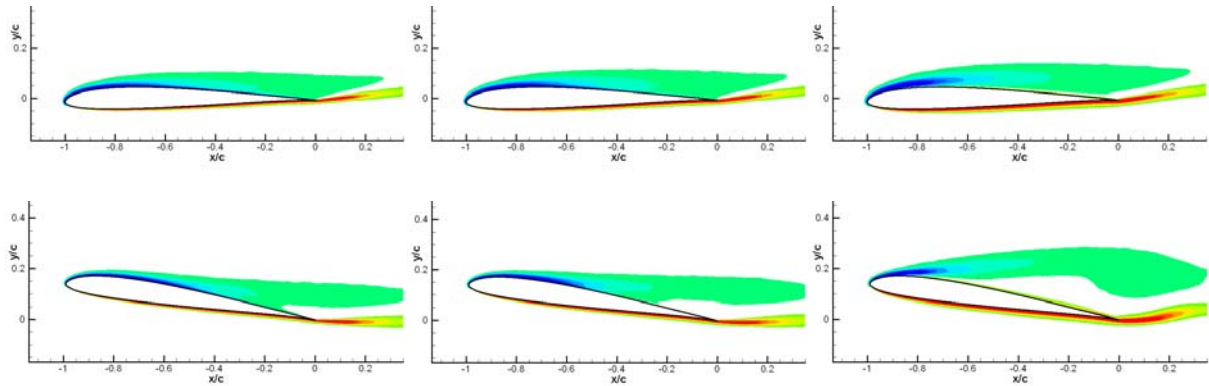


Figure 4-12: University of Michigan Computations; Phases $\Phi = 90$ (top row) and 180 (bottom row); $Re = 60$ K (left column), 30 K (middle column) and 10 K (right column).

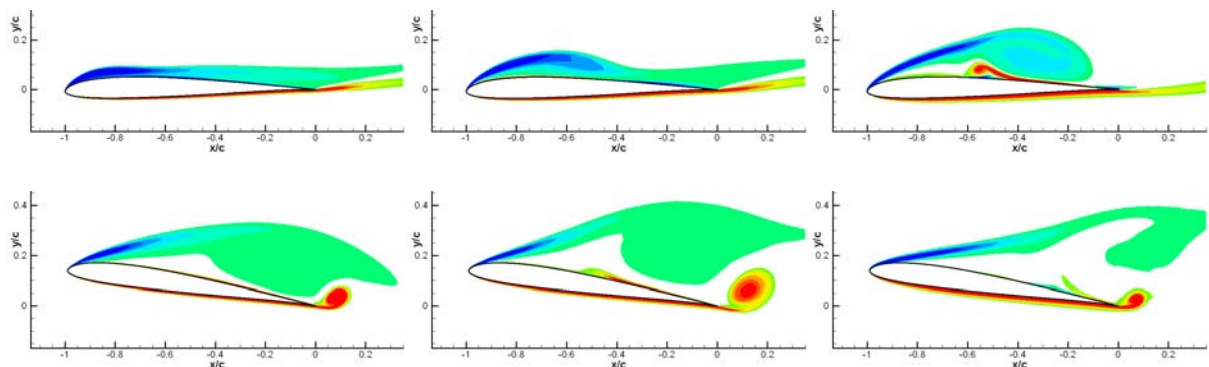
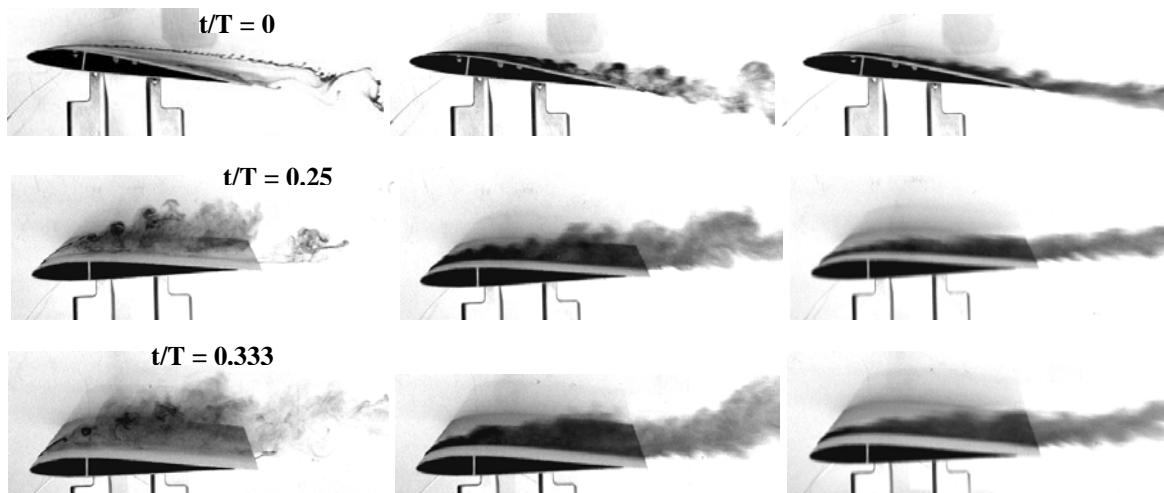


Figure 4-13: Middle East Technical University Computations; Phases $\Phi = 90$ (top row) and 180 (bottom row); $Re = 60$ K (left column), 30 K (middle column) and 10 K (right column).



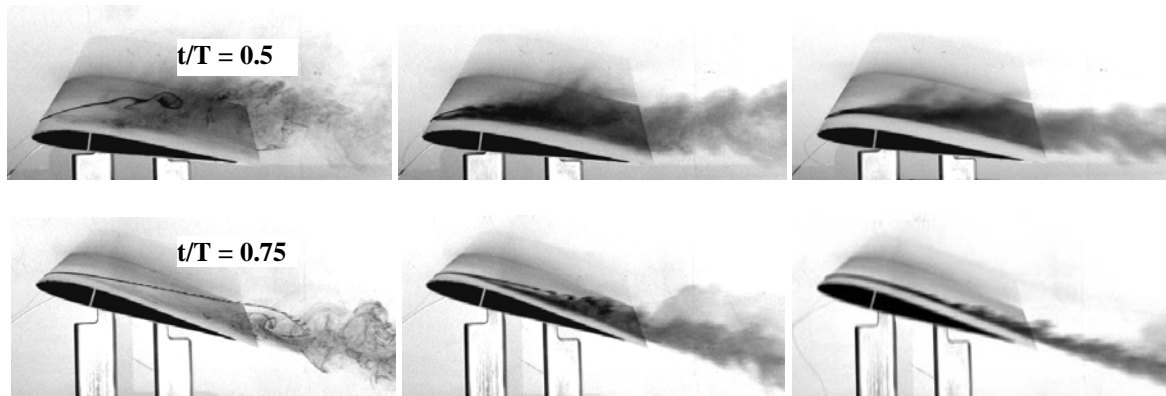


Figure 4-14: AFRL Water Tunnel Dye Injection; Phases $\Phi = 0, 90, 120, 180$ and 270 ; $Re = 10$ K (left column), 30 K (middle column) and 60 K (right column).

We next consider how the various differences in the flowfield – due to computational methods or experimental setups, and Reynolds number – translate into differences in aerodynamic force coefficients.

4.3 AERODYNAMIC FORCE COEFFICIENTS

As with the pure-plunging case, we are interested in comparing the flowfield evolution history with the aerodynamic coefficient time history, again principally the lift. Lift coefficient, plotted vs. motion phase and vs. effective angle of attack, is given in Figure 4-15, while drag is shown in Figure 4-16. Once again, the quasi-steady approximation and Theodorsen's formula are the simplest models, followed by the vortex-particle method, then by the two RANS computations, from the University of Michigan and METU, and finally by the LES computation (NRC).

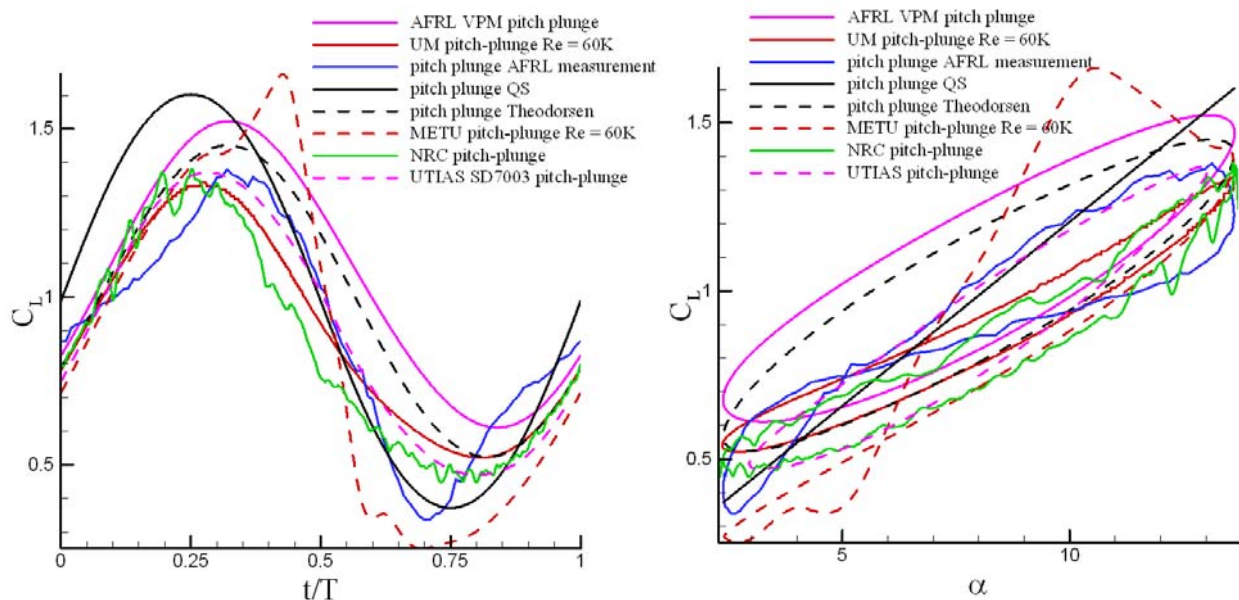
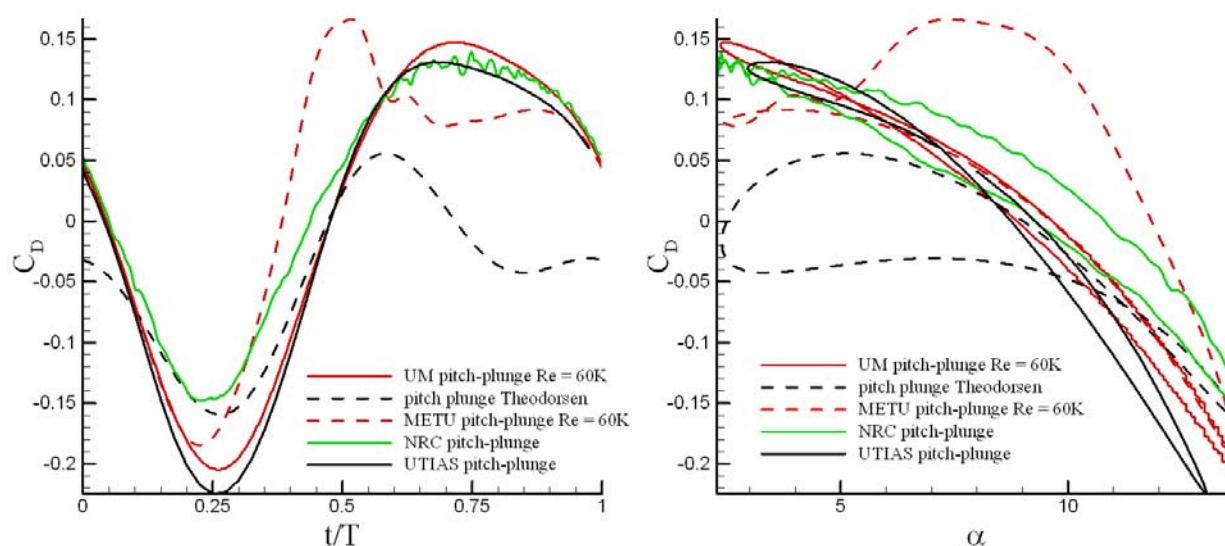


Figure 4-15: Lift Coefficient Time History, SD7003 Pitch-Plunge; $Re = 60$ K; Plotted vs. Motion Phase (left) and Effective Angle of Attack (right).



**Figure 4-16: Drag Coefficient Time History, SD7003 Pitch-Plunge; Re = 60 K;
Plotted vs. Motion Phase (left) and Effective Angle of Attack (right).**

With this large of a spread in data, it is difficult to make a statement about method complexity vs. method accuracy, to the level possible with the pure-plunge case. Nevertheless, one can make some qualitative observations. Comparing the two RANS computations, we find that indeed the more “laminar like” (METU) predicts stronger vortical effects on $C_L(t)$, than does the more “turbulent like” (UM). The UM RANS computation and the NRC LES are quite close, and the AFRL experiment is not far from the two. Theodorsen over-predicts lift in $t/T < 0.25 < 0.75$, and interestingly enough, the Theodorsen prediction appears *worse* for pitch-plunge than for pure-plunge!

The UTIAS lumped-vortex and AFRL VPM are conceptually close, but the UTIAS result tracks closer with what might be termed the average lift time history, evidently because it has a static and dynamic stall model, whereas the AFRL vortex particle method is a classical attached-flow approach. This probably also explains why the UTIAS method appears to perform well in drag prediction (Figure 4-16); it tracks very closely with the UM RANS, which of course is conceptually an entirely different approach. The NRC 2D LES predicts a lower thrust at $t/T \sim 0.25$, evidently due to the larger predicted separation. Contrary to the pure-plunge case discussed in the previous chapter, Theodorsen’s formula is fairly successful in at least qualitative prediction of the drag coefficient history, except late in the motion upstroke, where evidently turbulent skin friction drag is main cause of discrepancy.

We next consider dependency of lift and drag with Reynolds number (Figure 4-17), again comparing three RANS computations (UM, METU and TUD). Unlike the pure-plunge case, reduction in Re from 60 K to 30 K to 10 K does show significant changes in lift and drag and significant scatter between the computations.

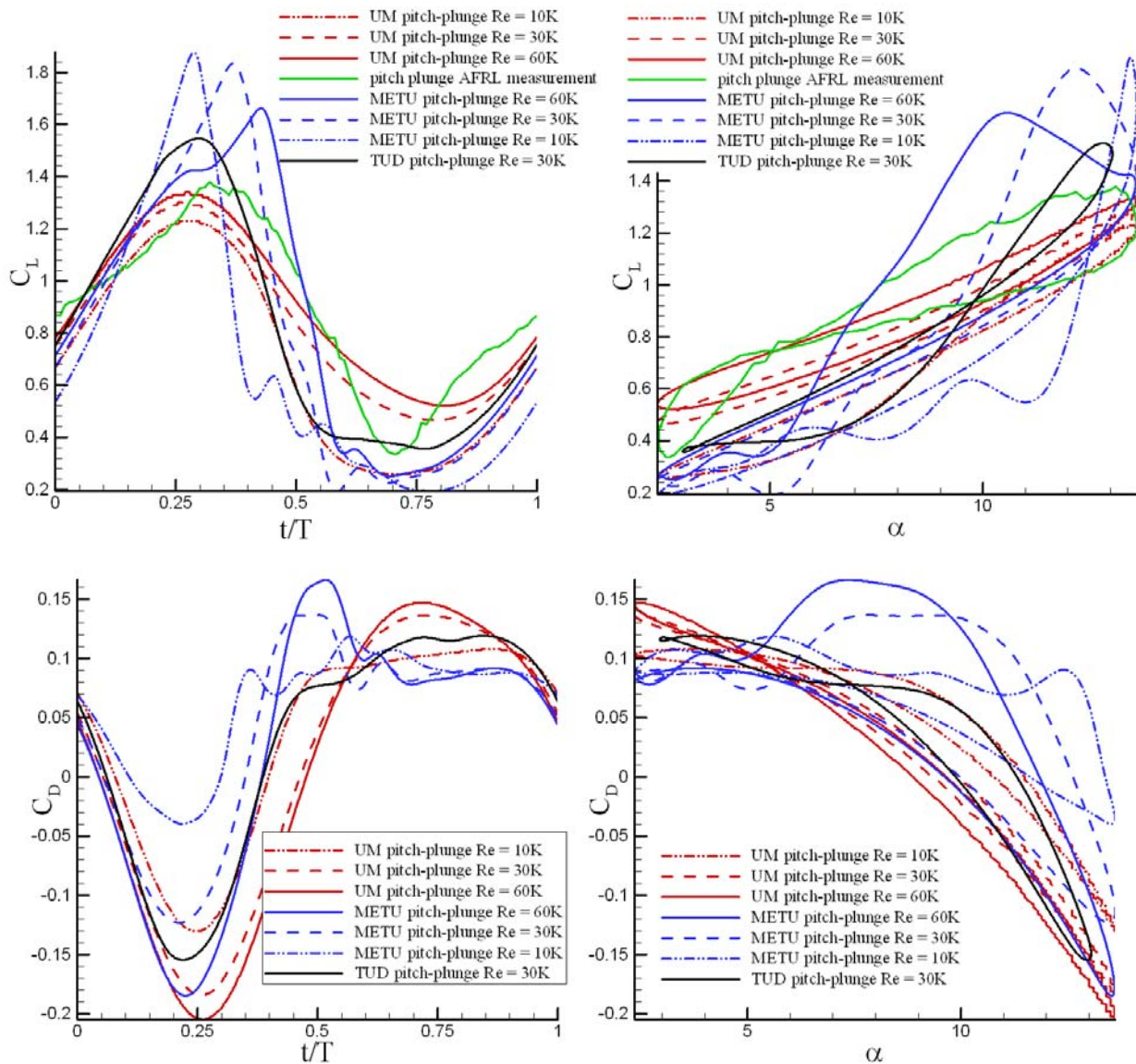


Figure 4-17: Trends in Lift Coefficient (top row) and Drag Coefficient (bottom row) for SD7003 Pitch-Plunge vs. Reynolds Number (60 K, 30 K and 10 K).

As with the pure-plunge case, we compare the “standard” and “modified” UM RANS with the METU RANS, to assess the significance of implementation of nominally the same turbulence model. Again, the “modified” version of the UM computation agrees very closely with the METU computation. But unlike the pure-plunge case, the respective differences are qualitatively significant, and are not merely wiggles here and there. This, in the shallow-stall case even more caution is required in turbulence model implementation than in the deep-stall case. As we shall see in the next chapter, the differences between the various results are significantly attenuated when there is a forcing of separation (and presumably transition) due to sectional geometry, as we turn to the case of a flat plate of round leading edges.

COMBINED PITCH-PLUNGE OF THE SD7003 AIRFOIL

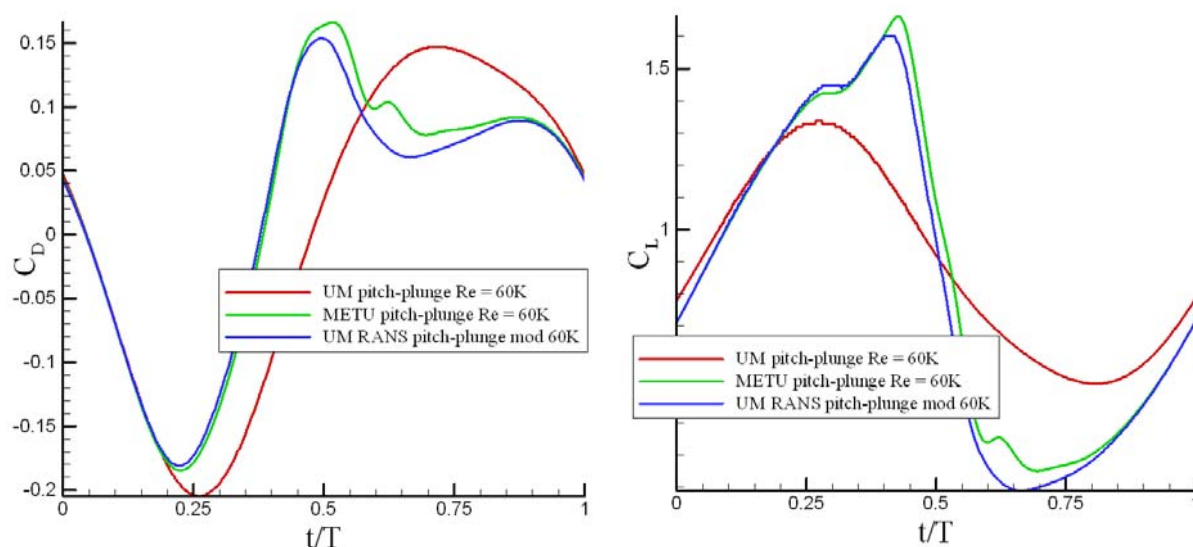


Figure 4-18: Lift Coefficient (left) and Drag Coefficient (right) Comparison Between METU and Standard vs. Modified UM RANS.

The pitch-plunge case was selected not only to explore effects of Reynolds number, transition, turbulence models, facility flow quality and so forth – but to consider a case suitable for propulsive flapping-wing flight, in the sense of flight of large birds, as discussed in Chapter 1. Does the subject motion indeed produce net thrust, where Garrick-type propulsion from leading edge suction [27] overcomes friction and pressure (laminar separation bubble, separated wake) drag? The findings are summarized in Table 4-1. Unfortunately there are no experimental results for drag, but all of computations that solve the Navier-Stokes equations predict a net drag. The UM RANS at $Re = 60\text{ K}$ comes close to net zero drag, and possibly at slightly higher Reynolds number there would be a net thrust. It appears, therefore, that even at $Re = 60\text{ K}$ the motion studied here is not net-propulsive because viscous effects overwhelm leading edge suction.

Table 4-1: Mean Lift and Drag Coefficients for SD7003 Pitch-Plunge

Data Set	Mean C_L	Mean C_D
UM RANS $Re = 10\text{ K}$	0.694	0.032
UM RANS $Re = 30\text{ K}$	0.839	0.011
UM RANS $Re = 60\text{ K}$	0.894	0.004
METU RANS $Re = 60\text{ K}$	0.856	0.022
METU RANS $Re = 30\text{ K}$	0.801	0.038
METU RANS $Re = 10\text{ K}$	0.682	0.061
NRC LES	0.849	0.023
UTIAS	0.882	-0.008
TUD RANS $Re = 30\text{ K}$	0.821	0.028
Theodorsen	0.985	-0.046

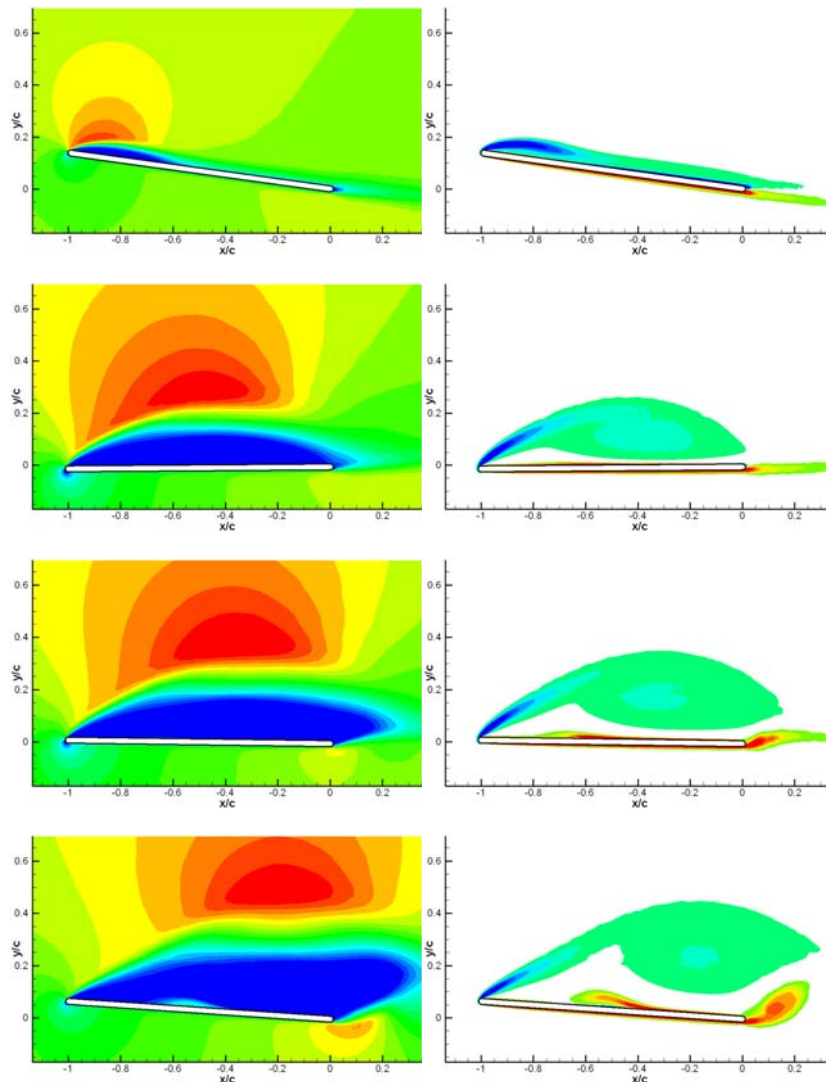
Chapter 5 – PLUNGE AND PITCH-PLUNGE OF A FLAT PLATE

Here our objective is to assess the role of sectional geometry, by comparing a flat plate with the SD7003 airfoil. The canonical Reynolds number remains at 60000, and the kinematics of motion are the same as in the prior two chapters.

5.1 RESUME OF EXPERIMENTAL AND COMPUTATIONAL RESULTS FOR THE FLOWFIELD: VELOCITY AND VORTICITY

5.1.1 Computations, Pitching-Plunging Plate

RANS computations were run by the University of Michigan (Figure 5-1) and Middle East Technical University (Figure 5-2). Clearly there is less difference in the velocity and vorticity contours for these two computations for the flat-plate, than there were for the corresponding SD7003 case.



PLUNGE AND PITCH-PLUNGE OF A FLAT PLATE

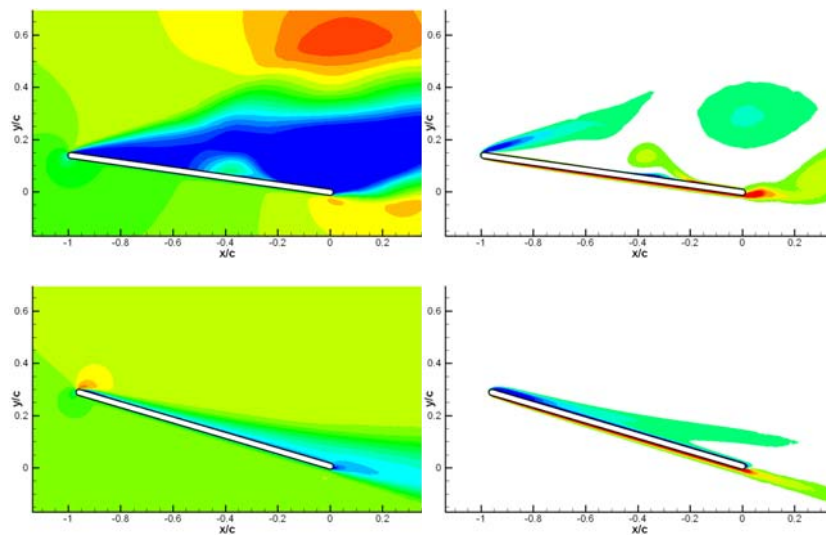
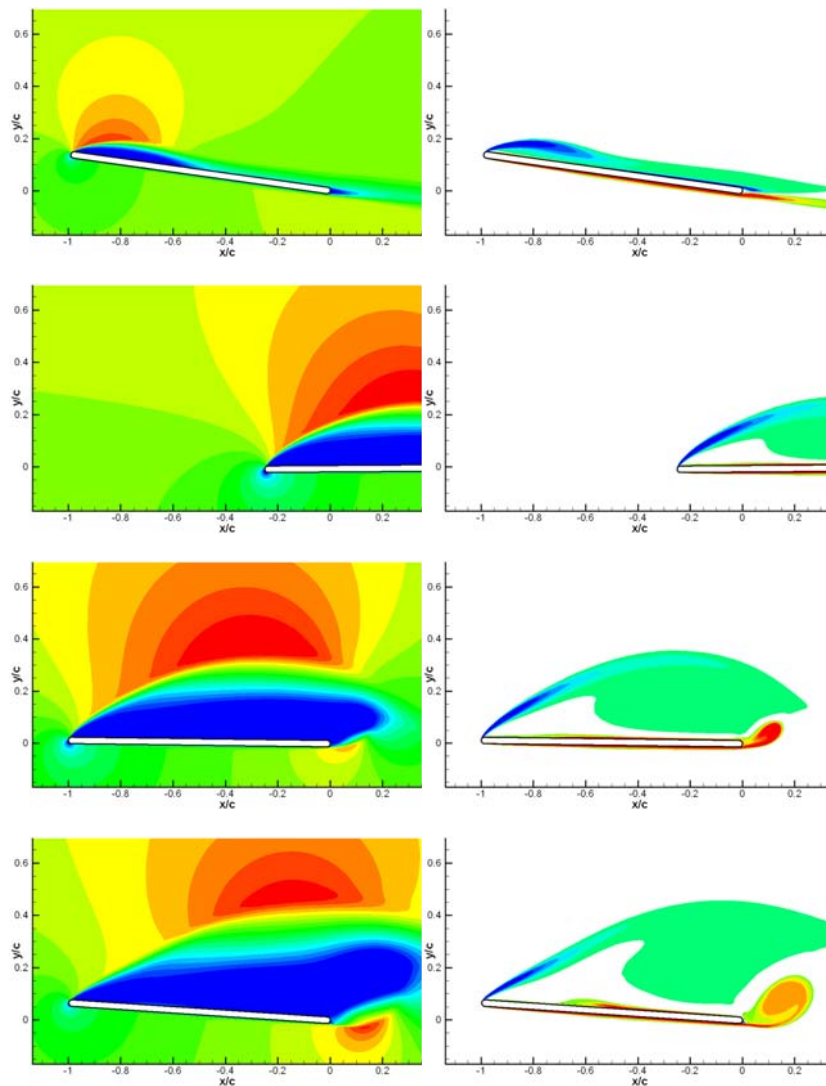


Figure 5-1: University of Michigan Computations; Phases $\Phi = 0, 90, 120, 150, 180$ and 270 .



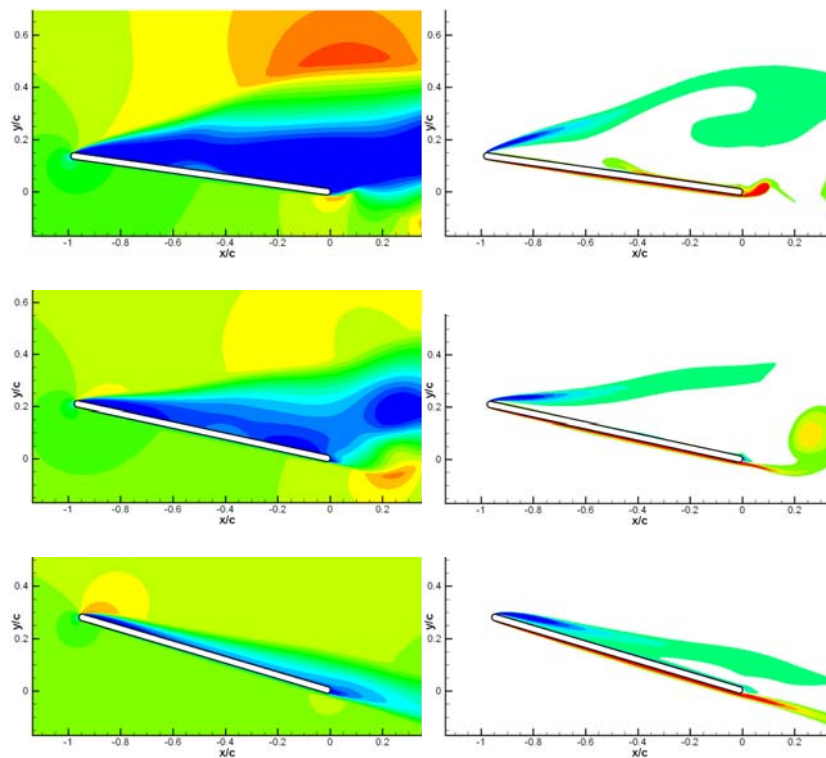
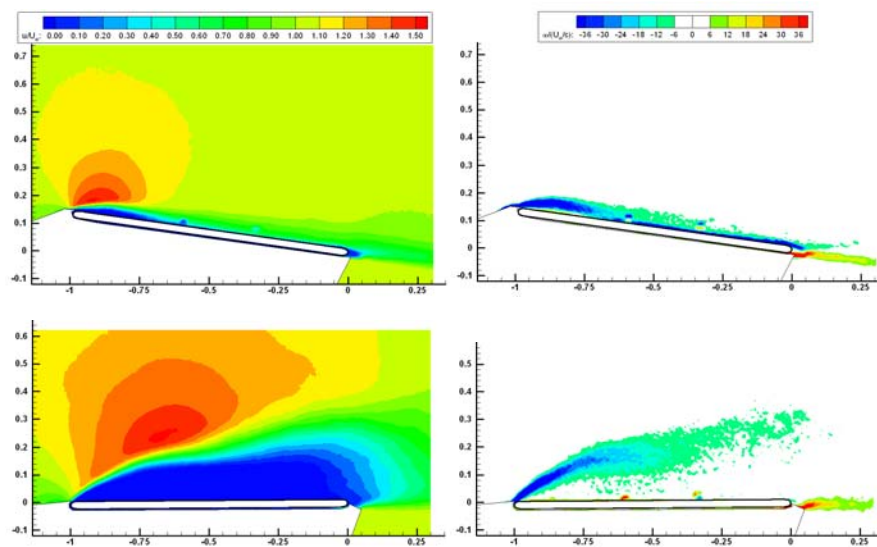


Figure 5-2: Flat-Plate Pitch-Plunge, METU Computations, Fluent, 2D; Phases $\Phi = 0, 90, 120, 150, 180, 210$ and 270 .

5.1.2 Experiments, Pitching-Plunging Plate

Experiments were limited to water tunnels: AFRL (Figure 5-3) and University of Michigan (Figure 5-4).



PLUNGE AND PITCH-PLUNGE OF A FLAT PLATE

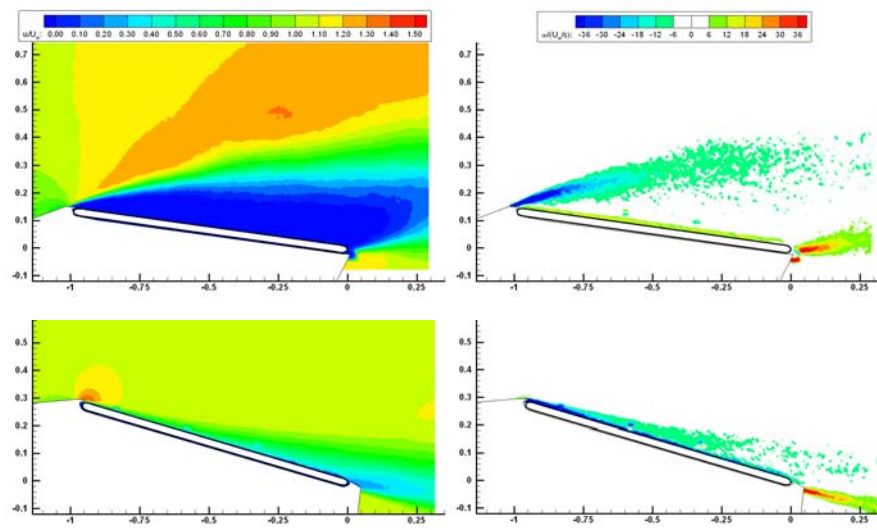


Figure 5-3: AFRL Water Tunnel; Phases $\Phi = 0, 90, 180$ and 270 .

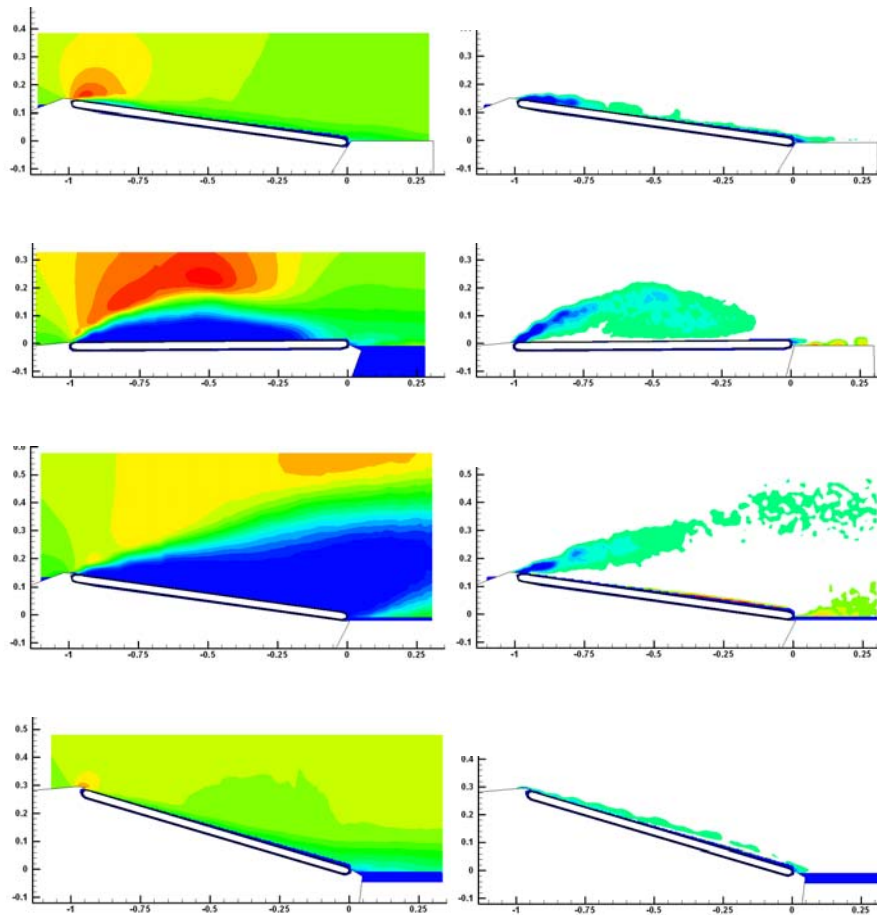


Figure 5-4: University of Michigan Water Tunnel; Phases $\Phi = 0, 90, 180$ and 270 .

5.2 REYNOLDS NUMBER EFFECTS

The flat-plate is much less sensitive to Reynolds number than is the SD7003 airfoil, because the plate's leading edge essentially forces transition, and because the plate has a very narrow range of angle of attack over which flow remains fully attached in the static case. This assertion is essentially confirmed in the dye injection survey at $Re = 20\text{ K}$ and 60 K in Figure 5-5.

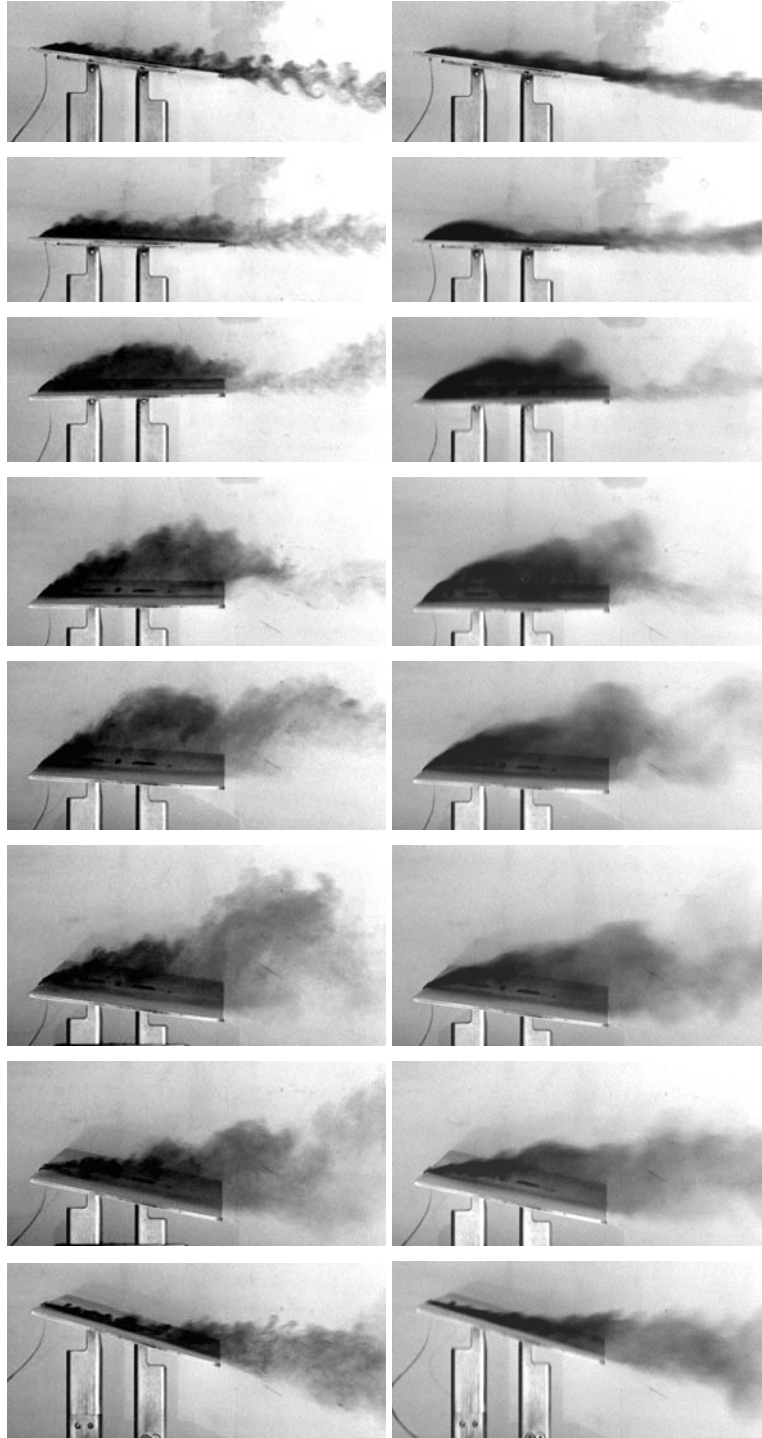
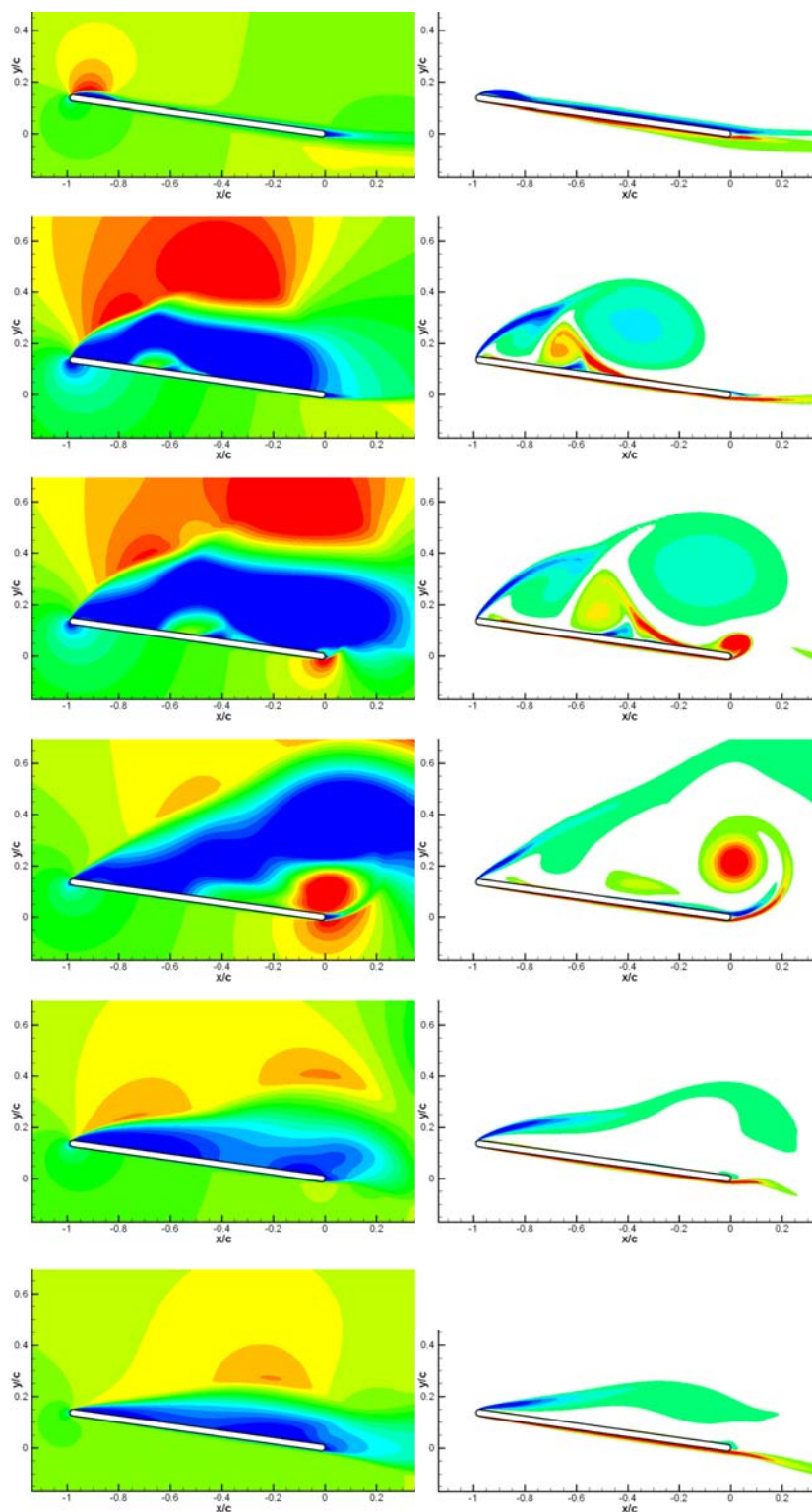


Figure 5-5: AFRL Water Tunnel Dye Injection for Pitching-Plunging Flat Plate; Phases $\Phi = 0, 45, 90, 120, 150, 180, 210$ and 270 ; $Re = 20\text{ K}$ (left column) and $Re = 60\text{ K}$ (right column).

5.2.1 Computations, Plate in Pure-Plunge

Computations for the wall-to-wall plate in pure-plunge were pursued by METU (Figure 5-6) and UM (Figure 5-7). The similarity between the two is quite close, and is much closer than for the SD7003 airfoil executing the same motion at the same Re .



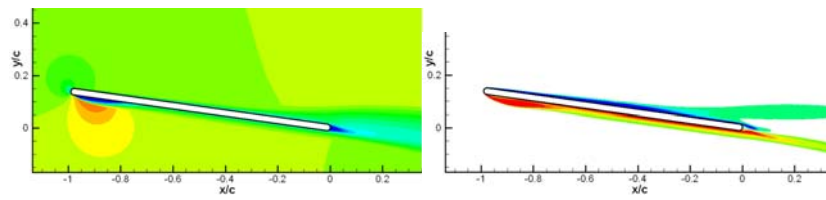
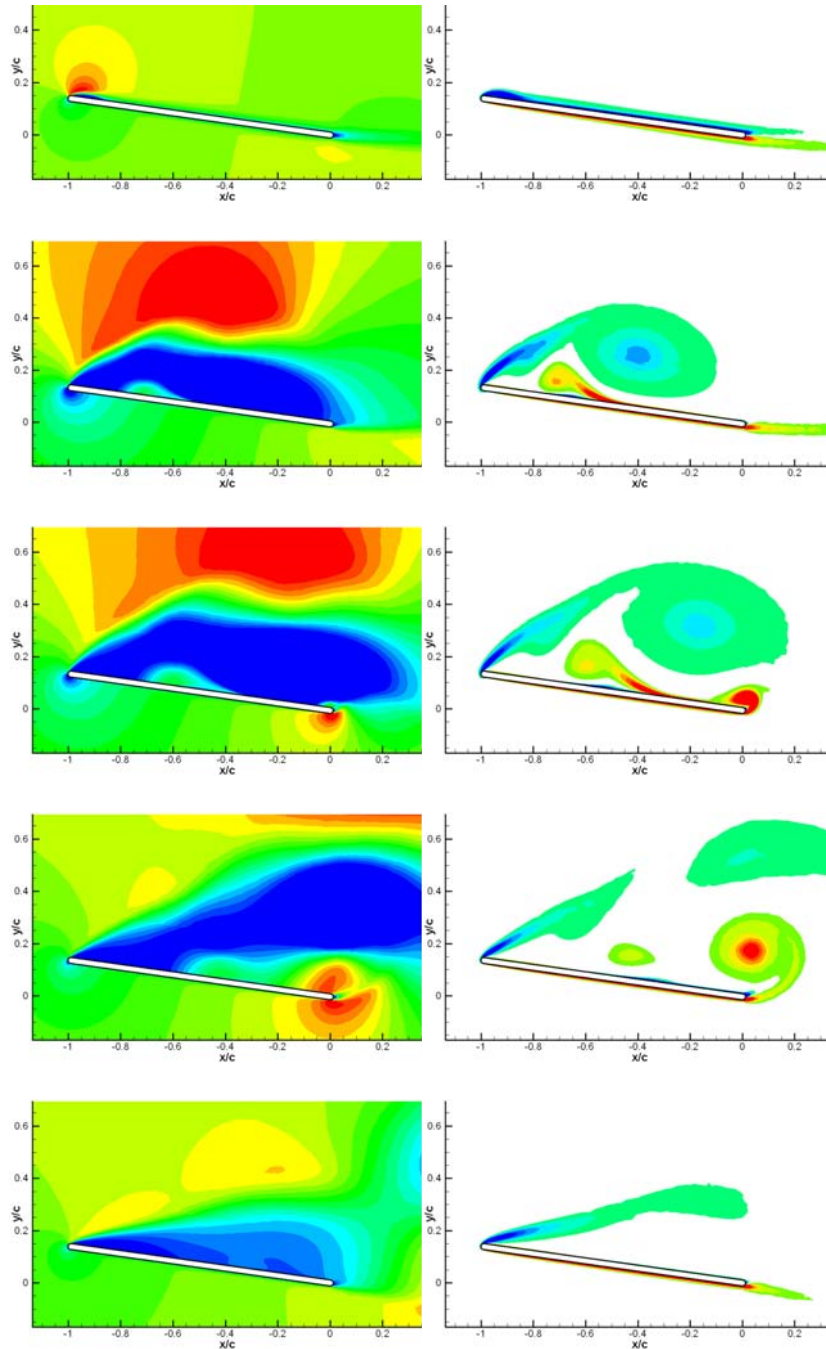


Figure 5-6: Flat-Plate Plunge, METU Computations, Fluent, 2D; Phases $\Phi = 0, 90, 120, 150, 180, 210$ and 270 .



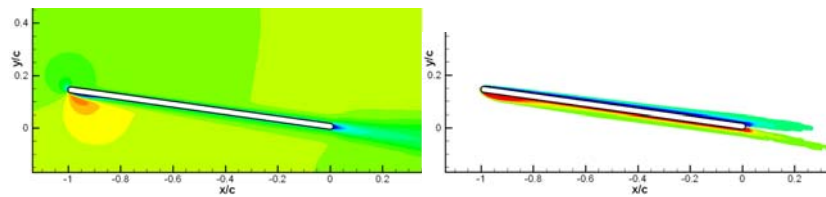


Figure 5-7: University of Michigan Computations, Wall-to-Wall Plunging Flat Plate; Phases $\Phi = 0, 90, 120, 150, 180$ and 270 .

5.2.2 Experiments, Plate in Pure-Plunge

Unfortunately only one series of experiments for the wall-to-wall plate in pure-plunge was available – from the University of Michigan water tunnel (Figure 5-8). As compared to experiments in the same facility for the SD7003 airfoil in pure-plunge, the differences are not great; the flat-plate LEV is somewhat larger and more diffuse than for the airfoil, and the low-speed region on the suction side towards the bottom of the downstroke persists less.

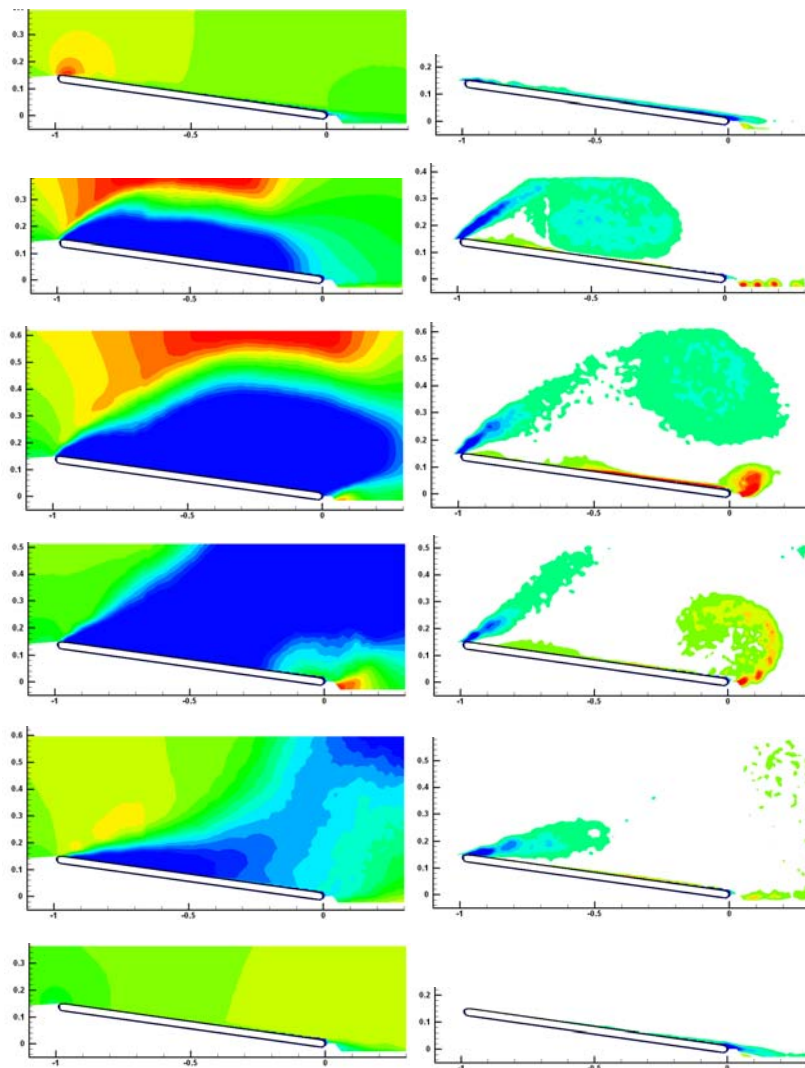


Figure 5-8: University of Michigan PIV, Wall-to-Wall Plunging Flat Plate; Phases $\Phi = 0, 90, 120, 150, 180$ and 270 .

5.3 AERODYNAMIC FORCE COEFFICIENTS FOR THE FLAT PLATE

5.3.1 Pure-Plunge

Following experience with the SD7003 airfoil in pure-plunge, we expect at most moderate variation in force coefficient time history amongst the various methods, at least for lift. Indeed, in Figure 5-9 the two RANS computations are very close. No LES for the flat-plate in pure-plunge was available, but simply reprinting the AFRL 3D LES result for the plunging SD7003 shows close tracking with the two plate RANS results. It is possible, in fact, the RANS is over-predicting the dynamic stall peak ($t/T \sim 0.25$). That said, the quasi-steady result is quite accurate on the downstroke, while Theodorsen is more accurate on the upstroke, respectively.

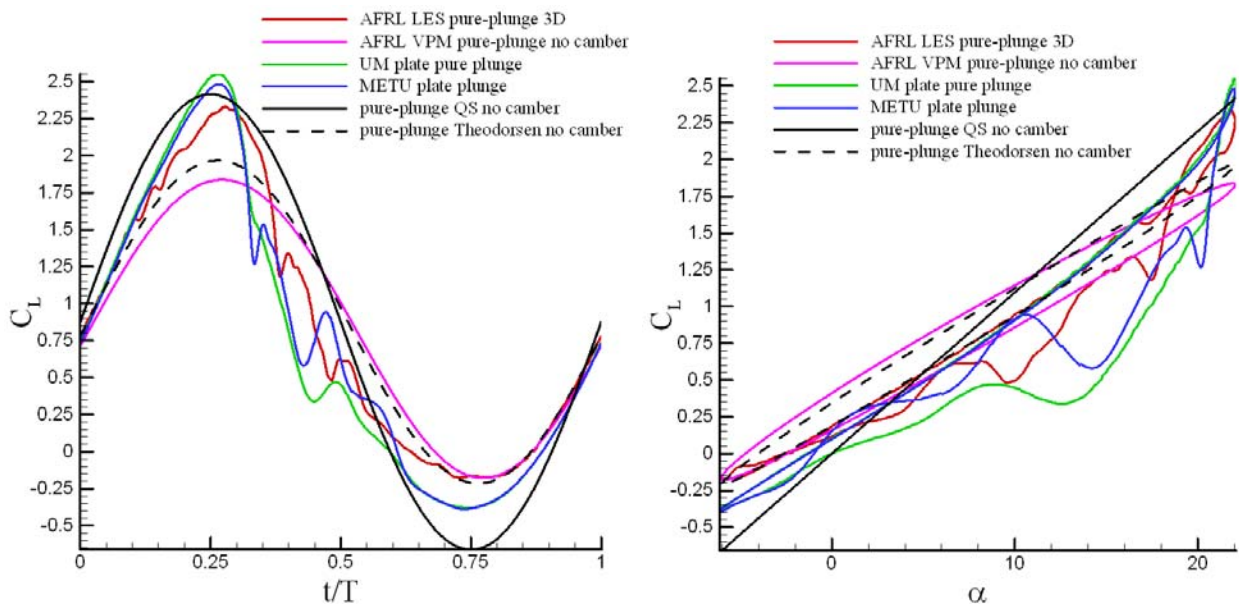


Figure 5-9: Lift Coefficient History for the Flat Plate in Pure-Plunge, Plotted vs. Time (left) and Angle of Attack (right). Theodorsen and quasi-steady calculations have camber removed and the AFRL LES is a reprint of the respective SD7003 result.

Trends for drag are shown Figure 5-10. Again the two RANS computations are very close, and both are close to the SD7003 LES from $t/T \sim 0.3$ onward.

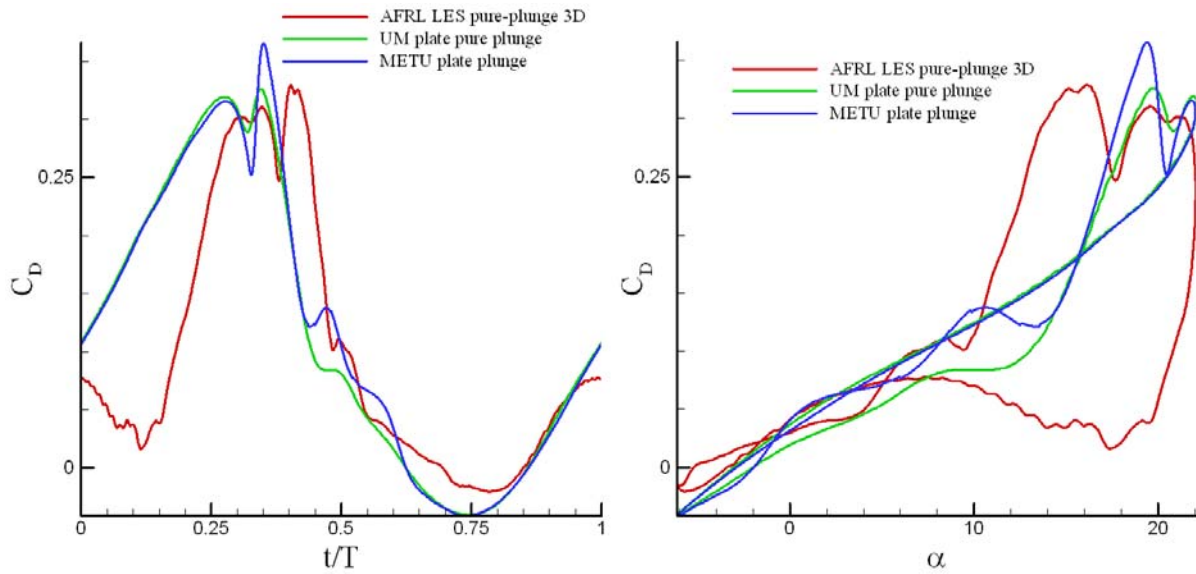


Figure 5-10: Drag Coefficient History for the Flat Plate in Pure-Plunge, Plotted vs. Time (left) and Angle of Attack (right) – The AFRL LES is a Reprint of the Respective SD7003 Result.

5.3.2 Pitch-Plunge

Finally we consider aerodynamic force coefficients for the wall-to-wall flat plate in pitch-plunge; that is, $\lambda = 0.6$: lift (Figure 5-11) and drag (Figure 5-12). For this case, one LES computation is available, from NRC, in 2D. Interestingly enough, the LES tracks very closely with the vortex particle method solution and Theodorsen. The quasi-steady solution, as usual, over-estimates lift at both crest ($t/T = 0.25$) and trough ($t/T = 0.75$). The two RANS computations, METU and UM, are very close, and predict much stronger lift peak due to the LEV and loss of lift as the LEV sweeps downstream away from the plate suction side.

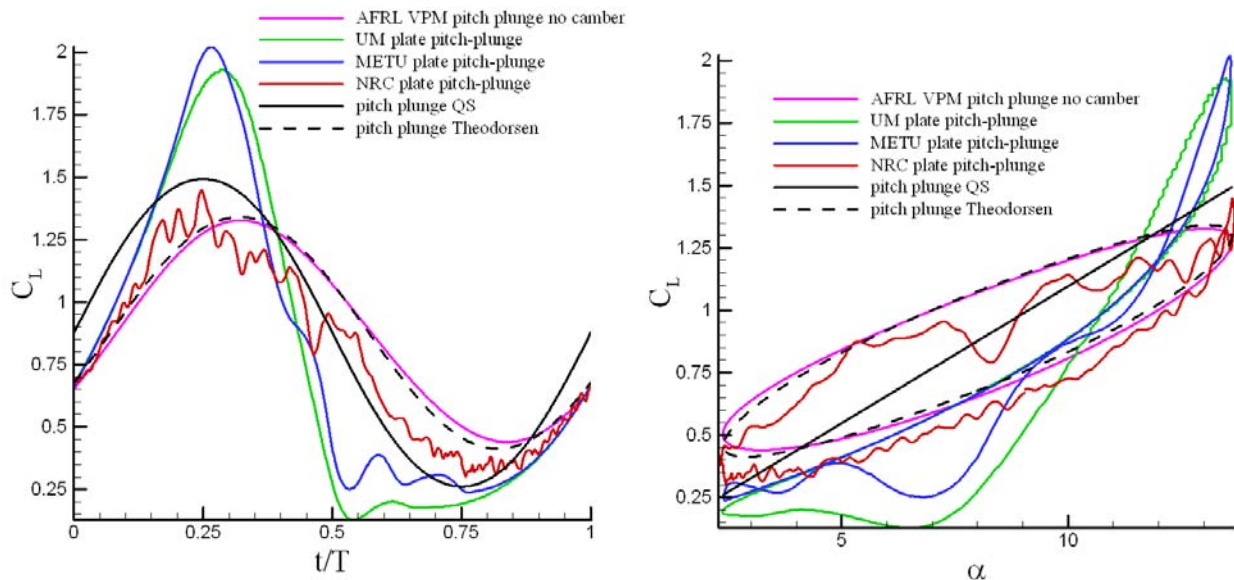


Figure 5-11: Lift Coefficient History for the Flat Plate in Pitch-Plunge, Plotted vs. Time (left) and Angle of Attack (right) – Theodorsen and Quasi-Steady Calculations have Camber Removed.

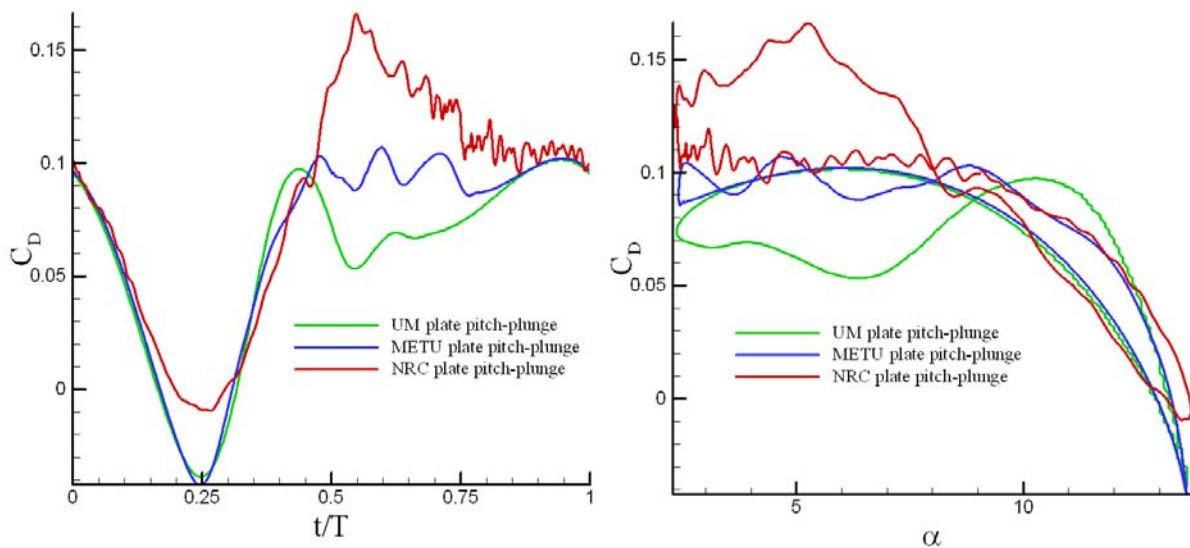


Figure 5-12: Drag Coefficient History for the Flat Plate in Pitch-Plunge, Plotted vs. Time (left) and Angle of Attack (right).

In drag, we are as usual left with the viscous-only methods, and unfortunately experimental data is not available. The two RANS results are again very close, and only deviate from the LES significantly at the start of the upstroke. As compared with the pitching-plunging airfoil, the drag trough at $t/T \sim 0.25$ is much less acute for the flat-plate, consistent with the separation on the suction side being more severe.

Finally, it is worth mentioning a word on the RANS solutions for the flat plate, especially since RANS is the most common computational scheme for these sorts of problems. Whatever the differences of turbulence modelling, production and dissipation between the METU and UM RANS approaches, these differences are essentially moot for the flat plate with round leading edge, evidently because this leading edge is strongly forcing towards transition. That is, it may be premature to claim with treatment of turbulence is “better” in which code, and in which circumstance – but one can observe that whatever the various differences may be, the upshot is essentially no difference for strongly forced flows. It is likely, further, that if we were to run a parameter study on k and kh , and looked at more violent motions, then the differences between the various approaches would be even smaller. This idea is pursued, if only episodically, in a subsequent chapter. But first we turn to finite-span effects, retaining the same sectional shape (thin flat plate with round edges), but now at $AR = 2$.

PLUNGE AND PITCH-PLUNGE OF A FLAT PLATE



Chapter 6 – FINITE ASPECT RATIO EFFECTS: PLUNGE AND PITCH-PLUNGE OF AN ASPECT RATIO 2 FLAT PLATE

6.1 MOTIVATIONS AND PROBLEM DEFINITION

Perhaps the most natural generalization from wall-to-wall models (in experimental facilities) and spanwise-periodic boundary conditions (in computations) is the finite-wing of high aspect ratio. By systematically reducing aspect ratio from some large but finite value, towards ever smaller values, it is possible to construct a consistent passage into 3D from 2D. This is sensible, for example, in terms of understanding the flapping-flight of large birds (see Chapter 1), which tend to be of high aspect ratio. However, in an experimental facility this introduces the problem of blockage or very low Reynolds number. To avoid blockage, the wingspan needs to be some fraction of the test section width, and at high aspect ratio this severely limits the chord. In turn the Reynolds number, based on chord, becomes very low. But very low Reynolds number problems, besides being inconsistent with the focus of earlier chapters, tend to be of comparatively low aspect ratio, as is the case for most insects. In computation, full resolution of high aspect ratio means a grid much longer in the spanwise than in the streamwise direction, which raises problems of computational size, if we wish to maintain high resolution in the streamwise direction.

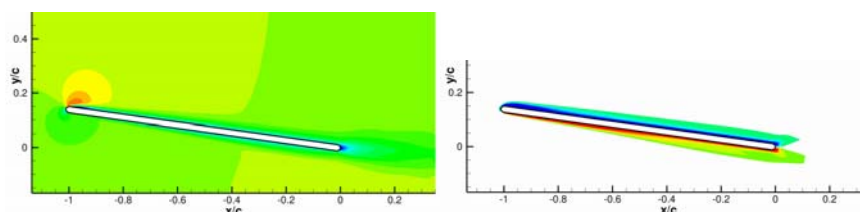
The alternative is to consider low aspect ratios. This is more amenable to investigation, but more importantly, it is especially interesting because of the strong interaction expected at low aspect ratio between leading edge vortices and wingtip vortices, where for example the latter might stabilize the former through spanwise pressure gradients. Low aspect ratio wings undergoing various longitudinal-plane manoeuvres are expected to evince a qualitatively different flow structure and loads time history from those of the same sectional geometry, but in 2D. A full treatment of the problem requires detailed 3D velocimetry, which unfortunately is beyond the scope of this study. In keeping with the above-reported results, flowfield data are presented in streamwise-parallel planes, typically at the $\frac{3}{4}$ -span location of the model. The featured configuration is the rectangular-planform flat plate of aspect ratio 2, with round edges on its entire periphery. Both the pure-plunge and the pitch-plunge case are considered. The canonical Reynolds number is now 40000 rather than the 60000 for the wall-to-wall cases, as blockage problems are reduced with a smaller model, and thus a smaller chord.

The sectional geometry of a thin flat plate with round edges was selected to deemphasize the role of boundary layer transition and to at least partially solve the problem of how to treat the airfoil section at the wingtips. Such shapes are also easy to manufacture, and in general easy to grid. Looking towards future work, they are amenable to generalization to flexible structures, such as membranes.

We begin with the pure-plunge kinematics, again considering velocity and vorticity contour plots, and load time history; then we continue with pitch-plunge.

6.2 THE PURE-PLUNGE CASE

6.2.1 Computations, AR = 2 Plate in Pure-Plunge



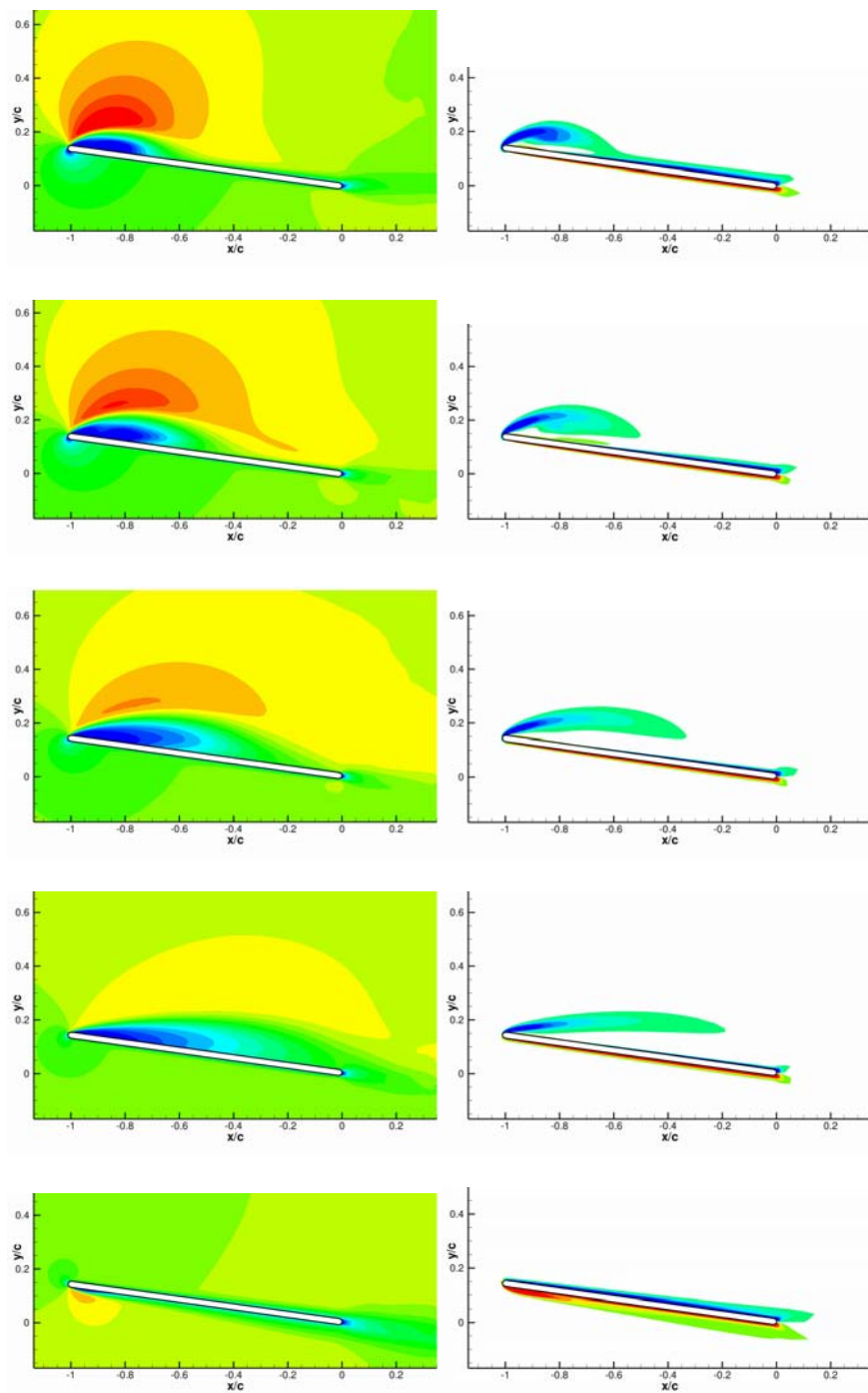


Figure 6-1: U of Michigan Computations, AR = 2 Plate in Pure-Plunge; Phases $\Phi = 0, 90, 120, 150, 180$ and 270 .

6.2.2 Experiments, AR = 2 Plate in Pure-Plunge

Experiments were run in the UM and AFRL water tunnels (Figure 6-2 and Figure 6-3, respectively), and in the U of Florida REEF wing tunnel (Figure 6-4).

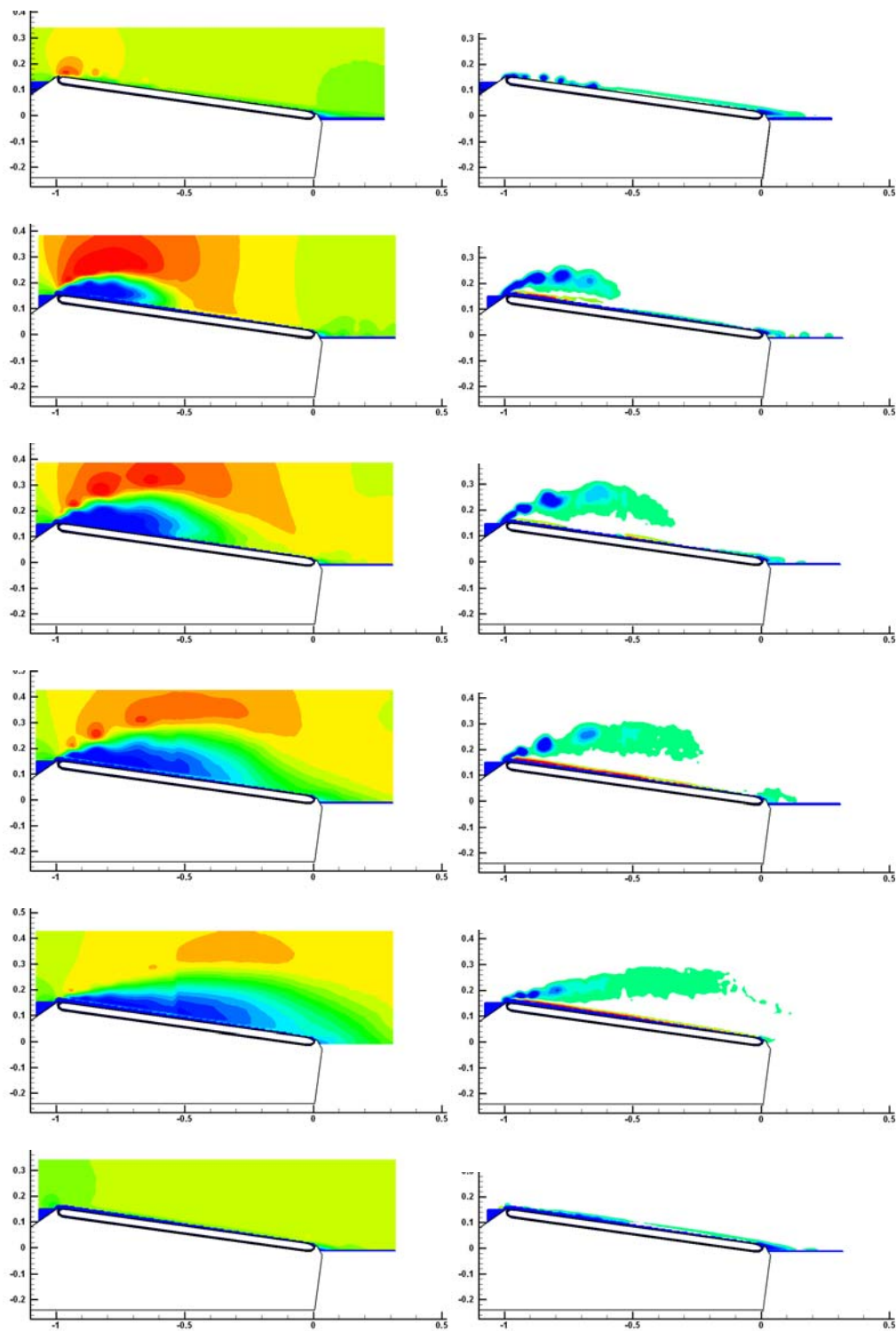
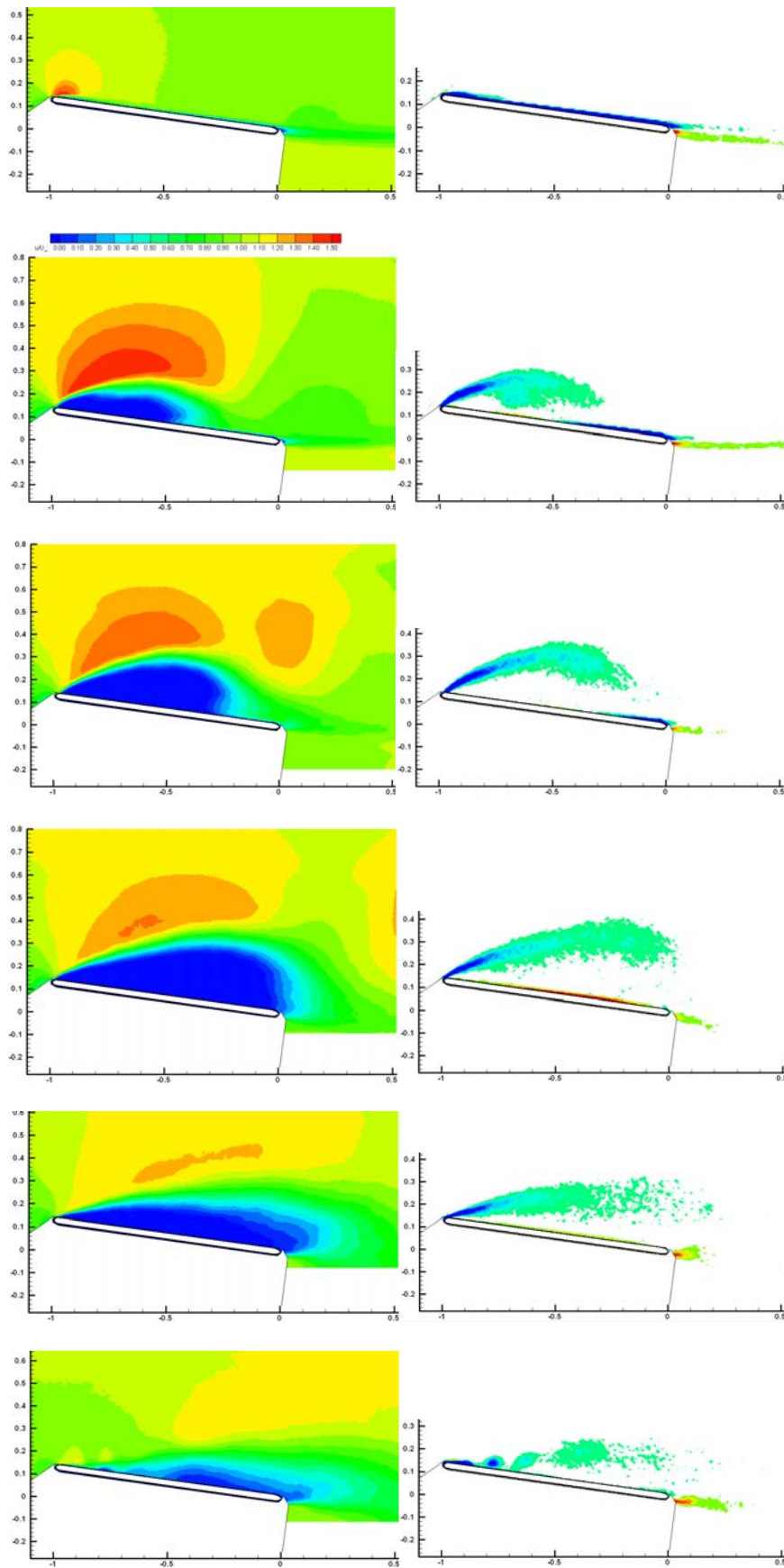


Figure 6-2: PIV, U of Michigan, AR = 2 Plate in Pure-Plunge; Phases $\Phi = 0, 90, 120, 150, 180$ and 270 .



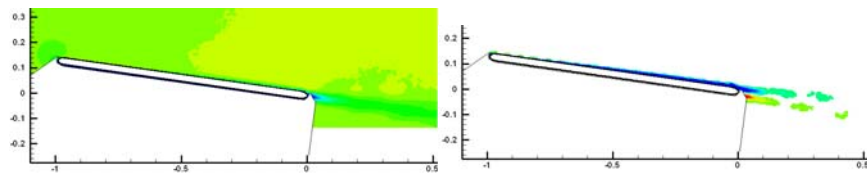


Figure 6-3: PIV, AFRL, AR = 2 Plate in Pure-Plunge; Phases $\Phi = 0, 90, 120, 150, 180, 210$ and 270 .

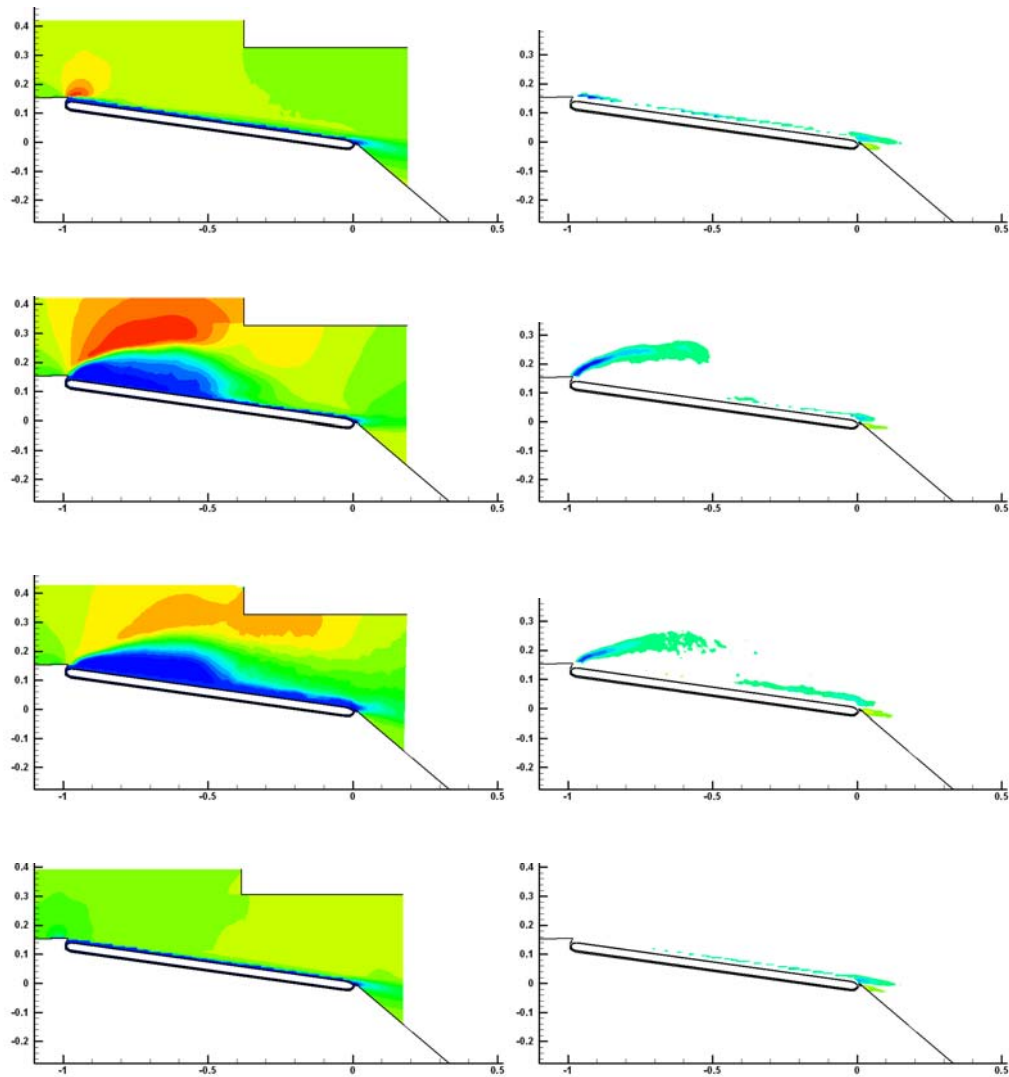


Figure 6-4: PIV, U of Florida REEF, AR = 2 Plate in Pure-Plunge; Phases $\Phi = 0, 90, 180$ and 270 .

6.3 THE PITCH-PLUNGE CASE

6.3.1 Computations, Pitching-Plunging Plate, AR = 2

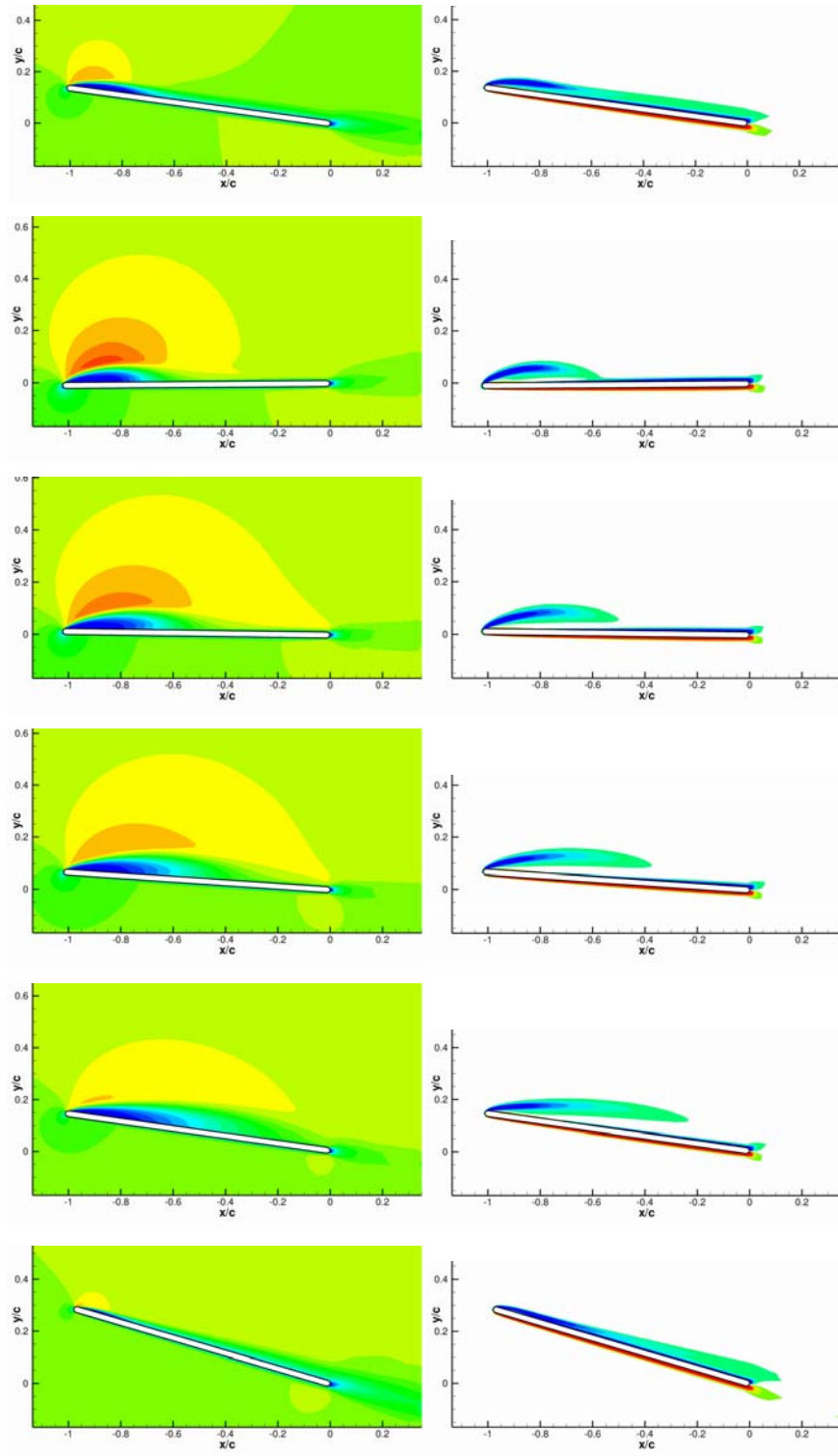


Figure 6-5: U of Michigan Computations, Pitching-Plunging
AR = 2 Plate; Phases $\Phi = 0, 90, 120, 150, 180$ and 270 .

6.3.2 Experiments, Pitching-Plunging Plate, AR = 2

Flowfield velocity and vorticity contours (PIV) were obtained from the University of Florida (Figure 6-6), AFRL (Figure 6-7), and the University of Michigan (Figure 6-8).

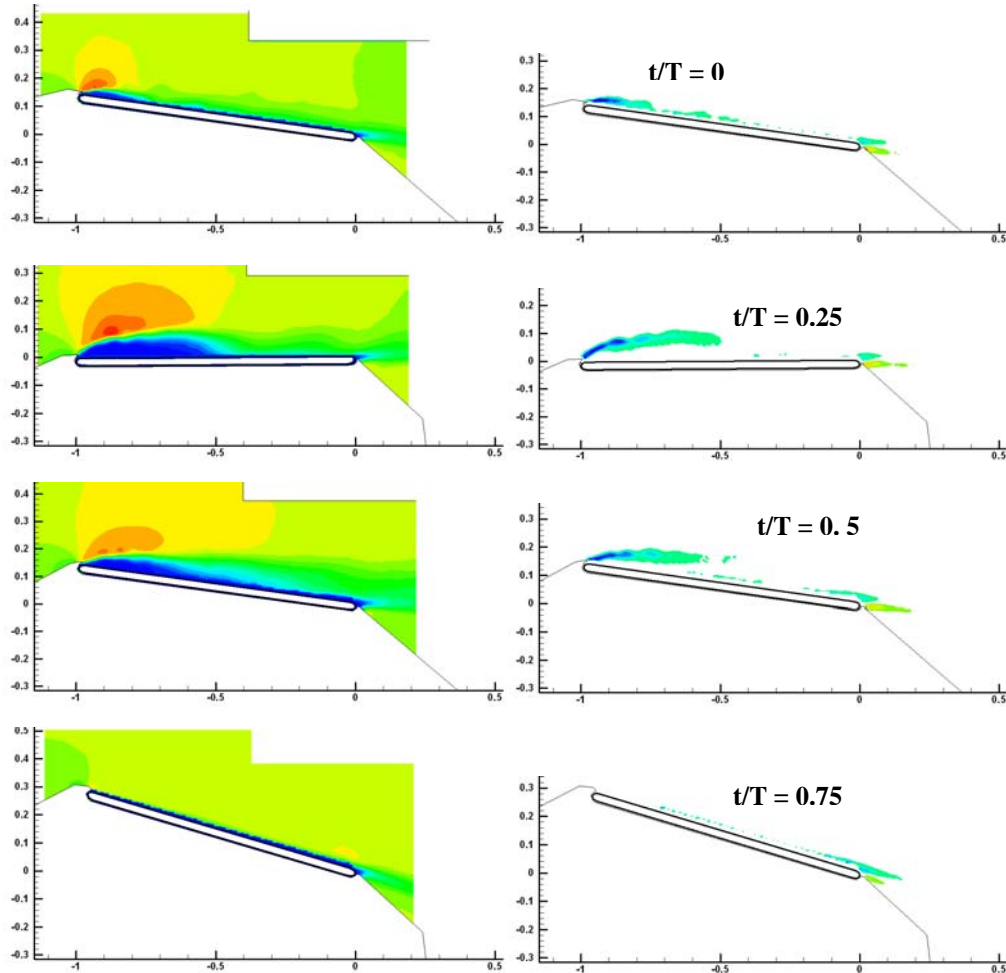
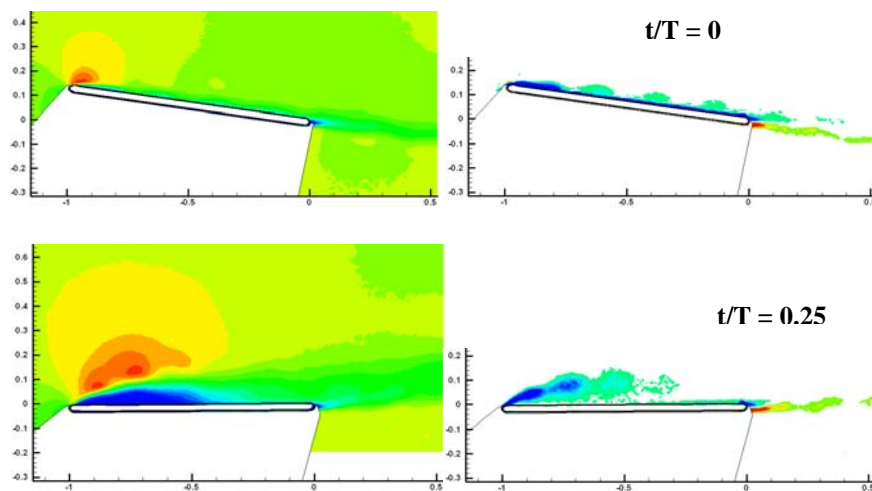


Figure 6-6: U of F REEF PIV Results for AR = 2 Plate Pitch-Plunge.



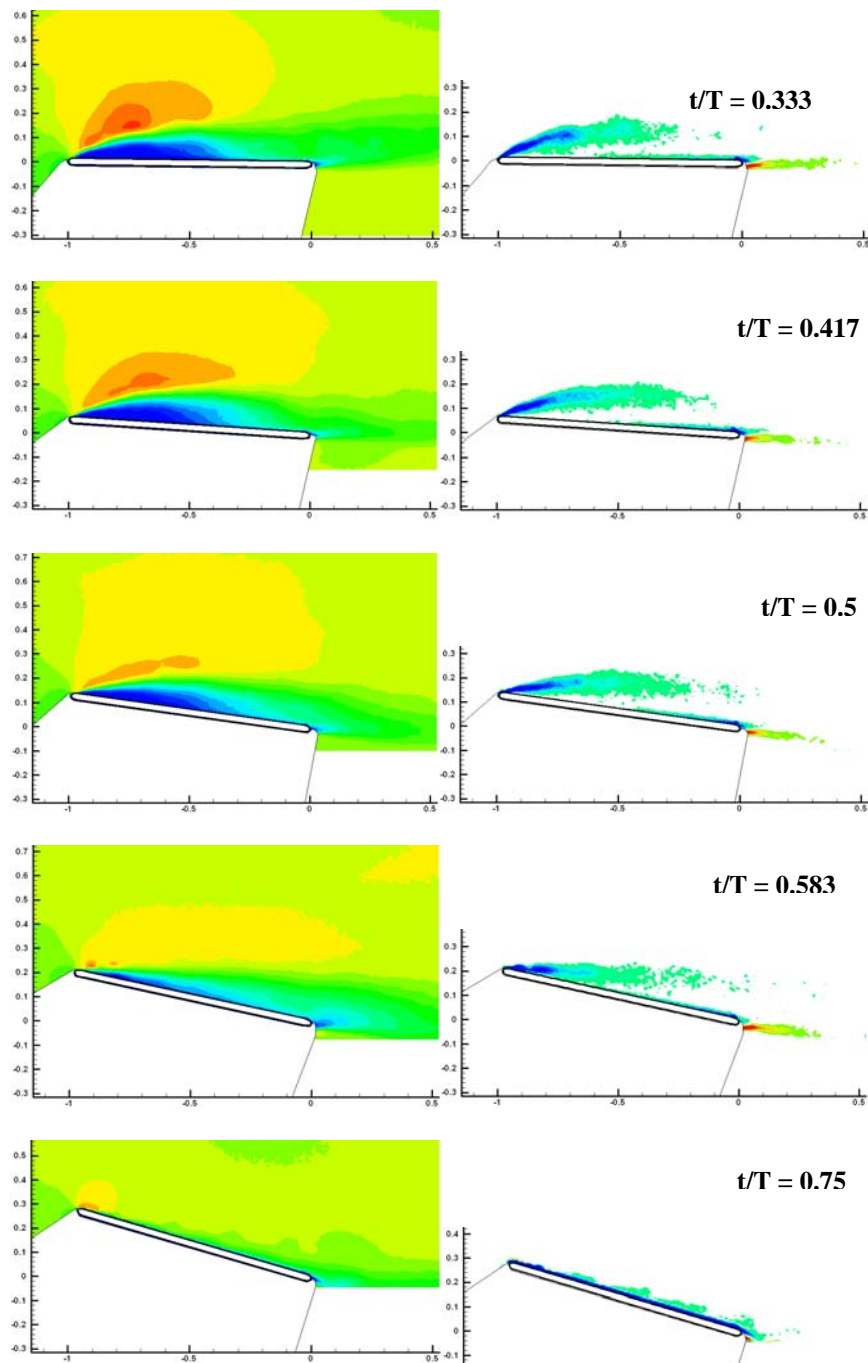


Figure 6-7: AFRL PIV Results for AR = 2 Plate Pitch-Plunge.

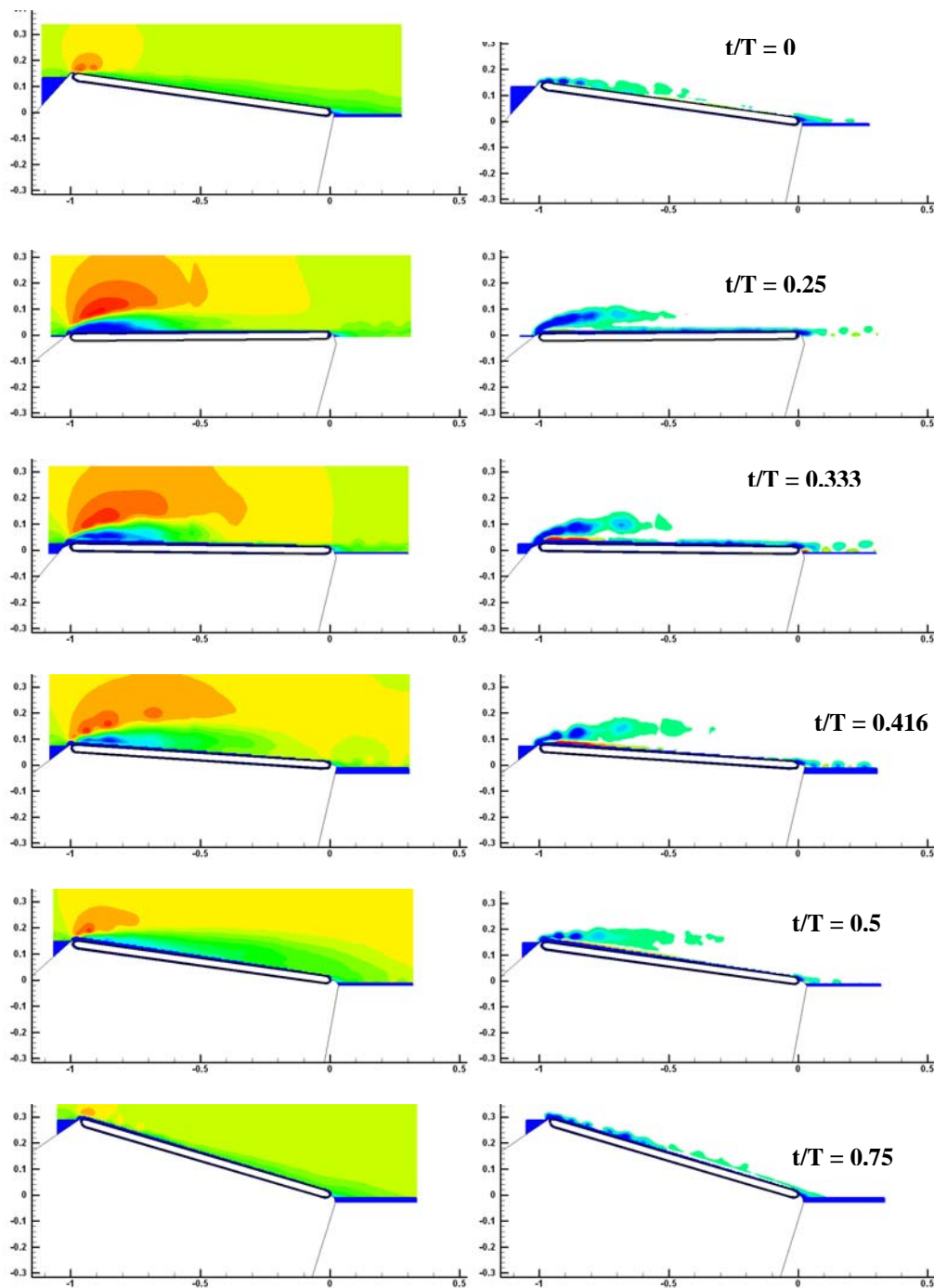


Figure 6-8: U of Michigan PIV Results for AR = 2 Plate Pitch-Plunge.

6.4 AERODYNAMIC FORCE TIME HISTORIES FOR THE AR = 2 FLAT PLATE

For $AR = 2$, both slender body theory and lifting line theory give a quasi-steady lift curve slope of π . For the steady case at angles of attack below stall, Kaplan et al. [53] measured a lift curve slope for a square-edged $AR = 2$ plate very close to π , with almost negligible non-linear deviations due to vortical effects such as loss

of leading-edge suction. The principal question now is whether the $AR = 2$ plate's behaviour in the unsteady problem is similarly simple.

6.4.1 Forces for the $AR = 2$ Plate in Pitch-Plunge

Lift coefficient results for the pitching-plunging case are shown in Figure 6-9. Force measurements from TUBS (the only available experimental data set for this case) are compared with the UM RANS computation and with the AFRL VPM 2D flat plate computation, UM RANS 2D flat plate computation and 2D quasi-steady result. The latter three are all divided by 2, in the spirit of quasi-steady thin airfoil or slender body theories, which both predict a lift curve slope of $\pi\alpha$. Rescaling of the UM 2D plate RANS computation gives a very different trend from the $AR = 2$ UM RANS computation. Rescaling of the AFRL VPM 2D plate computation under-predicts the lift coefficient variation and produces a phase lag missing in the other results, which appears as a hysteresis in the plot with respect to angle of attack. The other three curves – $AR = 2$ UM RANS, the rescaled quasi-steady solution, and the TUBS measurement – are all very close, showing very small (if any) phase lag and therefore very minor hysteresis. The resulting lift coefficient time history therefore has the appearance of behaviour fully consistent with linear theory: quasi-steady and with lift curve slope according to slender-body or lifting-line theory.

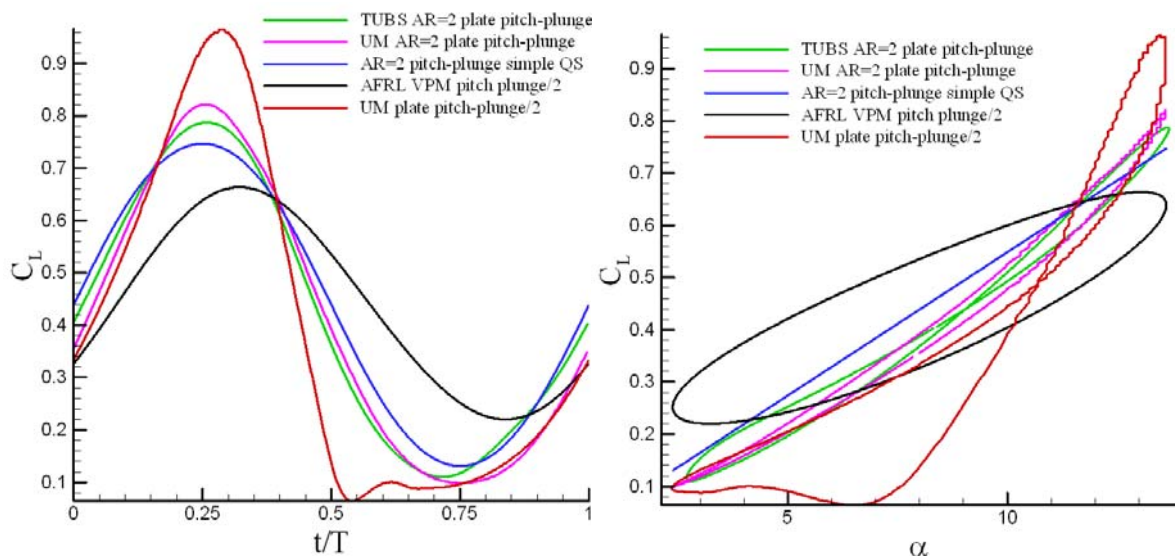
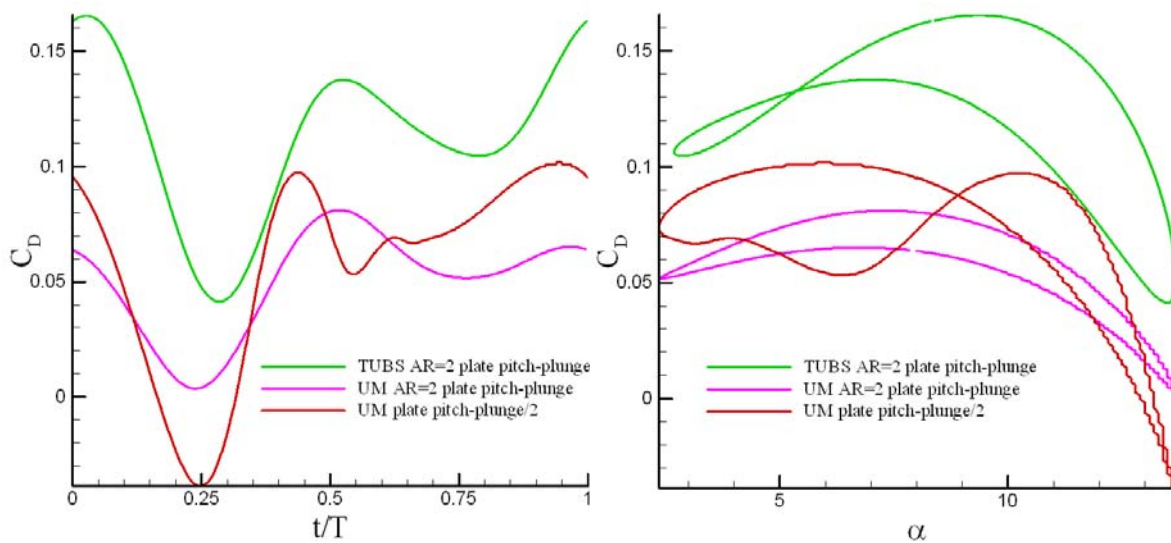


Figure 6-9: Lift Coefficient for $AR = 2$ Pitching-Plunging Plate; Time History (left) and vs. Angle of Attack (right).

Drag coefficient results for the pitching-plunging case are shown in Figure 6-10. The TUBS measurement has what looks like a steady offset of $C_D \sim 0.05$ above the two available computations, both from UM. Unlike for lift, the computed drag coefficient for the wall-to-wall plate is not divided by 2 to overlay with the $AR = 2$ result, but is taken directly as the infinite-span value. Of course, the entire scaling argument for drag is rather specious, as the $AR = 2$ plate will have induced drag that is not present in 2D. We can not, at this point, make a definitive argument in trends in drag coefficient. There is however a thrust spike near $t/T \sim 0.25$, evidently from the LEV. The mean streamwise force is a net drag.



**Figure 6-10: Drag Coefficient for AR = 2 Pitching-Plunging Plate;
Time History (left) and vs. Angle of Attack (right).**

6.4.2 Forces for the AR = 2 Plate in Pure-Plunge

Lift and drag coefficients for the pure-plunging case are given in Figure 6-11 and Figure 6-12, respectively. For pure-plunge, two experimental data sets are available: TUBS and UF REEF, both from wind tunnels. The intuitive desire is to remark that the trends in the SD7003 airfoil and wall-to-wall cases are followed for the AR = 2 plate, in that force coefficient variations for the pure-plunge kinematics are less than for pitch-plunge, when scaled by the peak-to-peak coefficient variation. While this assertion is not really false for the AR = 2 plate, it is largely moot, because both pitch-plunge and pure-plunge kinematics show such close agreement amongst the various data sets. As with the pitch-plunge case, the outliers are VPM, and in the bottom half of the downstroke, the $\frac{1}{2}$ -scaling of the UM 2D RANS. The scaled UM 2D RANS actually performs better for pure-plunge than pitch-plunge, so in that sense the above-mentioned assertion remains relevant. All of the other results are mutually very close with little or no phase lag, and follow the $\pi\alpha$ lift curve slope closely.

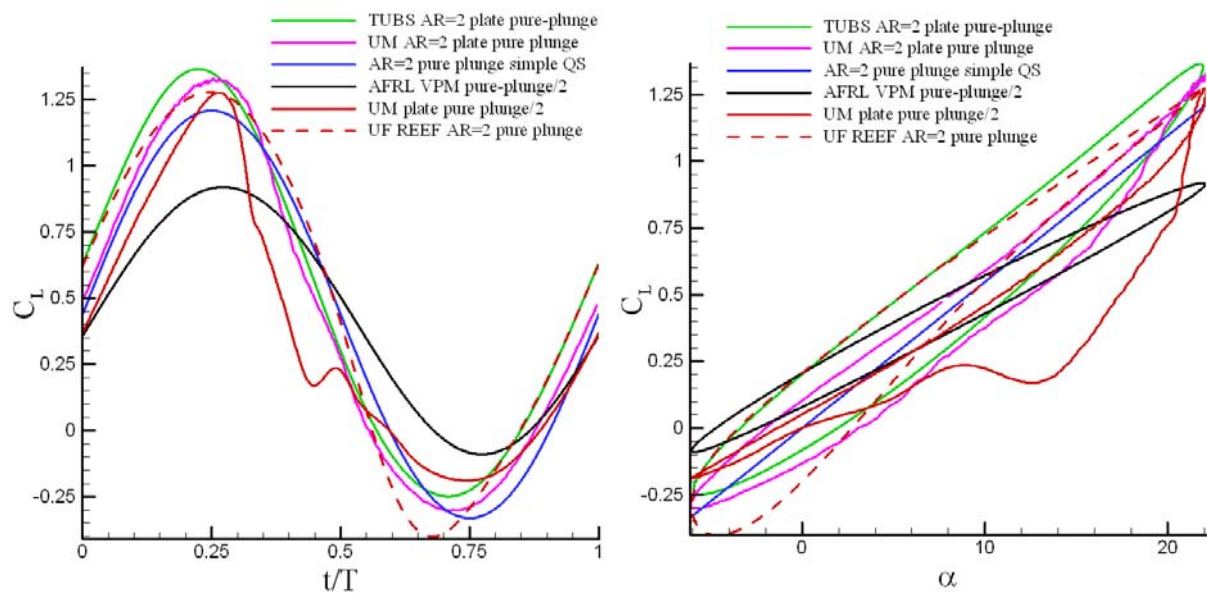


Figure 6-11: Lift Coefficient for AR = 2 Plate in Pure-Plunge;
Time History (left) and vs. Angle of Attack (right).

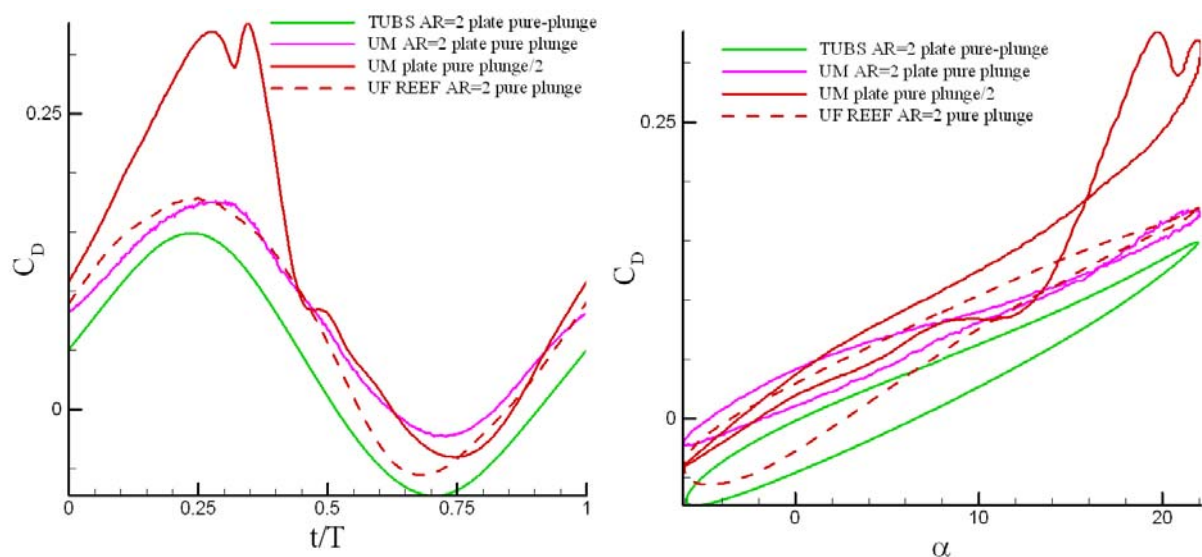


Figure 6-12: Drag Coefficient for AR = 2 Plate in Pure-Plunge;
Time History (left) and vs. Angle of Attack (right).

In drag coefficient, the TUBS measurement has a negative (thrusting) offset relative to the REEF measurement and UM AR = 2 RANS; as in the pitch-plunge case, the TUBS drag offset is on the order of 0.05, but in the opposite direction. Hysteresis is again low, and the drag curve is much more sinusoidal for pure-plunge than for pitch-plunge. Indeed, we find that AR = 2 plate results are more quasi-steady than for the wall-to wall (or 2D) plate. The rescaled UM wall-to-wall flat plate RANS tracks the AR = 2 result for $t/T > \sim 0.45$, where the flow is largely attached, but grossly overshoots earlier in the plunge downstroke, where evidently there is a marked difference between 2D and AR = 2 LEV evolution.

6.5 EXPERIMENTS ON $AR = 2$ PLATE PURE-PLUNGE AT SMALLER STROUHAL NUMBER

As with the SD7003 airfoil and wall-to-wall plate, it remains to run extended parameter studies on reduced frequency, reduced amplitude and so forth. One of our principal themes is the extent of validity of quasi-steady, linear assumptions to unsteady problems with flow separation. If there is an effective angle of attack and force coefficients depend on that angle of attack, then the actual kinematics of *how* that angle of attack was achieved are unimportant. Otherwise, if the kinematics inform the force coefficient time history directly, then the very concept of angle of attack breaks down, and with it superposition and so forth. One route of investigation, already suggested, is to vary the motion kinematics such that the reduced frequency k and effective angle of attack history (in the quasi-steady sense) are kept constant, by varying h and λ . This in fact was the approach taken by the DLR experimental group. The idea here is to consider a pure-plunge motion ($\lambda = 0$), but with effective angle of attack history the same or nearly the same as that of the pitch-plunge motion ($\lambda = 0.6$). For $k = 0.25$ this results in $h = 0.206$.

PIV streamwise-component velocity contour plots are given in Figure 6-13 for four phases of motion (top of plunge stroke, halfway down, bottom of stroke and halfway up). Regions in the flowfield plagued by laser reflections from the model surface are blanked-out.

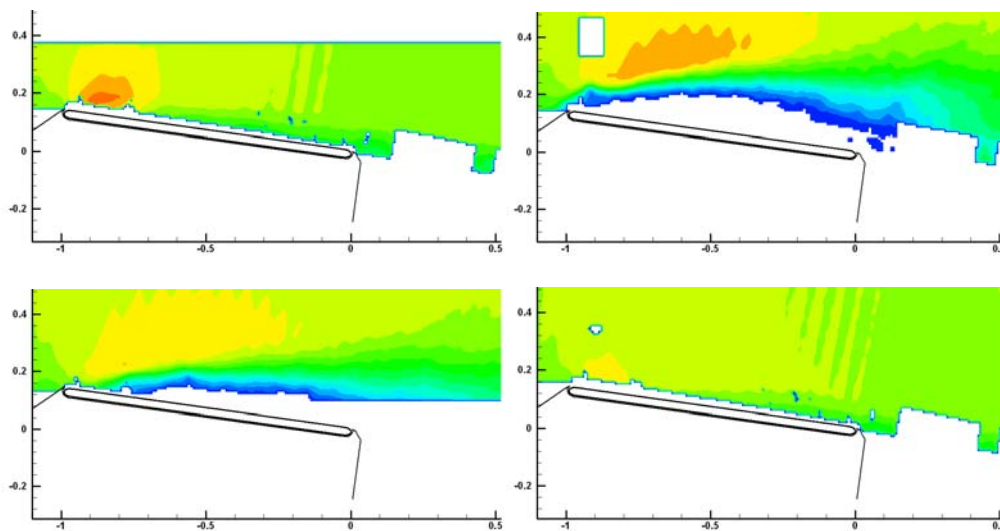


Figure 6-13: DLR PIV; $k = 0.25$ $h = 0.206$ Pure-Plunge of $AR = 2$ Plate, with $\alpha(t) \sim$ Pitch-Plunge of $\lambda = 0.6$; Phases $\Phi = 0$ (top left), 90 (top right), 180 (bottom left) and 270 (bottom right).

An alternative to the above, still retaining the same nominal angle of attack time history, is to reduce k by a factor of 2, while doubling h (Figure 6-14). Strouhal number is thus also unchanged. Streamwise velocity contours for this case are in. Qualitative similarity between the two cases is excellent, but unfortunately detailed comparison is precluded by reflections from the model surface. Direct force measurements are not available. Nevertheless, we have good supporting evidence in all of our cases that even moderate agreement between flowfields implies excellent agreement in lift time history (but certainly not vice versa!). We can conclude, at least preliminarily, that superposition is tenably valid in the sense of retaining a concept of effective angle of attack through various combinations of reduced frequency, reduced amplitude and λ . This, in turn, should have favourable implications for designers of MAV flapping wings, at least for motions in the frequency and angle of attack range considered so far.

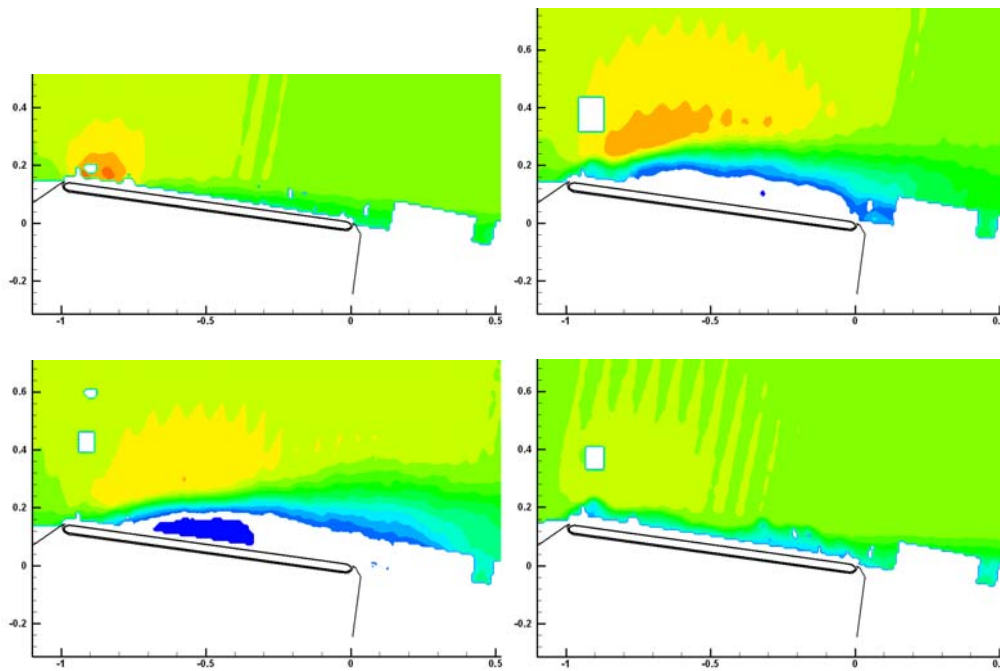


Figure 6-14: DLR PIV; $k = 0.125$ $h = 0.412$ Pure-Plunge of $AR = 2$ Plate, with $\alpha(t) \sim$ Pitch-Plunge of $\lambda = 0.6$; Phases $\Phi = 0$ (top left), 90 (top right), 180 (bottom left) and 270 (bottom right).

Next we turn to an entirely different problem, returning to the SD7003 airfoil, with an even lower amplitude but a much higher frequency. Here too we wish to investigate validity of quasi-steady concepts and traditional small-disturbance approximations in aerodynamics.

Chapter 7 – HIGH-FREQUENCY LOW-AMPLITUDE AIRFOIL PURE-PLUNGE OSCILLATIONS

7.1 MOTIVATIONS

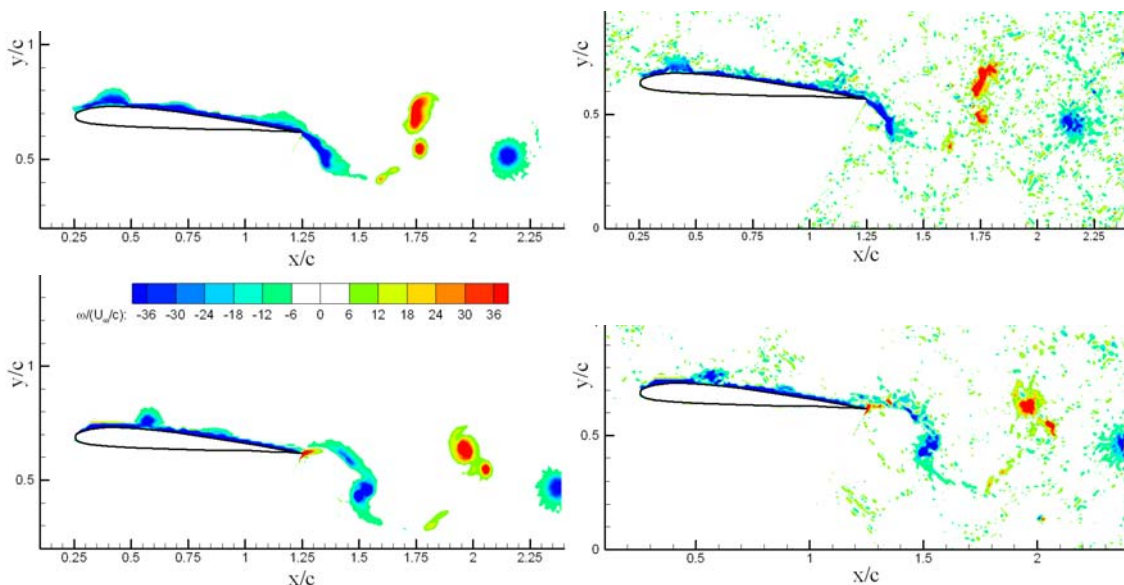
So far we have considered but a single reduced frequency, $k = 0.25$. This is likely representative of the flapping-flight of birds in cruise, and thus presumably of flapping-wing MAVs of the larger scale. And this is towards the extreme upper bound of reduced frequencies associated with classical dynamic stall. It is doubtless worthwhile to undertake a broad parameter study, say from $k = 0.05$ through 0.25, 1.0 and higher, but of course practical limitations such as lack of fanatically studious graduate students preclude this. As a partial effort, we consider a very high reduced frequency, relevant perhaps to the flapping-flight of smaller MAVs operating at speeds just above hover.

The $k = 3.93$, $h = 0.05$ ($St = 0.125$) pure-plunge was considered in a detailed study by Jones et al. [21] on the NACA 0012, at $Re \sim 10000$, as part of a parameter study of thrust efficiency and wake topology vs. Strouhal number. We consider this problem, also in pure-plunge, but for the SD7003, at $Re = 40000$ and at $Re = 10000$, and an offset angle of attack of 4° . Again we compare experiments and computations. As the motion is now too aggressive for wind tunnels, only a water tunnel run is considered on the experimental side, while for computation we again compare a vortex particle method, RANS and LES.

7.2 FLOWFIELD RESULTS

In the following, four phases of the plunge sinusoidal motion are reported. Phase $\phi = 0$ is halfway down on the plunge stroke, where the effective angle of attack is largest positive; $\phi = 90$ is at the bottom of the downstroke, where plunge-induced angle of attack is zero; $\phi = 180$ is halfway on the upstroke, where the effective angle of attack is maximally negative; and finally, $\phi = 270$ is the top of the plunge stroke, where again plunge-induced angle of attack is zero.

AFRL water tunnel instantaneous and phase-averaged PIV measurements for vorticity are presented in Figure 7-1, and Figure 7-2 gives phase-averaged streamwise component of velocity. Phase-averages are based on 115 PIV image pairs, from a sequence of 120; the first 5 pairs are neglected to avoid start-up transients [97].



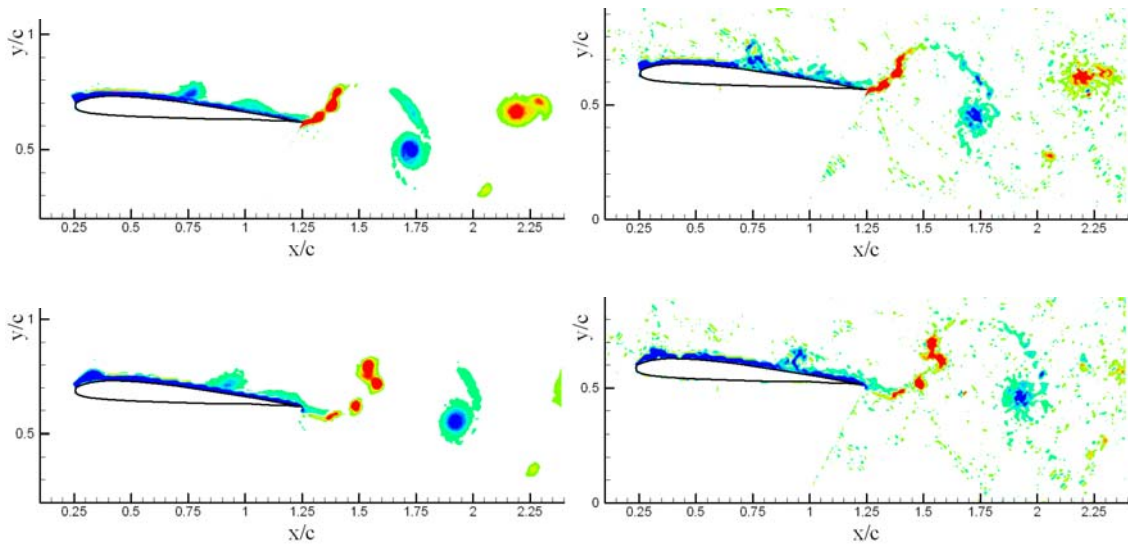


Figure 7-1: AFRL PIV; Re = 40 K; Vorticity Contours, $k = 3.93$ Plunge; Phases $\Phi = 0, 90, 180$ and 270 ; Phase-Averaged Measurements (left column) and Representative Instantaneous Measurements (right column).

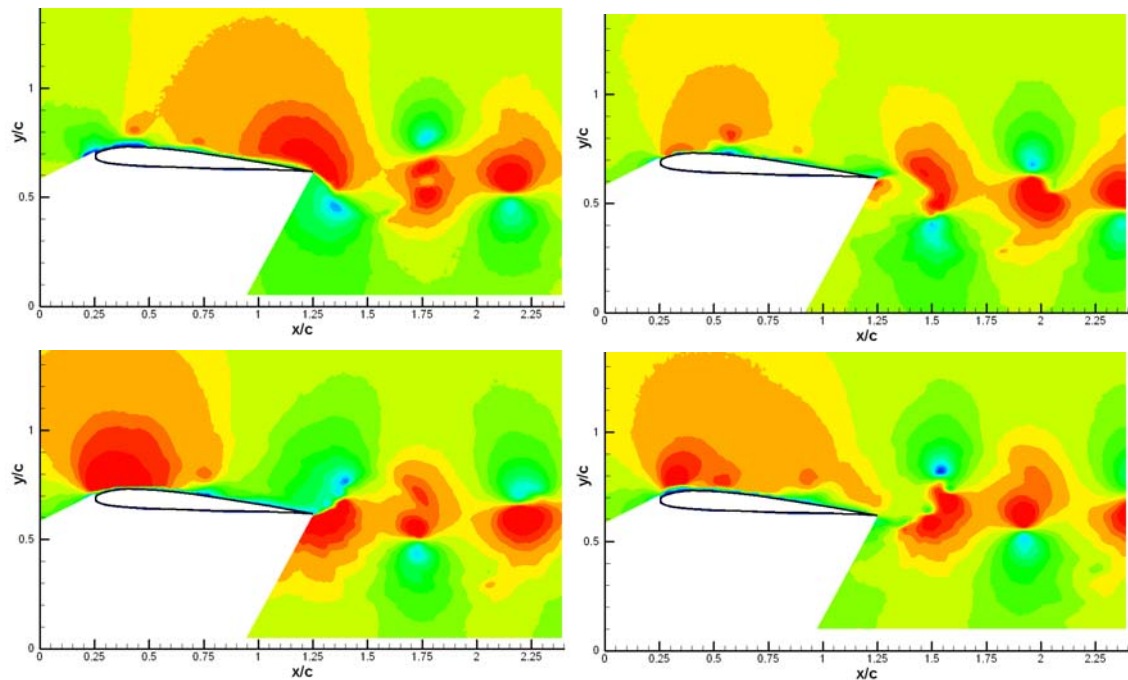


Figure 7-2: AFRL PIV; Re = 40 K; Velocity Contours, $k = 3.93$ Plunge; Phases $\Phi = 0$ (top left), 90 (top right), 180 (bottom left) and 270 (bottom right).

LES computations for instantaneous and phase-averaged vorticity, and for phase-averaged velocity, are in Figure 7-3 and Figure 7-4, respectively. Instantaneous and phase-averaged results show the same general flowfield structure away from the airfoil boundary layer, though of course the details of turbulence will be smeared in the average. Indeed the flow is transitional, in the sense that transition is associable with the wall-bounded small LEV visible in Figure 7-1 and Figure 7-3. The $Re = 10$ K case was also considered; details are reported by Visbal [98], and for brevity the present discussion is limited to instantaneous vs.

averaged vorticity contours at $\phi = 0$ (Figure 7-5). There transition does not occur until the trailing edge region and the near-wake, and the wall-bound LEV is a discrete, homogenous blob of vorticity that differs little between instantaneous and phase-averaged. The qualitative conclusion is that this flow is highly periodic at both Reynolds numbers, with a reverse Karman vortex street, and is therefore much akin to the findings for the NACA0012 at zero mean angle of attack [21]. In turn, this implies insensitivity to the airfoil shape and the Reynolds number.

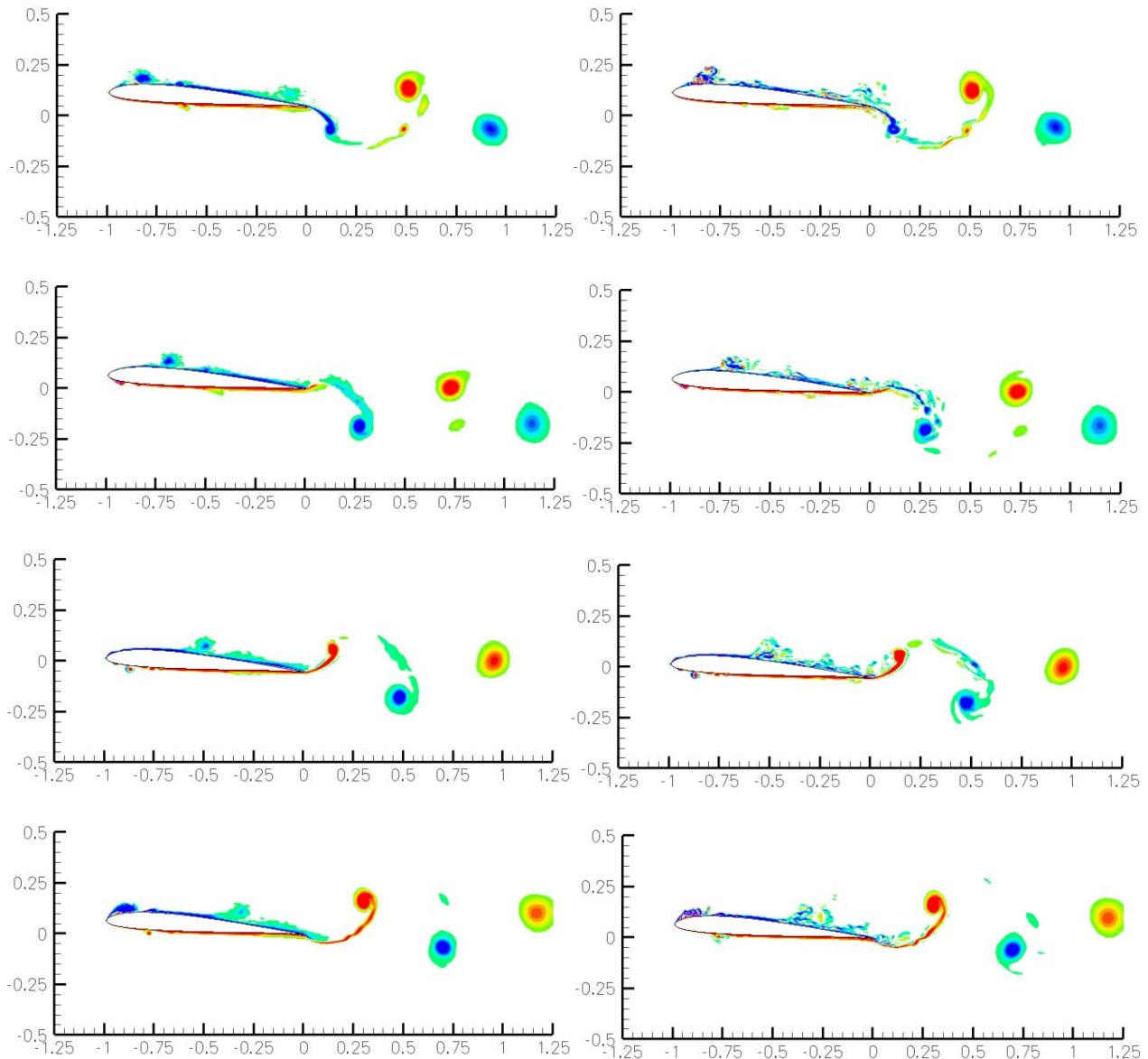


Figure 7-3: AFRL LES Computations; $Re = 40 K$; Vorticity Contours, $k = 3.93$ Plunge; Phases $\Phi = 0, 90, 180$ and 270 ; Phase-Averaged Measurements (left column) and Representative Instantaneous Measurements (right column).

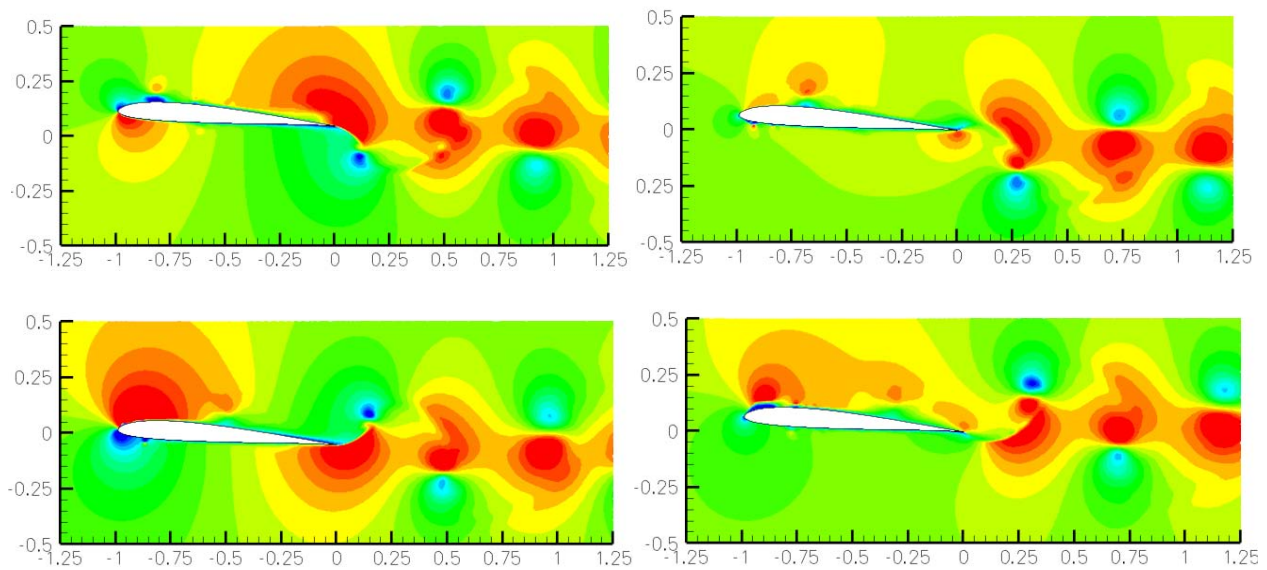


Figure 7-4: AFRL LES Computations; $Re = 40$ K, Velocity Contours, $k = 3.93$ Plunge; Phases $\Phi = 0$ (top left), 90 (top right), 180 (bottom left) and 270 (bottom right).

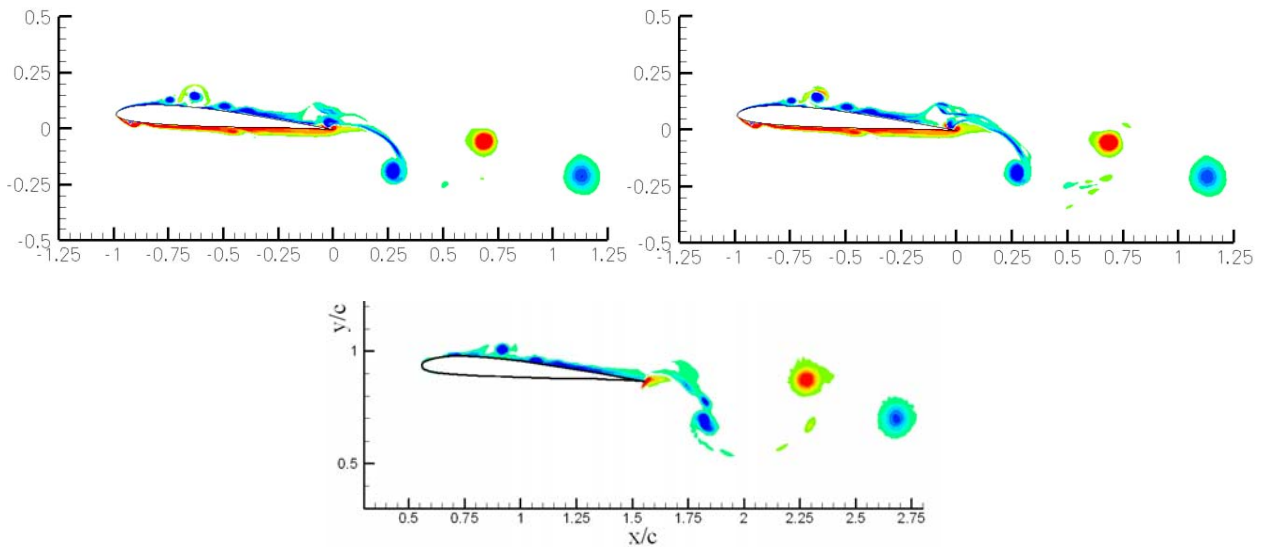


Figure 7-5: AFRL LES Computations; $Re = 10$ K; Vorticity Contours, $k = 3.93$ Plunge; Phase $\Phi = 0$; Phase-Averaged (top left) and Instantaneous (top right); and Phase-Averaged AFRL PIV (bottom).

Next we turn to RANS at $Re = 40$ K (University of Michigan). Velocity contours are shown in Figure 7-6, and vorticity is in Figure 7-7. Agreement with phase-averaged LES is very close, which is to say that RANS without a transition model is adequate for capturing the overall wake structure for this unsteady transitional periodic flow, in the sense of a phase-average.

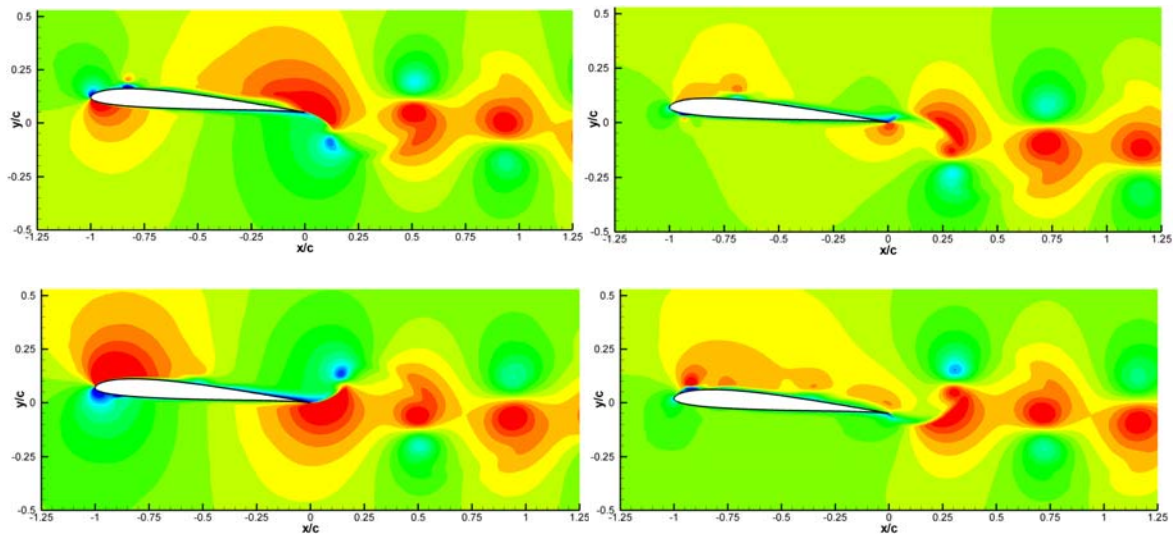


Figure 7-6: UM RANS Computations; $Re = 40$ K; Velocity Contours, $k = 3.93$ Plunge; Phases $\Phi = 0$ (top left), 90 (top right), 180 (bottom left) and 270 (bottom right).

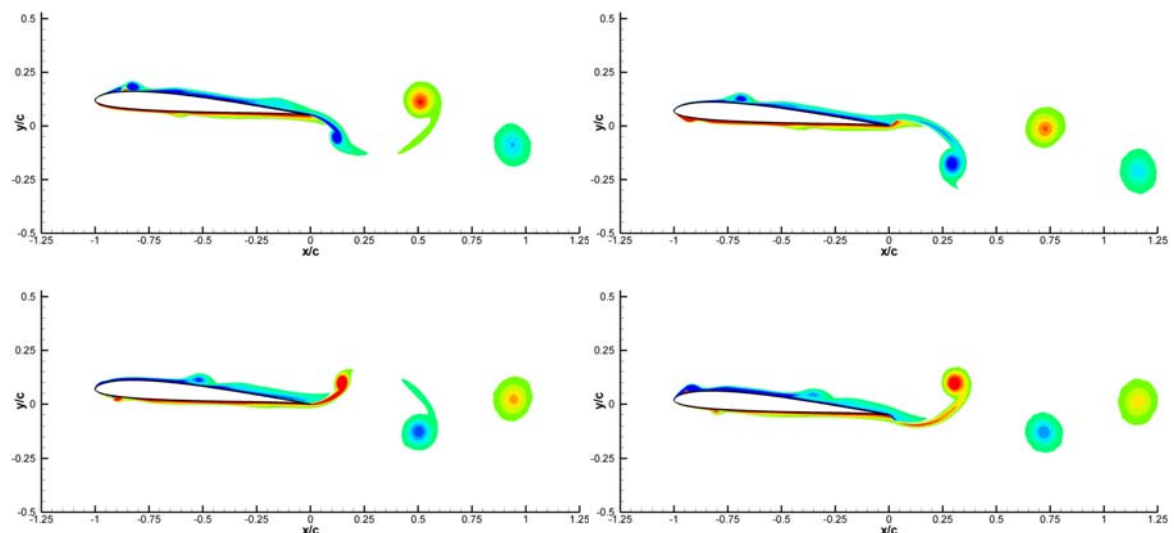


Figure 7-7: UM RANS Computations; $Re = 40$ K; Vorticity Contours, $k = 3.93$ Plunge; Phases $\Phi = 0$ (top left), 90 (top right), 180 (bottom left) and 270 (bottom right).

Finally, we compare with a 2D vortex-particle calculation (AFRL VPM). Traces of vortex particles released at the airfoil TE are shown in Figure 7-8, which are analogous to PIV vorticity in Figure 7-1 and LES vorticity in Figure 7-3; roughly, spatial concentration of vortex particles is akin to local intensity of vorticity. The present implementation of the VPM algorithm has no provision for shedding vorticity from the airfoil anywhere except for the trailing edge, in particular missing the leading-edge rollers on the airfoil suction surface. Nevertheless, the wake time history is very similar to those of the LES computation, the experiment and the RANS. It appears, therefore, that LEV production for this kind of flow is unimportant for the overall wake structure.

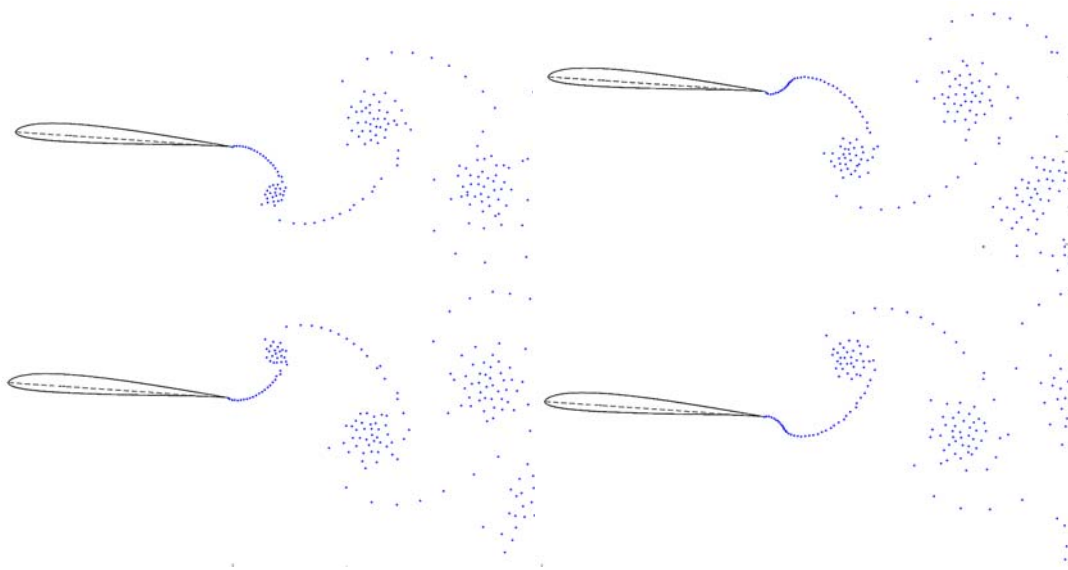


Figure 7-8: Vortex Particle Calculation for $k = 3.93$ Plunge; Phases $\Phi = 0$ (top left), 90 (top right), 180 (bottom left) and 270 (bottom right).

In sum, then, all of the computational methods give similar wake structure, though the fidelity of resolution of boundary layer structure goes in proportion to the complexity of the method. Following the by now established theme of our work, we next consider how the calculation of aerodynamic force compares amongst the various methods; if the computed flowfields are similar, the computed loads, if past performance is any guarantee of future results, should be even more similar.

7.3 FORCE COMPUTATIONS

Lift coefficient time history from LES computation at $Re = 40$ K and 10 K, RANS computations at $Re = 40$ K and from Theodorsen's formula, is given in Figure 7-9. Reynolds number seems to have essentially no effect between the two LES runs, despite the difference in boundary layer properties and role of transition. RANS splits the difference between LES and Theodorsen, which itself is not large. Thus Theodorsen's formula gives acceptable lift time history prediction despite the wake being far from planar, and the obvious presence of vortex shedding. This seems counterintuitive; why would Theodorsen's formula work despite the blatant violation of its underlying assumptions? The resolution is in the fact that non-circulatory force dominates circulatory force, as seen from comparing just the non-circulatory portion of Theodorsen's formula with the LES solution (green curve in Figure 7-9). Theodorsen's equation is valid for arbitrarily large frequency, but only small amplitude. Evidently, despite the reverse Karman vortex street, $h = 0.05$ is a "small enough" amplitude. Linear superposition also seems to be valid here.

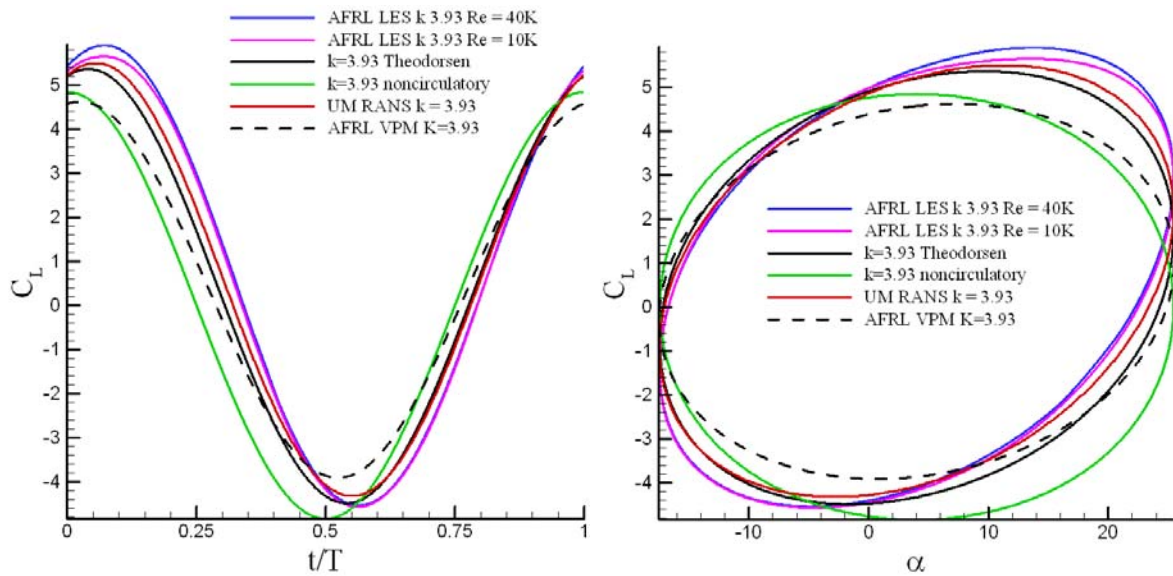


Figure 7-9: Lift Coefficient Time History (left) and vs. Angle of Attack (right); $k = 3.93$ $h = 0.05$ Pure-Plunge of SD7003 Airfoil at $Re = 40$ K and 10 K.

Drag coefficient is shown in Figure 7-10, and integrated lift and drag over the plunge cycle are tabulated in Table 7-1. Consistent with the reverse Karman vortex wake, a net thrust (negative drag) is produced. However, as Re decreases, evidently viscous drag increases, and the net thrust is attenuated.

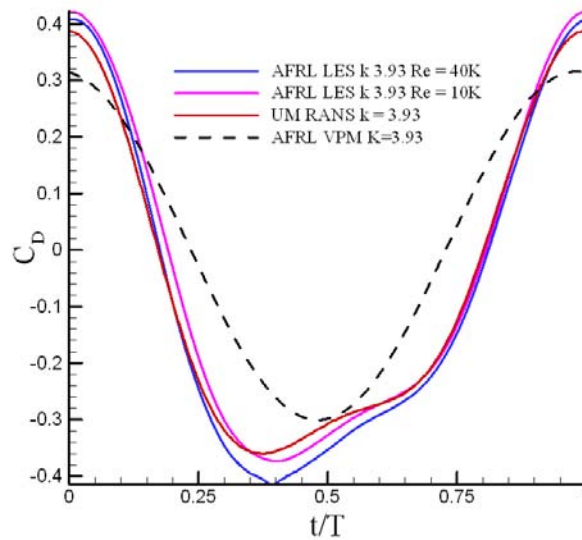


Figure 7-10: Drag Coefficient Time History; $k = 3.93$ $h = 0.05$ Pure-Plunge of SD7003 Airfoil at $Re = 40$ K and 10 K.

Table 7-1: Computed Integrated Force Coefficients; $k = 3.93$ $h = 0.05$ Pure-Plunge

	C_L	C_D
LES 40 K	0.73	-0.081
LES 10 K	0.66	-0.054
RANS 40 K	0.58	-0.069

It remains to explore higher amplitudes to see where Theodorsen's formula convincingly breaks down, and for that matter to find clear distinction between the results of vortex particle methods, RANS and LES. It also remains to consider start-up transients at the commencement of a periodic motion, or alternatively non-periodic problems such as pitch ramp-and-hold or ramp-and-return.

We conclude, at least tentatively, that high-frequency low-amplitude cases are “easy”, in the sense that the imposed motion dynamics constrains the aerodynamic solution to a periodicity amenable even to inviscid analysis, and at high enough reduced frequency the lift coefficient is dominated by the so-called non-circulatory loads. Of course, it is the fluid streamlines that determine the pressure gradients responsible for non-circulatory loads, and the shed and bound vortex strength, together with the trailing edge Kutta condition and no-flow-through boundary condition determine the streamlines. Thus all aerodynamic forces are in the end “circulatory”. The point, however, is that one may blithely disregard shed and even bound vortex strength, retaining in the equations only the terms related to fluid acceleration, and still obtain a workable approximation – if the reduced frequency is high enough. We leave as a future problem to ascertain how far this can be extended to moderate or large motion amplitudes, and to non-periodic motions.

Thus far our work has been exclusively on rectilinear or longitudinal-plane motions, where the airfoil or plate oscillates in a plane parallel to the free-stream and normal to the plane of the wing planform. This is the most straightforward abstraction for the flight of large birds, for example – but not necessarily for the smaller flying creatures such as insects or hummingbirds. While a collective treatment across multiple laboratories has in the present work been intractable for non-rectilinear motions, we present in the next chapter a promising line of investigation for a rotating or “whirling” motion.

Chapter 8 – NON-RECTILINEAR MOTIONS: WHIRLING FLAT PLATE

8.1 PURPOSE AND TYPE OF “WHIRLING” MOTIONS

8.1.1 Rotational Motions and Leading Edge Vortex Retention

There is presently considerable controversy about the stability of insect-flapping LEVs. As discussed above, many mechanisms for LEV stability have been proposed, and indeed the whole issue of LEV stability is but one of several mechanisms for explaining the unexpectedly high lift coefficients encountered in insect flapping-wing studies. One of the main controversies is whether there is something intrinsic to “flapping” in the sense of pivoting or swinging about a fixed-point at the wing root, as opposed to rectilinear translation, which was the subject of all of the preceding chapters in this report.

A quasi-steady setup developed by Usherwood and Ellington rotates a wing like a propeller in a water tank with no ambient flow [99]. When a wing undergoes a whirling propeller-like motion there is a velocity gradient from the wing root to tip not present in rectilinear motion. The propeller experiments preserve the three-dimensional flow as a velocity gradient, but neglect the starting and stopping that occurs at the beginning and end of the wing stroke. The idea is to observe the long-term properties of leading edge vortex formation, and retention or shedding; once formed, does the LEV stay resident near the wing leading edge for long dimensionless time, or does it detach and convect away from the wing, as we saw in the rectilinear periodic oscillations in previous chapters? In brief, the conclusion of the propeller-like experiments is that long-term LEV retention is possible, at least at the Reynolds numbers of the subject experiment [99].

But as an insect wing stroke is only 2 to 5 chord lengths [100,101], unsteady effects at the beginning and end of the flapping cycle can produce significant additional lift and raise questions beyond the propeller-type experiments on LEV formation/retention history and transient effects. One is interested in the role of starting transients – how acceleration profile and intensity affects the subsequent flowfield and lift coefficient evolution, and how long it takes to relax to quasi-steady (if one exists) state. This, of course, was ignored in our work reported above, where the experiments and computations were deliberately run long enough for starting transients to relax, so that phase-averages would be taken over at least nominally periodic conditions.

8.1.2 Details of Motion Kinematics

The waving wing experiment, described in an earlier chapter, is designed to mimic the translational phase of an insect wing stroke, building on Ellington-type propeller experiments to include wing starting and stopping. Three angular velocity starting profiles were considered: linear, sinusoidal, and exponential, each reaching the maximum velocity necessary to achieve a Reynolds number of 60000 in 0.10, 0.25, or 0.60 chord-lengths of travel referenced at 3/4 span. The commanded velocity and acceleration profiles are shown in Figure 8-1 as plotted vs. time, and in Figure 8-2 as plotted vs. angular displacement. An exponential rise in rotation rate vs. time produces a linear rise in rotation rate vs. angular displacement.

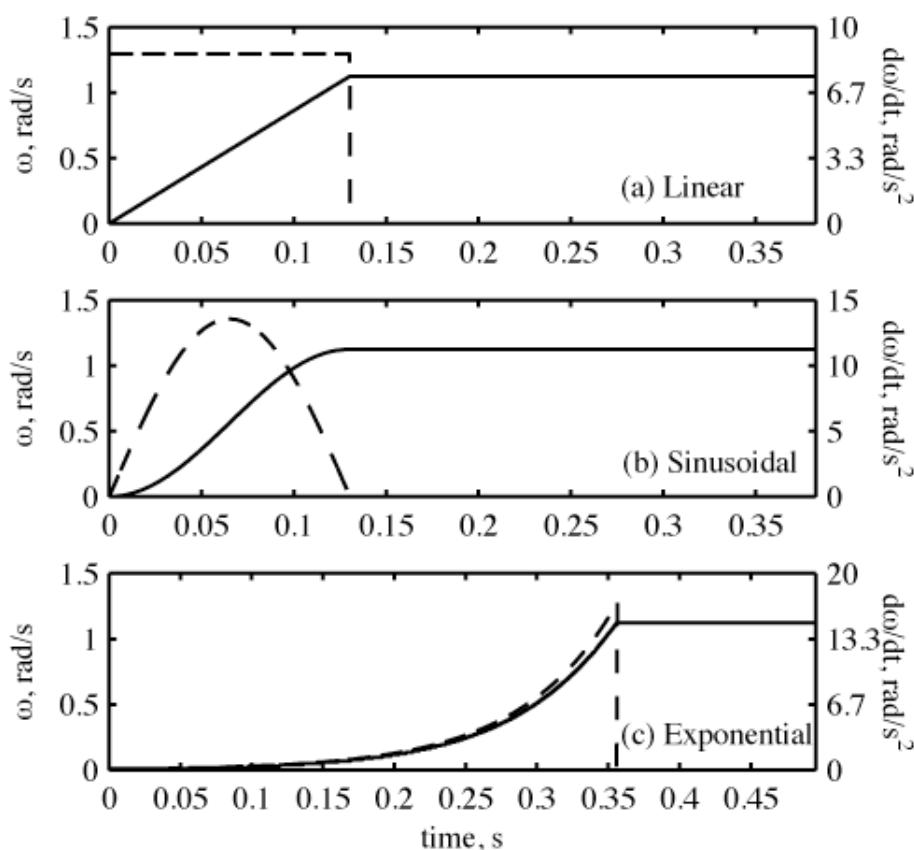


Figure 8-1: Commanded Wing Kinematics Plotted vs. Time, for First Quarter-Stroke Accelerating Over 0.25 c; Angular Velocity (solid) and Acceleration (dashed) as a Function of Time.

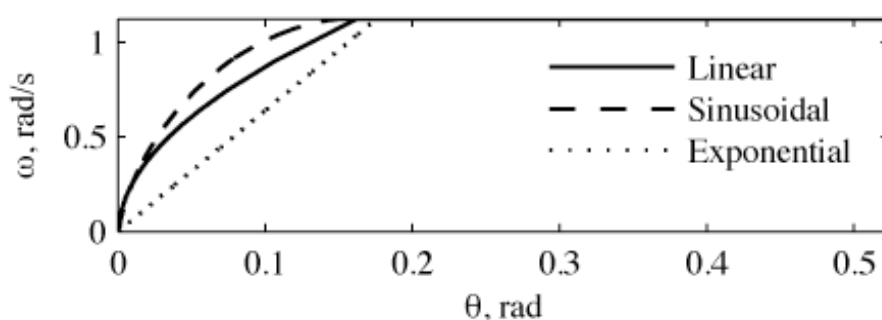


Figure 8-2: Commanded Wing Kinematics Plotted vs. Angular Displacement, for the First Quarter-Stroke; Angular Velocity for a Wing Accelerating Over the First 0.25 c of Travel.

8.2 FORCE DATA

Figure 8-3 shows the averaged and smoothed lift coefficients for a waving wing at a 5 and 15 degree angle of attack accelerating to maximum velocity in 0.10, 0.25 and 0.60 chords. It can be seen that changing the angle of attack primarily changes the magnitude of the measured force while the shape of the curve remains much the same. All of the curves are characterized by an initial steep increase in lift coefficient leading to a

lift peak, followed by a sharp drop and subsequent recovery to an intermediate level that is then maintained for the rest of the constant velocity portion of the wing stroke. It appears that after 2 to 3 chord-lengths of travel (at 3/4 span, corresponding to 34 to 51 degrees of rotation) the lift nears a steady-state value. The shape of the lift curve shown here, including the initial lift peak, is very similar to those reported by Dickinson and Götz at $Re < 1,000$ [102].

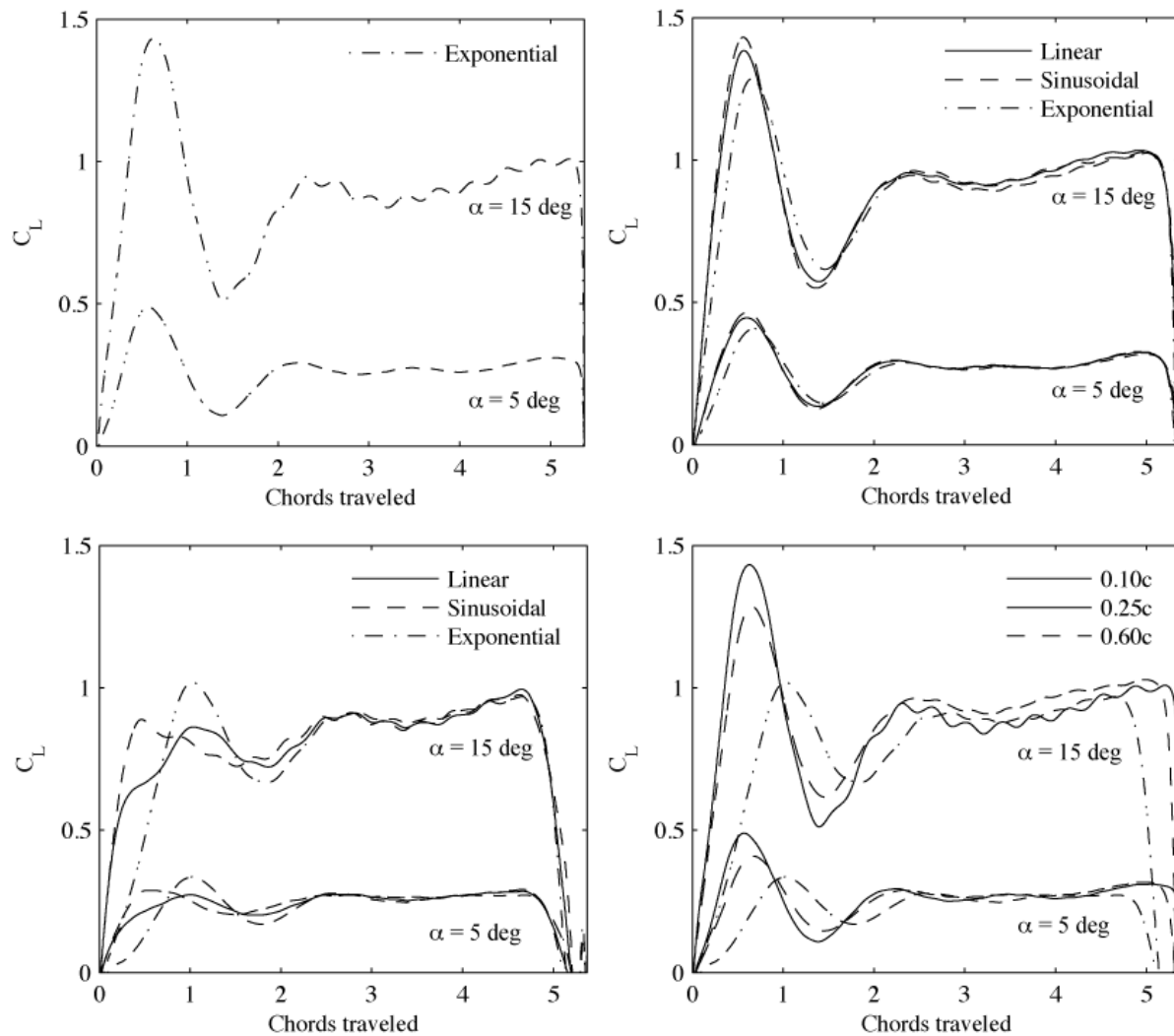


Figure 8-3: Lift Coefficients for a Waving Wing Accelerating Over 0.10 c (top left), 0.25 c (top right), 0.60 c (bottom left) and All Exponential Velocity Profiles (bottom right).

The main differences due to different acceleration patterns (Figure 8-4) are observed in the early stages of the wing stroke. The slowest acceleration profile is the exponential over 0.60 chords, not even visible in Figure 8-4, with the next slowest being the constant acceleration. Both of these velocity profiles result in a relatively low delayed lift peak past 1 chord of travel as in Figure 8-3. Maximum lift coefficients for the linear, sinusoidal, and exponential velocity profiles accelerating in 0.60 c are 0.87, 0.88 and 1.01.

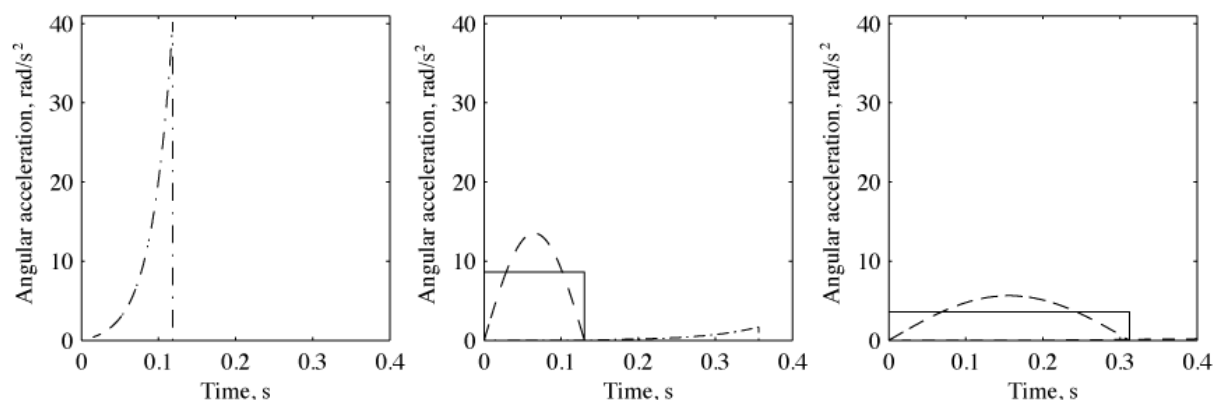


Figure 8-4: Angular Acceleration for the Three Velocity Profiles: Linear (solid line), Sinusoidal (dashed line) and Exponential (dash-dotted line) Over 0.10 c (left), 0.25 c (center) and 0.60 c (right).

At higher accelerations the effect of acceleration on the lift peak diminishes and all of the curves show a pronounced maximum approximately 50% above the steady state value near 0.60 chord-lengths travelled, well into the constant velocity portion of the wing stroke. The largest acceleration studied is the exponential over 0.10 chords, with a maximum of 40.2 rad/s^2 and a maximum lift coefficient of 1.42. Over 0.25 chords the maximum acceleration is 8.6, 13.6, and 1.6 rad/s^2 for the linear, sinusoidal, and exponential velocity profiles with maximum lift coefficients of 1.34, 1.39, and 1.26, respectively, as in Figure 8-2. Despite the large difference in the acceleration, the lift is of similar magnitude and timing. It is interesting to note that the timing of the transient lift peak does not change significantly whether the wing is accelerated over 0.10 or 0.25 chords, suggesting that the sharp lift peak evident in the force data is due to aerodynamic effects rather than inertia. Lift curves at a 5 degree angle of attack look much like those at 15 deg with a lower $C_{L\text{max}}$ and “steady-state” value. C_L levels off near 0.95 for $\alpha = 15$ deg or 0.27 for $\alpha = 5$ deg after 2.5 chords of travel for all wing kinematics. For any profile accelerating in 0.10 or 0.25 chords, the maximum C_L occurs near 0.6 chords of travel. Beckwith and Babinsky [103] performed experiments on an impulsively started flat plate wing towed in pure translation through a water tank. Figure 8-5 shows the unsteady lift coefficients measured on the waving wing as compared to their sliding wing. Only the constant acceleration over 0.60 c is shown here as faster accelerations are not available for the sliding wing. The force history for the two cases is very similar. Also shown is the expected lift according to Wagner’s theory using the long-term steady state value measured on the translating wing as the asymptotic lift coefficient. At a 5 degree angle of attack, below steady state stall, the unsteady development of lift coefficient for both experiments closely matches those predicted by Wagner [28]. At larger angles of attack and in the initial phase of the wing stroke other aerodynamic effects appear to dominate the force history. Lift curves at the higher angle of attack resemble those at Reynolds numbers less than 1,000 reported by Dickinson and Götz [102].

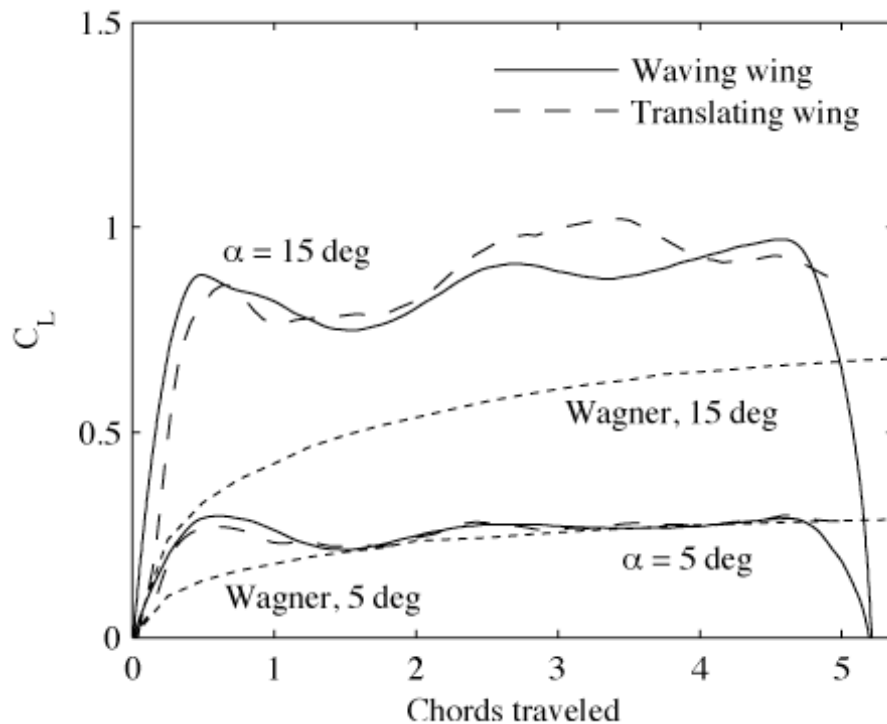


Figure 8-5: Comparison of Unsteady Lift Coefficients Observed for a Waving Wing and Translating Wing Accelerating Over 0.60 c.

C_L versus α for the waving wing (constant acceleration over 0.25 c) at an angle of attack from 0 to 25 degrees are given in Figure 8-6. Here, “max C_L ” is the maximum C_L achieved at the lift peak as shown in Figure 8-2. The steady C_L refers to the mean value measured between 3 and 4 chords of travel where lift levels out. Both lift coefficients appear to be linear in α . The line of best fit for the maximum lift coefficient is $1.82 \pi \alpha$ and $1.31 \pi \alpha$ for the quasi-steady lift coefficient. For comparison, Wagner predicts $1.6 \pi \alpha$ after 3.5 chords of travel. Also shown is the $2 \pi \alpha$ curve from thin airfoil theory and Theodorsen’s theory [26] where the Theodorsen function, $C(k)$, is $C(k) = 0.52 - 0.06 i$ for acceleration over 0.25 c. The maximum lift achieved on the waving wing is similar to the thin airfoil theory prediction despite the fundamental differences in the flow-field, especially at higher angles of attack. The extension of Theodorsen’s theory to the waving wing under-predicts lift at all of the tested angles of attack. Beckwith and Babinsky’s experiments on a sliding wing suggest that the true steady state lift is not achieved until the wing has travelled much further and is lower than the lift after 3 to 4 chord-lengths of travel [103]. This may explain the under-prediction shown here.

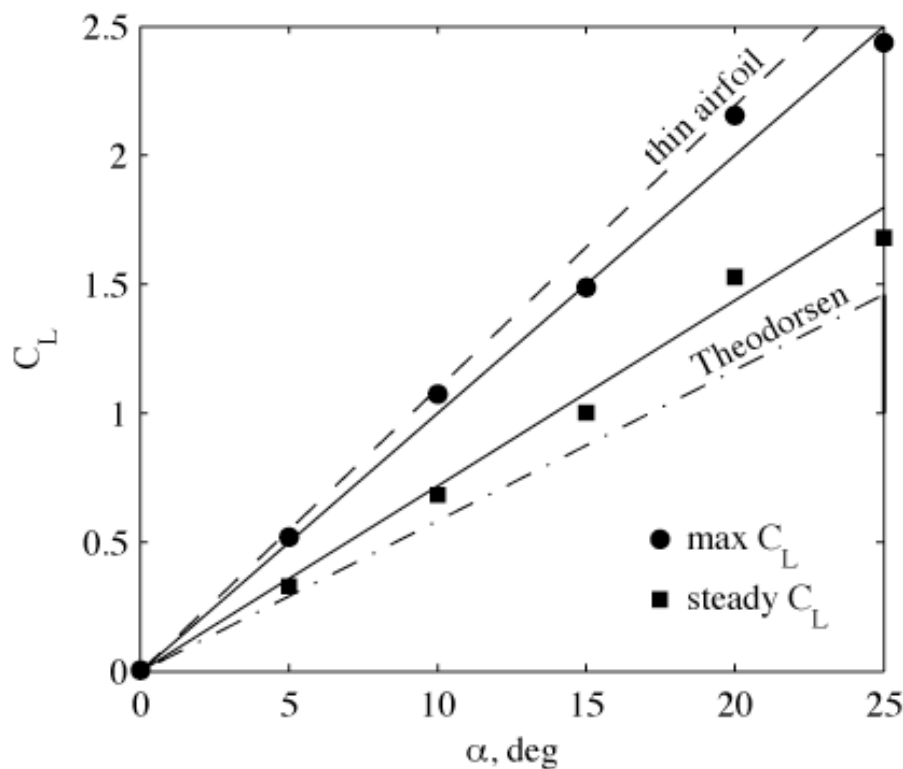


Figure 8-6: Lift Coefficient as a Function of Angle of Attack.

8.3 FLOWFIELD MEASUREMENTS WITH PARTICLE IMAGE VELOCIMETRY

8.3.1 Vortex Tracking

Considering the flow during the early stages of motion, Figure 8-7 compares both the velocity field and Λ contours to the force history at three points in time for the waving wing undergoing constant acceleration over 0.25 chord-lengths of travel at $\frac{3}{4}$ span. “ Λ ” is a scalar proxy for vorticity, which is useful in complex flows to isolate rotational effects from small concentrations of shearing and other perturbations [104], and contours of Λ are thus a form of vortex tracking. There are noticeable differences in the flow pattern at these points in time. First, (a) a distinct leading edge vortex forms on the suction side of the plate. The starting vortex is visible just downstream of the trailing edge. At the minimum lift point (b), this vortex has shed and moved downstream while a new leading edge vortex forms. As the lift approaches the steady-state value (c) several vortices coexist above the wing. After this time there is a continuous pattern of shedding vortices in a quasi-periodic fashion. The images in Figure 8-7 suggest that the rapid build-up of lift during the initial stages of the wing stroke is due to the development of the attached leading edge vortex and the movement of the starting vortex away from the wing.

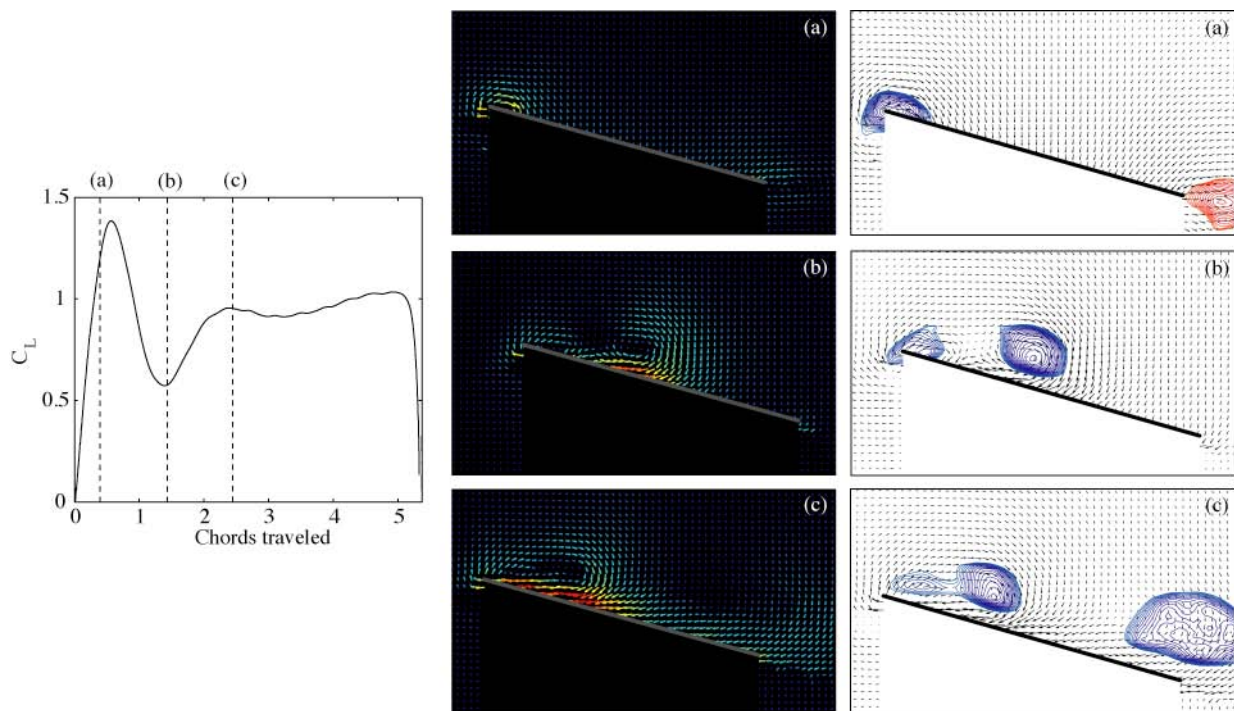


Figure 8-7: Flowfield Observed at Three Points During the Wing Stroke: (a) Near the Initial Peak at $x/c = 0.45 c$; (b) At the Lift Minimum at $x/c = 1.50 c$; and (c) At the Onset of the Quasi-Steady Period $x/c = 2.39 c$ – Force History (left), Velocity Field (centre) and Contours of Λ (right) for a Whirling Wing with Constant Acceleration Over $0.25 c$.

Recently it has been suggested that the attachment of the leading edge vortex is related not to the Reynolds number, but to the Rossby number. Lentink and Dickinson observed a stable LEV at low Rossby number ($Ro = \text{radius}/\text{chord}$) over a range of Reynolds numbers for a propeller-like motion [105]. The waving wing experiment has been performed at a Rossby number of both 2 and 4, well within the low Ro range identified by Lentink and Dickinson, but there is no evidence of an attached leading edge vortex over an extended period of time on the waving wing.

8.3.2 Leading Edge Vortex Circulation

Again considering a constant acceleration over $0.25 c$, the circulation of the LEV was computed by integrating along a contour of constant Λ to find the circulation in the usual way, $\Gamma = \oint u \cdot ds$. The computed circulation was then normalized by the local freestream velocity and wing chord. Figure 8-8 shows the normalized circulation of the first leading edge vortex formed at half-span at a 25° angle of attack. Each data point on the chart was computed from a separate snapshot of the velocity field as measured using PIV. The dashed line marks $x/c = 0.58$, the point of maximum lift.

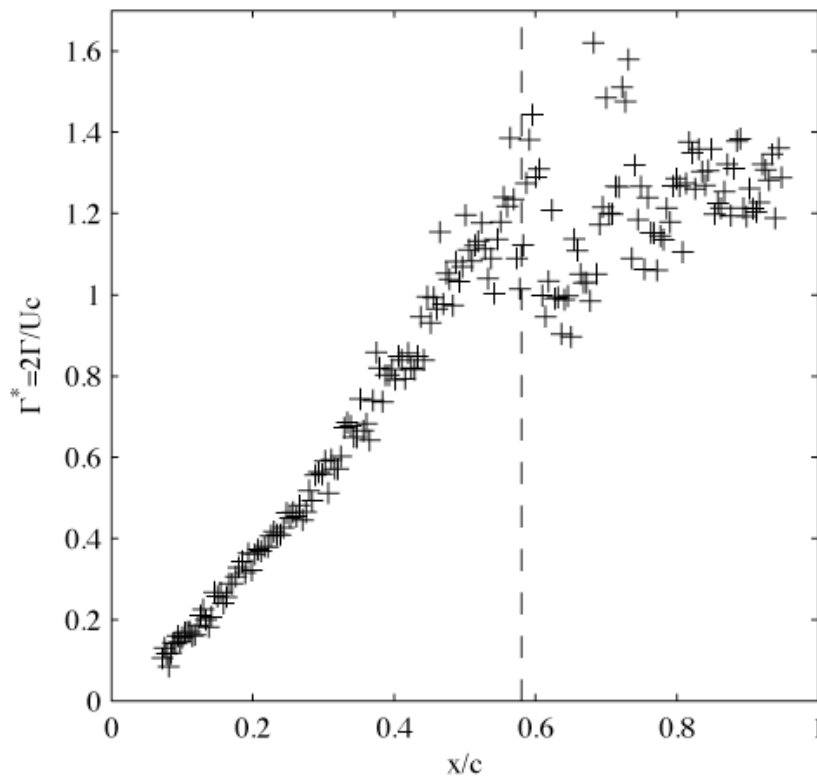


Figure 8-8: Normalized Circulation Computed from PIV Data at Half-Span; AR = 4, $\alpha = 25$ deg.

Figure 8-9 shows contours of $\Lambda \geq 0.6$ on top of the vorticity field for an aspect ratio 4 wing at a 25 degree angle of attack throughout the wing stroke. Each column represents a location on the wing span, and each row represents a wing stroke angle. From the start of the wing stroke, an attached leading edge vortex begins to form and almost all of the vorticity in the flowfield is contained in the $\Lambda = 0.6$ contour. The circulation of this leading edge vortex grows steadily until the point of maximum lift at $x/c = 0.58$. From Figure 8-8, the maximum strength of the attached leading edge vortex is near $\Gamma^* = 1.3$, at which point the leading edge vortex has elongated and a second region of high vorticity has appeared within the $\Lambda = 0.6$ contour. As the wing continues to move, the downstream portion of the leading edge vortex sheds and the two regions of vorticity become separate vortex cores.

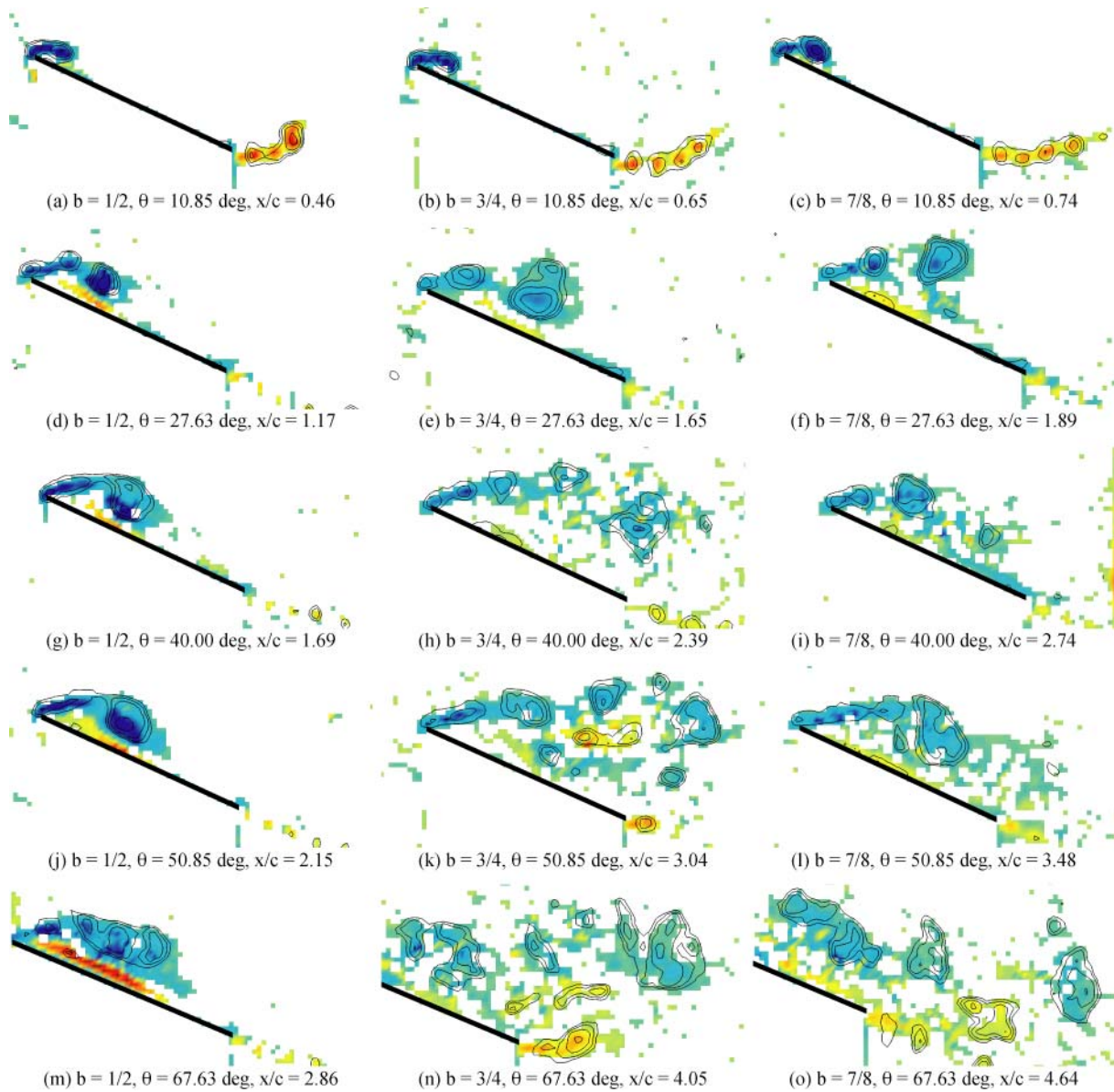


Figure 8-9: Chordwise View of Vorticity ($\omega/U'c$) and Λ -Contours; $AR = 4$, $\alpha = 25$ deg – each row represents the three stations on the wing at an instant in the wing stroke.

Near $x/c = 0.69$ it is difficult to reliably track the first vortex and Γ^* values jump between 1.0 and 1.3. Most of the vorticity is still contained within the higher-level Λ -contours, but there is also vorticity moving between the two vortex cores. As the wing stroke continues the separated leading edge vortex continues to move downstream and entrain this vorticity. Eventually this vortex rolls up into a more coherent structure at $x/c = 0.89$ and the Γ^* values become more reliable. The first vortex continues to move downstream and away from the still-attached second leading edge vortex. Vorticity is still present between the two vortex cores and the first vortex continues to entrain some of this vorticity causing the vortex to strengthen slightly.

8.3.3 Three-Dimensional Effects

The chordwise view presented in Figure 8-9 shows the vorticity field normalized by the local freestream velocity in order to reveal variations along the span. It can be seen that the normalized vorticity is higher near

NON-RECTILINEAR MOTIONS: WHIRLING FLAT PLATE

the wing root ($1/2$ span) than further outboard. This is particularly clear in (d) and (e). Also, the leading edge vortex is larger near the wingtip as shown in (a) – (c).

Figure 8-10 shows the spanwise view of the wing as the trailing edge passes through the light sheet at different points in the wing stroke (wing waving into the page, suction side of the wing on the right). There is a clear tip vortex visible from the start of the wing stroke (10.85 degrees) and a shear layer that becomes very clear at 67.63 degrees. Late in the wing stroke, the tip vortex is destroyed by the vorticity passing over the suction side of the wing. At lower angles of attack (5 and 15 degrees) the tip vortex persists throughout the wing stroke.

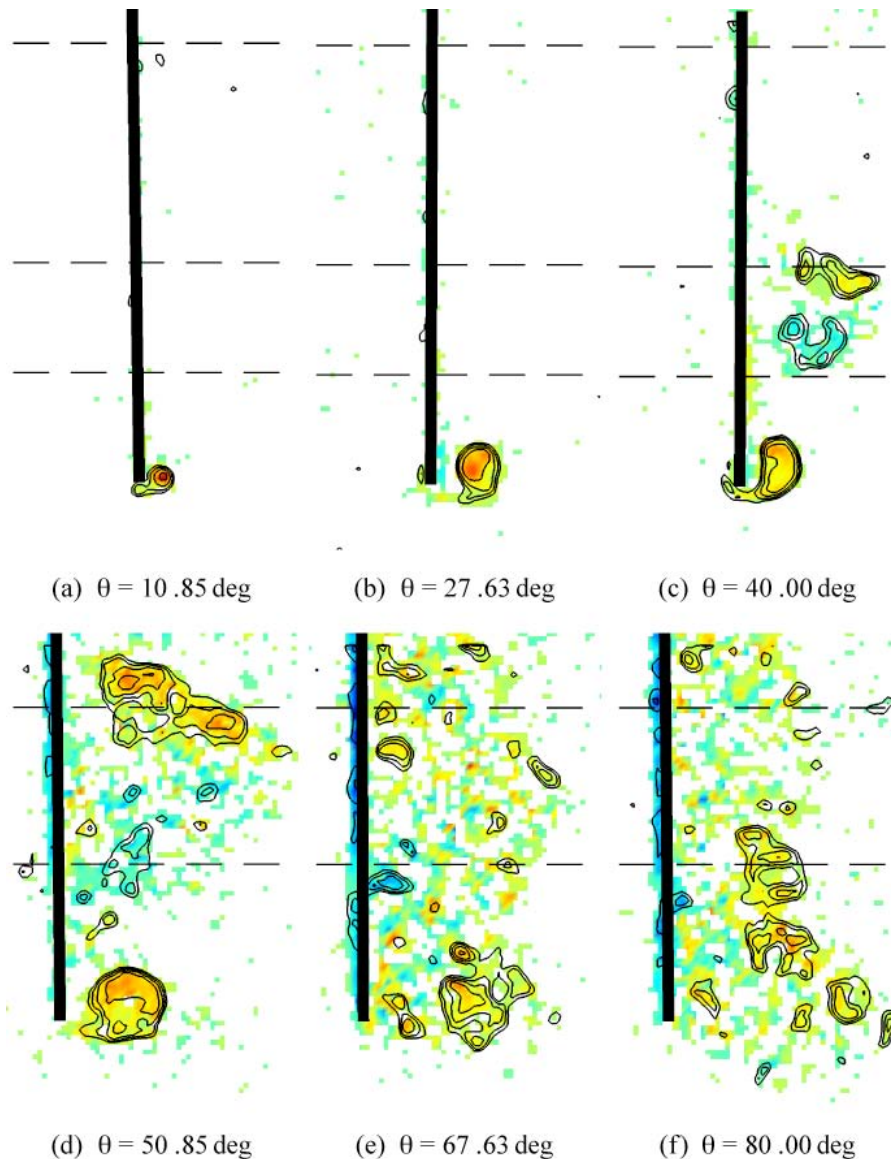


Figure 8-10: Spanwise View of Vorticity ($\omega/U'c$) and Λ -Contours; $AR = 4$, $\alpha = 25$ deg.

8.3.4 Flow Model Development

Based on these observations, we propose that the flow on an impulsively started waving wing develops over three stages as illustrated in Figure 8-11. At the start of the wing stroke, during the *initial transient*,

the flow-field is characterized by the growth of a strong leading edge vortex. Flow separates at the sharp leading edge and quickly forms a leading edge vortex that remains attached to the wing. During this phase the strengthening of the leading edge vortex causes a rapid increase in lift. This phase ends when the vortex sheds from the leading edge. The ultimate strength of the leading edge vortex and its development is influenced by the wing's acceleration pattern. Lower accelerations produce a slower vortex growth and reduce the strength at separation. However, above a certain level of acceleration the vortex development becomes independent from the kinematics.

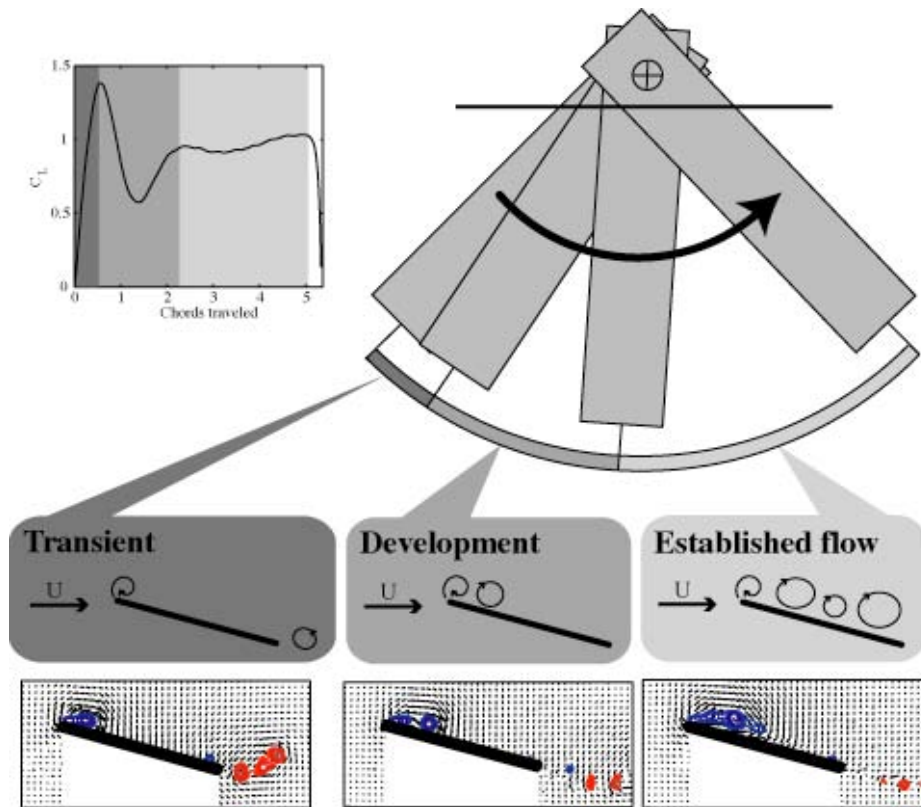


Figure 8-11: Proposed Model of Three Phases of Flowfield Development for the Whirling Plate.

The next flow observed on the waving wing is the developing flow, beginning with the separation of the initial leading edge vortex. Flow continues to separate over the leading edge and a second leading edge vortex forms. Because the first vortex is no longer close to the wing surface its effect on lift is diminished and the new leading edge vortex does not achieve the same ultimate strength before it sheds. In this phase the total lift is relatively low.

Finally, in the established flow phase a periodic pattern of vortex shedding from the leading edge is observed. During this phase there are typically three to four vortices present above the wing at all times producing a relatively high lift coefficient. At this point the structure of the flow-field appears to settle into a periodic vortex shedding but it is not yet certain how many chord-lengths must be traveled before the flow is truly in a periodic quasi-steady state.

8.4 SUMMARY OF THE WHIRLING WING EXPERIMENTS

The rotating wing experiment is a fully three-dimensional simplification of the flapping wing motion observed in nature for small flyers such as many insects. The spanwise velocity gradient and stopping and

NON-RECTILINEAR MOTIONS: WHIRLING FLAT PLATE

starting acceleration preserve key features of the wing stroke which are neglected by experiments concerned with established periodic flows.

All of the whirling-wing flows showed similar behavior. High lift (approximately 1.5 times the quasi-steady value) is achieved during the first chord-length of travel due to the strong attached leading edge vortex. After the initial leading edge vortex separates, lift values drop as the LEV passes downstream over the wing and a second LEV forms. LEVs continue to form, grow, and separate, but subsequent vortices are not as strong as the first one and lift values level out. Because the translational phase of the typical insect wing stroke is between 2 and 4 chord-lengths of travel, the initial lift transient and subsequent flow development phases on a waving wing are likely to be significant for lift production for MAV applications inspired by insect-type of flapping. Wing kinematics had only a small effect on the aerodynamic forces produced by the rotating wing. Quasi-steady lift and drag forces were very similar for all acceleration patterns tested. In the early stages of the wing stroke the velocity profile affected both the timing and magnitude of the lift peak for low accelerations. However, at high accelerations the velocity profile ceased to be significant. The measured circulation of the LEV agrees well with force data thus supporting, the proposed 3-stage model of flow development.

Of course, it remains to study whirling-wing motions at the high angles of attack more typical of insect-type of flight. But this can be said about all of the cases in our work, which have in general cleaved towards classical-dynamic stall motivation. As we conclude, we offer recommendations on how to generalize investigations both in extension of those presented above, and in conceptually new directions.

Chapter 9 – CONCLUSIONS AND OUTLOOK

9.1 RECAPITULATION OF THE TEST CASES IN THE PRESENT STUDY

There is a vast literature in unsteady aerodynamics at low Reynolds number, not just in applications to Micro Air Vehicles or natural flyers, but for airfoils in general, for aerodynamic testing of aerospace configurations in small-scale facilities where the Reynolds number happens to be low not by intention but by necessity, for fundamental studies such as oscillating circular cylinders, for flow-control experiments and on and on. Our objectives have been:

- 1) To extend to dynamic problems the recent work on static low Reynolds number airfoils, laminar separation bubbles, experimental and computational and methods for such airfoils;
- 2) To benchmark a broad range of experimental facilities and computational formulations established for research programs of the type that the present program is prototypical;
- 3) To assess the maturity and utility of various computational methods for low-Re unsteady aerodynamic predictions;
- 4) To assess the importance of flow quality in wind tunnels, water tunnels and tow tanks;
- 5) To observe how the low-Re unsteady aerodynamics problem might differ from the classical high-Re problem of dynamic stall; and most importantly; and
- 6) To begin to bridge the gap between practical MAV designers and the fluid mechanics community.

Such an endeavour is necessarily more grandiose in planning than in execution, and indeed the practical results are unavoidably episodic. We are limited to a few configurations and a few run conditions. We ignore important problems such as fluid-structure interaction, non-rectilinear motions, very low Re (below 10000), gust and other unsteady external forcing effects, and on and on.

Having established something of a baseline, it is now possible to be more systematic about pursuit of the various problems beyond the scope of the present study. Before passing towards enumeration of such possibilities, we pause to recapitulate the main findings from Chapters 3 – 8.

9.2 GENERAL CONCLUSIONS

At the juncture between fluid mechanics and MAV engineering, we are interested in the accurate prediction of aerodynamic forces – lift, thrust/drag, pitching moment and so forth (presently we are limiting focus on longitudinal quantities), as functions of motion kinematics, Reynolds number and model geometry. The flowfield structure is important in so far as we connect flowfield features such as LEV formation, growth, and shedding, with variations in the aerodynamic force time history, such as dynamic stall spikes in lift coefficient.

In this study we have considered primarily 6 cases: “deep stall” and “shallow stall” of three configurations: a SD7003 airfoil, a nominally 2D flat plate of 2 – 3% thickness and round edges, and an $AR = 2$ flat plate of the same sectional shape. These were studied primarily at a reduced frequency of 0.25 in sinusoidal periodic established motion. Broadly, we note that for the deep stall cases of all configurations, it is generally easier to capture the lift coefficient time history than for the shallow-stall case. Likewise, deep-stall flowfields vary less from shape to shape than do the shallow-stall cases. Lift coefficient history is easier to capture, in general, than drag coefficient history, and pitching moment is the most ornery of all. The importance of leading edge vortex resolution for force coefficient prediction goes in the same sequence.

CONCLUSIONS AND OUTLOOK

Classical analytical methods – inviscid quasi-steady lift curve slope and Theodorsen’s formula – deserve mention as predictions of lift coefficient time history for preliminary estimates, for example in parameter studies or conceptual design. We generally find that both shallow and deep dynamic stall at least in part effectively produce a trailing edge Kutta condition where statically the airfoil would be stalled. For the SD7003 in pure-plunge (deep stall), the simple-minded $2\pi\alpha$ has an error of ~ 0.4 CL at both peak and trough, while Theodorsen’s formula has an error of ~ 0.2 ; this should be regarded in the context of a peak-to-peak lift coefficient variation of about 2.5. The error bounds are somewhat larger for the 2D flat-plate, but absence of experimental data renders conclusions tenuous. On the other hand, $2\pi\alpha$ is a surprisingly successful approximation for the $AR = 2$ plate, in both pitch-plunge and pure-plunge. So caution is required in applying Theodorsen’s formula and quasi-steady attached-flow theory, and of course one should appreciate the bounds of studying only a few cases. Further, this predictive capability is generally suited only to lift – not drag and especially not pitch. Resolving the flowfield correctly is important for calculating aerodynamic loads that depend on the pressure distribution explicitly, and not just on its integration. Even so, the apparent suitability of the classical theoretical prediction for the $AR = 2$ plate is surprising and merits a rigorous parameter study of aspect ratio, effective angle of attack and other parameters.

Not surprisingly, the physics of boundary layer transition – facility flow quality and computational turbulence modelling, for example – become less important in overall flowfield and aerodynamic load prediction when there is a mechanism forcing transition, such as round leading edges of thin plates. Thus the scatter in our results for plate cases is much less than for airfoil cases.

Lacking prior experience, one might assert that inviscid methods, and even RANS, should predict aerodynamic force more accurately for shallow stall than for deep stall, because presumably complex viscous and transitional effects are more prevalent for separated flows. Our experience shows that for the infinite-span cases examined here, this is precisely not the case. Scatter amongst the computations and the experiments for shallow-stall was larger than for deep stall, and again larger for the airfoil than for the plate.

Only one finite aspect ratio case was considered: $AR = 2$. From these results, in deep and shallow stall, we find generally a smaller separation and a tighter LEV in the $AR = 2$ case than in the wall-to-wall (that is, 2D) cases, but no discernable difference in LEV stability. This should be considered in terms of insect-wing LEV stability mechanisms widely found in the literature, but again is only one data point and requires both a deeper examination and a wider parameter study.

At high reduced frequency, on the other hand, Theodorsen’s formula and vortex particle methods are excellent predictors of lift coefficient time history, because lift is traceable mathematically if not physically to so-called non-circulatory or inertial effects, which the inviscid theory captures. Of course, this is limited to periodic flows in periodic acceleration.

Finally, we made a brief examination of comparison between longitudinal motions and a rotating motion or “swinging” wing, where the latter has 3D effects such as spanwise pressure gradients. We did not find a large difference in vortex formation or lift time history between translation and rotation, at the Reynolds numbers and motion parameters of the present study. This, perhaps, is surprising in the context of recent literature – and again merits both deeper study and a larger parameter space investigation – of which we make suggestions below.

9.3 RECOMMENDATIONS FOR FURTHER WORK

Broadly, we suggest the following avenues for further research.

9.3.1 Extensions of Cases Studied in This Work

The first category is parameter studies based on the already achieved results, in particular to extend the findings on applicability of quasi-steady and Theodorsen's model, to explore the limits of effective angle of attack, to study aspect ratio effects and to find clear cases where leading edge vortices materially affect the lift coefficient time history. Ideas include:

- Sweep of the pitch parameter λ ; variation of λ such that effective angle of attack is held nearly constant, by varying h while keeping k constant, or vice versa, or both; there are many possibilities, all nominally equivalent if quasi-steady reasoning is valid. The purpose is to assess, for a given value of maximum effective angle of attack attained in the motion, indeed whether effective angle of attack makes sense.
- Parameter study to ascertain how common it is for there to simultaneously be a moment-stall but no lift-stall for sinusoidal pitch-plunge, plunge or pitch problems.
- Extension to higher Strouhal numbers to study deeper dynamic stall, to see if finally one finds a lift-stall and strong dynamic lift due to the leading edge vortex formation, shedding and convection.
- Further exploration of blockage effects and spanwise variations in ground-test facilities, for example by testing the same sectional geometry and Re but with different physical span to chord ratios (all nominally wall-to-wall) or by running computations in 3D that include the tunnel walls and the model support system.
- Parameter study of aspect ratio effects; $AR < 2$ and > 2 . Ideally this would involve volumetric velocimetry where one obtains not only three components but also a volume of data that includes the mid-span region and the tips.
- Extension of the recent studies on flapping-wing propulsive efficiency [18], to see for example how the various k - h - λ combinations affect thrust production and power consumption. This includes, of course, more robust direct-force measurements in experiments, and more thorough benchmarking of computations in predicting drag/thrust.
- Extension of waving-wing problems to the high angles of attack encountered in insect aerodynamics, where LEV production and retention is most critical to flight performance.
- Extension of waving-wing problems to much lower Reynolds number, bringing propeller-like experiments [100] with those studied under the present work.

9.3.2 Conceptual Departures Towards Other Kinds of Motions

Here we suggest possibilities in keeping with abstracted problems, but considering questions beyond those raised in the present study. Examples include:

- Transient longitudinal motions such as the classical problem of impulsive start of translational motion, pitch ramps or plunge ramps, and other non-periodic motions (trigonometric, linear or otherwise) where there are unsteady effects not only from the attained rate of motion, as would be the case with periodic problems too, but also from the start-up.
- Oscillatory problems in hover, where the nominal reduced frequency is infinite (because there is no free-stream) and vortices shed from each motion period remain nearby, to affect the flowfield and aerodynamic force history in the subsequent period.
- Combination of longitudinal-plane and non-longitudinal-plane motions, where the pitch varies sinusoidally but the model is rotating about a fixed point on one wing tip.

CONCLUSIONS AND OUTLOOK

9.3.3 Passage to More Flight-Like Problems

Ultimately the purpose of MAV-inspired aerodynamics research is to build better MAVs, on a foundation of scientific knowledge rather than mere intuition. To achieve this, the scientific community must transition its work to more flight-like problems, and to abstract questions encountered in flight applications to problems amenable to rigorous study in the lab. This has, of course, been a problem in all aeronautical applications, but the very novelty of MAVs makes the old problem new again. Examples of more flight-like investigations include:

- Study of passive fluid-structure interaction for flexible flight surfaces. This is a huge area, but one example generalizing our work would be flexible plates that passively camber, akin to bird wings, to attenuate leading edge separation at high instantaneous effective angles of attack, and hopefully produce better propulsive efficiency from flapping.
- Adaptation of both periodic and non-periodic motions to model atmospheric gusts relevant to MAV flight in urban environments. This involves both understanding gust spectra (spatial and temporal), and how to realize them in a ground test facility, for example by shuttering the tunnel or by using the motion rig to impose a motion (at high rate these two are demonstrably not equivalent).
- Study of motions in the frequency, amplitude and range of degrees of freedom relevant to aggressive manoeuvres of natural flyers, such as insects and bats.

Of course, no such list can ever presume to be comprehensive. Our only ambition is for it to be cogent and relevant – and, sadly, ineluctable biases stemming from one's own work make such an assessment impossible.

But let us conclude with optimism: Micro Air Vehicle aerodynamics is fascinating in its complexity, but this complexity need not be daunting for practical engineering approaches to aerodynamic force modelling for vehicle design. We already have a basic understanding of how flapping-wing MAVs and even natural flyers operate, or should operate. What remains is a thorough assessment, with the rigor and enthusiasm that aeronautical engineers applied to fixed-wing manned aircraft in the 1920s and 1930s, now recast in the new century of powered flight.

Chapter 10 – REFERENCES

- [1] Pines, D. and Bohorquez, F., “Challenges Facing Future Micro Air Vehicle Development”, *Journal of Aircraft*, Vol. 43, No. 2, pp. 290-305, 2006.
- [2] Shyy, W., Lian, Y., Tang, J., Viieru, D. and Liu, H., “Aerodynamics of Low Reynolds Number Flyers”, Cambridge University Press, 2008.
- [3] Mueller, T.J., “An Overview of Micro Air Vehicle Aerodynamics”, Fixed and Flapping Wing Aerodynamics for Micro Air Vehicle Applications, T.J. Mueller, Ed., *Progress in Aeronautics and Astronautics*, Vol. 195, AIAA, pp. 483-500, 2001.
- [4] Perkins, C.D. and Hage, R.E., “Airplane Performance, Stability and Control”, Wiley, 1958.
- [5] McCroskey, W.J., Carr, L.W. and McAlister, K.W., “Dynamic Stall Experiments on Oscillating Airfoils”, *AIAA J.*, Vol. 14, No. 1, pp. 57-63, 1976.
- [6] McCroskey, W.J., “Unsteady Airfoils”, *Ann. Rev. Fluid Mech.*, Vol. 14, pp. 285-311, 1982.
- [7] Carr, L., “Progress in Analysis and Prediction of Dynamic Stall”, *Journal of Aircraft*, Vol., 25, pp. 6-17, 1988.
- [8] Liiva, J., “Unsteady Aerodynamic and Stall Effects on Helicopter Rotor Blade Airfoil Sections”, *J. Aircraft*, Vol. 6, No. 1, pp. 46-51, 1969.
- [9] Carr, L. and McCroskey, W.J., “A Review of Recent Advances in Computational and Experimental Analysis of Dynamic Stall”, IUTAM Symposium on Fluid Dynamics of High Angle of Attack, 1992.
- [10] Ohmi, K., Coutanceau, M., Loc, T.P. and Dulieu, A., “Vortex Formation around an Oscillating and Translating Airfoil at Large Incidences”, *J. Fluid Mech.*, Vol. 211, pp. 37-60, 1990.
- [11] Ohmi, K., Coutanceau, M., Daube, O. and Loc, T.P., “Further Experiments on Vortex Formation around an Oscillating and Translating Airfoil at Large Incidences”, *J. Fluid Mech.*, Vol. 225, pp. 607-630, 1991.
- [12] Visbal, M. and Shang, J.S., “Investigation of the Flow Structure around a Rapidly Pitching Airfoil”, *AIAA J.*, Vol. 27, No. 8, pp. 1044-1051, 1989.
- [13] Ghosh Choudhuri, P. and Knight, D.D., “Effects of Compressibility, Pitch Rate, and Reynolds Number on Unsteady Incipient Leading-edge Boundary Layer Separation over a Pitching Airfoil”, *J. Fluid Mech.*, Vol. 308, pp. 195-217, 1996.
- [14] Platzer, M. and Jones, K., “Flapping Wing Aerodynamics – Progress and Challenges”, AIAA-2006-0500.
- [15] Koochesfahani, M.M., “Vortical Patterns in the Wake of an Oscillating Airfoil”, *AIAA J.*, Vol. 27, No. 9, pp. 1200-1205, September 1989.
- [16] McAlister, K.W. and Carr, L.W., “Water Tunnel Visualization of Dynamic Stall”, *Journal of Fluids Engineering*, Vol. 101, pp. 376-380, September 1978.

REFERENCES

- [17] Walker, J.M., Helin, H.E. and Strickland, J.H., "An Experimental Investigation of an Airfoil Undergoing Large-Amplitude Pitching Motions", *AIAA J.*, Vol. 23, No. 8, pp. 1141-1142, August 1985.
- [18] Anderson, J.M., Streitlien, K., Barrett, D.S. and Triantafyllou, M.S., "Oscillating Foils of High Propulsive Efficiency", *J. Fluid Mech.*, Vol. 360, pp. 41-72, 1998.
- [19] Triantafyllou, G.S., Triantafyllou, M.S. and Grosenbaugh, M.A., "Optimal Thrust Development in Oscillating Foils with Applications to Fish Propulsion", *J. Fluids and Structures*, Vol. 7, pp. 205, 224, 1992.
- [20] Young, J. and Lai, J.C.S., "Oscillation Frequency and Amplitude Effects on the Wake of a Plunging Airfoil", *AIAA Journal*, Vol. 42, No. 10, pp. 2042-2052, 2004.
- [21] Jones, K.D., Dohring, C.M. and Platzer, M.F., "Wake Structures Behind Plunging Airfoils: A Comparison of Numerical and Experimental Results", AIAA Paper 1996-0078.
- [22] Lian, Y. and Shyy, W., "Aerodynamics of Low Reynolds Number Plunging Airfoil under Gusty Environment", AIAA Paper 2007-0071.
- [23] Radespiel, R., Windte, J. and Scholz, U., "Numerical and Experimental Flow Analysis of Moving Airfoils with Laminar Separation Bubbles", *AIAA Journal*, Vol. 45, No. 6, pp. 1346-1356, June 2007.
- [24] Birnbaum, W., "Das ebene Problem des schlagenden Flügels", Dissertation, Universität Göttingen, 1922.
- [25] Küssner, H.G., "Schwingungen von Flugzeugflügeln", *Luftfahrtforschung*, 4, pp. 41-62, 1929.
- [26] Theodorsen, T., "General Theory of Aerodynamic Instability and the Mechanisms of Flutter", NACA Report No. 496, 1934.
- [27] Garrick, I.E., "Propulsion of a Flapping and Oscillating Airfoil", NACA Report No. 576, 1936.
- [28] Wagner, H., "Über die Entstehung des dynamischen Auftriebs von Tragflügeln", *ZAMM*, 5 (1), pp. 17-35, 1925.
- [29] Pendersen, C.B. and Zbikowski, R., "An Indicical Polhamus Aerodynamic Model of Insect-like Flapping Wings in Hover", In R. Liebe (Ed.), *Flow Phenomena in Nature*, Vol. 2, WIT Press, Southampton, UK, pp. 606-665, 2006.
- [30] Jones, K.D. and Platzer, M.F., "Numerical Computation of Flapping-Wing Propulsion and Power Extraction", AIAA 1997-0828.
- [31] Platzer, M.F., "Flapping Wing Aerodynamics: Progress and Challenges", *AIAA Journal*, 46, pp. 2137-2149, 2008.
- [32] Galbraith, M. and Visbal, M., "Implicit Large Eddy Simulation of Low Reynolds Number Flow Past the SD7003 Airfoil", AIAA 2008-0225.
- [33] Menter, F.R., Langtry, R.B., Likki, S.R., Suzen, Y.B., Huang, P.G. and Volker, S., "A Correlation-Based Transition Model Using Local Variables – Part I: Model Formulation", *Journal of Turbomachinery*, Vol. 128, 2006.

- [34] Radespiel, R., Windte, J. and Scholz, U., "Numerical and Experimental Flow Analysis of Moving Airfoils with Laminar Separation Bubbles", *AIAA Journal*, 45, pp. 1357-1369, 2007.
- [35] Lian, Y. and Shyy, W., "Laminar-Turbulent Transition of a Low Reynolds Number Rigid or Flexible Airfoil", *AIAA Journal*, 45, pp. 1501-1513, 2007.
- [36] Philips, P.J., East, R.A. and Pratt, N.H., "An Unsteady Lifting Line Theory of Flapping Wings with Application to the Forward Flight of Birds", *J. Fluid Mech.*, 112, pp. 97-125, 1981.
- [37] Hall, K.C. and Hall, S.R., "A Rational Engineering Analysis of the Efficiency of Flapping Flight", In T.J. Mueller (Ed.): Fixed and Flapping Wing Aerodynamics for Micro Air Vehicle Applications, *Progress in Astronautics and Aeronautics*, AIAA, Reston, VA, USA, pp. 249-274, 2001.
- [38] Ellington, C.P., "The Aerodynamics of Hovering Insect Flight", *Philosophical Transactions of the Royal Society of London*, Series B 305, pp. 1-181, 1984.
- [39] Walker, J.A. and Westneat, M.W., "Mechanical Performance of Aquatic Rowing and Flying", *Proceedings of the Royal Society of London*, Series B 267, pp. 1875-1881, 2000.
- [40] Sane, S.P. and Dickinson, M.H., "The Control of Flight Force by a Flapping Wing: Lift and Drag Production", *J. of Exp. Biology*, 204, pp. 2607-2626, 2001.
- [41] Rist, U., "Instability and Transition Mechanisms in Laminar Separation Bubbles", RTO-AVT-VKI Lecture Series 2004, November 24-28, 2004.
- [42] McMahon, T.A. and Bonner, J.T., "On Size and Life", *Sci. Am.*, Library: New York, USA, 1983.
- [43] Azuma, A., "The Biokinetics of Flying and Swimming", Springer-Verlag, Tokyo, Japan, Chap. 3, pp. 41-48, 1992.
- [44] Jones, A.R., Bakhtian, N. and Babinsky, H., "Low Reynolds Number Aerodynamics of Leading Edge Flaps", *J. Aircraft*, Vol. 45, No. 1, pp. 342-345, January-February 2008.
- [45] Tennekes, H., "The Simple Science of Flight", MIT Press, 1997.
- [46] McGahan, J., "Flapping Flight of the Andean Condor in Nature", *J. Exp. Biol.*, 58, pp. 239-253, 1973.
- [47] Brown, R.H.J., "The Flight of Birds", *Biol. Rev.*, 38, pp. 460-489, 1963.
- [48] Stolpe, M. and Zimmer, K., "Der Schwirrflug des Kolibri im Zeitlupenfilm", *J. Orn.*, Lpz. 87, pp. 136-155, 1939.
- [49] http://www.ae.uiuc.edu/m-selig/ads/coord_database.html.
- [50] Hanff, E., et al., "Low Reynolds Number Aerodynamics of Micro/Mini and High Altitude Vehicles", RTO-TR-AVT-101 AC/323(AVT-101)TP/110, Final Report.
- [51] Taylor, G.K., Nudds, R.L. and Thomas, A.L.R., "Flying and Swimming Animals Cruise at a Strouhal Number Tuned for High Power Efficiency", *Nature*, London, UK, Vol. 425, pp. 707-11, 2003.
- [52] Ol, M.V., McAuliffe, B.R., Hanff, E.S., Scholz, U. and Kaehler, Ch., "Comparison of Laminar Separation Bubble Measurements on a Low Reynolds Number Airfoil in Three Facilities", AIAA 2005-5149.

REFERENCES

- [53] Kaplan, S., Altman, A. and Ol, M.V., "Wake Vorticity Measurements for Low Aspect Ratio Wings at Low Reynolds Number", *Journal of Aircraft*, Vol. 44, No. 1, pp. 241-251, 2007.
- [54] Willert, C.E. and Gharib, M., "Digital Particle Image Velocimetry", *Experiments in Fluids*, Vol. 10, No. 4, January, 1991.
- [55] Ol, M.V., Bernal, L., Kang, C.-K. and Shyy, W., "Shallow and Deep Dynamic Stall for Flapping Low Reynolds Number Airfoils", *Experiments in Fluids*, Vol. 46, Issue 5, pp. 883-901, May 2009.
- [56] Bansmer, S., Scholz, U., Windte, J., Kähler, C.J. and Radespiel, R., "Flow Field Measurements on an Oscillating Airfoil for Flapping Wing Propulsion", AIAA-2008-0581.
- [57] Bansmer, S., Mazlum, E. and Radespiel, R., "A Comparison of Numerical RANS Simulations and Flow Field Measurements of an Oscillating Airfoil for Flapping Wing Propulsion", 26th ICAS Congress, Anchorage, AK, USA, September 2008.
- [58] Kirmse, T. and Wagner, A., "Advanced Methods for In-Flight Flap Gap and Wing Deformation Measurements in the Project AWIATOR", Proc. of 1st CEAS European Air and Space Conference, Berlin, Germany, Paper 206, pp. 7, 10-13th September 2007.
- [59] Konrath, R., Klein, C., Schröder, A. and Kompenhans, J., "Combined Application of Pressure Sensitive Paint and Particle Image Velocimetry to the Flow Above a Delta Wing", *Exp. Fluids*, Vol. 44, pp. 357-366, 2008.
- [60] Rao, Y.-J., "In-Fibre Bragg Grating Sensors", *Meas. Sci. Tech.*, Vol. 8, No. 4, pp. 355-375, April 1997.
- [61] http://www.micronoptics.com/sensing_instruments.php.
- [62] Wokoeck, R., Möller, T., Emge, M. and Radespiel, R., "Experimental Investigations of the Aerodynamic Properties of Micro Air Vehicles in Motion", Proceedings EMAV 2008 Conference, 8-10 July 2008.
- [63] Möller, T., Wokoeck, R., Emge, M., Schüssler, J. and Radespiel, R., "Experimental Investigations of the Aerodynamic Characteristics of Moving Micro Air Vehicle Wings", Paper DLRG 2008-81304, Deutscher Luft- und Raumfahrtkongress 2008, Darmstadt, Germany, 23-25 September 2008.
- [64] Beal, D.N., Hover, F.S., Triantafyllou, M.S., Liao, J.C. and Lauder, G.V., "Passive Propulsion in Vortex Wakes", *J. of Fluid Mech.*, Vol. 549, pp. 385-402, 2006.
- [65] Rival, D. and Tropea, C., "Characteristics of Pitching and Plunging Airfoils under Dynamic-Stall Conditions", *J. of Aircraft* (in press).
- [66] Rival, D., Prangemeier, T. and Tropea, C., "The Influence of Airfoil Kinematics on the Formation of Leading-Edge Vortices in Bio-Inspired Flight", *Experiments in Fluids*, Vol. 46, No. 5, pp. 823-833, 2009.
- [67] Anderson, D.A., Tannehill, J.C. and Pletcher, R.H., "Computational Fluid Mechanics and Heat Transfer", McGraw-Hill Book Company, 1984.
- [68] Visbal, M.R. and Rizzetta, D.P., "Large-Eddy Simulation on Curvilinear Grids Using Compact Differencing and Filtering Schemes", *Journal of Fluids Engineering*, 124:836-847, 2002.

-
- [69] Visbal, M.R., Morgan, P.E. and Rizzetta, D.P., “An Implicit LES Approach Based on High-Order Compact Differencing and Filtering Schemes”, AIAA Paper 2003-4098.
 - [70] Visbal, M.R. and Gaitonde, D.V., “High-Order-Accurate Methods for Complex Unsteady Subsonic Flows”, *AIAA Journal*, Vol. 37, No. 10, pp. 1231-1239, 1999.
 - [71] Visbal, M.R. and Gaitonde, D.V., “On the Use of High-Order Finite-Difference Schemes on Curvilinear and Deforming Meshes”, *Journal of Computational Physics*, 181:155-185, 2002.
 - [72] Katz, J. and Plotkin, A., “Low Speed Aerodynamics”, Cambridge University Press, 2006.
 - [73] Karamcheti, K., “Principles of Ideal-Flow Aerodynamics”, Krieger Publishing Company, 1980.
 - [74] Fluent v.6.3 User’s Guide, 2006.
 - [75] Menter, F.R., “Two-Equation Eddy-Viscosity Turbulence Models for Engineering Applications”, *AIAA Journal*, Vol. 32, No. 8, pp. 1598-1605, August 1994.
 - [76] Gunaydinoglu, E. and Kurtulus, D.F., “Numerical Investigation of Pure Plunge and Pitch/Plunge Motions at Low Reynolds Numbers”, International Symposium of Light-Weight Unmanned Aerial Vehicle Systems and Subsystems, Ostend, Belgium, March 2009.
 - [77] Menter, F.R., Kuntz, M. and Langtry, R., “Ten Years of Industrial Experience with the SST Turbulence Model”, In: Hanjalic, K., Nagano, Y. and Tummers, M. (Eds.), *Turbulence, Heat and Mass Transfer 4*, Begell House, pp. 625-632, 2003.
 - [78] Menter, F.R., “Two-Equation Eddy-Viscosity Turbulence Models for Engineering Application”, *AIAA J.*, Vol. 32, pp. 269-289, 1994.
 - [79] Kamakoti, R., Thakur, S., Wright, J. and Shyy, W., “Validation of a New Parallel All-Speed CFD Code in a Rule-Based Framework for Multidisciplinary Applications”, AIAA 2006-3063.
 - [80] Shyy, W., “A Study of Finite Difference Approximations to Steady-State, Convection-Dominated Flow Problems”, *Journal of Computational Physics*, Vol. 57, No. 3, pp. 415-438, 1985.
 - [81] Shyy, W., “Computational Modeling for Fluid Flow and Interfacial Transport”, Elsevier, Amsterdam, Netherlands, 1994.
 - [82] Thomas, P.D. and Lombard, K., “The Geometric Conservation Law – A Link between Finite-Difference and Finite-Volume Methods of Flow Computation on Moving Grids”, AIAA 1978-1208.
 - [83] Shyy, W., Udaykumar, H.S., Rao, M.M. and Smith, R.W., “Computational Fluid Dynamics with Moving Boundaries”, Taylor & Francis, Washington, DC, (1996, Revised printing 1997, 1998 & 2001), Dover, NY, USA, 2007.
 - [84] Kang, C., Baik, Y., Bernal, L., Ol, M.V. and Shyy, W., “Fluid Dynamics of Pitching and Plunging Airfoils of Reynolds Number between 1×10^4 and 6×10^4 ”, AIAA 2009-536.
 - [85] Kang, C., Aono, H., Trizila, P., Baik, Y., Rausch, J., Bernal, L., Ol, M.V. and Shyy, W., “Modeling of Pitching and Plunging Airfoils at Reynolds Number between 1×10^4 and 6×10^4 ”, AIAA 2009-4100.
 - [86] Yuan, W. and Khalid, M., “Computation of Unsteady Flows Past Aircraft Wings at Low Reynolds Numbers”, *Canadian Aeronautics and Space Journal*, 50(4): 261-271, 2004.
-

REFERENCES

- [87] Yuan, W., Khalid, M., Windte, J., Scholz, U. and Radespiel, R., "Computational and Experimental Investigations of Low-Reynolds-Number Flows Past an Airfoil", *The Aeronautical Journal*, 111(1115):17-29, 2007.
- [88] Yuan, W., Xu, H., Khalid, M. and Radespiel, R., "A Parametric Study of LES on Laminar-turbulent Transitional Flows Past an Airfoil", *International Journal of Fluid Dynamics*, 20(1):45-54, 2006.
- [89] Yuan, W. and Khalid, M., "Preliminary CFD Studies of Flapping-Wing Aerodynamics", *Canadian Aeronautics and Space Journal*, 54(3/4):51-63, 2008.
- [90] Patankar, S.V., "Numerical Heat Transfer and Fluid Flow", Hemisphere Publishing Corporation, Washington, New York, London, 1980.
- [91] Ferziger, J.H. and Perić, M., "Computational Methods for Fluid Dynamics", Springer-Verlag, Berlin & Heidelberg, Germany, 1996.
- [92] Yuan, W. and Schilling, R., "Numerical Simulation of the Draft Tube and Tailwater Flow Interaction", *Journal of Hydraulic Research*, 40(1):73-81, 2002.
- [93] Demirdžić, I. and Perić, M., "Finite Volume Method for Prediction of Fluid Flow in Arbitrarily Shaped Domains with Moving Boundaries", *International Journal for Numerical Methods in Fluids*, 10:771-790, 1990.
- [94] Barth, T.J., Pulliam, T.H. and Buning, P.G., "Navier-Stokes Computations for Exotic Airfoils", AIAA-1985-109.
- [95] DeLaurier, J.D., "An Aerodynamic Model for Flapping-Wing Flight", *Aeronautical Journal*, April 1993.
- [96] Prouty, R., "Helicopter Performance, Stability and Control", Krieger Publishing Company, Florida, USA, 1989.
- [97] Ol, M.V., "Vortical Structures in High Frequency Pitch and Plunge at Low Reynolds Number", AIAA 2007-4233.
- [98] Visbal, M., "High-Fidelity Simulation of Transitional Flows past a Plunging Airfoil", AIAA 2009-0391.
- [99] Usherwood, J.R. and Ellington, C.P., "The Aerodynamics of Revolving Wings: I. Model Hawkmoth Wings", *Journal of Experimental Biology*, Vol. 205, pp. 1547-1564, 2002.
- [100] Ellington, C.P., "The Aerodynamics of Hovering Insect Flight, III. Kinematics", *Philosophical Transactions of the Royal Society of London, Series B, Biological Sciences*, Vol. 305, No. 1122, pp. 41-78, February 1984.
- [101] Dudley, R., "The Biomechanics of Insect Flight", Princeton University Press, 2000.
- [102] Dickinson, M.H. and Götz, K.G., "Unsteady Aerodynamic Performance of Model Wings at Low Reynolds Numbers", *Journal of Experimental Biology*, Vol. 174, No. 1, pp. 45-64, January 1993.
- [103] Beckwith, R. and Babinsky, H., "Impulsively Started Flat Plate Wing", *Accepted to Journal of Aircraft*, 2009.

- [104] Graftieaux, L., Michard, M. and Grosjean, N., “Combining PIV, POD and Vortex Identification Algorithms for the Study of Unsteady Turbulent Swirling Flows”, *Measurement Science and Technology*, Vol. 12, pp. 1422-1429, 2003.
- [105] Lentink, D. and Dickinson, M., “Rotational Accelerations Stabilize Leading Edge Vortices on Revolving Fly Wings”, *Journal of Experimental Biology*, Vol. 212, pp. 2705-2719, 2009.

REFERENCES



REPORT DOCUMENTATION PAGE																	
1. Recipient's Reference	2. Originator's References	3. Further Reference	4. Security Classification of Document														
	RTO-TR-AVT-149 AC/323(AVT-149)TP/332	ISBN 978-92-837-0118-7	UNCLASSIFIED/ UNLIMITED														
5. Originator	Research and Technology Organisation North Atlantic Treaty Organisation BP 25, F-92201 Neuilly-sur-Seine Cedex, France																
6. Title	Unsteady Aerodynamics for Micro Air Vehicles																
7. Presented at/Sponsored by	Final Report of Task Group AVT-149.																
8. Author(s)/Editor(s)	Multiple		9. Date September 2010														
10. Author's/Editor's Address	Multiple		11. Pages 160														
12. Distribution Statement	There are no restrictions on the distribution of this document. Information about the availability of this and other RTO unclassified publications is given on the back cover.																
13. Keywords/Descriptors	<table border="0"> <tbody> <tr> <td>Airfoil</td> <td>Micro Air Vehicles (MAV)</td> </tr> <tr> <td>Dynamic lift</td> <td>Pitching</td> </tr> <tr> <td>Dynamic stall</td> <td>Plunging</td> </tr> <tr> <td>Flapping</td> <td>Quasi-steady</td> </tr> <tr> <td>Leading edge vortex</td> <td>Unsteady aerodynamics</td> </tr> <tr> <td>Low aspect ratio</td> <td>Vortex shedding</td> </tr> <tr> <td>Low Reynolds number</td> <td></td> </tr> </tbody> </table>			Airfoil	Micro Air Vehicles (MAV)	Dynamic lift	Pitching	Dynamic stall	Plunging	Flapping	Quasi-steady	Leading edge vortex	Unsteady aerodynamics	Low aspect ratio	Vortex shedding	Low Reynolds number	
Airfoil	Micro Air Vehicles (MAV)																
Dynamic lift	Pitching																
Dynamic stall	Plunging																
Flapping	Quasi-steady																
Leading edge vortex	Unsteady aerodynamics																
Low aspect ratio	Vortex shedding																
Low Reynolds number																	
14. Abstract	<p>Recognizing that the flowfield environments encountered by Micro Air Vehicles (MAVs) are fundamentally unsteady – whether for fixed-wing, rotary-wing or flapping-wing configurations, AVT-149 seeks to address fundamental questions in unsteady low Reynolds number aerodynamics to establish a better knowledge base for aerodynamic MAV design. AVT-149 studied computationally, experimentally and analytically a progression of abstracted configurations, from 2D airfoils in pure-plunge through 3D wing planforms in plunge and pitch-plunge, to better understand the interplay between the motion, the flowfield, and the resulting aerodynamic loads history. We also compare translational and rotational transient motions.</p>																





BP 25

F-92201 NEUILLY-SUR-SEINE CEDEX • FRANCE
Télécopie 0(1)55.61.22.99 • E-mail mailbox@rta.nato.int**DIFFUSION DES PUBLICATIONS**
RTO NON CLASSIFIEES

Les publications de l'AGARD et de la RTO peuvent parfois être obtenues auprès des centres nationaux de distribution indiqués ci-dessous. Si vous souhaitez recevoir toutes les publications de la RTO, ou simplement celles qui concernent certains Panels, vous pouvez demander d'être inclus soit à titre personnel, soit au nom de votre organisation, sur la liste d'envoi.

Les publications de la RTO et de l'AGARD sont également en vente auprès des agences de vente indiquées ci-dessous.

Les demandes de documents RTO ou AGARD doivent comporter la dénomination « RTO » ou « AGARD » selon le cas, suivi du numéro de série. Des informations analogues, telles que le titre et la date de publication sont souhaitables.

Si vous souhaitez recevoir une notification électronique de la disponibilité des rapports de la RTO au fur et à mesure de leur publication, vous pouvez consulter notre site Web (www.rto.nato.int) et vous abonner à ce service.

CENTRES DE DIFFUSION NATIONAUX**ALLEMAGNE**

Streitkräfteamt / Abteilung III
Fachinformationszentrum der Bundeswehr (FIZBw)
Gorch-Fock-Straße 7, D-53229 Bonn

BELGIQUE

Royal High Institute for Defence – KHID/IRSD/RHID
Management of Scientific & Technological Research
for Defence, National RTO Coordinator
Royal Military Academy – Campus Renaissance
Renaissancelaan 30, 1000 Bruxelles

CANADA

DSIGRD2 – Bibliothécaire des ressources du savoir
R et D pour la défense Canada
Ministère de la Défense nationale
305, rue Rideau, 9^e étage
Ottawa, Ontario K1A 0K2

DANEMARK

Danish Acquisition and Logistics Organization (DALO)
Lautrupbjerg 1-5, 2750 Ballerup

ESPAGNE

SDG TECEN / DGAM
C/ Arturo Soria 289
Madrid 28033

ETATS-UNIS

NASA Center for AeroSpace Information (CASI)
7115 Standard Drive
Hanover, MD 21076-1320

FRANCE

O.N.E.R.A. (ISP)
29, Avenue de la Division Leclerc
BP 72, 92322 Châtillon Cedex

GRECE (Correspondant)

Defence Industry & Research General
Directorate, Research Directorate
Fakinos Base Camp, S.T.G. 1020
Holargos, Athens

HONGRIE

Hungarian Ministry of Defence
Development and Logistics Agency
P.O.B. 25
H-1885 Budapest

ITALIE

General Secretariat of Defence and
National Armaments Directorate
5th Department – Technological
Research
Via XX Settembre 123
00187 Roma

LUXEMBOURG

Voir Belgique

NORVEGE

Norwegian Defence Research
Establishment
Attn: Biblioteket
P.O. Box 25
NO-2007 Kjeller

PAYS-BAS

Royal Netherlands Military
Academy Library
P.O. Box 90.002
4800 PA Breda

POLOGNE

Centralna Biblioteka Wojskowa
ul. Ostrobramska 109
04-041 Warszawa

PORTUGAL

Estado Maior da Força Aérea
SDFA – Centro de Documentação
Alfragide
P-2720 Amadora

REPUBLIQUE TCHEQUE

LOM PRAHA s. p.
o. z. VTÚLaPVO
Mladoboleslavská 944
PO Box 18
197 21 Praha 9

ROUMANIE

Romanian National Distribution
Centre
Armaments Department
9-11, Drumul Taberei Street
Sector 6
061353, Bucharest

ROYAUME-UNI

Dstl Knowledge and Information
Services
Building 247
Porton Down
Salisbury SP4 0JQ

SLOVAQUIE

Akadémia ozbrojených síl gen.
M.R. Štefánika, Distribučné a
informačné stredisko RTO
Demänová 393, Liptovský Mikuláš 6
031 06

SLOVENIE

Ministry of Defence
Central Registry for EU and
NATO
Vojkova 55
1000 Ljubljana

TURQUIE

Milli Savunma Bakanlığı (MSB)
ARGE ve Teknoloji Dairesi
Başkanlığı
06650 Bakanlıklar
Ankara

AGENCES DE VENTE**NASA Center for AeroSpace
Information (CASI)**

7115 Standard Drive
Hanover, MD 21076-1320
ETATS-UNIS

**The British Library Document
Supply Centre**

Boston Spa, Wetherby
West Yorkshire LS23 7BQ
ROYAUME-UNI

**Canada Institute for Scientific and
Technical Information (CISTI)**

National Research Council Acquisitions
Montreal Road, Building M-55
Ottawa K1A 0S2, CANADA

Les demandes de documents RTO ou AGARD doivent comporter la dénomination « RTO » ou « AGARD » selon le cas, suivie du numéro de série (par exemple AGARD-AG-315). Des informations analogues, telles que le titre et la date de publication sont souhaitables. Des références bibliographiques complètes ainsi que des résumés des publications RTO et AGARD figurent dans les journaux suivants :

Scientific and Technical Aerospace Reports (STAR)

STAR peut être consulté en ligne au localisateur de ressources
uniformes (URL) suivant: <http://www.sti.nasa.gov/Pubs/star/Star.html>
STAR est édité par CASI dans le cadre du programme
NASA d'information scientifique et technique (STI)
STI Program Office, MS 157A
NASA Langley Research Center
Hampton, Virginia 23681-0001
ETATS-UNIS

Government Reports Announcements & Index (GRA&I)

publié par le National Technical Information Service
Springfield
Virginia 2216
ETATS-UNIS
(accessible également en mode interactif dans la base de
données bibliographiques en ligne du NTIS, et sur CD-ROM)



BP 25

F-92201 NEUILLY-SUR-SEINE CEDEX • FRANCE
Télécopie 0(1)55.61.22.99 • E-mail mailbox@rta.nato.int



DISTRIBUTION OF UNCLASSIFIED RTO PUBLICATIONS

AGARD & RTO publications are sometimes available from the National Distribution Centres listed below. If you wish to receive all RTO reports, or just those relating to one or more specific RTO Panels, they may be willing to include you (or your Organisation) in their distribution.

RTO and AGARD reports may also be purchased from the Sales Agencies listed below.

Requests for RTO or AGARD documents should include the word 'RTO' or 'AGARD', as appropriate, followed by the serial number. Collateral information such as title and publication date is desirable.

If you wish to receive electronic notification of RTO reports as they are published, please visit our website (www.rto.nato.int) from where you can register for this service.

NATIONAL DISTRIBUTION CENTRES

BELGIUM

Royal High Institute for Defence – KHID/IRSD/RHID
Management of Scientific & Technological Research
for Defence, National RTO Coordinator
Royal Military Academy – Campus Renaissance
Renaissancelaan 30
1000 Brussels

CANADA

DRDKIM2 – Knowledge Resources Librarian
Defence R&D Canada
Department of National Defence
305 Rideau Street, 9th Floor
Ottawa, Ontario K1A 0K2

CZECH REPUBLIC

LOM PRAHA s. p.
o. z. VTÚLaPVO
Mladoboleslavská 944
PO Box 18
197 21 Praha 9

DENMARK

Danish Acquisition and Logistics Organization (DALO)
Lautrupbjerg 1-5
2750 Ballerup

FRANCE

O.N.E.R.A. (ISP)
29, Avenue de la Division Leclerc
BP 72, 92322 Châtillon Cedex

GERMANY

Streitkräfteamt / Abteilung III
Fachinformationszentrum der Bundeswehr (FIZBw)
Gorch-Fock-Straße 7
D-53229 Bonn

GREECE (Point of Contact)

Defence Industry & Research General Directorate
Research Directorate, Fakinos Base Camp
S.T.G. 1020
Holargos, Athens

HUNGARY

Hungarian Ministry of Defence
Development and Logistics Agency
P.O.B. 25
H-1885 Budapest

ITALY

General Secretariat of Defence and
National Armaments Directorate
5th Department – Technological
Research
Via XX Settembre 123
00187 Roma

LUXEMBOURG

See Belgium

NETHERLANDS

Royal Netherlands Military
Academy Library
P.O. Box 90.002
4800 PA Breda

NORWAY

Norwegian Defence Research
Establishment
Attn: Biblioteket
P.O. Box 25
NO-2007 Kjeller

POLAND

Centralna Biblioteka Wojskowa
ul. Ostrobramska 109
04-041 Warszawa

PORTUGAL

Estado Maior da Força Aérea
SDFA – Centro de Documentação
Alfragide
P-2720 Amadora

ROMANIA

Romanian National Distribution
Centre
Armaments Department
9-11, Drumul Taberei Street
Sector 6, 061353, Bucharest

SLOVAKIA

Akadémia ozbrojených síl gen.
M.R. Štefánika, Distribučné a
informačné stredisko RTO
Demänová 393, Liptovský Mikuláš 6
031 06

SLOVENIA

Ministry of Defence
Central Registry for EU & NATO
Vojkova 55
1000 Ljubljana

SPAIN

SDG TECEN / DGAM
C/ Arturo Soria 289
Madrid 28033

TURKEY

Milli Savunma Bakanlığı (MSB)
ARGE ve Teknoloji Dairesi
Başkanlığı
06650 Bakanlıklar – Ankara

UNITED KINGDOM

Dstl Knowledge and Information
Services
Building 247
Porton Down
Salisbury SP4 0JQ

UNITED STATES

NASA Center for AeroSpace
Information (CASI)
7115 Standard Drive
Hanover, MD 21076-1320

SALES AGENCIES

NASA Center for AeroSpace Information (CASI)

7115 Standard Drive
Hanover, MD 21076-1320
UNITED STATES

The British Library Document Supply Centre

Boston Spa, Wetherby
West Yorkshire LS23 7BQ
UNITED KINGDOM

Canada Institute for Scientific and Technical Information (CISTI)

National Research Council Acquisitions
Montreal Road, Building M-55
Ottawa K1A 0S2, CANADA

Requests for RTO or AGARD documents should include the word 'RTO' or 'AGARD', as appropriate, followed by the serial number (for example AGARD-AG-315). Collateral information such as title and publication date is desirable. Full bibliographical references and abstracts of RTO and AGARD publications are given in the following journals:

Scientific and Technical Aerospace Reports (STAR)

STAR is available on-line at the following uniform resource
locator: <http://www.sti.nasa.gov/Pubs/star/Star.html>
STAR is published by CASI for the NASA Scientific
and Technical Information (STI) Program
STI Program Office, MS 157A
NASA Langley Research Center
Hampton, Virginia 23681-0001
UNITED STATES

Government Reports Announcements & Index (GRA&I)

published by the National Technical Information Service
Springfield
Virginia 2216
UNITED STATES
(also available online in the NTIS Bibliographic Database
or on CD-ROM)